The University Of Sheffield.

Nitrogen-Rich Heterocycles – A Study of the Use of Tetrazole and Pentazole as Ligands

By:

Benjamin Francis Crozier

A thesis submitted in partial fulfilment of the requirements for the degree of Doctor of Philosophy

The University of Sheffield
Faculty of Science
School of Chemistry

1st June 2016

Acknowledgments

Firstly, thanks to all the technical staff who have made it possible to get all the supporting analytical data for this thesis. Thanks to all members of the Portius research group, past and present, who have been excellent soundboards for ideas, mentors for difficult concepts and team-mates in the summer 6-a-side football tournament. Thank you to Peter for his expertise, advice and drive, without which I would not have completed this investigation. Finally thank you to all my family and friends for their encouragement, especially Naomi who despite phoning me during my PhD interview has been the constant supporting presence during this testing time.

Abbreviations

4-MPTZ	4-methylphenyltetrazole
MOF	Metal Organic Framework
HOMO	Highest Occupied Molecular Orbital
TNT	Trinitrotoluene
HEDM	High Energy Density Material
ESI-MS	Electrospray Ionisation Mass Spectrometry
atrz	4,4'-azo-1,2,4-triazole
PPN	Bis(triphenylphosphine)iminium
^{mes}nacnac	Mesityl beta-diketiminate
FTIR	Fourier Transform Infra-Red
NMR	Nuclear Magnetic Resonance
THF	Tetrahydrofuran
DCM	Dichloromethane
M.p.	Melting point
Cp*	Pentamethylcyclopentadienyl
TMS-	Trimethylsilyl-
DSC	Differential Scanning Calorimetry
Gd	Guanidinium
py	Pyridine
bipy	2,2-bipyridine
DMAP-	Dimethylaminophenyl-
TBA	Tetrabutylammonium
OPP	Oxophenylpentazole
WCA	Weakly Co-ordinating Anion

Abstract

Conventional energetic materials are often hazardous to health, which can be caused by the inclusion of heavy metals or the release of harmful by-products such as perchlorates. Nitrogen-rich compounds have seen intensive research in the hope that they offer a “green” alternative to the energetic materials commonly used today.

The initial area of concentration of this investigation focussed on the refinement of the current preparation of homoleptic hexakistetrazolato main group complexes of the type $(PPN)_2[E(CHN_4)_6]$ (E = Si, Ge) in order to obtain accurate analytical data. This preparation did not produce the unreported tin analogue $(PPN)_2[Sn(CHN_4)_6]$. The reaction between 1-trimethylsilyl-tetrazole and tin(IV) fluoride provided the required driving force to allow the isolation and characterisation of $(PPN)_2[Sn(CHN_4)_6]$. This preparative technique was subsequently extended to the low-valent tin(II) fluoride in order to produce the first reported homoleptic tetrazolato tin co-ordination polymer. An additional route to the homoleptic poly(tetrazolato) main group compounds was also explored. It has been shown that by heating an acetonitrile solution containing main group co-ordinated azides, the azide groups can undergo a [3+2] cycloaddition, producing a methyltetrazolate ligand. This transformation has been previously observed for a series of bis(tetrazolato) diazido silicon complexes $Si(N_3)_2(5\text{-}R\text{-}CN_4)_2(L)$, where R = CH_3, C_6H_5, and L = 2,2’-bipyridine, 1,10-phenanthroline. However the transformation has not been catergorically proven for the homoleptic compounds. For this reason various azido co-ordinated species were synthesised and reacted with acetonitrile. The resulting precipitates were analysed using infra-red (IR) and nuclear magnetic resonance (NMR) spectroscopy.

A final study attempted the isolation of a free pentazole ring through the reduction of arylpentazoles. The reducing agents sodium naphthalenide and the (^{mes}nacnac)Mg−Mg(nanac^{mes}) dimer were used, whilst the potential for selective cleavage of the C-N bond and stabilisation of the produced pentazolate anion was evaluated using IR and ^{1}H NMR spectroscopy. In parallel to this various re-crystallisations of arylpentazoles were attempted in order to widen the availability of pure starting materials.

Contents

1. Introduction

1.1 Synthesis of 1*H*-tetrazole

1*H*-tetrazole, a five-membered ring consisting of four nitrogen atoms and a single carbon, was first prepared via a reaction between dicyanophenylhydrazine and nitrous acid, yielding 2-phenyl-2*H*-tetrazole-5-carbonitrile. A convenient synthesis for the 5-substituted tetrazoles can be achieved through the reaction between cyanide and azide via a [1+3] dipolar cycloaddition.[1] However, for the preparation of 1*H*-tetrazole, this reaction would require hydrogen cyanide, an extremely toxic compound. A reaction between sodium azide and ammonium chloride in the presence of triethyl orthoformate yields 1*H*-tetrazole, without the danger posed by the production of hydrazoic acid, [2] whilst also avoiding the use of hydrogen cyanide.[1]

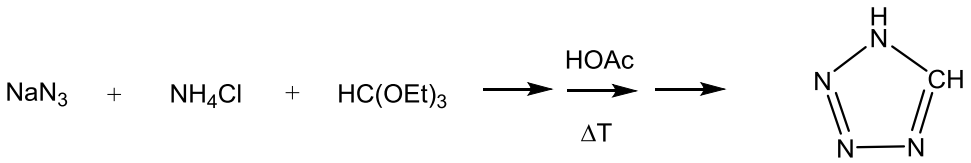

Scheme 1 – Modernised synthesis of 1*H*-tetrazole.[3]

The triethyl orthoformate, $HC(OEt)_3$, is the key reagent in this particular synthesis, as the ethoxy groups are efficient leaving groups in a protic environment. Following protonation by acetic acid, the C-O bond can be broken, allowing for sequential carbonium formation, which in turn allows for nucleophilic attack (scheme 2).

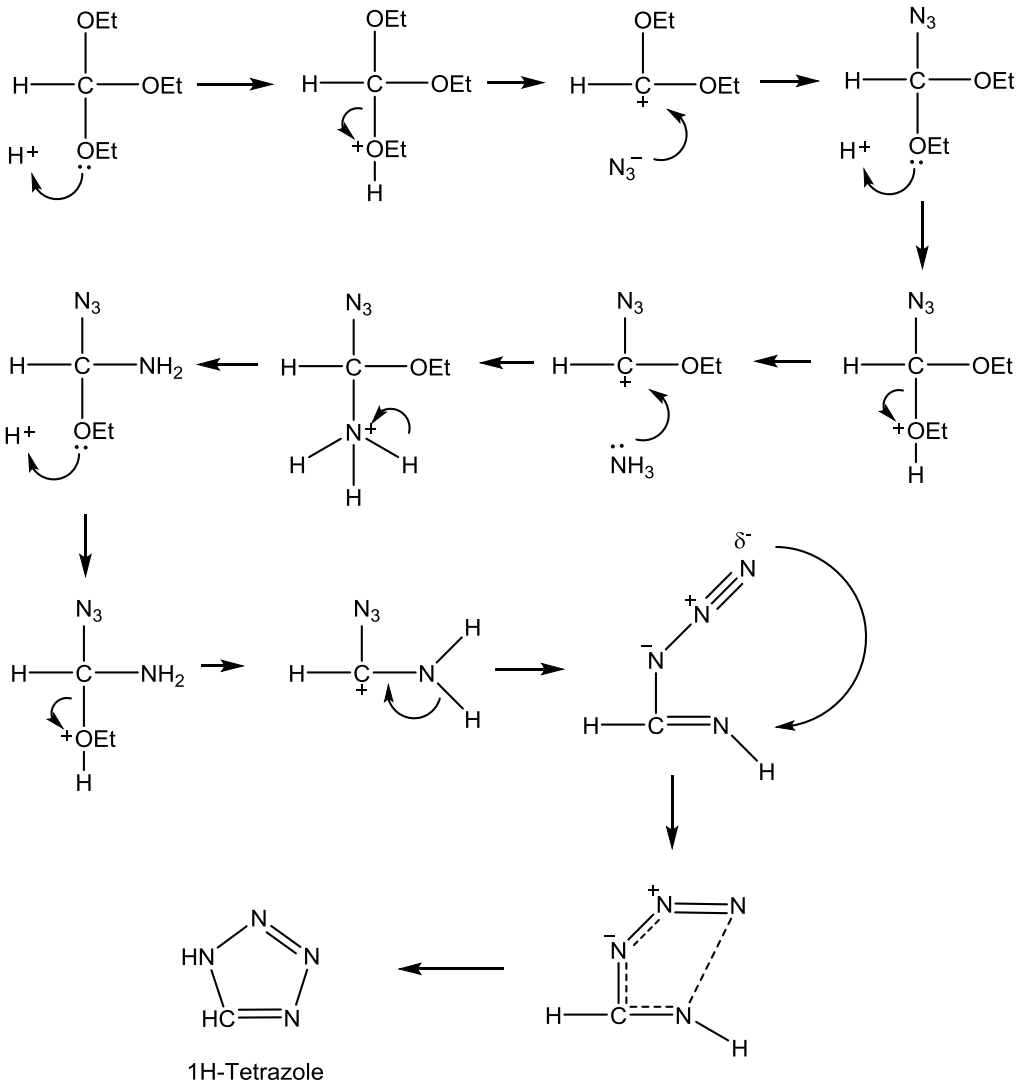

Scheme 2 – Mechanism for the formation of 1*H*-tetrazole from the reaction between NaN_3, NH_4Cl and triethyl orthoformate.[3]

The proton at the *N*-1 position is relatively acidic, with a pK_a of 4.9. This allows for its reaction with basic solutions to produce salts, providing a simple route in diverse areas of chemistry: co-ordination chemistry, pharmaceuticals,[3] components in explosives and historically in photography.[4] Deprotonation of 1*H*-tetrazole using base produces a tetrazolate salt.[4] The formation of metal tetrazolato complexes is well known for Li, Na, K, Rb, Cs and Sr,[2] accomplished through the combination of tetrazole and the corresponding metal hydroxide (Li, Na, Rb, Sr) or carbonate (K, Cs). The ammonium and hydrazonium tetrazolato salts can also be prepared by reacting the tetrazole with ammonia and hydrazinium hydroxide, respectively.[2]

1.2 Tetrazole-based Co-ordination Complexes

In addition to the extensive chemistry that can be realised through the functionalisation of the tetrazole ring, the molecule in question can also be associated to a metal centre. This type of compound is often referred to as a co-ordination complex, and can take a variety of forms. This diversity stems from tetrazole's ability to form bonds through a number of atoms. A co-ordination complex can refer to a standalone complex or more complicated extended structure in which bridging ligands join individual co-ordination centres together. These are described as co-ordination polymers. Franke et al. have shown that reacting metal(II) tetrafluoroborates with 1-alkyltetrazoles will produce complexes with the general formula $[ML_6](BF_4)_2$ where M = Mn, Co, Cu, Zn and L = 1-methyltetrazole, 1-ethyltetrazole and 1-propyltetrazole.[5] The same preparative technique can also be applied to ferrous iron to generate the $[FeL_6](BF_4)_2$ series of complexes (L = 1-methyltetrazole, 1-ethyltetrazole, 1-propyltetrazole and 1-isopropyltetrazole).[7]

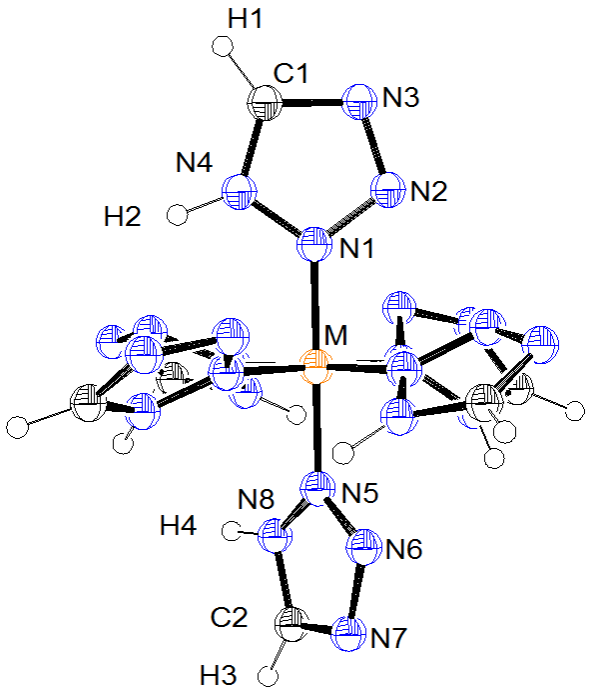

Figure 1 – General structure of ML_6 within the complex $[ML_6](BF_4)_2$ where M = Mn, Co, Cu, Zn and L = 1-methyltetrazole, 1-ethyltetrazole and 1-propyltetrazole. All tetrazole molecules are bound in the κ(N2) bonding mode. Diagram reproduced from Ref. 7.

These poly(tetrazolyl) iron complexes are a very interesting class of materials due to their ability to exhibit spin crossover events triggered by light.[6,7] Similarly, thermal spin transitions have been shown to occur within mixed-metal tetrazole complexes containing iron and zinc.[8] Molybdenum(II) azides react with dipolarophiles such as tetracyanoethylene, 4-nitrobenzonitrile, acrylonitrile, diethylacetylenedicarboxylate, and carbon disulfide.[9] This reaction results in [1+3] dipolar cycloaddition, made possible by the dipolar nature of the azide ligand. This is the same process as seen for the preparation of 1*H*-tetrazole as seen on pg. 2. The generation of Mo-bound tetrazolate is achieved through the use of nitriles as the dienophile.

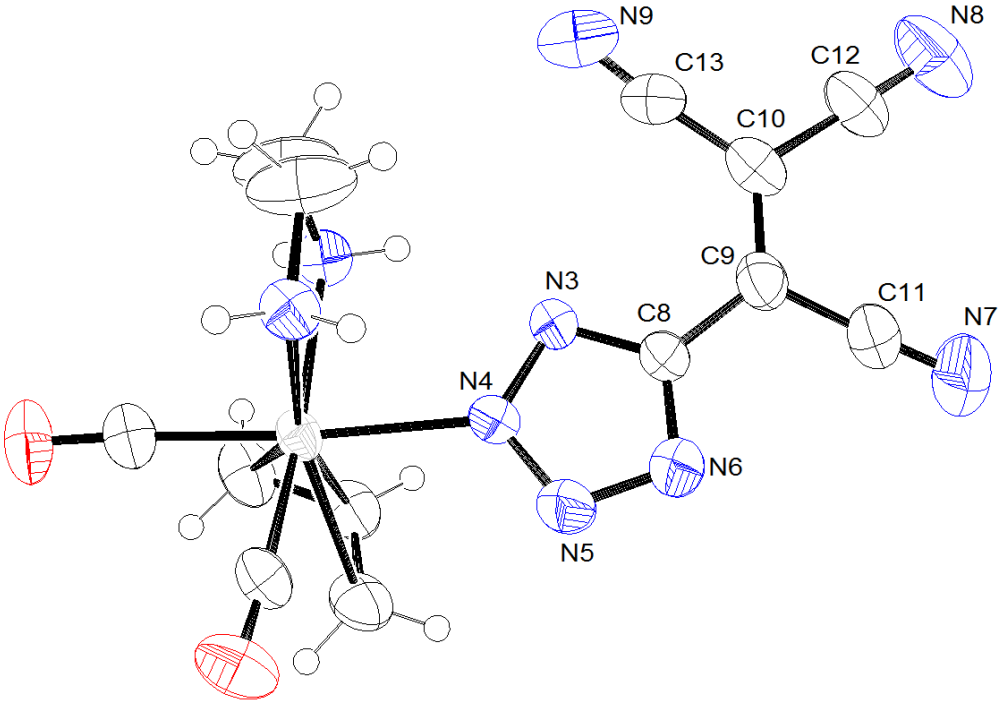

Figure 2 – X ray structure of Mo(η^3-C_3H_5)$(CO)_2$(en)($N_4C(C(CN))(C(CN)_2)$), rotated to emphasise the attachment of the tetrazolate ring. Again the binding mode is κ(N2). Diagram reproduced from Ref. 10.

The more exotic transition metals exhibit more unusual characteristics. Ruthenium tetrazole complexes are electroluminescent; furthermore they can be "tuned" through the exchange of the auxiliary ligands.[10] A yellow emission can be achieved through the attachment of 2,2'-bipyridine, whilst the analogous complex with 1,10-phenanthroline emits green light.

Co-ordination polymers can also be described as a form of co-ordination complex. These are elegant, extended structures in which the metal centre is bound by ligands that possess the ability to further interact with adjacent co-ordination centres. Depending on the nature of the co-ordinating ligand, the extended structure can exist as a 1D, 2D or 3D architecture.[11] Intricate frameworks utilising the tetrazole unit can be formed due to the ligand's many possible co-ordination modes. The tetrazole ligand can bind through 12 different co-ordination modes, illustrated in figure 3.

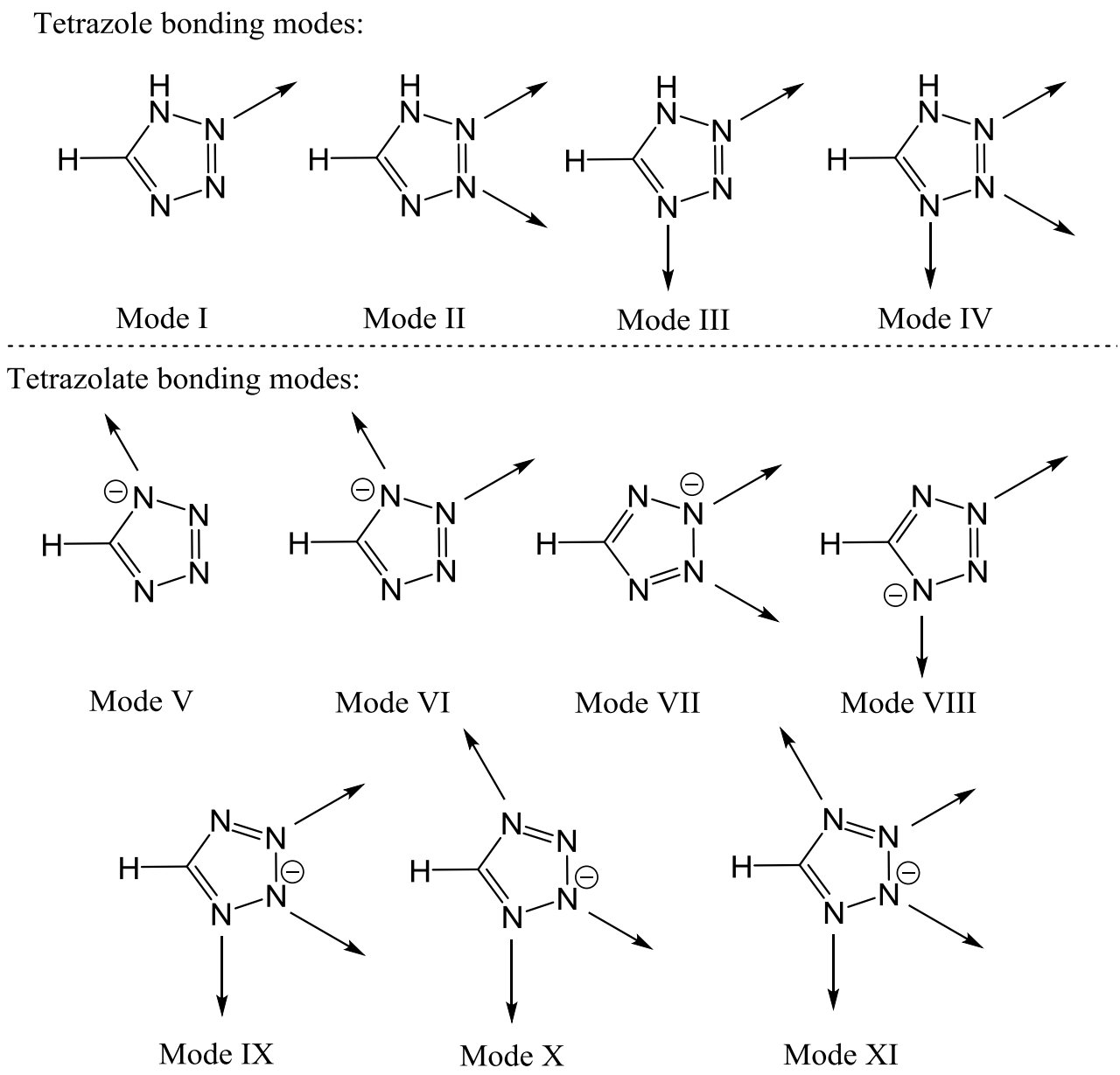

Figure 3 – Various co-ordination modes of the tetrazole and the deprotonated tetrazolato ligands.[12]

As shown in the above figure, the neutral 1*H*-tetrazole ring can bind as a mono-, di- and tri-coordinate ligand. Upon deprotonation the tetrazolate unit exhibits additional flexibility, binding to one, two, three or four different metal centres. This binding ability stems from the electron-rich nature of the ligand. Each co-ordinating nitrogen atom is sp^2 hybridised, with either a lone pair or negative charge available for co-ordinating to a metal centre.

The [2+3] cycloaddition reaction of sodium azide with acetonitrile in the presence of $Zn(ClO_4)_2$ can be used to synthesise two example of a tetrazolate-based co-ordination complex possessing a zinc metal centre.[13] The heteroleptic complex $\{Zn(CH_3CN_4)_2\}_n(H_2O)_4$ contains the in situ synthesised 5-methyltetrazolato ligand, which acts as a tridentate bridging ligand, with each individual ligand binding to three zinc metal centres.[14] Conversely, each zinc atom is bound to six 5-methyltetrazolato ligands, forming an octahedral co-ordination environment. The ability of the 5-methyltetrazole ligand to bind to three individual zinc centres allows the structure of $\{Zn(CH_3CN_4)_2\}_n(H_2O)_4$ to extend into three dimensions as shown in figure 4.

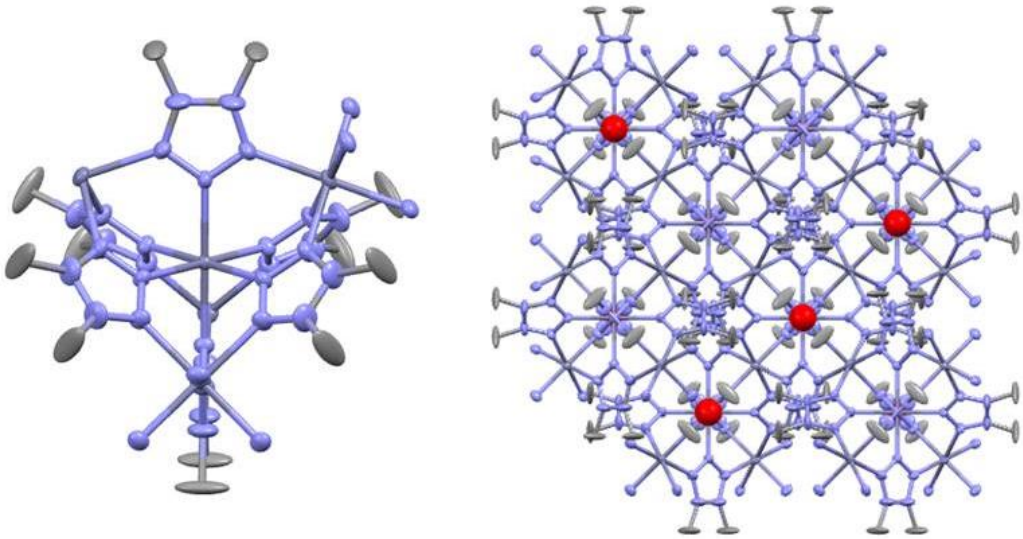

Figure 4 – Octahedral geometry at the Zn metal centre (left) and the extended co-ordination network (right) of the $\{Zn(CH_3CN_4)_2\}_n(H_2O)_4$ 3D network. Hydrogen atoms are omitted for clarity. Diagram reproduced from Ref. 14.

This investigation also yielded other examples of homoleptic tetrazole-containing co-ordination polymers. This describes a complex which contains a metal centre with a single type of ligand. These are traditionally much less common and are therefore of higher structural interest. The reaction of $Zn(ClO_4)_2$, NaN_3 and 4-methylbenzonitrile yields $\{Zn(4\text{-}MPTZ)_2\}_n$ where 4-MPTZ = 4-methylphenyltetrazole.[14] Using X-ray crystallography it was again possible to determine the extended network of the co-ordination system. In contrast to the previously discussed $[Zn(CH_3CN_4)_2]_n(H_2O)_4$, each metal centre within $\{Zn(4\text{-}MPTZ)_2\}_n$ has a distorted tetrahedral environment. It is likely that the cause of this geometric shift is the larger steric bulk of the 4-MPTZ ligand in comparison to the simpler 5-methyltetrazole. Each 4-MPTZ ligand acts in a bidentate fashion and each Zn metal centre is connected to three other metal centres through the bidentate 4-MPTZ ligands. This produces a 2D network that can be seen in figure 5. The network illustrated in the below figure highlights how two adjacent frameworks can interact with each other, via π-π stacking.

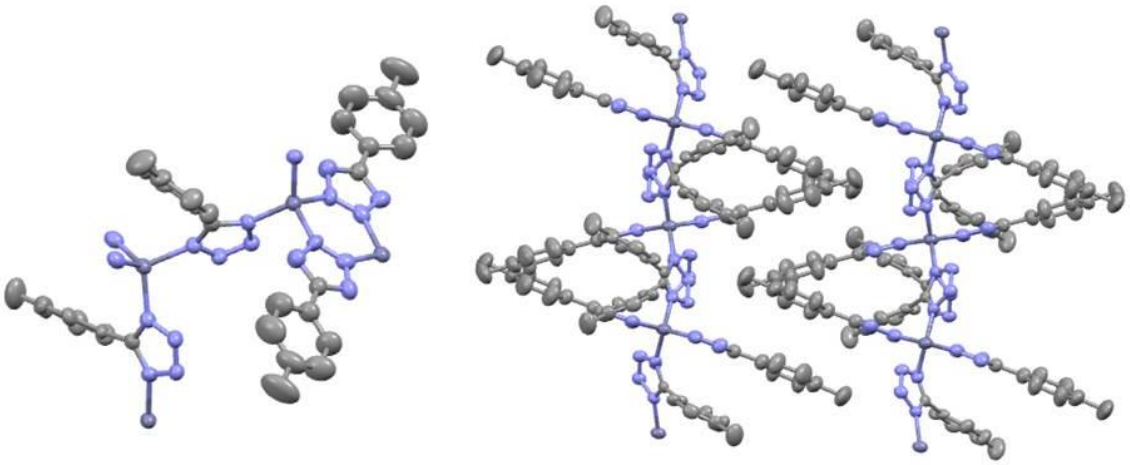

Figure 5 – Close view of the tetrahedral co-ordination geometry (left) and the extended framework (right) of the $\{Zn(4\text{-}MPTZ)_2\}_n$ co-ordination polymer. Hydrogen atoms omitted for clarity. Diagram reproduced from Ref. 14.

The simplest example of a zinc-tetrazole co-ordination polymer, $\{Zn(CHN_4)_2\}_n$, can be synthesised through the reaction between $Zn(OAc)_2$ and 1*H*-tetrazole.[14] Examination of the crystalline structure of $\{Zn(CHN_4)_2\}_n$ reveals that it forms an extended 3D network, with the bidentate tetrazole ligand connecting two adjacent zinc centres. Each co-ordination centre is bound to four individual ligands, producing a distorted tetrahedral geometry.

This geometry was observed within the $\{Zn(4\text{-MPTZ})_2\}_n$ co-ordination polymer and its presence was rationalised by the larger steric bulk of the 4-MPTZ ligand. However, the simple tetrazole ring is much smaller and the distorted tetrahedral geometry remains. It was hypothesised that this observation could be explained by the different reaction pathways. The direct reaction between $Zn(OAc)_2$ and 1*H*-tetrazole will produce the thermodynamically more stable tetrahedral co-ordination environment.[14]

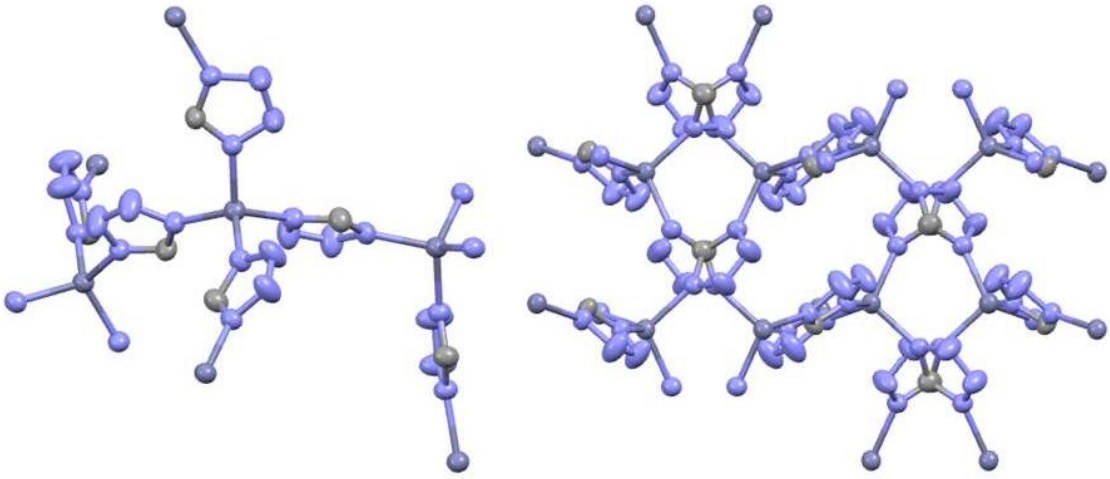

Figure 6 – Close view of the co-ordination geometry (left) and the extended framework (right) of the $[Zn(CHN_4)_2]_n$ co-ordination polymer. Hydrogen atoms omitted for clarity. Diagram reproduced from Ref. 14.

There are also interesting examples of extended tetrazole networks that utilise cadmium as the co-ordination centre. A synthetic study performed by Lu in 2006 produced two unique 3D tetrazole-based MOF systems.[14] The first example is the $[Cd_5(CHN_4)_9(OH)(H_2O)]_n \cdot 5nH_2O$ framework, synthesised through the simple reaction between the $Cd(NO_3)_2$ hydrate and 1*H*-tetrazole in water; another example which uses 1*H*-tetrazole as a direct reagent rather than relying upon its in situ generation. The active tetrazole agent is the deprotonated tetrazolate anion, which can co-ordinate to the Cd metal centre.

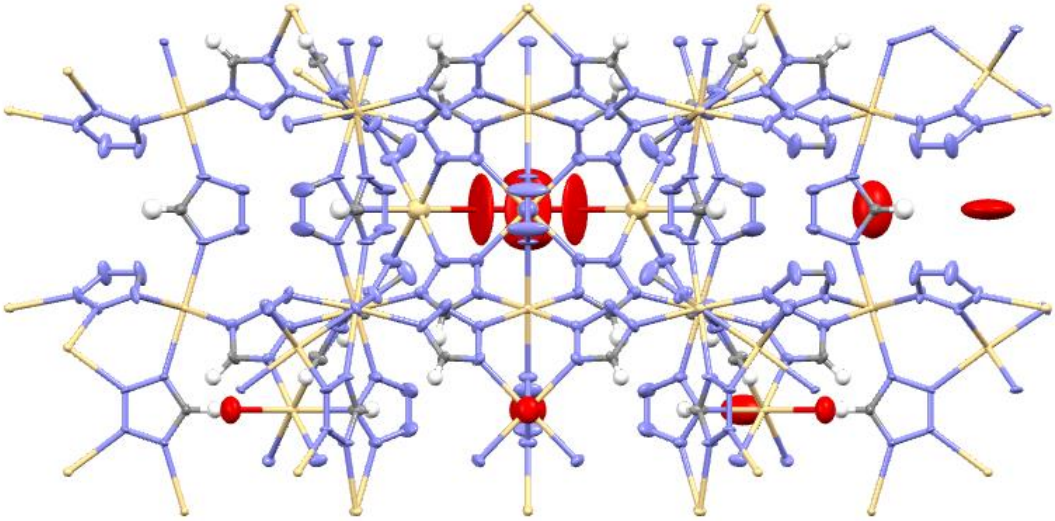

Figure 7 – Extended 3D network of the $[Cd_5(CHN_4)_9(OH)(H_2O)]_n \cdot 5nH_2O$ co-ordination polymer, viewed along the *c* axis. Diagram reproduced from Ref. 15.

The $[Cd_5(CHN_4)_9(OH)(H_2O)]_n \cdot 5nH_2O$ network contains five crystallographically independent Cd atoms.[15] Each of these is orientated into a distorted octahedral co-ordination geometry, with the tetrazole ligands bound through a variety of co-ordination modes. This example illustrates perfectly the attractive qualities of the tetrazole ring; its co-ordination flexibility allows for the generation of elegantly arranged co-ordination networks. The second framework $[Cd_5(5\text{-}NH_2CHN_4)_9(NO_3)]_n \cdot 3nH_2O$ uses analogous reaction conditions to the synthesis of $[Cd_5(CHN_4)_9(OH)(H_2O)_n \cdot 5nH_2O$ but exchanges 5-aminotetrazole for the un-substituted 1*H*-tetrazole.[15] This results in 5-aminotetrazolate ligands bridging between the two independent Cd centres. The type of bonding to each metal centre is different, with the 5-aminotetrazolate ligands binding through co-ordination modes III for Cd(1) and IV for Cd(2).[15] As observed in $[Cd_5(CHN_4)_9(OH)(H_2O)]_n \cdot 5nH_2O$, the geometries of the individual metal centres are again distorted octahedral.

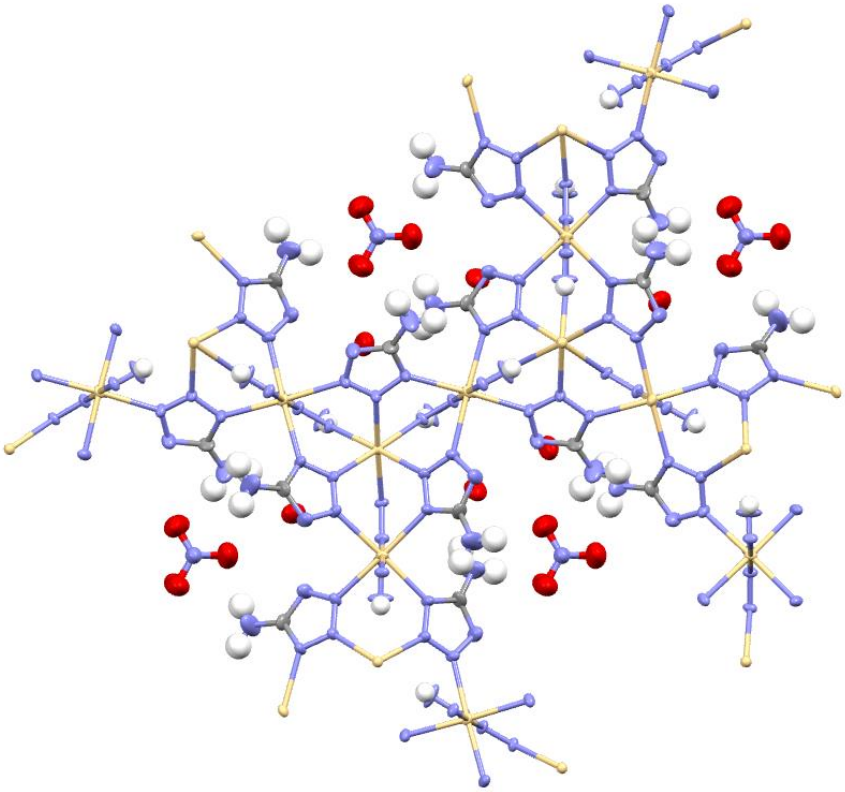

Figure 8 – Extended structure of the $[Cd_5(5\text{-}NH_2CHN_4)_9(NO_3)]_n \cdot 3nH_2O$ framework, viewed along the c axis. The distorted octahedral geometries at each Cd metal centre are clearly visible, as are the bridging 5-aminotetrazolate ligands. Diagram reproduced from Ref. 15.

The synthesis of co-ordination polymers can also be extrapolated to include copper as the metal centre.[15] $[Cu_2(CHN_4)_3(OH)]_n$ contains a single crystallographically unique Cu(II) co-ordination site, which orientates into the uncommon distorted square pyramidal geometry. Four tetrazolate groups are bound equatorially via the co-ordinations mode VII (See figure 3) meanwhile the hydroxyl group is bound in the single axial bonding position. The 3D network is composed of 2D layers that are connected through the oxygen atoms of the axial hydroxyl ligands and the multidentate tetrazolate groups.

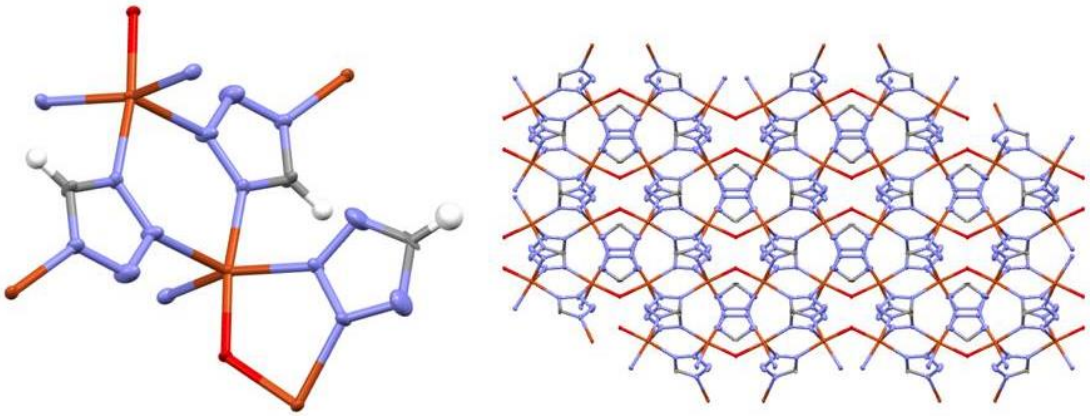

Figure 9 – Unusual square-based pyramidal co-ordination geometry (left) and the extended framework (right) of the $[Cu_2(CHN_4)_3(OH)]_n$ co-ordination polymer. Diagram reproduced from Ref. 16.

The investigation also produced an analogous extended 3D system $[Cd_2(CHN_4)_3Br]_n$, utilising a cadmium metal centre and bromide anions rather than the hydroxyl ligand. Within this framework there are two distinct distorted octahedral co-ordination centres. The first consists of a cadmium centre bound by six tetrazolate nitrogen atoms (**a**) whilst co-ordination centre **b** is co-ordinated by five nitrogen atoms belonging to individual tetrazolate ligands but also the bromide ion.

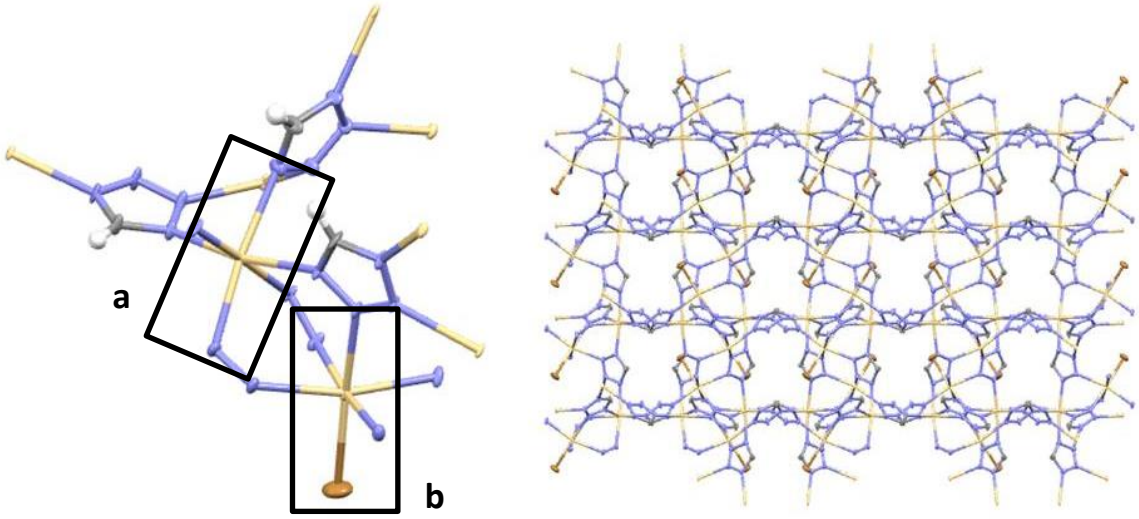

Figure 10 – Two distinct co-ordination geometries (left) and the extended framework (right) of the $[Cd_2(CHN_4)_3Br]_n$ co-ordination polymer. Diagram reproduced from Ref. 16.

1.3 Co-ordination of 1*H*-tetrazolate to Main Group Elements

Tetrazole-containing co-ordination complexes based upon transition metal centres are well known and as discussed in the previous section have been extensively studied. Extrapolation to the main group is a pathway that has not been investigated in any detail. A select few examples exist encompassing a main group element bound to a single tetrazolate ring.[16–18] $Si(CH_3)_2(N_4CH)_2$ is perhaps the only fully characterised main group poly(tetrazolato) compound in the literature.[16] The reaction between 1*H*-tetrazole and $SiMe_2Cl_2$ in the presence of 2,6-lutidine yields the bis(1-tetrazolato)dimethylsilane (Scheme 3).

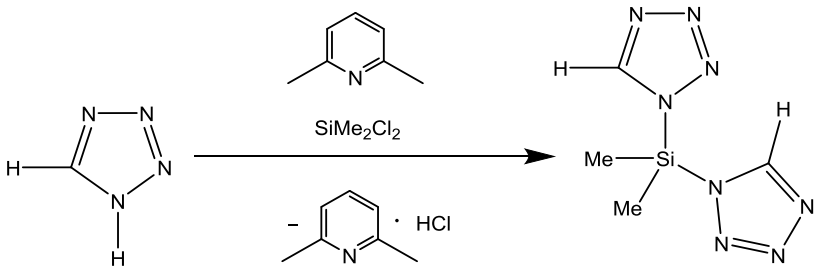

Scheme 3 – The generation of a poly(tetrazolato) silane complex.[16]

Elements such as silicon, tin and germanium are attractive due to their capacity to hypercoordinate. This phenomenon describes the ability for an element to exceed the formal requirement for eight valence electrons, and was first proposed by Jeremy Musher.[19] The traditionally accepted definition for hypervalence concentrates upon the availability of low-lying, unfilled *d*-orbitals, which can be occupied by the additional valence electrons. The bonding within hypervalent molecules can be explained with an example, such as sulphur hexafluoride (SF_6). The valence-bond theory approach is limited in the sense that it assumes that each atomic orbital on the central atom (sulphur) can only participate in one bond. Using molecular orbital theory it is much easier to illustrate the orbital interactions that are taking place. Using the *s*- and *p*- orbitals of the sulphur and one *p*- orbital from each of the fluoro- ligands it is possible to construct ten molecular orbitals (figure 11).

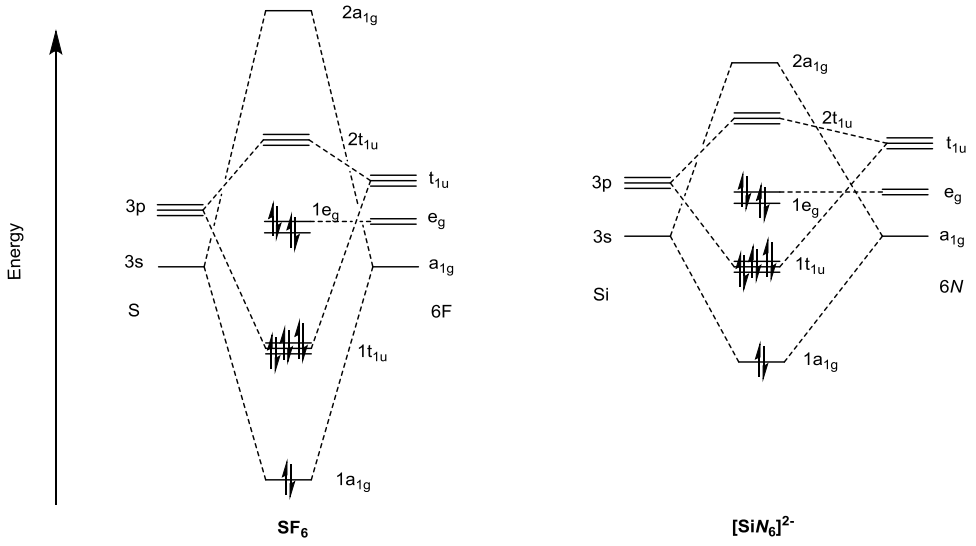

Figure 11 – Molecular orbital diagram for SF_6,[20] compared to a molecular orbital diagram for the complex type $[SiN_6]^{2-}$ (*N* = nitrogen bound ligand).

There are four fully occupied bonding orbitals, giving a bond order of four. As there are six bonds it indicates that each S-F bond has a bond order of less than one. This is possible due to the delocalisation of the molecular orbitals, which allows an electron pair to contribute to the bonding of more than two atoms.[20] This will result in each S-F bond being longer than its equivalent two centre two electron (2c2e) bond. This is the typical covalent bond in which two atoms share two electrons. When extrapolated to potential hypervalent silicon-nitrogen complexes of the type SiN_6, the molecular orbital diagram will be distorted. The energy level of the atomic orbitals of silicon and nitrogen will be energetically higher than those of sulphur and fluorine. Also, the smaller electronegativity difference between silicon and nitrogen when compared to sulphur and fluorine will cause the molecular orbitals to be closer in energy. The electrons that cause the (2−) charge on the complex reside within the e_g non-bonding orbital, which is energetically the highest occupied molecular orbital (HOMO). The advantage of such a complex is that the (2−) charge upon the complex would allow the formation of a salt. This adds important flexibility into the investigation; the use of an nitrogen-rich cation would produce an energetic, high-nitrogen salt. Conversely the use of an unreactive, carbon-rich cation would allow the safe study of the main group co-ordination centre.

1.5 High Energy Density Materials (HEDMs)

The potential of hypervalent compounds containing multiple tetrazolato ligands becomes apparent when the high nitrogen content of the tetrazole ring is taken into account. At 80% nitrogen by mass, 1*H*-tetrazole has the unusual combination of high nitrogen content and relative kinetic stability in comparison to other high-nitrogen compounds. For this reason, tetrazole and compounds containing tetrazole groups are commonly found in the preparation of next generation high energy density materials.

Energy density is defined as the energy released per unit volume or mass of the material. The Gibbs free energy of certain compounds is easily released, due to a lower energy barrier to decomposition. Due to their highly energetic decomposition to thermally stable products, these compounds are described as highly endothermic. Energetic materials can therefore act as an "energy sink", storing the energy put into their creation, allowing for its release upon decomposition. It is this large amount of stored chemical energy that gives rise to high energy compounds, allowing for certain endothermically synthesised molecules to be used as propellants, explosives and pyrotechnics. The endothermicity of a compound can be increased via the attachment of explosophoric groups. Explosophoric groups are functional groups that can be attached to relatively unreactive molecules to imbue an energetic nature. Explosophoric groups can be divided into eight types:

$-NO_2$ (nitro), $-ON=O$ (nitrite) and $-ONO_2$ (nitrate)	The three most common explosophoric groups in use. Their popularity stems from their strong explosive nature, due to their ability to form the very stable dinitrogen
$-N=N-$ (azo) and $-N=N^+=N^-$ (azide)	The azo and azide explosophoric groups are also common, again because of the in situ production of dinitrogen.
$-R_nNX_m$	The halogenated nitrogen group (e.g. NI_3).
$-C^-=N^+-O-$	The fulminate group.
ClO_3^- (chlorate) and ClO_4^- (perchlorate)	The chlorate and perchlorate groups, which can be combined with metal cations.
$-O-O-$ (peroxide) and $-O_3$ (ozonide)	The peroxide and ozonide explosophoric groups. Unstable due to the weak O-O bond.
$^-C\equiv C^-M^+$/ C_2^- M^+	Metal bound acetylides.
M*	Pyrophoric metals.

Table 1 – Types of explosophoric groups.

Traditional high energy density compounds such as trinitrotoluene (TNT) are examples of carbon-based HEDMs, meaning the energy is produced via the internal oxidation of the carbon chain.

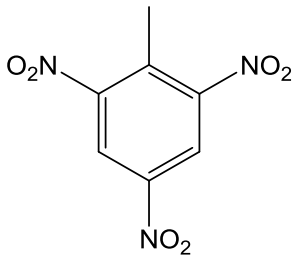

$$2\ C_7H_5N_3O_6 \longrightarrow 3\ N_2 + 5\ H_2O + 7\ CO + 7\ C$$

Figure 12 – Structural representation of trinitrotoluene and a formula for its explosive decomposition.

A problem with the use of TNT is its toxicity. It is an irritant, and long periods of exposure can lead to liver damage. This is a common theme with current HEDMs; the materials produce harmful by-products that contaminate the environment. These include carbon monoxide, perchlorates, lead and highly toxic metal oxides such as BaO and BeO, which are produced by the oxidation of pyrotechnics. BaO has the added danger of being water soluble, facilitating in its entry into groundwater.

The metal pollutants often result from their use as colourants within pyrotechnics, in which certain metal compounds generate the colours required. The consequence of burning these materials is that the size of the polluted area is increased, as the airborne pyrotechnic propels the hazardous compounds over a larger distance.

1.6 Polynitrogen

An alternative to conventional HEDMs are polynitrogen compounds. Elemental nitrogen exists naturally only as molecular nitrogen, N_2. Recently, it was found that under extreme conditions it is possible to synthesise other allotropes of nitrogen. Eremets et al. have generated evidence of an allotrope of nitrogen where all atoms are bound via single covalent bonds.[21] Molecular nitrogen was placed in a laser-heated diamond cell, and was then exposed to temperatures above 2000 K and pressures in excess of 110 GPa. The resultant material is metastable, existing at room temperature under a pressure of 42 GPa.

In theory, other polynitrogen species such as N_5^+ could be stable, as they exist as minima on the potential energy surface.[22–25] As opposed to carbon-based HEDMs, the energy stored within polynitrogen arises from the formation of small, strongly bonded molecules. Decomposition results in dinitrogen, which possesses a bond dissociation enthalpy of 946 kJ mol^{-1}, a huge driving force (see Table. 2). It is clear from the bond enthalpies tabulated, that nitrogen is exceptional amongst elements, forming strong multiple bonds due to the very large difference of the single and triple N–N bond dissociation enthalpies, which are unmatched by any other element.

Bond	Bond enthalpy [kJ mol^{-1}]
H–H	436
C–C	346
C–O	358
C=O	799
C=C	598
C≡C	813
N–N	159
N=N	≈400
N≡N	946

Table 2 – Bond enthalpies of common bonds.[26]

The use of a polynitrogen material would require a large enthalpy of formation, decomposing to yield molecular nitrogen, N_2, which is very stable and environmentally benign. The gaseous nature of the by-product will provide an entropic driving force which in addition to the large enthalpic gain results in a very exothermic and exergonic transformation. Other charged species that consist of only nitrogen are also under investigation. Of particular interest are N_5^+ and N_5^- (the pentazolate anion).

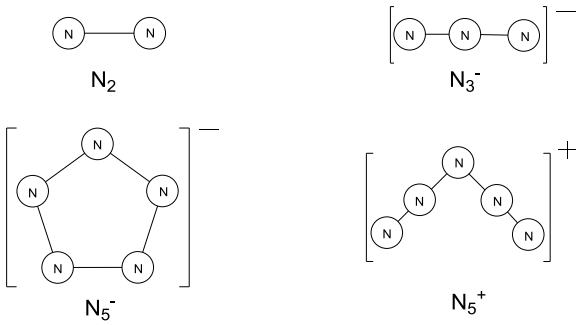

Figure 13 – Ball-and-stick diagrams of certain polynitrogen species.[22]

The N_5^+ cation could in principle provide the ideal counter-ion for the azide, N_3^-. The combination of the two ions would create a salt containing only nitrogen atoms - an interesting prospect.[27] However, its preparation proved to be problematic. Christe et al. succeeded, preparing the N_5^+ ion [25,28] by using $[AsF_6]^-$ as well as $[SbF_6]^-$ and $[Sb_2F_{11}]^-$ as the counter-ions.

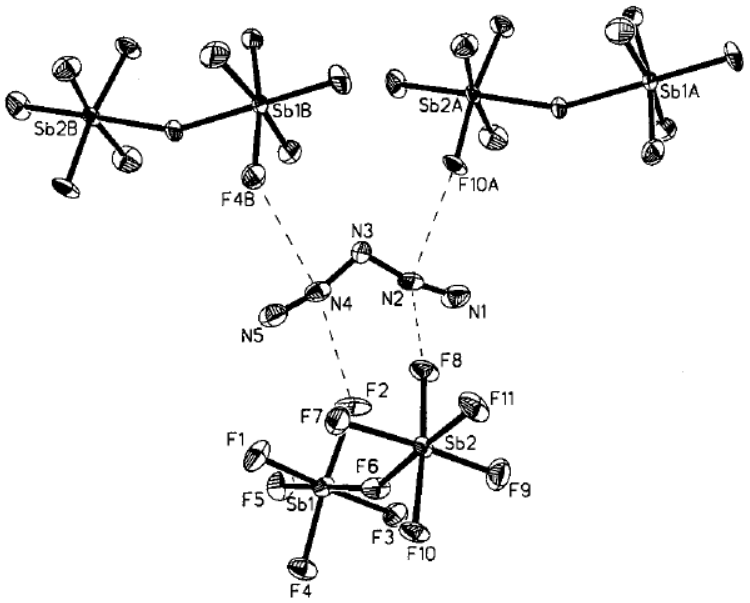

Figure 14 – Best available molecular structure of $N_5^+[Sb_2F_{11}]^-$ obtained by X-ray diffraction, showing the stabilising N_β – F interactions. Figure adapted from Ref. 24.

The $N_2F^+[SbF_6]^-$ salt is produced by a reaction of *cis*-N_2F_2 with AsF_5 [24] and the resulting $N_2F^+[SbF_6]^-$ was combined with hydrazoic acid, HN_3. It is of paramount importance that the reaction mixture is completely free of water, as water hydrolyses the N_5^+ cation, leading to the reformation of SbF_5 which can cause the unwanted side reaction generating $H_2N_3^+[SbF_6]^-$.[29]

$$N_2F^+[SbF_6]^- + HN_3 \xrightarrow[-78^oC \text{ to } 25^oC]{HF} N_5^+[SbF_6]^- + HF$$

Scheme 4 – Method for the production of $N_5^+[SbF_6^-]$. Scheme adapted from Ref. 24.

The isolation of the N_5 cation in 1999[30] sparked a resurgent interest in other theoretically stable all-nitrogen compounds. The pentazolate anion, N_5^-, is a theoretically stable isomer of N_5, with a calculated gas phase decomposition barrier of 22 $Kcalmol^{-1}$.[31] Its presence has been detected using *in situ* analytical methods,[32,33] but despite its theoretical stability, it is yet to be isolated. The synthesis of phenylpentazole via the reaction of the diazonium salt with NaN_3[34] was the first example of an N_5 ring, albeit bound to an aromatic system. The extended electronic resonance provided by the attached phenyl ring improves the stability of the N_5 ring by acting as an electron withdrawing group, allowing for its isolation. Phenylpentazole can be stored at temperatures below -20°C, above which it decomposes to phenyl azide and gaseous nitrogen.

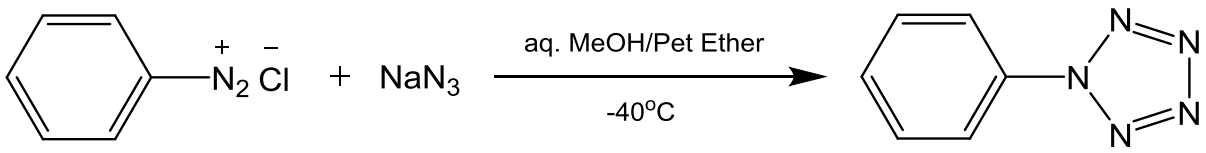

Scheme 5 – Preparation of phenylpentazole from the phenyldiazonium salt.[36]

Functionalisation at the *para*-position of the phenyl ring with an electron-donating group has since been shown to increase the stability of the arylpentazole. Computational analysis provided an explanation for this additional stability.[35] Phenylpentazole is orientated with the pentazole rotated out of the plane with respect to the phenyl ring. The coplanar orientation of the aryl azides that are produced by the decomposition of these compounds suggests that decomposition proceeds via a transition state in which the phenyl ring and the pentazole are coplanar. When extrapolated to *p*-substituted arylpentazoles, it became clear that the attachment of an electron-withdrawing group strengthens coplanar configuration, whilst electron-donating groups allowed easier out-of-plane rotation.[37] It is this subtle structural difference that dictates the order of stability for *p*-substituted arylpentazoles.

Substituted phenylpentazole	Decomposition rate, k x 10^4 /s^{-1}
H	8.4
p-NO_2	59
p-$(CH_3)_2NH^+$	51
p-Cl	12.1
p-CH_3	7.6
p-$(CH_3)_2N$	1.7
p-$(CH_3)_2O$	3.0
p-O^-	0.9
p-OH	3.2

Table 3 – Decomposition rates of various *p*-substituted phenylpentazoles.[36]

The solvent system of reactions utilising arylpentazoles will also have a significant impact upon the lifetime of the reagent, and must be carefully considered. It was found by Ugi that polar solvents can increase the stability of phenylpentazole.[37] This indicates that the decomposition transition state is less polar than the phenylpentazole ground state, and that decomposition would be facilitated by more non-polar solvents.

Solvent system	Decomposition rate, k x 10^4 /s^{-1}
n-hexane	45.2
Toluene	12.4
THF	10.4
Methanol	9.8
Acetonitrile	4.1
Methanol/water	5.7
Acetone	7.7

Table 4 – Solvent dependence of phenylpentazole decomposition rate.[36]

The functionalisation of phenylpentazole allows for further investigation of the pentazole ring system. Inserting a ^{15}N atom into *p*-dimethylaminophenylpentazole allows for the decomposition pathway to be experimentally monitored by ^{15}N NMR spectroscopy.[38] The decomposition results in the *p*-dimethylaminophenyl azide and nitrogen gas, which produces a peak in the ^{15}N NMR spectrum at δ = -73. The presence of *p*-dimethylaminophenyl azide was confirmed using chemical shift data of phenyl azides.[39] However, the measurement before decomposition yields a series of peaks, δ = -324.6 (assigned to the $-N(CH_3)_2$ group) and three peaks that are assigned to the pentazole ring: δ = -80.0 (N-1), δ = -27.1 (N-2) and δ = 4.9 (N-3). The peak at δ = -80.0 is due to a nitrogen atom with three substituents, supporting the presence of a pentazole ring.

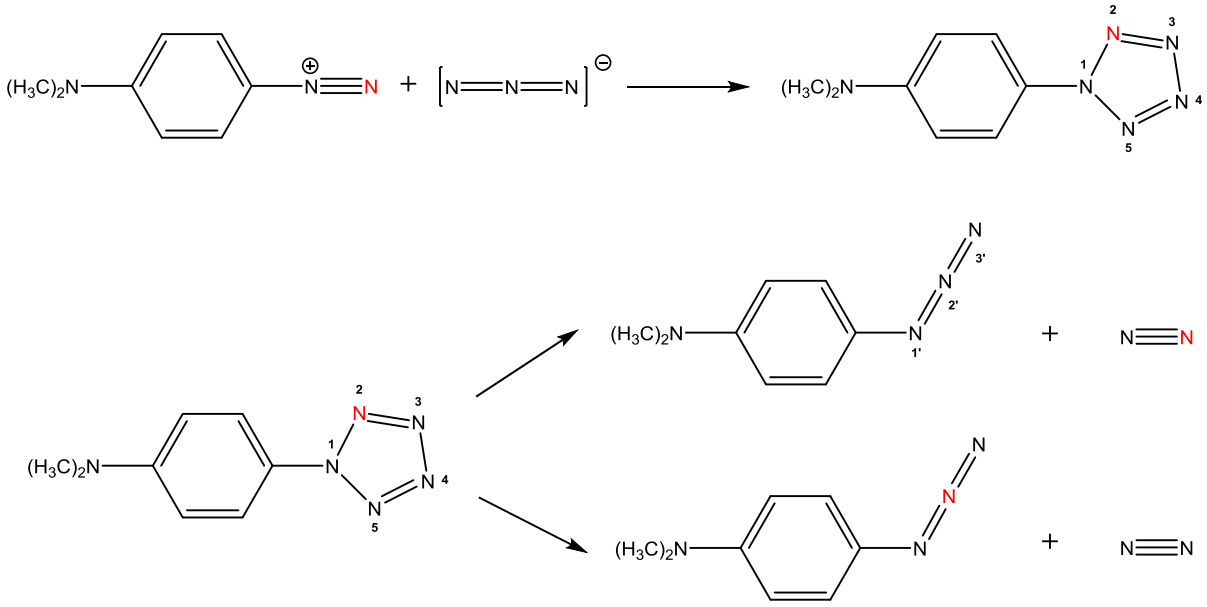

Scheme 6 – Decomposition pathway of ^{15}N labelled *p*-dimethylaminophenylpentazole (N represents ^{15}N). The presence of ^{15}N in both decomposition products supports the pentazole ring structure. Scheme adapted from Ref. 39.

Several attempts have been made to cleave the C-N bond between the substituted phenyl ring and the attached pentazole. The first experimental evidence for the formation of the N_5 anion was obtained following the cleavage of *para*-substituted phenylpentazoles using negative-ion electrospray ionisation mass spectrometry (ESI–MS).[35]

The use of highly π-electron donating groups at the *para* position of the phenyl ring allowed for the maximum amount of electron density transfer to the pentazole ring. This accomplished two things: i) increase the stability of the pentazole ring; and ii) weaken the connecting C-N bond between the phenyl and pentazole ring, allowing for easier cleavage.[33] A peak at *m/z* = 70 could only be caused by a N_5 anion, and its presence was further supported by a peak at *m/z* = 42 which corresponds to an azide group (N_3^-) (see scheme 7). This azide anion could only have resulted from the decomposition of the free pentazole ring, as the *m/z* peaks at 134 and 106 correspond to the 4-azidophenolate ion and a quinone imide after the loss of N_2.

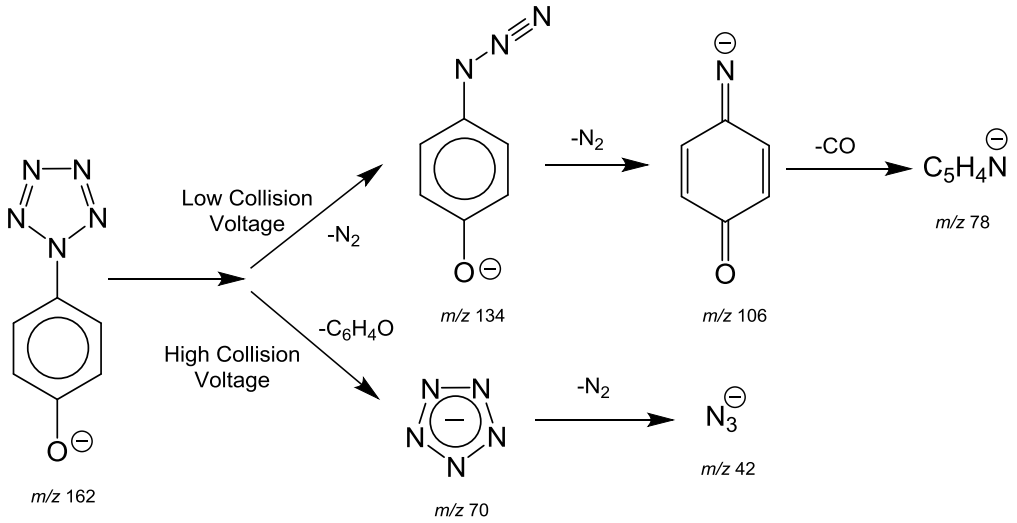

Scheme 7 – Decomposition pathway for the *para*-hydroxyphenylpentazole. Scheme adapted from Ref. 35.

Another investigation focused upon the use of cerium(IV) ammonium nitrate (CAN) as a N-dearylation agent.[32] When combined with an arylpentazole, the CAN will split the azole from the aromatic anchor, producing pentazolic acid, HN_5. Butler et al. used ^{15}N labelling to prove that the azide anions present within the reaction mixture can only have come from degradation of HN_5.[32] However, unequivocal evidence for the isolation of the N_5^- anion has yet to be accepted.[40]

1.7 Nitrogen-Rich HEDMs

While these materials would be ideal candidates for next generation HEDMs, the difficulty involved with their manufacture means that the viable use of a polynitrogen compound remains beyond the horizon. A convenient middle ground is to synthesise compounds that contain a high percentage of nitrogen (>60%). High nitrogen compounds of this nature have similar applications as the hypothetical polynitrogen compounds; they are excellent HEDMs, finding applications within propulsion, engineering, as well as smoke free, "green" pyrotechnics.[41] The energetic nature of nitrogen-rich compounds stem not from the oxidation of a carbon backbone as seen with conventional HEDMs, but from the high positive heats of formation that are associated with their generation.

The heat of formation describes the enthalpy change caused by the creation of one mole of a compound from the chemical elements in their most stable allotrope at standard temperature and pressure. A highly positive heat of formation, i.e. a large amount of energy is required to generate the compound, implies that the compound itself will be energetic. Nitrogen-rich materials always produce the extremely stable dinitrogen upon decomposition, providing another driving force for reaction. As illustrated previously the N≡N bond is far stronger than the analogous single or double bond, explaining the favoured formation of dinitrogen. Nitrogen is in fact exceptional in this regard, as the (N≡N)−(N-N) bond dissociation enthalpy difference is the largest for all homo-atomic bonds. The 1*H*-tetrazole molecule contains by mass almost 80% nitrogen. Its aromaticity causes the relative stability, awarding the molecule the rare balance between stability and performance,[42] explaining its widespread use in the creation of new energetic materials. A common feature of the preparation of these tetrazole-based energetics is the use of 5-aminotetrazole. The versatility of the amino group allows for the compound to be readily converted into various other 5-substituted tetrazoles, a much easier process then the analogous reactions using 1*H*-tetrazole.

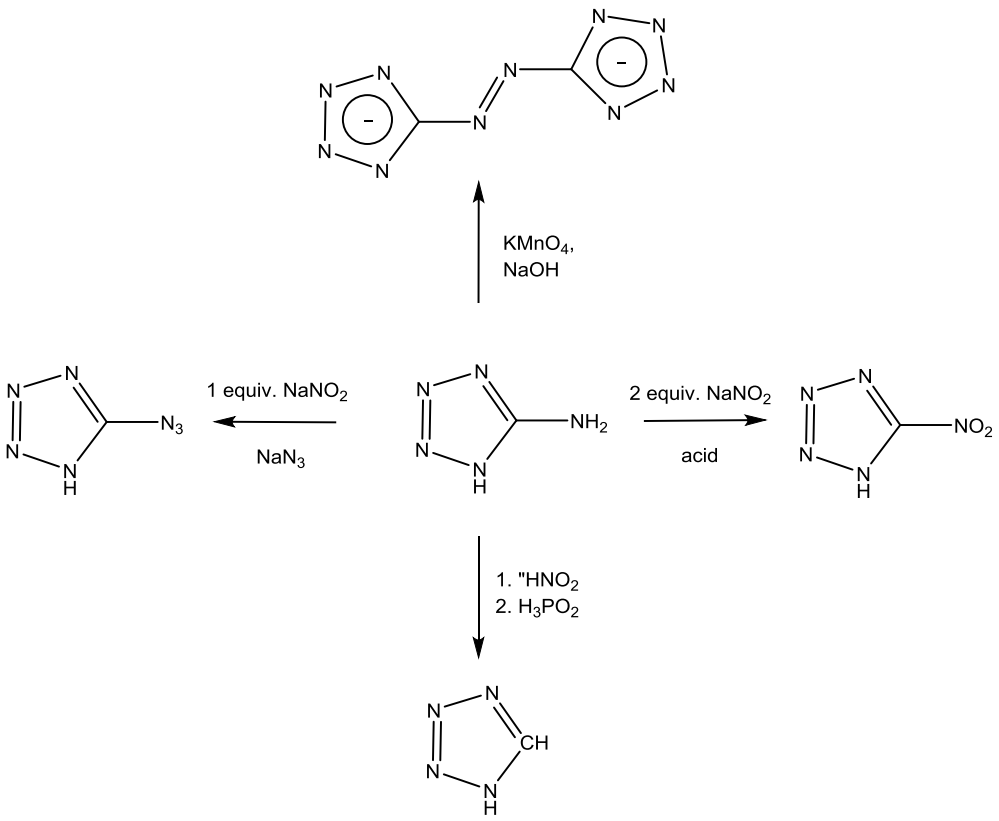

Scheme 8 – Reactions illustrating the use of 5-aminotetrazole as a reagent in the generation of tetrazole-based HEDMs. Scheme adapted from Ref. 43.

The advent of computing has made it possible to evaluate reactions and theoretical compounds without performing experimental chemistry. Computational chemistry programs like the Gaussian suite, which make use of modelling methods such as density functional theory and Hartree-Fock calculations, are quickly becoming invaluable in all research areas. A study into the potential use of tetrazole derivatives as HEDMs calculated the heats of formation (HOF), densities, thermal stability and bond dissociation energies to estimate the performance of various tetrazole based molecules.[43] The variable within the study was the attachment of one or more nitro-groups, a common explosophoric group. It was concluded by the investigation that tetrazole derivatives show promise as HEDMs, and that the addition of nitro groups instigated a large improvement in the predicted explosive performance. T4 was found to have the best explosive performance, possessing both a high density and a high HOF, closely followed by T1, T2 and T3 respectively (see figure 15).

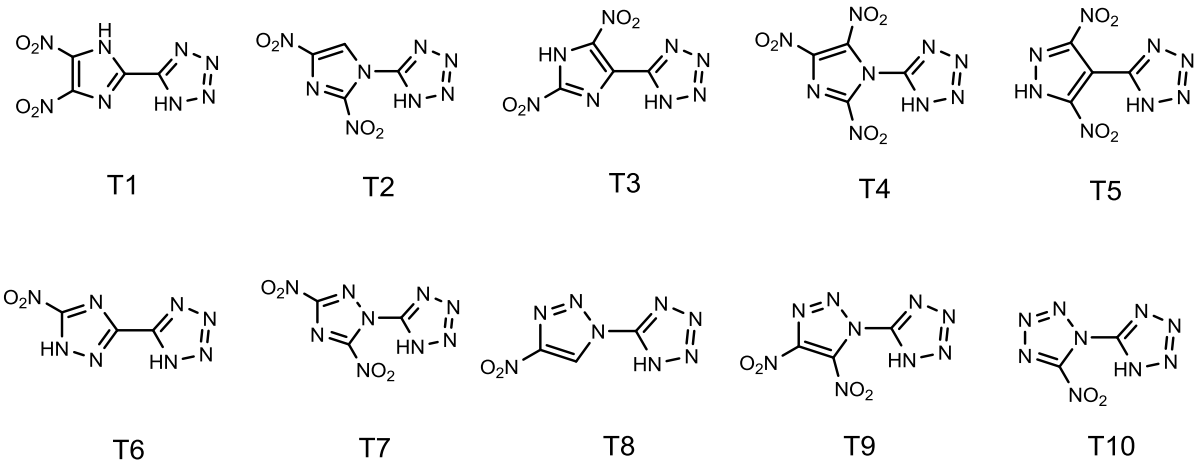

Figure 15 – Tetrazole derivatives used to computationally evaluate the effect of nitro-groups on the explosive performance. Diagram reproduced from Ref. 44.

The attachment of multiple explosophoric groups extenuates their effect. This can be illustrated using the example of 5-(trinitromethyl)-2*H*-tetrazole (Figure 16).[44] 5-(trinitromethyl)-2*H*-tetrazole is a highly energetic compound that is highly sensitive to impact as well as mechanical stress. The thermal stability is moderate; the compound can be heated to approximately 100°C, at which point it violently explodes. As with 1*H*-tetrazole, it is possible to deprotonate 5-(trinitromethyl)-2*H*-tetrazole, which can be combined with a number of cations such as NH_4^+, Rb^+, Cs^+, Ag^+, Cu^{2+}, $N_2H_5^+$ and K^+.[44]

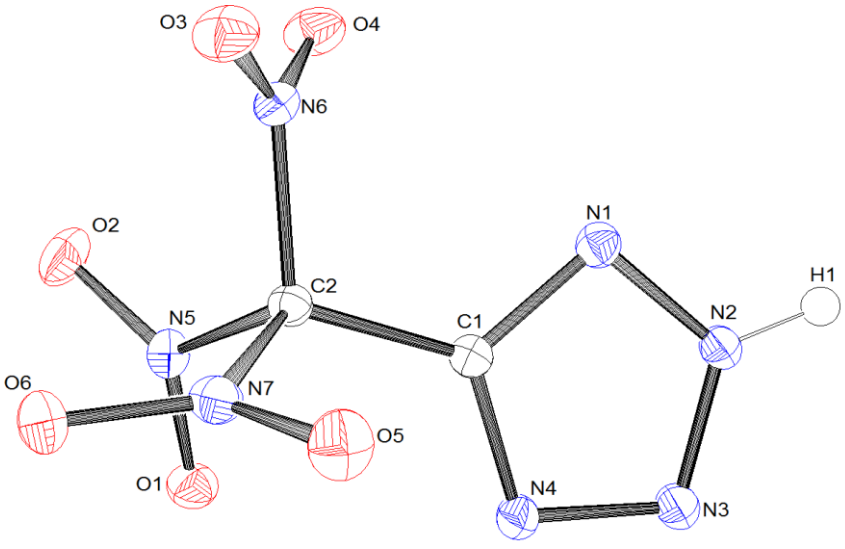

Figure 16 – Vibrational ellipsoid plot of 5-(trinitromethyl)-2H-tetrazole in the crystal. Molecular structure determined by single crystal X-ray diffraction. Diagram adapted from Ref. 45.

Adding complexity, other energetic heterocyclics can be used as a scaffold for the tetrazole rings. An example is the attachment of tetrazole groups to a tetrazine centre, a six-membered ring containing four nitrogen and two carbon atoms.[45] These molecules can be described as “nitrogen-rich polyheterocyclic compounds”.

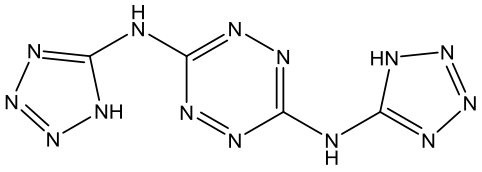

BTATz

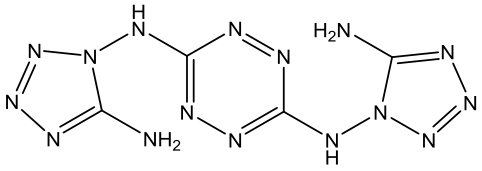

BATATz

Figure 17 – BTATz and BATATz.[45]

Both compounds shown in figure 17 hold promise as next-generation HEDMs, with high values for their heat of formation and kinetic stabilities. 3,6-bis(1*H*-1,2,3,4-tetrazol-5-ylamino)-1,2,4,5-tetrazine, or BTATz[46] forms a solid material, which is insensitive to friction and impact, non-explosive, and decomposes to nitrogen gas when exposed to heat. Unlike previous examples, it shows promise as a gas generant rather than an explosive material. The nitrogen produced displaces the oxygen in the environment, indicating a possible use as a fire retardant.[46]

As discussed previously, tetrazoles can be deprotonated. The anionic nature of the tetrazolate requires a balancing charge, allowing for the introduction of a nitrogen-rich cation. The inclusion of a second nitrogen-rich moiety increases the nitrogen content of the overall salt further, improving the energetic performance. The added aromatic stability of the tetrazolate anion eases the sensitivity concerns that are usually associated with high nitrogen compounds. In addition to this, the lattice enthalpy linked with the formation of a salt inhibits the two species from dissociating, preventing destabilisation of the complex.[47] This describes the enthalpy change upon the formation of one mole of the salt from its constituent gas-phase ions at 0 K.

The coulombic attraction between the oppositely charged ions causes them to combine, releasing energy on the formation of the salt. To revert back to the separate gaseous ions, it is necessary to contribute the same amount of energy that was released on its formation, an energetically expensive transition. Disodium 5,5'-azotetrazolate (Na_2ZT) can be prepared from the oxidation of aminotetrazole with potassium permanganate (Scheme 9).[48]

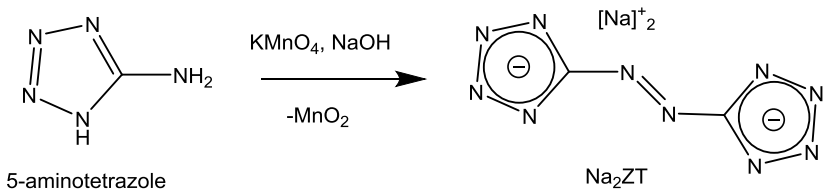

Scheme 9 – Method used for the production of Sodium 5,5'-azotetrazolate (Na_2ZT).[49]

The separated dianion 5,5'-azotetrazolate (2^-) possesses a high nitrogen content of 85%, making it a popular starting point for investigations into the energetic nature of tetrazolate-based salts.[50–52] Metal cations (Na^+, K^+, Ca^{2+}, Ba^{2+}, Ag^+, Hg^+, Pb^{2+}) as well as protonated nitrogen molecules (NH_4^+, NH_3OH^+, $N_2H_6^+$) have been combined with the energetic anion. [49] The salts all contained water of crystallisation, and its removal increased the compounds sensitivity towards stimuli such as shock and friction dramatically. The use of nitrogen rich cations such as azidoformamidinium and guanidinium can also be combined with the 5,5'-azotetrazolate to generate high-nitrogen salts.[53] Bis(azidoformamidinium) 5,5'-azotetrazolate (AFZT), bis(guanidinium) 5,5'-azotetrazolate (GZT), bis-(aminoguanidinium) 5,5'-azotetrazolate (AGZT), and bis-(triaminoguanidinium) 5,5'-azotetrazolate (TAGZT) all show promise as energetic materials, with GZT and TAGZT finding use as gas generators and propellants.[53]

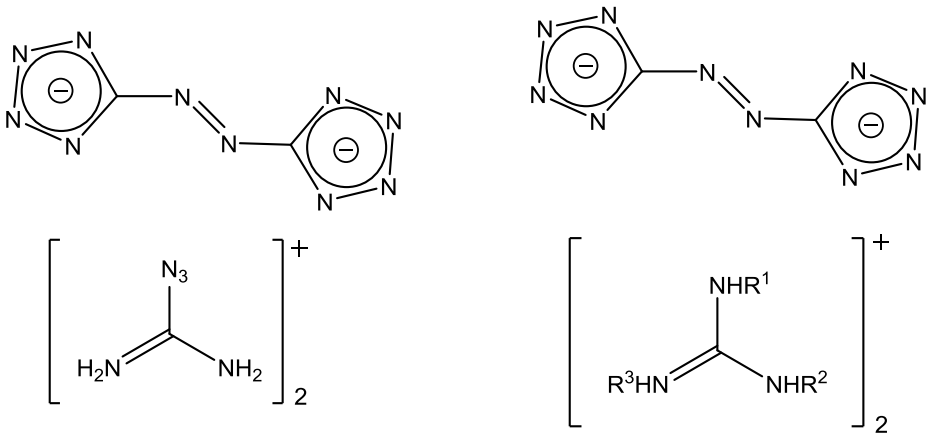

Figure 18 – Useful salts Bis(azidoformamidinium)-5,5’-azotetrazolate (AFZT) and bis(guanidinium)-5,5’-azotetrazolate (GZT).[54]

The addition of hydroxy groups encourages hydrogen bonding in the solid state, increasing the density of the material, whilst ensuring a more balanced oxygen content, allowing for the maximum output upon decomposition.[54] 1*H*,1’*H*-5,5’-Bitetrazole-1,1’-diol can be deprotonated when in an aqueous solution by nitrogen-rich bases. The dihydrazinium salt, the 5-aminotetrazolium salt and the diaminotetrazolium salt were encouraging examples; however, they are limited by their high sensitivity.[54] Alternatively, the oxidation of the tetrazole ring to the tetrazole-N-oxides allows for a greater explosive performance, whilst reducing friction-stability.[42] This can be demonstrated through the synthesis of 1-hydroxy-5-aminotetrazole resulting from the combination of cyanogen azide and aqueous hydroxylamine. An oxidation by potassium permanganate will yield the azo-linked 1,1’-dihydroxy-5,5’-azotetrazole. The hydroxyl proton can be removed through the combination with a base, yielding various salts which possess a higher chemical and thermal stability than their analogous azotetrazolate salts.

1.8 Extended Energetic Structures - Metal Organic Frameworks

The preparation of metal organic frameworks (MOFs) has been quickly gaining traction due to their potentially ground-breaking characteristics. Their porous nature is the source of the interest; the pore size and composition can be tuned to meet specific objectives such as gas separation and storage,[55–57] drug delivery[58–60] and catalysis.[61,62] They also have a environmentally significant ability to adsorb and store CO_2.[63,64] The inclusion of nitrogen at pore sites is desirable as the electron-donating nature of nitrogen atoms can significantly increase the adsorption of CO_2 caused by the dipole-quadrupole interactions between the CO_2 molecule and the nitrogen atom.[63] The inclusion of nitrogen containing heterocycles such as tetrazole into the MOF framework is advantageous due to their varied modes of attachment.[64] A recently suggested material is an energetic MOF.[65] This describes a metal-based system in which the framework consists of mostly nitrogen. This can be achieved by using heterocycles that possess a high nitrogen content, such as bridging tetrazolate ligands. This is a concept of high interest as the system will have an extremely high density, which has a large influence upon the material's explosive characteristics. A high performing example is the co-ordination polymer zinc(II) hydrazine azide, $[Zn(N_2H_4)_2(N_3)_2]_n$.[66] This 1D network consists of repeating Zn atoms co-ordinated by four equatorial bridging hydrazine molecules in addition to two axial azido ligands.

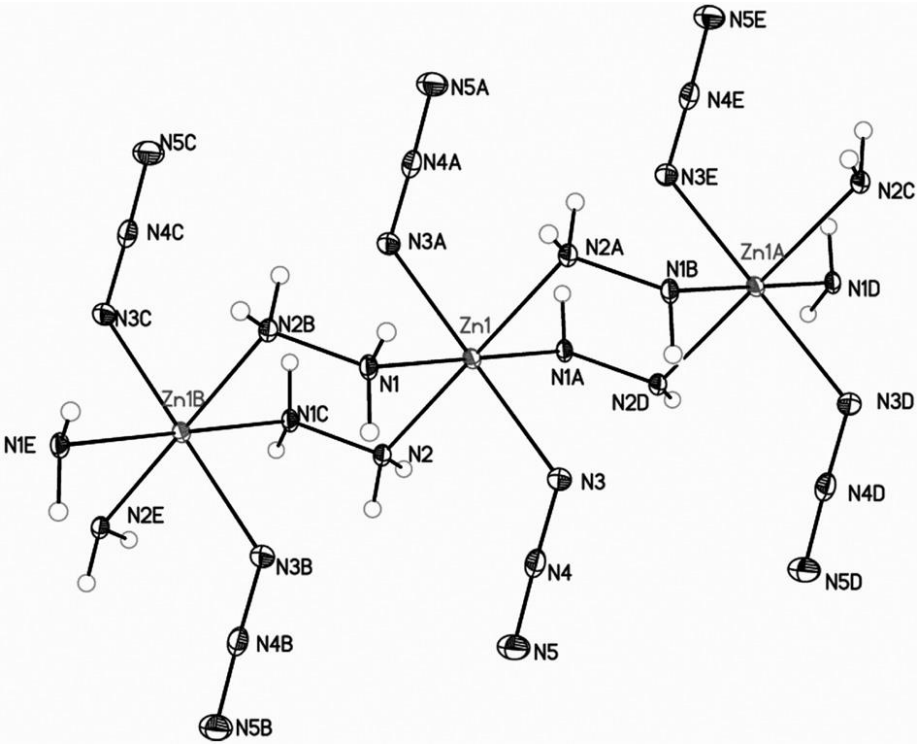

Figure 19 – Ellipsoid diagram of the $[Zn(N_2H_4)_2(N_3)_2]_n$ 1D co-ordination polymer. Diagram reproduced from Ref. 67.

The MOF has a nitrogen content of 65.6% and a heat of combustion is 5.45 $MJkg^{-1}$, approximately half that of the conventional secondary explosive RDX. Utilising the same technique, a number of energetic frameworks have been prepared. The preparation of nickel hydrazine perchlorate (NHP), cobalt hydrazine perchlorate (CHP) and nickel hydrazine nitrate (NHN) show the variety that can be achieved through simple experimentation with the metal centre or anionic molecule.[67]

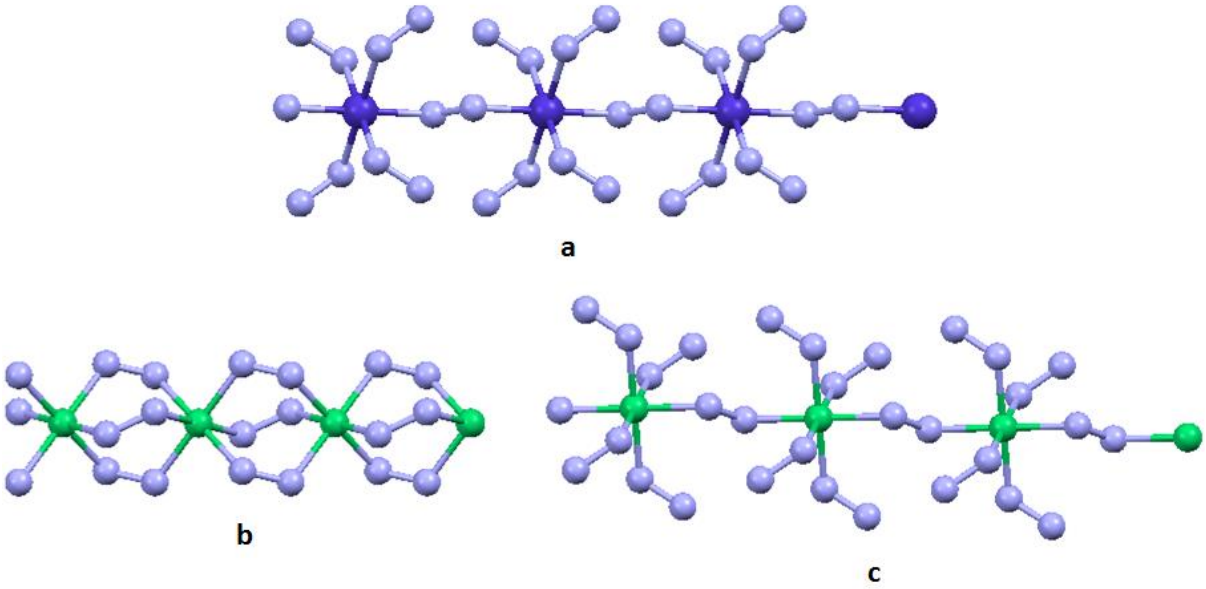

Figure 20 – Further examples of 1D co-ordination polymers : nickel hydrazine perchlorate (a), cobalt hydrazine perchlorate (b) and nickel hydrazine nitrate (c). The respective perchlorate and nitrate anions have been omitted for clarity. Diagram reproduced from Ref. 68.

It could be argued that these systems can not strictly be considered MOFs as they contain no carbon atoms. However, this should not defer their importance and the potential of this chemistry. These 1D systems also exhibit high heats of detonation; however, this is accompanied by a high sensitivity to flame, spark and impact. The sensitivity of the MOF can be reduced by expanding the framework into a 2D structure. This is due to the increasingly complex nature of the bonds that hold the framework together.

$[Co_2(N_2H_4)_4(N_2H_3CO_2)_2][ClO_4]_2{\cdot}H_2O$ (CHHP) and $[Zn_2(N_2H_4)_3(N_2H_3CO_2)_2][ClO_4]_2{\cdot}H_2O$ (ZnHHP) were early examples of an energetic 2D MOF.[65] This was achieved through the use of the hydrazinecarboxylate anion, which can be utilised as a multidentate ligand, vital for the construction of higher order metal organic frameworks. The additional non-nitrogen content reduces their energetic performance and consequently their sensitivity. This is counteracted by the inclusion of the perchlorate oxygen donor. Both materials exist as alternating sheets of the MOF framework and a layer of the perchlorate anions. CHHP forms a linear sheet polymer that consists of octahedral cobalt co-ordination centres, each bound to three hydrazine ligands, two of which bridge between metal centres. The third is a monodentate capping ligand which restricts the MOF to a 2D system.

The hydrazinecarboxylate ligand acts as a tridentate linker between two cobalt atoms, occupying the remaining three co-ordination sites.

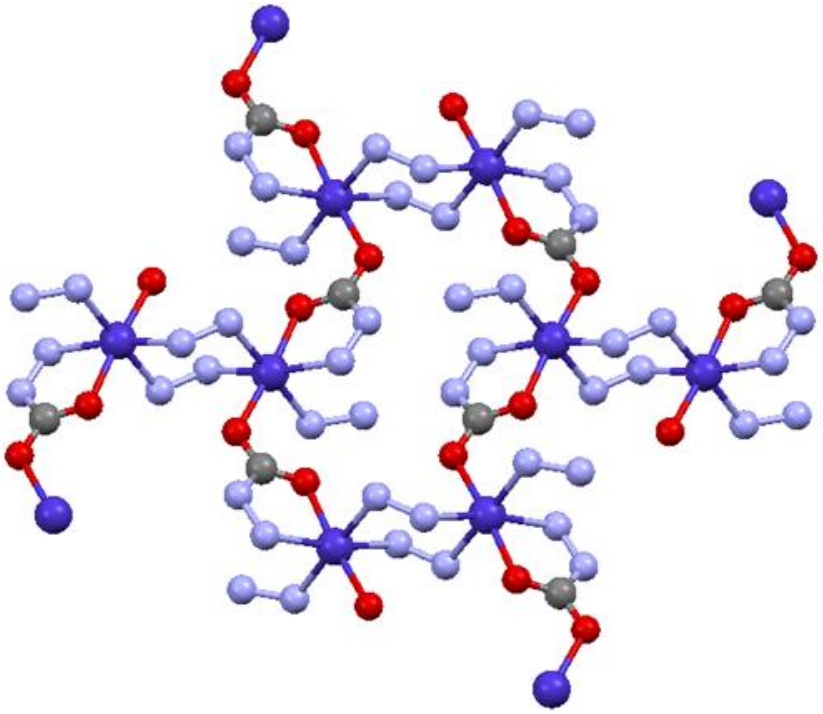

Figure 21 - 1D cobalt-based copolymer CHHP. X-ray diagram shows the extended structure orientated in the BC plane. Diagram adapted from Ref. 66.

The ZnHHP forms a much more complex crystalline structure. This is due to the higher degree of co-ordination flexibility available to the zinc centre.[66] The first co-ordination centre (**a**) is octahedral; bound in the four equatorial positions by bridging hydrazine ligands, whilst two hydrazinecarboxylate groups bind in the axial position via a single oxygen atom. In (**b**), the zinc metal centre is square pyramidal rather than octahedral. It again possesses equatorial bridging hydrazine ligands, but in this case only two are present. A hydrazinecarboxylate molecule occupies the final equatorial position and an axial co-ordination site through its nitrogen and oxygen atoms. A hydrazinecarboxylate ligand is bound in the final axial position, much like in the zinc environment shown in (**a**). The third and final zinc centre (**c**) is octahedral, with two hydrazinecarboxylate groups and two axial monodentate hydrazine ligands, limiting the MOF to a two-dimensional nature.

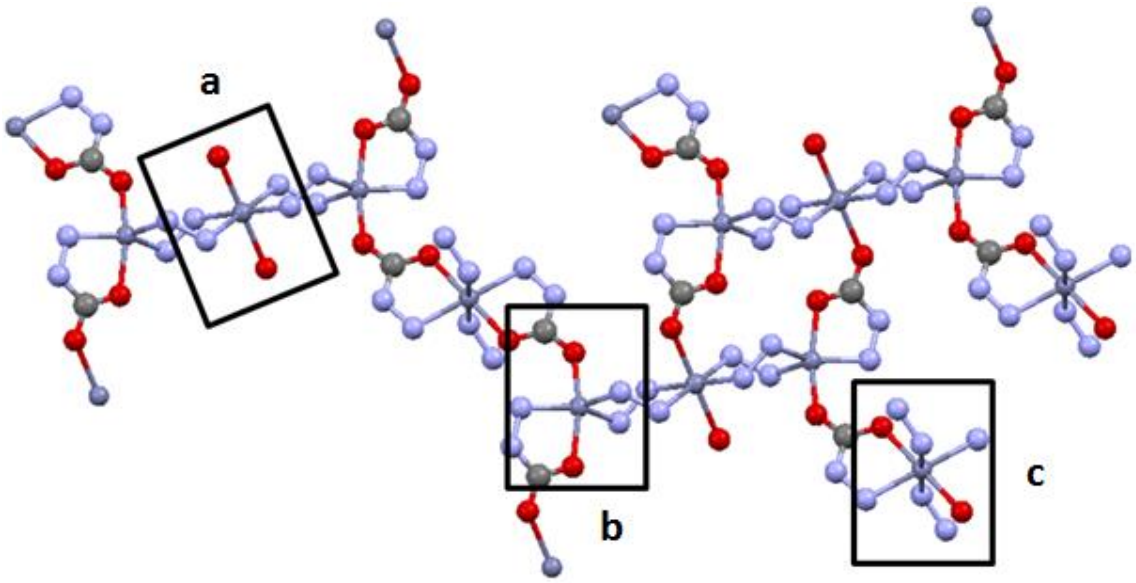

Figure 22 – X-ray diagram highlighting the three different co-ordination modes found within ZnHHP. Diagram is adapted from Ref. 66.

Both materials show a reduced sensitivity in comparison to the previously synthesised 1D metal organic frameworks. Traditionally an increase in nitrogen content is associated with an increase in sensitivity. These systems indicate the interconnected 3D network provide a higher stability, whilst also yielding a comparably higher density and therefore higher explosive performance. For this reason a 3D nitrogen-rich, energetic MOF is highly sought after as a "green" replacement for conventional explosives.

Replacing the hydrazine unit used previously with 4,4'-azo-1,2,4-triazole (atrz) yielded a series of 3D MOF systems, $[Cu(atrz)_3(NO_3)_2]_n$ and $[Ag(atrz)_{1.5}(NO_3)]_n$.[11] The inclusion of this organic spacer provides a high-nitrogen content with a decomposition temperature of 313°C, much higher than hydrazine. This provides additional stability to the framework. As mentioned previously, nitrogen-rich heterocycles also have access to additional binding modes, satisfying the bonding requirement for the three dimensional structure.

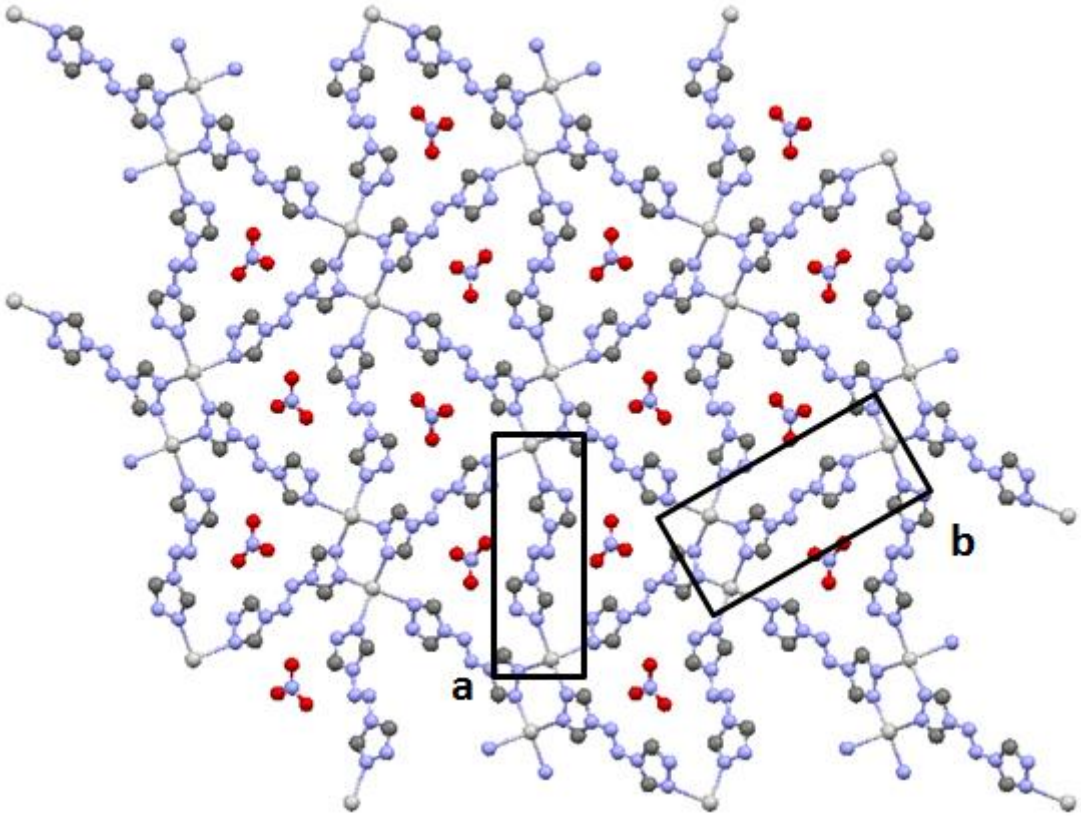

Figure 23 – Extended structure of the 3D triazole-based $[Ag(atrz)_{1.5}(NO_3)]_n$ co-ordination polymer, highlighting the porous nature of the framework.[12]

Both the $[Ag(atrz)_{1.5}(NO_3)]_n$ and $[Cu(atrz)_3(NO_3)_2]_n$ networks have porous structures, caused by the ability of the atrz organic spacer to bind to multiple co-ordination centres. This is observable in the above diagram, with the atrz ligand binding in a bidentate (**a**) and tridentate (**b**) fashion. The Ag co-ordination geometry is also evident; each silver atom is co-ordinated by four atrz ligands, occupying a tetrahedral environment. The inclusion of the heavier Ag co-ordination centre results in a higher density for $[Ag(atrz)_{1.5}(NO_3)]_n$ of 2.16 gcm^{-3}, compared to $[Cu(atrz)_3(NO_3)_2]_n$ at 1.68 gcm^{-3}. This serves to highlight the effect of metal centre exchange; the energetic characteristics can be altered by simply changing the co-ordination centre to a heavier element. In comparison to $[Ag(atrz)_{1.5}(NO_3)]_n$, the $[Cu(atrz)_3(NO_3)_2]_n$ has a much more ordered extended network, with well-defined pores. Each Cu(II) co-ordination centre has an octahedral geometry, with each atrz ligand bidentally bound forming a symmetrical, triangular structure.

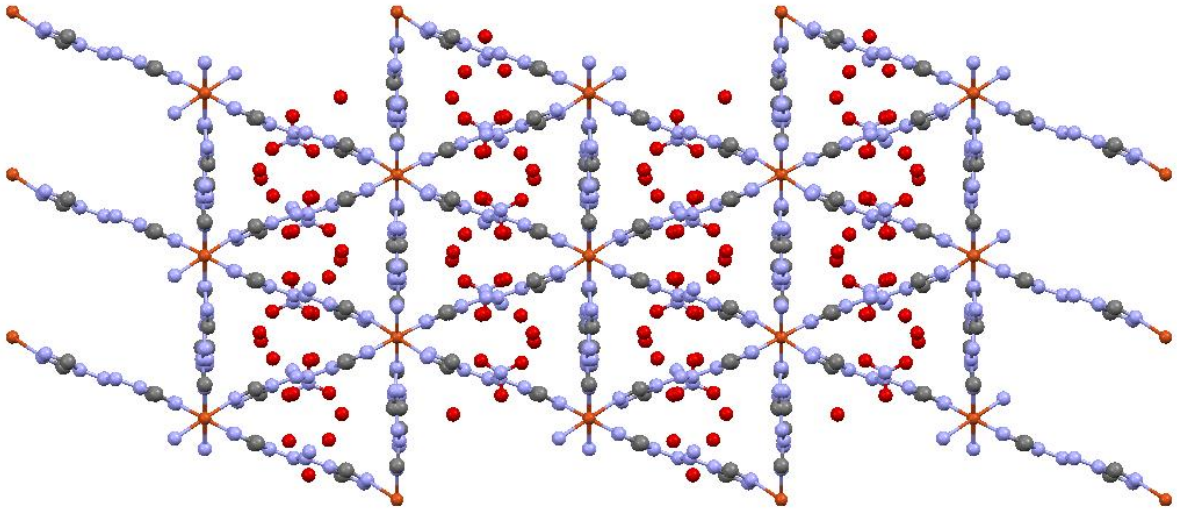

Figure 24 – Extended structure of the analogous $[Cu(atrz)_3(NO_3)_2]_n$ co-ordination polymer.[12]

The extended 3D network provides a high decomposition temperature to both MOFs. $[Ag(atrz)_{1.5}(NO_3)]_n$ decomposes at 257°C whilst $[Cu(atrz)_3(NO_3)_2]_n$ decomposes at 243°C. However of the two complexes synthesised it is $[Cu(atrz)_3(NO_3)_2]_n$ which has the most promising energetic complex. Under analysis, its explosive performance exceeded that of CL-20 and octonitrocubane. Although in its infancy, the preparation of energetic metal organic frameworks is a field that has already produced a number of exciting examples. Beginning with a simple 1D structure, the chemistry has quickly advanced in complexity, with 2D and 3D systems following. The 3D MOF $[Cu(atrz)_3(NO_3)_2]_n$ is an extremely attractive compound, showing a high heat of detonation, higher than that of most conventional explosives. The increased geometric nature of 3D systems when compared to 2D and 1D examples also provides additional stability; the highly interconnected nature of a 3D system reduces the propensity of the MOF to decompose.

1.9 Outline

The idea of creating homoleptic poly(tetrazolato) complexes is poorly represented in the literature, with homoleptic poly(tetrazolato) complexes based upon a main group co-ordination centre remaining unexplored. The lack of information available on this subject provides an opportunity; is it possible to co-ordinate multiple tetrazolato ligands to a main group co-ordination centre? Could a homoleptic polytetrazolato main group complex be synthesised?

The energetic nature of tetrazole and its associated compounds has prompted an enthusiastic research interest. However, the use of tetrazole and the tetrazolate anion as a *ligand* has been grossly overlooked in the literature. The creation of a hypervalent main group complex containing tetrazolate ligands would possess a high-nitrogen content, producing a new class of energetic materials. This could be accomplished through the reaction of the main group tetrachlorides and tetrazolate salts (illustrated in scheme 10). This could be studied safely through the use of a large, weakly co-ordinating cation, such as bis(triphenylphosphine)iminium (PPN^+).

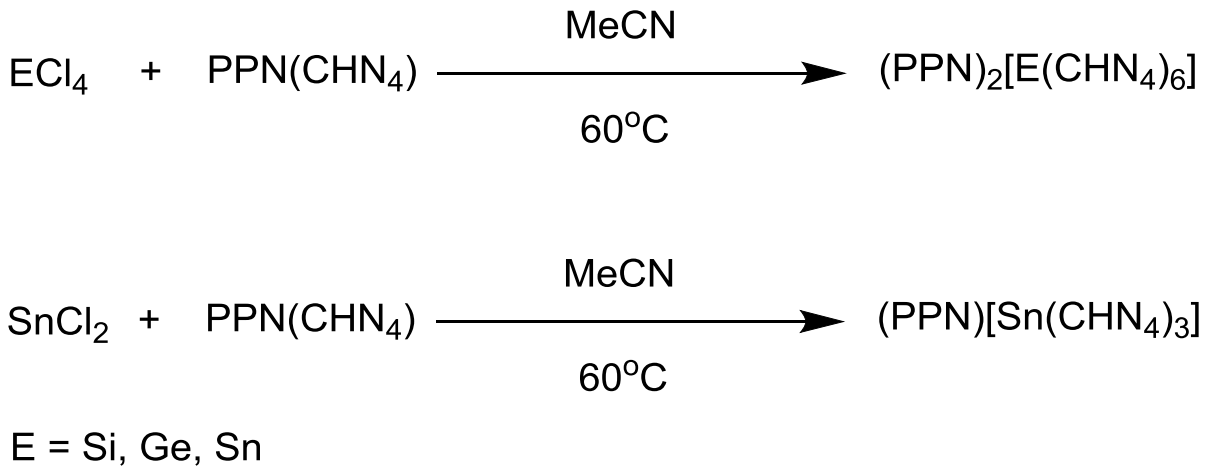

Scheme 10 – Suggested preparative methods to yield main group poly(tetrazolato) co-ordination complexes.

The ability of the tetrazole ligand to co-ordinate to multiple metal sites and the co-ordinatively unsaturated nature of the low valent (PPN)[$Sn(CHN_4)_3$] complex could potentially result in the formation of extended co-ordination polymers. The isolation and characterisation of such a framework would represent a first, with no other main group homoleptic tetrazolato co-ordination polymer existing in the literature. In addition to the tetrazole study a second investigation will concentrate upon cleaving the C–N bond within certain arylpentazoles through the use of metal-based reducing agents, specifically sodium naphthalenide and the (^{mes}nacnac)Mg–Mg(nanac^{mes}) species. With respect to the arylpentazoles that will be investigated, the *para* substituted *p*-dimethylaminophenylpentazole and *p*-hydroxyphenylpentazole[68] will be utilised due to their comparably high stability. The reaction with the respective reducing agent will be monitored using IR and NMR spectroscopy.

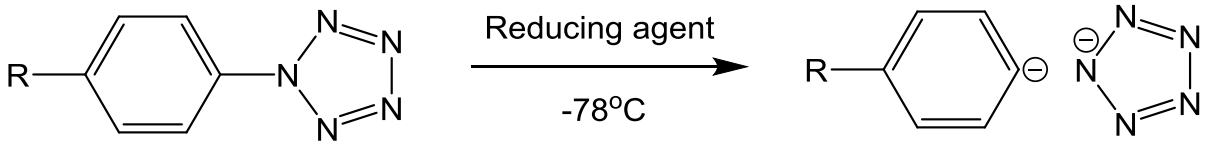

R = $N(CH_3)_2$, OH

Scheme 11 – Cleavage of the C–N bond within *p*-substituted arylpentazoles using a reducing agent.

2. Experimental

2.1 Instrumentation

2.1.1 Nuclear Magnetic Resonance Spectroscopy

All ^{1}H and ^{13}C NMR spectra were recorded using a 400 MHz Bruker Avance 400 spectrometer. ^{31}P spectra were recorded on a 250 MHz Bruker Avance 250 spectrometer. All chemical shifts are reported in ppm. Spectroscopic grade deuterated solvents were used and samples were prepared in the glove box and filtered through glass wool if necessary. NMR chemical shift calibration was achieved through the assigning of the residual solvent peak to its expected ppm value.[69] Spectra were processed using Topspin®.

Acetonitrile-d_3 – 1.96 ppm

Benzene-d_6 – 7.15 ppm

Dichloromethane-d_2 – 5.32ppm

Chloroform-d – 7.26 ppm

2.1.2 Elemental Analysis

Elemental analyses were carried out by the microanalysis service at the University of Sheffield. Carbon, hydrogen and nitrogen contents were determined using a Perkin Elmer 2400 CHNS/O Series II elemental analyser, calibrated by the measurement of three acetanilide samples, which is known as a very reliable calibrant. Elemental analysis uses a combustion method in a pure oxygen environment to convert the accurately weighed sample into combustion products. The masses of these combustion products can be used to calculate the composition of the sample. Values for the reference substances are accurate within +/-0.1%. Samples were stored in the glove box, transported to the analyser in a vial wrapped in Parafilm® where they are weighed into a tin boat and the boat folded to provide a seal. After this the sample is combusted immediately. The accepted deviation up to which an analysis is regarded to still support a sum formula is ±0.3%.

2.1.3 Infra-red Spectroscopy

IR spectra were obtained in solution using a transmission cell equipped with CaF_2 windows (4000 – 1200 cm^{-1}) for liquids, or as a Nujol suspension between NaCl windows (4000 – 500 cm^{-1}). Spectral measurements were performed using a Bruker Tensor 27 Fourier transform infra-red (FTIR) spectrometer, as well as a Bruker Alpha spectrometer located within the glove box; this is used for air sensitive samples. Both spectrometers operate at a spectral resolution of 2 cm^{-1}. All data was analysed using Bruker OPUS software. Samples of solutions were either prepared in the glove box by dissolving compounds in dry solvent and recording the spectrum against a background of the same solvent, or removed from reaction mixtures using a argon-filled glass syringe under a constant flow of argon. Solid samples were mulled with Nujol between the NaCl windows to give a suspension (mull). Peaks of the Nujol mulling agent at 2933 cm^{-1}, 2853 cm^{-1}, 1462 cm^{-1}, 1377 cm^{-1} and 721 cm^{-1} are removed from the peak lists.

2.1.4 X-ray Diffraction

Routine X-ray diffraction studies were performed for the determination of molecular and crystal structures using single crystal X-ray diffractometers equipped with Bruker Smart or Kappa CCD area detectors. Typically, crystals were scooped out of the mother liquor and immersed in Fomblin® immediately so as to avoid loss of potential solvent and reaction with air. Crystals were selected under the microscope and investigated for extinction of polarised light. Suitable crystals are mounted onto the goniometer using the Fomblin® as an adhesive. During the collection of reflection data, the crystals were placed in a cold stream of nitrogen set at a temperature of 100 K. Small adjustments are made upon the mount to centre the crystal in the X-ray beam path. The crystal's length, width and height are measured using the internal camera, and a simple scan is used to evaluate the quality of diffraction peaks of the analysed crystal. The unit cell is determined by a short X-ray scan, producing a diffraction pattern, consisting of "spots" caused by constructive interference resulting from diffraction of the X-ray beam by the lattice planes within the crystal. The spots can be “harvested” by the software, and using either a fast Fourier transform algorithm or the differential vectors algorithm. Each algorithm is assigned a score, with the most suitable method possessing the highest value.

An estimate for the unit cell lengths (a, b, c) and angles (α, β, γ) can then be generated. Also calculated is the position of all spots associated with the crystal. The software generates an overlay upon the visualisation of the diffraction pattern, allowing for the comparison between the experimental data and the theoretical spot positions. A series of refinements improve upon these estimates. The combination of the algorithm and the information harvested from the recorded diffraction pattern provides an agreement with the crystal's Bravais lattice. The software provides an option for all 14 lattice types, and each is quantified between 0 and 1. Once the suitable Bravais lattice has been chosen, a final refinement provides the accurate unit cell data.

The collection strategy can then be planned, with the opportunity to control total experiment time, exposure per frame (ie each individual measurement), level of completeness and redundant data. The level of redundancy allows for a more precise error model, reducing the level of experimental uncertainty. The measurement can then take place. The resulting diffraction pattern is integrated using Bruker APEX2® software suite, transforming the data into the intensity plot, containing “spots” of electron density. The integration also results in an internal R-factor for the data set. The R-factor serves as an indicator for the agreement between the crystallographic model and the diffraction data recorded. In effect, it shows the extent at which the refined structure predicts the data that are available.

The diffraction pattern can be opened using the Shelxtl software to generate a plot of electron density, as a series of "Q" peaks. These can be labelled as their respective elements. Through cycles of labelling the "Q" peaks and refinement, the R-factor can be reduced. An R-factor that is close to the initial value generated by the integration indicates that the structure is accurate. Anisotropy and hydrogen atoms can then be added, completing the unknown compound’s structure. The finished structure was visualised using the Mercury® and Ortep® software packages.

2.2 General Experimental Procedures

Unless stated otherwise, all preparations were carried out under strict exclusion of air and moisture using standard Schlenk tube and vacuum line techniques. BOC pureshield argon (purity 99.98%) was used as protective gas, which was released from a pressure cylinder and passed at a gauge pressure of 0.3 bar. Vacuum was generated using a Leybold trivac® E2 mineral oil sealed rotary vane pump. The ultimate vacuum achievable at the manifold was between $1x10^{-2}$ and $1x10^{-3}$ mbar, measured using a Leybold thermovac pressure gauge. For the preparation of Nujol suspensions, solutions for NMR and FTIR measurements, for storage purposes and for experiments involving the reaction of small amounts of starting material, a glove box was used, which was filled with argon. The box argon was kept oxygen, water (both < 0.1 ppm) and solvent vapour free by continuous circulation of the box atmosphere through molecular sieves, CuO molecular-sieves and activated charcoal filters. When interpreting FTIR spectra, all peaks below 5% of the maximum peak intensity are not reported.

Solutions were left to crystallise by placing closed vessels in a freezer maintained at a temperature of ca. -20°C. The rate of temperature change in solutions intended for the growth of larger crystals was reduced by placing vessels within insulating flasks containing a coolant initially at the temperature of the solution. Unless stored in the glove box, compounds were typically stored in the freezer.

2.3 Starting Materials and Solvents

The solvents CH_2Cl_2 (HPLC grade), THF (HPLC grade) and Et_2O (100%) were obtained from VWR and MeCN (99%) was sourced from Sigma-Aldrich, in addition to pyridine (99%, Sigma-Aldrich). All were treated by stirring with CaH_2 overnight, performing a trap-to-trap condensation and degassing prior to use and then stored inside ampoules closed by Young taps. Care must be taken with pyridine as it is highly toxic. Solvents were transferred typically to the reaction vessel via a stainless steel cannula. The deuterated solvents acetonitrile-d_3 (degree of deuteration 99.96%), DCM-d_2 (degree of deuteration 99.8%) and chloroform-*d* (degree of deuteration 99.8%) were purchased from Fluorochem. They were dried over CaH_2 at r.t., then trap-to-trap condensed and stored in ampoules closed with Youngs taps inside the glove box.

Other starting materials were obtained from commercial sources (Sigma-Aldrich, Fisher, Alfa Aesar) and used without further purification with the following exceptions;

$SiCl_4$ (99% purity, Sigma-Aldrich), stirred over Na_2CO_3 and trap-to-trap condensed prior to use.

$GeCl_4$ (99% purity, Sigma-Aldrich), stirred over Na_2CO_3 and trap-to-trap condensed prior to use.

$SnCl_4$ (99% purity, Sigma-Aldrich), stirred over Na_2CO_3 and trap-to-trap condensed prior to use.

SnF_2 (99% purity, Fisher), dried under high vacuum at 110^{o}C and stored in argon-filled glove box.

SnF_4 (99% purity, Fisher), dried under high vacuum at 110^{o}C and stored in argon-filled glove box.

SbF_3 (98% purity, Sigma-Aldrich), dried under high vacuum at 110^{o}C and stored in argon-filled glove box.

PPh_4Cl (98% purity, Sigma-Aldrich), dried under high vacuum at 110^{o}C and stored in argon-filled glove box.

2.4 Synthetic Procedures

2.4.1 PPN(Cl)

(Procedure adapted from ref. 71)

PPh_3 (196.7 g, 0.750 mol) was added to a 1L three-necked round bottomed flask. Distillation equipment was then attached and 1,1,2,2-tetrachloroethane (305 mL) was added. The solution was heated to 50°C and stirred until all the PPh_3 has dissolved. Without cooling, PCl_5 (109.5 g, 0.526 mol) was added slowly with stirring, causing a darkening from light yellow to dark orange. The mixture was then heated to 150°C and stirred for 1 h at this temperature. The by-product PCl_3 was removed from the reaction solution by vacuum distillation. The distillation typically occurs at a head temperature between 60-80°C, and usually results in the removal of approximately 100 cm^3 of a PCl_3/1,1,2,2-tetrachloroethane azeotrope. After the distillation was complete, a condenser was fitted and $NH_2OH \cdot HCl$ (18.33 g, 0.264 mol) was added using a spatula and the mixture was heated to 140°C for 8 h. A dual bubbler system was attached and the secondary bubbler half-filled with water (see figure 25). At the onset of the reaction, bubbles of HCl gas were produced, which dissolve in the water. When the system was cooled, the drop in pressure pulls the water into the primary bubbler, ensuring no water was inadvertently drawn into the reaction mixture.

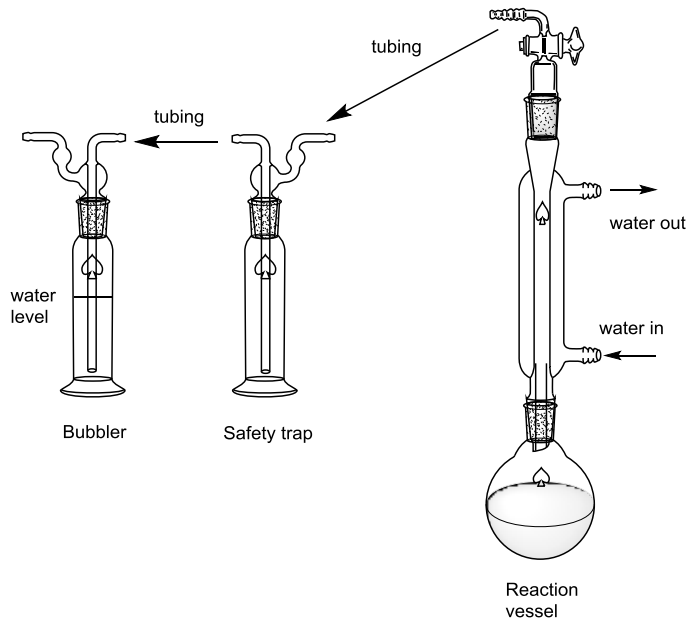

Figure 25 – Schematic of bubbler system to trap HCl gas produced during the PPN(Cl) synthesis.

The cold reaction solution was extracted with n-hexane (~1000 mL). Further portions of n-hexane were added until the organic extracts were no longer cloudy (approximately 5 x 100 mL). This process removes impurities, in particular PPh_3O. An ethyl acetate : n-hexane mix (1:5 720 mL) was then added to the extract residue, resulting in a yellow slurry. The crude products were filtered and washed (ethyl acetate 3 x 100 mL, n-hexane 3 x 100 mL), then left to dry overnight in air. The dry yellow solid was dissolved in the minimum amount of hot water, resulting in an aqueous/oil two-phase system. 35% HCl (3 x 100 mL) was added with stirring once the mixture has cooled to 55°C, leading to the diminishment of the orange oil and the production of a white precipitate. Filtration was used to remove the solid, which was then washed with cold water (3 x 100 mL) and 35% HCl (3 x 100 mL). The solid was re-crystallised using a 1:10 DCM:THF solvent mix. The crude product was dissolved in the minimum amount of hot DCM, and the corresponding amount of cold THF was added with stirring. Solution was allowed to cool to room temperature, and then stored overnight at -20°C. Clear, slightly yellow crystals were isolated by filtration and dried *in vacuo* overnight at 150°C (98.10 g, 68%). M.p. = 270-272°C. IR (Nujol, cm^{-1}) ν = 1586, 1434, 1325, 1265, 1179, 1113, 1025, 994, 849, 799, 748, 690, 614. ^1H NMR ($CDCl_3$) δ [ppm] = 7.75-7.62 (m), 7.58-6.84 (m). ^{31}P NMR ($CHCl_3$–*d*) δ [ppm] = 21.08. All analytical data match the literature source for the synthesis.

2.4.2 1*H*-tetrazole

(Procedure adapted from ref. 3)

The compounds NaN_3 (37.58 g, 0.578 mol) and NH_4Cl (23.05 g, 0.431 mol) were mixed in a 500 mL two-necked round bottomed flask with $CH(OEt)_3$ (131 mL, 0.788 mol). Under argon flow whilst stirring, acetic acid (100%, 150 mL) was added, resulting in the immediate precipitation of a white solid. A condenser and mercury bubbler were attached and the argon tap was closed, maintaining a positive argon gauge pressure over the course of the reaction. The mixture was heated to 85°C and stirred for 24 h. Upon reaching the 85°C reaction temperature the thick white suspension has thinned sufficiently to stir. The reaction vessel was cooled to room temperature, and HCl(aq) (35%, 15 mL) was added slowly to the reaction mixture with stirring. The precipitate (NaCl) was removed by filtration and discarded. The filtrate solvent was removed *in vacuo,* leaving behind the crude product.

Once dry, ethanol (180 mL) was added and the remaining NaCl removed using filtration. The solvent volume was reduced *in vacuo* until the onset of crystallisation, after which the flask was stored overnight at -20°C. The crystals were separated and re-crystallised from the minimum amount of hot acetone, yielding the pure 1*H*-tetrazole (27.84 g, 92%). IR (Nujol, cm^{-1}) ν = 3158, 1525, 1256, 1145, 1087, 1047, 1017, 907, 663. ^{1}H NMR (DMSO) δ [ppm] = 9.39 (CH). ^{1}H NMR (CH_3CN-d^3) δ [ppm] = 9.02 (CH), 14.4-13.3 (broad, NH). All analytical data match the literature source for the synthesis.

2.4.3 Na(CHN_4)

(Procedure adapted from ref. 3)

1*H*-tetrazole (2.80 g, 38.9 mmol) was added to a solution of NaOH (2.78 g, 0.0712 mol) in 40 mL of water and was heated to reflux for five minutes. The stirring solution was allowed to cool to room temperature. The water was removed *in vacuo*, and the white solid re-crystallised from hot ethanol. The crystals were collected using filtration and dried *in vacuo* at 100°C overnight (3.21 g, 87%). M.p. = 260-262°C. IR (Nujol, cm^{-1}) ν = 1588, 1438, 1245, 1221, 1184, 1115, 1024, 997, 885, 802, 747, 725, 691. ^{1}H NMR (D_2O) δ [ppm] = 8.51 (CH). All analytical data match the literature source for the synthesis.

2.4.4 PPN(CHN_4)

(Procedure adapted from ref. 71)

A Schlenk tube was charged with a mixture consisting of (PPN)Cl (10.00 g, 17.4 mmol) and a slight excess of sodium tetrazolate, Na(CHN_4) (1.71 g, 18.6 mmol). Dry MeCN (35 mL) was added and the white suspension was immersed in an oil bath set at 45°C and the reaction mixture was stirred overnight. After this time, the mixture was allowed to cool to r.t. and it was subsequently filtered, separating yellow solution from the white residue (mostly NaCl). The solvent volume of the filtrate was reduced *in vacuo* to ½ its original volume. Any solid was re-dissolved and the Schlenk tube was stored at −25°C overnight. Large, colourless crystals were isolated by filtration, and purified by a second re-crystallisation from the minimum amount of hot acetonitrile. The large, colourless crystals were dried *in vacuo* at 45°C overnight (5.54 g, 53% with respect to PPN(Cl)). M.p. = 224-225°C. IR (Nujol, cm^{-1}) ν = 3147, 3055, 1587, 1482, 1435, 1256, 1181, 1110, 1027, 996, 859, 797, 746, 689.

^{1}H NMR (CH_3CN-d^3) δ [ppm] = 8.10 (s, tetrazolate C-H), 7.78-7.40 (m, PPN). ^{13}C NMR (CH_3CN-d^3) δ [ppm] = 149.67 (s, tetrazolate C-H), 135.07 (s, PPN), 133.68 (t, PPN), 130.84 (t, PPN), 129.24 (s, PPN), 128.15 (s, PPN). ^{31}P NMR (CH_3CN-d^3) δ [ppm] = 20.75 (PPN). Elemental analysis calculated for $C_{37}H_{31}N_5P_2$ (607.64 g mol^{-1}): C, 73.14; H, 5.14; N, 11.53%, Found: C = 72.90%, H = 5.00%, N = 11.64%.

X-ray diffraction data, a = 12.19 Å, b = 14.88 Å, c = 17.39 Å, α = 90°, β = 100.32°, γ = 90° (Monoclinic C).

2.4.5 $(PPN)_2[Si(CHN_4)_6]$

$PPN(CHN_4)$ (6.39 g, 10.5 mmol) was dissolved in ca. 30 mL of dry acetonitrile. It was imperative that excess solvent was used, to ensure that all intermediary products remain in solution as it was produced. $SiCl_4$ (0.200 mL, 1.79 mmol) was added under a constant stream of argon with a volumetric pipette. The reaction mixture was heated to 60°C and stirred for 2 h. After cooling to room temperature, the mixture was cannula-filtered and concentrated *in vacuo*. The filter residue was discarded. The solution was stored overnight at -20°C, producing white crystals that were separated by cannula-filtration. The filtrate was discarded. These crystals were the intermediary $(PPN)_2[Si(CHN_4)_xCl_y]$ species, and require further reaction (2.02 g). The crystals were re-dissolved in dry acetonitrile. A second batch of $PPN(CHN_4)$ (1.59 g, 2.56 mmol) was dissolved in dry acetonitrile in a separate Schlenk tube. The $PPN(CHN_4)$ solution was cannula-transferred to the reaction solution with stirring, and the mixture was heated to 60°C and stirred for 2 h.

Once at room temperature, the reaction mixture was filtered and concentrated *in vacuo*. The solution was stored in the freezer at -20°C, producing colourless crystals (1.88 g, 67%). M.p. = 222-223°C (probable decomposition, gas generated and colourless solid turned yellow). IR (Nujol, cm^{-1}) ν = 1588, 1454, 1436, 1324, 1263, 1166, 1115, 1060, 1024, 997, 963, 876, 804, 746, 690, 616. ^{1}H NMR (CH_3CN–d^3) δ [ppm] = 8.49, 8.38, 8.22 (CH-tetrazolate), 7.74-7.01 (m, PPN). Elemental analysis calculated for $C_{78}H_{66}N_{26}P_4Si$ (1518.47 gmol^{-1}): C= 61.64%, H= 4.38%, N = 23.98%. Found: C = 61.87%, H = 4.26%, N = 24.11%. X-ray diffraction data, a = 9.10 Å, b = 25.67 Å, c = 16.23 Å, α = 90°, β = 105.58°, γ = 90° (Monoclinic P).

2.4.6 $(PPh_4)_2[Al(N_4CMe)_x(N_3)_y]$ (x+y=5)

Orange crystals of $(PPh_4)[Al(N_3)_5]$ (130 mg, 0.226 mmol) were dissolved in approximately 10 mL of dry, degassed acetonitrile. The resulting orange solution was heated to 90°C and stirred for 8 h. The progress of the reaction was monitored by IR spectroscopy, showing the diminishing N_3^- peak at 2004 cm^{-1}, and the growth of a new peak at 2138 cm^{-1} (HN_3). The solvent was removed under vacuum, leaving behind a white solid. Hot, dry acetonitrile (~3 mL) was added and the flask stored at -20°C overnight. A small amount of white precipitate was produced. More dry acetonitrile (~5 mL) and dry diethyl ether (~15 mL) was added.

The solution was heated to 40°C and cooled slowly in an iso-propanol bath, which was stored at -20°C overnight. A white solid precipitated out of the solution. All solvent was removed under vacuum and the solid re-dissolved in ~15 mL of dry acetonitrile. The cloudy solution was filtered and reduced in volume to induce crystallisation. Crystals were found to be $PPh_4(N_3)$ based on unit cell data found during single crystal X-ray analysis. IR (solution cell, cm^{-1}) ν = 2138, 2129, 2026, 2004. X-ray diffraction data, a = 9.662 Å, b = 10.15 Å, c = 11.17 Å, α = 72.29°, β = 69.59°, γ = 80.12° (Triclinic).

2.4.7 $Na_2[Si(N_3)_6]$

(Procedure adapted from ref. 73)

A Schlenk tube was charged with NaN_3 (1.09 g, 16.7 mmol) and was suspended in 20 mL of dry, degassed acetonitrile. The mixture was stirred vigorously and $SiCl_4$ (0.260 mL, 2.30 mmol) was added via a volumetric pipette under a protective stream of argon gas. The suspension was stirred overnight, after which it was cannula filtered to remove the solid. The colourless solution was weighed, and assuming 100% completion the relative concentration of the solution can be calculated (0.170 mmol per mL). IR (solution cell, cm^{-1}) ν = 3397, 3180, 3132, 2119 (N_3), 1316, 1174, 1040, 982, 589.

2.4.8 $Na_2[Si(N_3)_x(N_4CMe)_y]$ (x+y=6)

$Na_2[Si(N_3)_6]$ (5.00 mL, 0.170 mmol per mL, 0.850 mmol) was diluted with approximately 10 mL of dry, degassed acetonitrile and was heated to 90°C and stirred at this temperature for 36 h. The reaction progress was monitored using IR spectroscopy, with a diminishing peak at 2147 cm^{-1} and the growth of peaks at 2138 cm^{-1}, 2161 cm^{-1} and 2032 cm^{-1}.

After 26 h, the original colourless solution has changed to a slighty yellow solution over an off-white solid. The solid was insoluble in common solvents, and re-crystallisation was futile. IR (Nujol, cm^{-1}) ν = 2158, 1561, 1361, 1349, 1230, 1198, 1148, 707, 595.

2.4.9 $PPN(N_3)$

(Procedure adapted from ref. 72)

The PPN(Cl) (10.0 g, 0.174 mol) and NaN_3 (56.6 g, 0.871 mol) were dissolved separately in the minimum amount of hot water (approximately 60°C). The solutions were combined with stirring and the resulting mixture was allowed to stir for 15 minutes. The orange (water was too hot, which caused the discolouration) suspension was placed in an ice bath for 1h. The orange solid was filtered out and the solution was discarded. The solid was dried *in vacuo* for 30 minutes. Acetone (50 mL) was added and any solid removed by filtration. The acetone solution was concentrated to approximately 10 mL, and diethyl ether (~100 mL) was added until precipitation stopped. The solid was recrystallized from hot acetonitrile (5.50 g, 54%). IR (Nujol, cm^{-1}) ν = 2005, 1998, 1990, 1640, 1587, 1437, 1264, 1181, 1115, 1025, 996, 859, 800, 749, 694, 629.

2.4.10 $(PPN)_2[Si(N_3)_6]$

(Procedure adapted from ref. 73)

$PPN(N_3)$ (0.189 g, 0.326 mmol) was dissolved in dry acetonitrile. The solution was cooled to 0^oC and $Na_2[Si(N_3)_6]$ (10.0 mL, 0.163 mmol) was cannula transferred to the $PPN(N_3)$ solution. The reaction mixture was stirred for 10 minutes at 0^oC and then allowed to warm to room temperature. The mixture was then stirred for 4 h. The cloudy white suspension was cooled to 0^oC and filtered. The clear solution was concentrated at 0^oC until crystallisation began. The mixture was warmed slightly to room temperature and then placed in the freezer at -20^oC overnight, causing crystallisation. Crystals were isolated and dried *in vacuo* for 30

minutes. (0.466 g, 69%). IR (Nujol, cm^{-1}) ν = 3403, 2102, 1983, 1905, 1822, 1777, 1674, 1587, 1482, 1313, 1259, 1184, 1114, 1026, 996, 928, 858, 802, 749, 690, 593, 513.

2.4.11 $(PPN)_2[Si(N_3)_x(N_4CMe)_y]$ (x+y) = 6

$(PPN)_2[Si(N_3)_6]$ (190 mg, 0.140 mmol) was dissolved in approximately 20 mL dry acetonitrile. The colourless solution was heated to 90°C and stirred for 9 h. The solvent volume was reduced to 1 mL and the Schlenk tube was stored at -20°C overnight. Small, colourless crystals were observed, and were analysed using single crystal X-ray diffraction. The crystals were shown to be PPN methyltetrazolate, $PPN(N_4CMe)$. IR (solution cell, cm^{-1}) ν =3415, 3144, 2250, 2110, 1990, 1913, 1832, 1662, 1588, 1483, 1300, 1254, 1184, 1113, 997, 854, 692, 593, 545. X-ray diffraction data, a = 15.93 Å, b = 14.36 Å, c = 16.87 Å, α = 90°, β = 11.86°, γ = 90° (Monoclinic P).

2.4.12 $Ag(CHN_4)$

(Procedure adapted from ref. 3)

The compounds 1H-tetrazole (3.50 g, 0.0500 mol) and $AgNO_3$ (4.33 g, 0.0250 mol) were dissolved separately in ~30 mL of water. The colourless solutions were combined with stirring, immediately causing precipitation of a white solid. 30 mL of freshly made 1 M NaOH solution was added with stirring to the reaction mixture, which was stirred for 1 h. The precipitate was isolated by filtration and washed with 100 mL water, 100 mL ethanol and finally 100 mL acetone. The solid was dried *in vacuo* for 8 h at 40°C (4.33 g, 97%). IR (Nujol, cm^{-1}) ν = 3166, 1850, 1443, 1301, 1193, 1142, 1132, 1079, 1006, 931, 868, 696. Analytical data matched that for pure $Ag(CHN_4)$ from the literature.

2.4.13 Attempted synthesis of $Si(CHN_4)_4$

1*H*-tetrazole (3.40 g, 50.0 mmol) was added to a Schlenk tube and was suspended in 30 mL dry, degassed toluene. The suspension was cooled to 0°C with stirring. 2,6-lutidine (4.00 mL, 35.0 mmol) was added and the reaction mixture was stirred for 30 minutes at 0°C. In a separate Schlenk tube $SiCl_4$ (5.55 mL, 50.0 mmol) was dissolved in 10 mL dry toluene, and cooled to 0°C. The $SiCl_4$ solution was added drop-wise to the 1*H*-tetrazole suspension, producing a large amount of precipitate. The reaction mixture was stirred for 24h at 0°C. The reaction mixture is filtered at 0°C and the precipitate (2,6-lutidine.HCl) discarded. The

clear, colourless solution was stored overnight at -25°C. Analysis shows the presence of 1*H*-tetrazole, indicating the reaction does not proceed to the expected product.

2.4.14 Synthesis of $(PPN)_2[Ge(CHN_4)_6]$

$PPN(CHN_4)$ (3.34 g, 5.50 mmol) was added to a Schlenk tube and was dissolved in ca. 30 mL dry, degassed acetonitrile. Once dissolved, $GeCl_4$ (0.100 mL, 0.888 mmol) was added under a protective flow of argon. The reaction mixture was heated in an oil bath at 62°C and stirred for 16 h. After this, the reaction solution was cooled to room temperature, and the solvent volume halved. The Schlenk tube was stored overnight at -25°C. The supernatant solution was removed using cannula-filtration, and the crystals were re-dissolved in dry acetonitrile. $PPN(CHN_4)$ (0.900 g, 1.50 mmol) was added to a separate Schlenk tube and was dissolved in dry acetonitrile. Both solutions were combined and the reaction solution was again heated in an oil bath set at 62°C for 4 h. The solution was cooled to room temperature and the solvent volume halved. The Schlenk tube was stored overnight at -25°C. The crystals were isolated by cannula-filtration and the supernatant solution was discarded. The crystals were re-dissolved in the minimum amount of hot, dry acetonitrile. The Schlenk tube was placed within a warm alcohol bath and stored at -25°C in order to cool slowly, producing large cube-like crystals (0.384 g, 30%). M.p. = 228-230°C. IR (Nujol, cm^{-1}) ν = 1590, 1438, 1377, 1314, 1232, 1164, 1117, 1054, 1016, 997, 966, 879, 801, 766, 725, 694, 615, 553. ^1H NMR (CH_3CN-d^3) δ [ppm] = 9.01, 8.43, 8.37, 8.30, 8.01 (CH-tetrazolate), 7.74-7.14 (m, PPN). Elemental analysis calculated for $C_{78}H_{66}N_{26}P_4Ge$ (1518.47 $gmol^{-1}$): C= 59.90%, H= 4.25%, N = 23.28%. Found: C = 59.72%, H = 4.12%, N = 23.23%. X-ray diffraction data, a = 9.14 Å, b = 25.87 Å, c = 16.27 Å, α = 90°, β = 105.82°, γ = 90° (Monoclinic P).

2.4.15 Synthesis of *p*-dimethylaminophenylpentazole

(Procedure adapted from ref. 93)

N,N-dimethylphenylenediamine (1.01 g, 7.38 mmol) was dissolved in 10 mL water, producing a purple solution. This was cooled to 0°C in an ice bath, and stirred for 5 minutes. 1.5 mL HCl (35%) was slowly added and the purple solution changes to red, with slight bubbling. $NaNO_2$ (0.561 g, 8.13 mmol) was added spatula-wise to the stirring mixture under argon flow, turning the red solution dark green. In a separate Schlenk tube, NaN_3 (0.531 g, 8.17 mmol) was dissolved in 7.5 mL methanol. An additional Schlenk tube was filled with

10.5 mL methanol and 4 mL hexane. Both Schlenk tubes were cooled to -35^{o}C. The methanol/hexane solution was cannula-transferred to the dark green solution.

The NaN_3/methanol solution was then cannula-transferred onto the green solution at -35^{o}C. The reaction mixture was stirred at -60^{o}C for 1 h. An additional 5 mL cold methanol (-35^{o}C) was added to dilute the dark green suspension. Using a cold jacket filter kept below -25^{o}C using dry ice, the suspension was filtered, yielding a green suspension and a grey solid upon the sinter. The solid was washed with methanol (3x5 mL), acetone (2x5 mL) and hexane (1x2 mL). The green suspension was discarded.

Dichloromethane (25 mL) was cooled to -30^{o}C and was added onto the sinter, partially dissolving the grey solid and producing a dark red solution. The suspension was manipulated using a cold spatula over 5 minutes, ensuring all solid was loose from the sinter. The red suspension was poured into a pre-cooled (-25^{o}C) Schlenk tube and was stirred at -25^{o}C for 10 minutes. The suspension was then filtered into a Schlenk tube cooled in dry ice and the solution was left overnight to crystallise. The solution was removed by crystallisation and the pure brown needle-like crystals were dried *in vacuo* at -30^{o}C (0.578 g, 21%). IR (Nujol, cm^{-1}) ν = 2124 (N_3 – due to decomposition), 2092 (N_3 – due to decomposition), 1603, 1520, 1489, 1442, 1382, 1295, 1238, 1196, 1129, 1056, 1002, 973, 948, 810, 760, 718, 610.

2.4.16 Synthesis of dimethylaminophenylazide

(Procedure adapted from ref. 93)

Dimethylaminophenylpentazole (158 mg, 0.83 mmol) was dissolved in room temperature dichloromethane, producing a yellow-green solution with a red precipitate. The suspension was filtered to give a green, clear solution. The solvent was removed *in vacuo* and the solid stored overnight at -25^{o}C. The solid was transferred to a sublimation apparatus and heated *in vacuo* to 48^{o}C for 2 h. A yellow semi-crystalline material collects on the coldfinger, leaving behind a black solid. Due to light-sensitivity the yellow solid was stored in darkness at -25^{o}C (95 mg, 71%). IR (Nujol, cm^{-1}) ν = 2091, 2024, 2018, 1855, 1611, 1513, 1456, 1354, 1292, 1226, 1168, 1128, 1063, 947, 813, 729, 615, 525.

2.4.17 Synthesis of ^{Mes}NacNac-Li

(Procedure adapted from ref. 98)

^{Mes}NacNac-H (1.00 g, 3.00 mmol) was added to a Schlenk tube and was dissolved in ca. 20 mL Grubbs hexane. The clear solution was cooled to -78^{o}C with stirring, resulting in a white suspension. The Schlenk tube was degassed and n-BuLi (2.00 mL, 3.20 mmol) was added via syringe under a protective flow of argon. This results in a clear, slightly yellow solution. Stirring was continued for 10 minutes at -78^{o}C, then 2 h at room temperature. Over this time the solution darkened to a bright yellow. The solvent volume was halved *in vacuo*, and was briefly heated to re-dissolve the yellow precipitate. The solution was cooled to room temperature and stored overnight at -25^{o}C. The yellow solid was isolated by filtration. It was washed with cold hexane (3x2 mL) and then the off-white solid was dried *in vacuo* for 2 h (0.725 g, 71%). ^{1}H NMR (C_6D_6) δ [ppm] = 6.93 (s, 4H, Ar-H), 4.79 (s, 1H, β-CH), 2.30 (s, 6H, *p*-CH_3), 2.03 (s, 12H, *o*-CH_3), 1.69 (s, 6H, α-CH_3). Analytical results match that from the published data.

2.4.18 Synthesis of MgI_2

(Procedure adapted from ref. 98)

In a Schlenk tube, magnesium turnings (0.500 g, 20.0 mmol) were suspended in approximately 50 mL dry Et_2O and was stirred for 5 minutes. Iodine (2.48 g, 18.0 mmol) was added spatula-wise, turning the colourless solution dark brown. Over 15 minutes the reaction mixture warms up and gradually lightens in colour. The suspension was stirred for a further 1 h. The residual black solid was removed by filtration and the colourless solution was concentrated *in vacuo* until the onset of crystallisation. The Schlenk tube was stored overnight at -25^{o}C.

The colourless dietherate crystals were isolated via filtration. The crystals were then dried *in vacuo* at 40^{o}C for 6 h to remove to co-ordinated solvent (2.97 g, 93%). IR spectrum shows just peaks attributed to Nujol. MgI_2 vibrations were not visible between 4000 cm^{-1} and 500 cm^{-1}. However, this blank spectrum indicates that the pure compound has been synthesised, and no solvent remained.

2.4.19 Synthesis of Mg(^{mes}nacnac)I.OEt$_2$

(Procedure adapted from ref. 98)

Li(^{mes}nacnac) (0.725 g, 2.13 mmol) was dissolved in 20 mL dry Et_2O in a Schlenk tube. MgI_2 . $2Et_2O$ (0.638 g, 2.13 mmol) was suspended in 20 mL dry Et_2O in a separate Schlenk tube. Both Schlenk tubes were cooled in an ice bath. The Li(^{mes}nacnac) solution was cannula-transferred on to the MgI_2 . $2Et_2O$ suspension. The reaction mixture was stirred at 0^{o}C for 10 minutes, then warmed to room temperature and stirred for 3 h. After 3 h, the slightly cloudy solution was filtered, giving a clear, colourless solution. The solvent volume was reduced *in vacuo* to ca. 5 mL. A white precipitate was produced and the suspension was heated briefly to re-dissolve all solid. The slightly yellow solution was stored overnight at -25^{o}C. The white crystals were isolated by filtration and washed with cold Et_2O (-50°C, 2 x 2 mL). Crystals were dried *in vacuo* for 1 h. (0.593 mg, 47%). ^{1}H NMR (C_6D_6) δ [ppm] = 0.51 (6H, s, OCH_2CH_3), 1.60 (6H, s $NCCH_3$), 2.10 (6H, s, o-CH_3), 2.16 (6H, s, o-CH_3), 2.64 (6H, s, p-CH_3), 3.15 (4H, q, OCH_2CH_3), 4.91 (1H, s, CH), 6.81 (4H, s, ArH). Analytical data match that from the literature.

2.4.20 Synthesis of (^{mes}nacnac)Mg-Mg(^{mes}nacnac)

(Procedure adapted from ref. 98)

A Schlenk tube was coated in a sodium mirror by heating 0.7 g of sodium under dynamic vacuum. Mg(^{mes}nacnac)I.OEt_2 (1.71 g, 3.05 mmol) was dissolved in 20 mL dry toluene and 1 mL dry Et_2O. The slightly white suspension was cannula-transferred to the sodium-mirror containing Schlenk tube and was stirred for 5 days. After 3 days the sodium mirror was scraped from the Schlenk tube walls to encourage further reduction. Once the 5 day stir was complete the green suspension was filtered, yielding a yellow solution and a green-black solid. The solvent volume was reduced *in vacuo* to approximately 10 mL. The yellow suspension was heated briefly in a water bath then stored at -25^{o}C. The yellow solid was isolated by cannula filtration and dried *in vacuo* (0.576 g, 78%). ^{1}H NMR (C_6D_6) δ [ppm] = 6.85 (s, 8H, Ar-H), 4.80 (s 2H, β-CH), 2.29 (s, 12H, *p*-CH_3), 1.91 (s, 24H, *o*-CH_3), 1.54 (s, 12H, $NCCH_3$). Analytical data match that from the literature.

2.4.21 Synthesis of $(PPN)_2[Sn(CHN_4)_3Cl_3]$

$PPN(CHN_4)$ (3.47 g, 5.71 mmol) was dissolved in ca. 30 mL dry acetonitrile. $SnCl_4$ (0.100 mL, 0.900 mmol) was added via a volumetric pipette under a protective flow of argon. The reaction solution was heated within an oil bath set at 65°C and was stirred for 5 days. After 5 days the solvent volume was halved. The Schlenk tube was stored at -25°C overnight. The crystals were isolated by cannula-filtration and were re-dissolved in dry acetonitrile. $PPN(CHN_4)$ (1.44 g, 2.37 mmol) was dissolved in dry acetonitrile and cannula-transferred to the intermediate reaction solution. The reaction mixture was heated in an oil bath set at 65°C for 5 days. The solvent volume was halved under dynamic vacuum and the solution stored at -25°C overnight. Crystals isolated and washed with cold, dry acetonitrile. Crystals analysed using single crystal X-ray Diffraction. The crystals were shown to be $(PPN)_2[SnCl_3(CHN_4)_3]$. Colourless, crystalline solid dried *in vacuo* and stored in a glove box (0.582 g, 32%). IR (Nujol, cm^{-1}) ν = 3359, 3052, 1589, 1486, 1440, 1313, 1287, 1194, 1174, 1115, 1077, 1051, 1026, 997, 939, 893, 760, 699, 618, 540. ^1H NMR (DCM-d_2) δ [ppm] = 9.01-8.80 (m, various tetrazolate C-H), 8.20 (s, unreacted $PPN(CHN_4)$), 7.71-7.20 (m, PPN). X-ray diffraction data, a = 15.52 Å, b = 15.39 Å, c = 17.24 Å, α = 90°, β = 114.09°, γ = 90° (Monoclinic P).

2.4.22 Synthesis of Sodium Naphthalenide

(Procedure adapted from ref. 97)

Sodium (0.374 g, 16.3 mmol) was added to a dry, argon filled Schlenk tube. Naphthalene (1.05 g, 8.19 mmol) was placed in a separate Schlenk tube and was then dissolved in 25 mL dry THF. The clear, colourless solution was subsequently cooled by immersion into an ice bath to 0°C. The solution was cannula-transferred onto the sodium and the suspension was stirred at 0°C for 5 minutes. The colourless solution quickly turned yellow, before changing to a dark green suspension. The suspension was allowed to warm to room temperature and was stirred overnight. The remaining sodium was removed via filtration and the solution was stored at -25°C. (1.24 g, 26.0 mL, 0.315 mmol mL^{-1}).

2.4.23 Combination of *p*-dimethylaminophenylpentazole and Sodium Naphthalenide

p-dimethylaminophenylpentazole (0.107 g, 0.560 mmol) was added to a cold Schlenk tube, which was placed under dynamic vacuum for 15 minutes. Dry THF (20 mL) was added, producing a yellow solution. The solution was cooled to -78^{o}C within a dry ice bath. Small amount of the *p*-dimethylaminophenylpentazole precipitates out of the dry THF solution.

Aliquot of sodium naphthalenide solution (1.80 mL, 0.560 mmol) was added using a volumetric pipette under a protective flow of argon. Upon the addition of sodium naphthalenide, a gentle bubbling was produced, and no residual dark green colour of the sodium naphthalenide remains. Upon closer examination, the slight smell of naphthalene was found. The precipitated *p*-dimethylaminophenylpentazole suspended in the THF solution also disappears on addition of the sodium naphthalenide, producing a clear yellow/orange solution. IR (Nujol, cm^{-1}) ν = 2024, 2091, 2018, 1855, 1611, 1513, 1456, 1354, 1292, 1226, 1168, 1128, 1063, 947, 813, 729, 615, 525. Solution contains solely *p*-dimethylaminophenylazide.

2.4.24 Synthesis of ^{mes}H-nacnac

(Procedure adapted from ref. 98)

2,4,6-trimethylaniline (18.5 mL, 137 mmol) and 2,4-pentadione (4.50 mL, 43.8 mmol) were added to a stirred 200 mL of ethanol. The slightly blue solution was stirred for 2 minutes. HCl (35%, 5.00 mL) was added, turning the solution yellow. The reaction mixture was heated within an oil bath set at 85^{o}C and was refluxed for 3 days. The red-orange solution was allowed to cool to room temperature and the solvent was removed by rotary evaporation. Hexane (300 mL) was added to the orange-brown solid and the suspension was refluxed for 1 h. Once cool, the suspension was filtered, leaving behind a light brown solid. The solid was added to a saturated solution of Na_2CO_3 in water (400 mL). With stirring, dichloromethane (600 mL) was added and the mixture stirred for 10 minutes. The organic layer was extracted and washed with distilled water (3x50 mL). The organic solution was dried over $MgSO_4$ and then filtered. The solvent was removed using rotary evaporation and the resultant brown oil was dried by high vacuum for 20 minutes. Cold methanol (2x50 mL, 0^{o}C) was used to wash

the solid, leaving an off-white solid. The solid was re-crystallised from 300 mL hot acetonitrile (24.3 g, 61%).

^{1}H NMR ($CHCl_3$–*d*) δ [ppm] = 12.16 (s, 1H, *o*-CH_3), 6.86 (s, 4H, Ar-H), 4.86 (s 1H, β-CH), 2.26 (s, 6H, *p*-CH_3), 2.12 (s, 12H, *o*-CH_3), 1.69 (s, 6H, *p*-CH_3). Analytical data match that from the literature.

2.4.25 Reaction of (^{mes}nacnac)Mg–Mg(nanac^{mes}) with *p*-dimethylaminophenylpentazole

p-Dimethylaminophenylpentazole (106 mg, 0.550 mmol) was added to a cold Schlenk tube, which was then evacuated for 15 minutes and refilled with cold, dry toluene (20 mL), producing a yellow solution. The solution was then cooled to -78^{o}C in a dry ice bath. (^{mes}nacnac)Mg–Mg(nanac^{mes}) (0.395 g, 0.550 mmol) was added to a separate Schlenk tube and dissolved in dry toluene. The (^{mes}nacnac)Mg–Mg(nanac^{mes}) solution was cooled to -50^{o}C and was subsequently added drop-wise to the stirring *p*-dimethylaminophenylpentazole solution, which remains at -78^{o}C. No observable changes were seen. The reaction solution was stirred at -78^{o}C for 1 h. The reaction solution was allowed to warm to room temperature whilst analysing using solution-cell IR spectroscopy. No reduction was observed, only simple decomposition of *p*-dimethylaminophenylpentazole to produce *p*-dimethylaminophenylazide. This was likely due to the warming of the solution to room temperature rather than the (^{mes}nacnac)Mg–Mg(nanac^{mes}) itself.

2.4.26 Synthesis of *p*-dimethylaminophenyldiazo tetrafluoroborate

(Procedure adapted from ref. 91)

N,N-dimethylphenyldiamine (2.06 g, 15.1 mmol) was dissolved in water (12 mL) and the purple solution was cooled to 0^{o}C with stirring. 50% aqueous HBF_4 ((3.00 mL, 35%) was slowly added to the stirring solution, turning the solution red and producing bubbles of gas. $NaNO_2$ (1.18 g, 17.1 mmol) was dissolved in water and added to the red solution, immediately producing a green/brown precipitate. An additional 20 mL of cold water was added to facilitate easier stirring. The reaction mixture was stirred at 0^{o}C for 1 h. The solution was filtered and the black-red solid was washed with cold methanol (3 x 8 mL, -25^{o}C) and cold hexane (5 mL, -25^{o}C), giving an orange solid (0.981 g, 28%). IR (Nujol, cm^{-1}) =

3409, 3318, 3225, 3116, 2704, 2249, 2160 (N=N stretch), 1584, 1390, 1120, 1050, 933, 826. ^{1}H NMR (CH_3CN-d_3) δ [ppm] = 8.02 (d, 2H, Ar-H), 6.96 (d, 2H, Ar-H), 3.28 (s, 6H, NMe_2).

2.4.27 Synthesis of {RhCp*Cl_2}$_2$

(Procedure adapted from ref. 92)

$RhCl_3.3H_2O$ (509 mg, 1.93 mmol) and 20 mL methanol were added to a 100 mL round-bottomed flask, and the red-brown suspension was degassed. Cp*H (270 mg, 1.98 mmol) was added and a condenser was attached. The system was again degassed, and the reaction mixture was heated in an oil bath set at 65^{o}C. The suspension was refluxed for 48 h. Once cool, the red suspension was concentrated and cooled to -25^{o}C for 1 h. Supernatant orange solution filtered off and red precipitate was washed with cold hexane (0^{o}C, 2 x 10 mL). Red solid dried *in vacuo* (532 mg, 89%).

2.4.28 Synthesis of {RhCp*(N_3)}$_2$

(Procedure adapted from ref. 92)

$RhCl_2Cp^*$ (0.500 g, 1.62 mmol) was suspended in 40 mL acetone and the mixture was degassed. The suspension was cooled to 0^{o}C and NaN_3 (0.671 g, 10.3 mmol) was added with stirring. The red-brown mixture was stirred at 0^{o}C for 10 minutes then 4 h at room temperature. After 4 h the red suspension was filtered and the precipitate was washed with acetone. The filtrate solvent was removed and the red solid washed with acetone. Both solids combined and dried *in vacuo* (486 mg, 93%). ^{1}H NMR (CH_3CN-d_3) δ [ppm] = 1.63 (s, 15H, Cp*).

2.4.29 Synthesis of RhCp*(N_3)$_2$(PPh_3)

(Procedure adapted from ref. 92)

$RhCp^*(N_3)_2$ (412 mg, 1.28 mmol) was dissolved in approximately 20 mL acetone. PPh_3 (341 mg, 1.30 mmol) was added with stirring and the reaction solution was stirred at room temperature for 1 h. The solvent was removed under dynamic vacuum. Red-brown residue washed with approximately 10 mL DCM and the solution is concentrated *in vacuo* until the onset of crystallisation. Suspension was cooled to -20^{o}C and 45 mL hexane was added, causing precipitation. Red solid isolated by filtration, and washed with cold hexane (0^{o}C, 2 x

5 mL) Red solid dried *in vacuo* (709 mg, 95%). ^{1}H NMR (DCM-d_2) δ [ppm] = 7.54-7.28 (m, 15H, PPh_3), 1.45 (s, 15H, Cp*).

2.4.30 Reaction of *p*-dimethylaminophenyldiazo tetrafluoroborate and {RhCp*$(N_3)_2$}$_2$

In separate Schlenk tubes, RhCp*$(N_3)_2$ (60.0 mg, 0.180 mmol) and *p*-dimethylaminophenyldiazo tetrafluoroborate (60.0 mg, 0.260 mmol) were dissolved in dry DCM at -30^{o}C. The solutions were combined and stirred at -15^{o}C for 1 h. The progress of the reaction was monitored using solution cell IR spectroscopy. Reaction shows evidence in the IR analysis of production and then decomposition of pentazole.

2.4.31 Synthesis of 4-hydroxyphenyldiazonium trifluoroacetate

4-aminophenol (1.00 g, 9.12 mmol) was suspended in 25 mL DCM, giving an orange suspension. Trifluoroacetic acid (1.40 mL, 18.9 mmol) was added via volumetric pipette under a protective flow of argon. Over 20 min the suspension turned white and thickened. Amyl nitrite (1.50 mL, 10.8 mmol) was slowly added under argon over 5 min. The white/purple suspension was stirred at 2^{o}C for 1 h, yielding a dark green solution and a grey precipitate. The Schlenk tube was cooled to -78^{o}C and pre-cooled diethyl ether (-78^{o}C, 20 mL) was added and stirred for 2 min. The yellow orange solution was removed by filtration and the grey precipitate was washed with diethyl ether (2 x 15 mL). The grey solid was dried *in vacuo* (1.91 g, 89%). Used immediately without analysis.

2.4.32 Synthesis of 4-hydroxyphenylpentazole

(Procedure adapted from ref. 69)

4-hydroxyphenyldiazonium trifluoroacetate (2.34 g, 10.0 mmol) was suspended in 6 ml methanol at -30^{o}C. Pre-cooled petroleum ether (40-60, 7 mL) was added. The purple suspension was stirred for 5 min. NaN_3 (1.30 g, 20.0 mmol) was dissolved in 5 mL H_2O and the solution was degassed. The NaN_3 solution was added dropwise to the diazonium suspension. The orange/brown suspension was stirred for 90 min. The pink/orange suspension was filtered, yielding a pink/grey precipitate and a brown solution, which was discarded. The precipitate was dried under vacuum (250 mg, 16%). IR (Nujol, cm^{-1}) = 3311,

3093, 2113 (N_3 – due to decomposition), 2073 (N_3 – due to decomposition), 1911, 1602, 1574, 1505, 1219, 1119, 982, 828, 707, 634.

2.4.33 Synthesis of PPN[$PbCl_3$]

PPN(Cl) (2.60 g, 4.54 mmol) and $PbCl_2$ (1.26 g, 4.53 mmol) were both added to a Schlenk tube. Dry, degassed THF (35 mL) was added and the white suspension was stirred for 1 h. The temperature of the reaction mixture was elevated to 50^{o}C, and the white suspension was stirred overnight. Reaction progress was difficult to observe, as visually the reaction mixture does not change. White solid dried *in vacuo* (3.03 g, 78%). M.p. = 235-237^{o}C. IR (Nujol, cm^{-1}) = 3057, 1585, 1466, 1285, 1250, 1182, 1114, 1029, 997, 851, 794, 753, 721, 691. Elemental analysis calculated for $C_{36}H_{30}NP_2Cl_3Pb$ (852.14 $gmol^{-1}$): C = 50.74%, H = 3.55%, N = 1.64%. Found: C = 50.98%, H = 3.67%, N = 1.71%. Poor solubility limits analytical investigation.

2.4.34 Attempted Synthesis of PPN[$Pb(CHN_4)_3$]

PPN[$PbCl_3$] (0.200 g, 0.230 mmol) and Na(CHN_4) (0.216 g, 2.30 mmol) were both added to a Schlenk tube. Dry, degassed MeCN was added and the white suspension was stirred for 66 h at RT. The solution was removed by cannula filtration and the white solid (shown to be Na(CHN_4) using IR spectroscopy) was discarded. Solvent was removed *in vacuo*, leaving behind a small amount of white solid. ^{1}H NMR (DCM-d_2) δ [ppm] = 8.37 (s, tetrazolate C-H), 7.79-7.71 (m, PPN).

2.4.35 Synthesis of PPN[$SnCl_3$]

PPN(Cl) (3.02 g, 5.27 mmol) and $SnCl_2$ (1.00 g, 5.27 mmol) were both added to a Schlenk tube. Dry, degassed DCM (20 mL) was added and the orange solution was heated to 50^{o}C and stirred for 16 h. Solvent was removed *in vacuo* and the solid was shown using IR spectroscopy to be a PPN salt. Dry, degassed THF (approximately 20 mL) was added in order to separate unreacted PPN(Cl), which was insoluble in THF. Any solid was removed by cannula filtration, and the solvent volume of the supernatant solution was reduced *in vacuo* to 3 mL. 20 mL of dry, degassed Et_2O was added and the white solid isolated by cannula filtration. Product dried *in vacuo* (3.89 g, 97%). M.p. = 160-162^{o}C. IR (Nujol, cm^{-1}) = 3055, 1588, 1464, 1248, 1187, 1110, 1024, 996, 804, 745, 723, 690. Elemental analysis calculated

for $C_{36}H_{30}P_2NCl_3Sn$ (763.65 $gmol^{-1}$): C = 56.62%, H = 3.96%, N = 1.83%. Found: C = 56.29%, H = 3.89%, N = 1.61%.

2.4.36 Attempted synthesis of PPN[Sn(CHN$_4$)$_3$]

PPN[$SnCl_3$] (0.250 g, 0.33 mmol) and Na(CHN_4) (0.301 g, 3.3 mmol) were combined in a Schlenk tube. Dry, degassed MeCN (20 mL) was added and the reaction suspension was stirred overnight at 60^{o}C. After 16 h a yellow suspension has formed. Clear, colourless solution isolated by cannula filtration, leaving behind a yellow solid. Solution was concentrated *in vacuo*, producing an oil. ^{1}H NMR (DCM-d^2) δ [ppm] = 11.95 (very small, broad, $HCHN_4$ N-H), 8.67 (s, tetrazolate C-H), 7.79-7.71 (m, PPN).

2.4.37 Synthesis of 1-Trimethylsilyl-tetrazole

(Procedure adapted from ref. 18)

TMS-Cl (8.60 mL, 67.8 mmol) was added to a Schlenk tube and dry, degassed toluene (20 mL) was added. In a separate Schlenk tube, 1*H*-tetrazole (4.75 g, 67.8 mmol) was suspended in 40 mL dry toluene. To the white tetrazole suspension, dry Et_3N (9.46 mL, 67.8 mmol) was added, changing the white suspension to an easily settled, "cloud-like" suspension. Reaction mixture was stirred for 5 min, and was subsequently cooled to 0^{o}C within an ice bath. TMS-Cl solution was added dropwise using a cannula, causing an immediate precipitation. The reaction mixture was stirred at 0^{o}C for 24 h. Supernatant solution filtered into a 3 necked, 100 mL round bottomed flask. Vacuum distillation apparatus attached and toluene removed at 84^{o}C and 5 x 10^{-1} mbar. 35 mL collected in receiving flask and was shown using NMR spectroscopy to be toluene. Yellow oil left in distillation flask was pipetted under a protective flow of argon into an ampoule. Viscous, yellow liquid dried *in vacuo* to remove residual Et_3N and toluene (2.513 g, 26%). %). ^{1}H NMR (CH_3CN-d_3) δ [ppm] = 8.89 (s, CH), 0.60 (s, TMS). Analytical data match that from the literature.

2.4.38 Synthesis of Sn(CHN$_4$)Cl(py)$_2$

$SnCl_2$ (150 mg, 0.79 mmol) and Na(CHN_4) (1.10 g, 11.8 mmol) were both added to a Schlenk tube. To the white suspension, dry pyridine (10 mL) was added, giving an immediate yellow suspension. The reaction suspension was stirred at RT for 46 h. The yellow suspension was filtered, giving a bright yellow, clear solution and a pale yellow solid. The solid was dried *in*

vacuo and was shown using IR spectroscopy to be unreacted $Na(CHN_4)$. The yellow solution was concentrated *in vacuo* to approximately 1 mL, and stored at -25°C. Small amount of crystals grown from the solution were analysed using single crystal X-ray diffraction and were shown to be $Sn(CHN_4)Cl(py)_2$. X-ray diffraction data, a = 5.89 Å, b = 7.36 Å, c = 15.87 Å, α = 89.80°, β = 83.79°, γ = 89.61° (Monoclinic P).

2.4.39 Synthesis of $\{Sn(CHN_4)_2(py)_2\}_n$ Co-ordination Polymer

SnF_2 (150 mg, 0.957 mmol) was added to a Schlenk tube in a glove box. Dry pyridine (10 mL) was added and the resulting white suspension was stirred. $TMS(CHN_4)$ (300 mg, 2.11 mmol) was weighed in a sample vial and added using a pipette. On addition of the TMS(CHN4) the SnF_2 dissolves, giving a clear, colourless solution. The Schlenk tube was removed and stirred at RT for 16 h. After approximately 4 h a precipitate forms. On completion of the 16 h stir, the solution was isolated by cannula filtration, leaving behind a white solid. Solid was dried *in vacuo* and stored in a glove box (248 mg, 62% with respect to SnF_2). M.p. = 288°C (probable detonation). IR (Nujol, cm^{-1}) ν = 1595, 1458, 1298, 1276, 1214, 1193, 1097, 1033, 972, 881, 753, 686, 618. ^{1}H NMR (CH_3CN-d^3) δ [ppm] = 8.94 (s, tetrazolate C-H), 8.54 (s, py). 7.75 (s, py), 7.35 (s, py). ^{13}C NMR (CH_3CN-d^3) δ [ppm] = 144.56 (s, tetrazolate C-H), 151.24 (s, py), 137.34 (s, py), 125.71 (s, py). X-ray diffraction data, a = 10.05 Å, b = 10.04 Å, c = 10.66 Å, α = 90.04°, β = 90.02°, γ = 90.01° (Triclinic).

2.4.40 Synthesis of $PPh_4(CHN_4)$

PPh_4Cl (2.00 g, 5.33 mmol) and $Na(CHN_4)$ (0.49 g, 5.33 mmol) were both added to a Schlenk tube. Dry MeCN (20 mL) was added and the pale yellow suspension was stirred at r.t. for 1 h. The suspension develops a whiter colour. The white suspension was heated to 50°C and stirred for 1 h. The suspension was filtered to yield a clear, colourless solution and an off-white solid. The residue is discarded and the solution is concentrated *in vacuo* to ½ of the original volume, at which a solid precipitates. The solid is re-dissolved with gentle heating and the Schlenk tube was stored at -25°C to allow crystallisation (1.79g, 82% with respect to PPh_4Cl). M.p. = 256-259°C. IR (Nujol, cm^{-1}) ν = 3118, 3056, 1584, 1435, 1263, 1186, 1149, 1138, 1107, 1026, 994, 979, 843, 752, 689, 615. ^{1}H NMR (CH_3CN-d^3) δ [ppm] = 8.32 (s, tetrazolate C-H), 7.98-7.39 (m, PPh_4). ^{13}C NMR (CH_3CN-d^3) δ [ppm] = 149.67 (tetrazolate C-H), 136.81 (d, PPh_4), 136.15 (d, PPh_4), 131.77 (d, PPh_4), 119.81 (s, PPh_4). ^{31}P NMR (CH_3CN-d^3)

δ [ppm] = 22.82 (PPh_4). X-ray diffraction data, a = 17.49 Å, b = 6.94 Å, c = 22.27 Å, α = 90°, β = 105.13°, γ = 90° (Monoclinic P).

2.4.41 Synthesis of $PPh_4\{Sn(CHN_4)_3\}_n$ co-ordination polymer

$PPh_4(CHN_4)$ (261 mg, 0.64 mmol), TMS-CHN_4 (300 mg, 2.00 mmol) and SnF_2 (100 mg, 0.64 mmol) were all added to a Schlenk tube within the glove box. The reagents were suspended in dry THF (15 mL) within the glove box and the white suspension was stirred at r.t. After 1 h the suspension had thickened. The Schlenk tube was removed from the glove box and the solvent was removed *in vacuo* leaving a white solid. Dry MeCN (15 mL) was added and the suspension was heated briefly to re-dissolve the majority of solid. The slight suspension was filtered, giving a clear solution. The solution was concentrated *in vacuo* to approximately 2 mL and the Schlenk tube was stored at -25°C. Crystal were produced and analysed using analytical methods (124 mg, 23%). M.p. = 130-133°C. IR (Nujol, cm^{-1}) ν = 3140, 3056, 1586, 1310, 1224, 1138, 1108, 1044, 981, 892, 757, 689, 528. ^{1}H NMR (CH_3CN-d^3) δ [ppm] = 8.70 (s, tetrazolate C-H), 8.00-7.60 (m, PPh_4). ^{13}C NMR (CH_3CN-d^3) δ [ppm] = 147.13 (s, tetrazolate C-H), 136.81 (d, PPh_4), 136.15 (d, PPh_4), 131.77 (d, PPh_4), 119.81 (s, PPh_4). ^{31}P NMR (CH_3CN-d^3) δ [ppm] = 22.91 (s, PPh_4). X-ray diffraction data, a = 9.65, b = 9.81, c =32.80 α = 90, β = 97.59, δ = 90. (Monoclinic P).

2.4.42 Synthesis of $PPN[Sb_3F(CHN_4)_6]$

SbF_3 (100 mg, 0.55 mmol), TMS-CHN_4 (398 mg, 2.8 mmol) and $PPN(CHN_4)$ (334mg, 0.55 mmol) were all added to a Schlenk tube. Dry MeCN (15 mL) was added to the reagents and the white suspension was stirred at RT. After 30 min. the suspension had become a hazy solution. After 31 h, a thick white suspension had formed. Reaction suspension was stirred for a further 15 h and the solvent was then removed *in vacuo* leaving a white solid. Dry THF (20 mL) was added to the crude product and the majority of the white solid dissolved. The suspension was filtered to produce a clear solution. Dry Et_2O (approx. 2 mL) was added and the Schlenk tube was stored at -25°C. Crystals were produced and analysed (112 mg, 15% with respect to SbF_3). M.p. = 186-188°C. IR (Nujol, cm^{-1}) ν =3157, 3117, 3059, 1587, 1463, 1323, 1216, 1190, 1141, 1116, 1043, 998, 908, 782, 749, 691, 532. ^{1}H NMR (CH_3CN-d^3) δ [ppm] = 8.77 (CH-tetrazolate). ^{13}C NMR (CH_3CN-d^3) δ [ppm] = 146.38 (tetrazolate C-H), 135.07 (s, PPN), 133.68 (t, PPN), 130.84 (t, PPN), 129.24 (s, PPN), 128.15 (s, PPN). ^{31}P NMR

(CH_3CN-d^3) δ [ppm] = 20.78 (s, PPN). Elemental analysis calculated for $C_{42}H_{36}N_{25}P_2Sb_3F$ (1337.02 $gmol^{-1}$): C= 37.73%, H= 2.71%, N = 26.18%. Found: C = 53.45%, H = 4.14%, N = 20.52%. X-ray diffraction data, a = 31.32, b = 8.95, c =30.46, α = 90, β = 114.54, δ = 90. (Monoclinic C).

2.4.43 Synthesis of $(PPN)_2[Sn(CHN_4)_6]$

SnF_4 (100 mg, 0.51 mmol) and $PPN(CHN_4)$ (686 mg, 1.13 mmol, 2.2 eq) were suspended in dry MeCN in a glove box. TMS-CHN_4 (365 mg, 2.57 mmol, 5 eq) was added via pipette and the slight white suspension (unreacted SnF_4) stirred at RT for 2 h. After 1 h the reaction mixture was thinned considerably. Schlenk tube taken out of the glove box and the solution was filtered, giving a clear colourless solution. The solution was concentrated *in vacuo* to 5 mL and heated briefly to ensure all solid was dissolved. Crystals isolated and investigated using single crystal X-ray diffraction. Crystals were confirmed to be the product (0.56 g, 71% with respect to SnF_4). M.p. = 206-208°C. IR (Nujol, cm^{-1}) ν = 1588, 1438, 1308, 1276, 1230, 1184, 1151, 1116, 1047, 997, 964, 797, 692. ^{1}H NMR (CH_3CN-d^3) δ [ppm] = 8.79, 8.68, 8.65, 8.60, 8.51 (m, various tetrazolate C-H), 7.91-7.24 (m, PPN). ^{13}C NMR (CH_3CN-d^3) δ [ppm] = 148.52 (s, tetrazolate C-H), 135.07 (s, PPN), 133.72 (t, PPN), 130.84 (t, PPN), 129.23 (s, PPN), 128.15 (s, PPN). ^{31}P NMR (CH_3CN-d^3) δ [ppm] = 20.78 (s, PPN). Elemental analysis calculated for $C_{78}H_{66}N_{26}P_4Sn$ (1518.47 $gmol^{-1}$): C= 58.19%, H= 4.13%, N = 22.61%. Found: C = 61.24%, H = 4.69%, N = 18.65%. X-ray diffraction data, a = 9.24 Å, b = 26.22 Å, c = 16.11 Å, α = 90°, β = 104.61°, γ = 90° (Monoclinic P).

2.4.44 Attempted Synthesis of $PPN[Bi(CHN_4)_4]$

BiF_3 (100 mg, 0.38 mmol), TMS-CHN_4 (220 mg, 1.54 mmol) and $PPN(CHN_4)$ (228 mg, 0.38 mmol) were all added to a Schlenk tube. Dry MeCN (15 mL) was added to the reagents and the white suspension was stirred at RT. After 5 min. the reaction has produced a uniform suspension that settled easily. After 24 h, the suspension was allowed to settle and cannula-filtered to produce a colourless solution and a white solid. White solid is shown using IR spectroscopy to be unreacted BiF_3 and was discarded. The colourless solution was dried *in vacuo*, leaving an oil. Dry THF (10 mL) was added to the crude product and concentrated *in vacuo* to approximately 5 mL. Dry Et_2O (approx. 2 mL) was added and the Schlenk tube was stored at -25°C. Semi-crystalline solid was isolated and analysed using IR and NMR

spectroscopy (50 mg, 13% with respect to BiF_3). IR (Nujol, cm^{-1}) ν = 3110, 3055, 1587, 1483, 1437, 1353, 1184, 1116, 1043, 998, 905, 856, 690, 530. ^{1}H NMR (CH_3CN-d^3) δ [ppm] = 8.70 (tetrazolate C-H), 7.83-7.24 (m, PPN). ^{13}C NMR (CH_3CN-d^3) δ [ppm] = 146.50 (tetrazolate C-H), 135.07 (s, PPN), 133.72 (t, PPN), 130.84 (t, PPN), 129.23 (s, PPN), 128.15 (s, PPN). ^{31}P NMR (CH_3CN-d^3) δ [ppm] = 20.75 (s, PPN).

2.4.45 Attempted Synthesis of $\{Sn(CHN_4)_4\}_n$

SnF_4 (100 mg, 0.51 mmol) and TMS-CHN_4 (362 mg, 2.55 mmol) were both added to a Schlenk tube and suspended in dry MeCN (20 mL). The white suspension was stirred at RT for 10 days. No observable changes in the white suspension were recorded. The reaction suspension was heated to 55^{o}C for 3 h, and the amount of white precipitate visibly increases. The reaction suspension was filtered, resulting in a slightly turbid solution that does not settle and a white solid. Melting point analysis for the white solid indicated that it was the SnF_4 starting material. The turbid solution was filtered again, removing most of the remaining precipitate and the solvent volume of the supernatant solution was diminished *in vacuo.* Semi-crystalline material was produced upon cooling to -25^{o}C which was analysed using IR and ^{1}H NMR spectroscopy. The analytical data suggests that this was 1*H*-tetrazole, produced by the decomposition of the TMS-CHN_4 reagent. IR(Nujol, cm^{-1}) ν = 3157, 1814, 1524, 1256, 1143, 1083, 1014, 907, 799, 663. ^{1}H NMR (CH_3CN-d^3) δ [ppm] = 13.69 (br, tetrazole-NH), 8.96 (tetrazole CH).

3. Synthesis and Characterisation of Homoleptic Main Group Complexes of the Type $(PPN)_2[E(CHN_4)_6]$ (E = Si, Ge, Sn)

3.1 Overview

The aim of the investigation is the establishment of a general method for the synthesis of homoleptic poly(tetrazolato) complexes as a new class of complexes of main group elements. This will build upon a recently discovered method [70] by refining the preparative process already in place for silicon and germanium and extending the procedure to include tin. The PPN salt was utilised as it has proven to be a useful cation to facilitate crystallization, and its bulky structure will lower the overall nitrogen content of potential products to a completely safe working level, allowing for full characterisation of the complex. The tetrazolate salt can be produced via the reaction between PPN(Cl) and the sodium salt of 1*H*-tetrazole. The compounds $(PPN)_2[E(CHN_4)_6]$ (E = Si, Ge) have previously been characterised, but in this study were both obtained in a highly pure fashion for the first time.

The first attempt at the synthesis of $(PPN)_2[Sn(CHN_4)_6]$ was performed. It is hoped that $(PPN)_2[Sn(CHN_4)_6]$ can be isolated and characterised using NMR, IR, elemental analysis and single crystal X-ray diffraction studies. An alternative pathway to poly(tetrazolato) main group compounds was explored in detail for the first time, heating poly(azido) silicon and aluminium salts in dry acetonitrile. The products from these reactions have been investigated by IR spectroscopy.

3.2 Synthesis and Characterisation of $(PPN)_2[E(CHN_4)_6]$ (E = Si, Ge, Sn)

The rare nature of main group tetrazole complexes requires a tentative and open-minded approach to experimental work. The initial challenge of this investigation was the preparation of all starting materials in high purity. 1*H*-tetrazole can be prepared through the reaction between NaN_3, NH_4Cl and $CH(OEt_3)_3$. The reaction mixture was heated to reflux for 24h, and the crude 1*H*-tetrazole can be recrystallized from ethanol. A second re-crystallisation is performed using hot acetone, obtaining analytically pure 1*H*-tetrazole.

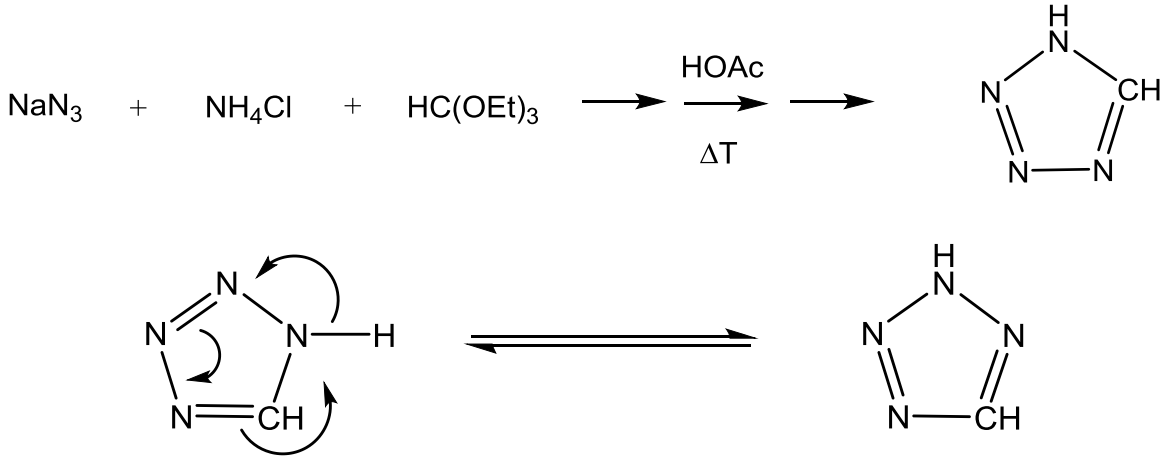

Scheme 12 – Revised synthesis of 1*H*-tetrazole (above).[2] 1*H*-tetrazole can undergo sigmatropic re-arrangement which broadens the amine proton peak observed in the ^1H NMR spectrum (figure 26)

The colourless crystals were analysed using IR and ^1H NMR spectroscopy.

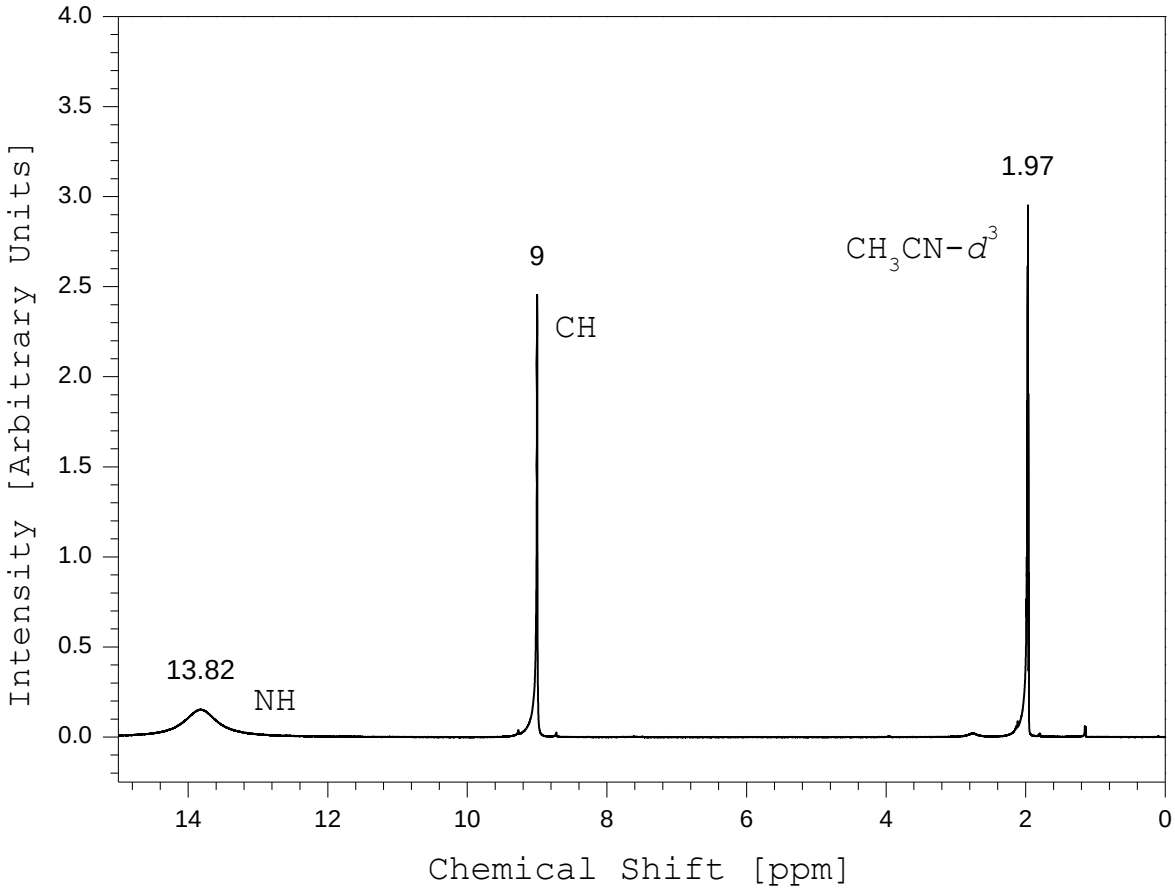

Figure 26 – ^{1}H NMR spectrum of 1*H*-tetrazole in CH_3CN-d_3.

The two peaks are due to the two proton environments found on 1*H*-tetrazole, the CH (9.00 ppm) and the NH (13.82 ppm). The broadening of the NH signal is due to its either sigmatropic re-arrangement, or dissociation of the hydrogen. As 1*H*-tetrazole is an acidic molecule, the proton readily exchanges in solution, which causes the peak to broaden. Using an NMR solvent that does not readily exchange allows this environment to be easily observed. The tetrazole can then be converted to the sodium salt through reaction with aqueous NaOH. The 1*H*-tetrazole is dissolved in water and added to the aqueous NaOH with stirring. The reaction mixture is stirred at reflux temperature for five minutes and the water is then evaporated under vacuum to give the crude product. A problem arose when attempting to re-crystallise the compound. The literature[2] dictates the use of ethanol as a re-crystallisation solvent; however, in practice the $Na(CHN_4)$ was too insoluble in the ethanol. The reaction results in just H_2O as the by-product, so the re-crystallisation was at this point deemed unnecessary. Ethanol was instead utilised as a simple washing solvent, removing any residual NaOH that has not been consumed during the reaction.

The $PPN(CHN_4)$ salt can be then prepared by a reaction of the sodium salt with PPN(Cl), precipitating out NaCl whilst leaving the pure product in solution. It is at this point where the first purification difficulties were encountered. The reaction with the main group tetrachlorides, ECl_4, is believed to be in equilibrium with the $[E(CHN_4)_x(Cl)_y]^{2-}$ intermediates, where x + y = 6. Initially, it was found that the $PPN(CHN_4)$ was contaminated by the PPN(Cl) starting material. The presence of any PPN(Cl) will act as chlorine reservoir, preventing the complete conversion of the ECl_4 to the $[E(CHN_4)_6]^{2-}$, instead halting the reaction at the $E(CHN_4)_x(Cl)_y$ intermediates.

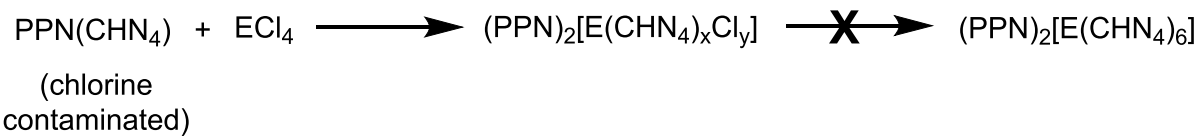

Scheme 13 – Effect of using chlorine contaminated $PPN(CHN_4)$ in the attempted synthesis of the $(PPN)_2[E(CHN_4)_6]$ complexes.

The reaction could not progress with the chlorine contamination. It was necessary to experiment with re-crystallisation solvents in order to find a system that would precipitate the pure $PPN(CHN_4)$, whilst keeping the remaining PPN(Cl) in solution. Hot acetonitrile was found to be suitable, giving excellent results based upon elemental analysis, with no chlorine present.

Element	Percentage expected [%]	Percentage found [%]	Variation [%]
Carbon	73.12	72.90	-0.22
Hydrogen	5.15	5.00	-0.15
Nitrogen	11.53	11.64	+0.11
Chlorine	0	<0.3 (detection limit)	0

Table 5 - Elemental analysis of a batch of $PPN(CHN_4)$ produced using an acetonitrile re-crystallisation.

Once the $PPN(CHN_4)$ was obtained in a pure fashion, it was possible to attempt the synthesis of $(PPN)_2[Si(CHN_4)_6]$. Dry, pure $SiCl_4$ was dissolved in dry acetonitrile and the $PPN(CHN_4)$ was added in a batch-wise fashion to generate the expected $(PPN)_2[Si(CHN_4)_6]$ product.

The batch approach was utilised to first produce the $Si(CHN_4)_x(Cl)_y$ intermediates, which could be isolated from the chlorine containing by-products. The second batch of $PPN(CHN_4)$ is then added to force the equilibrium to shift in favour of the completely substituted product.

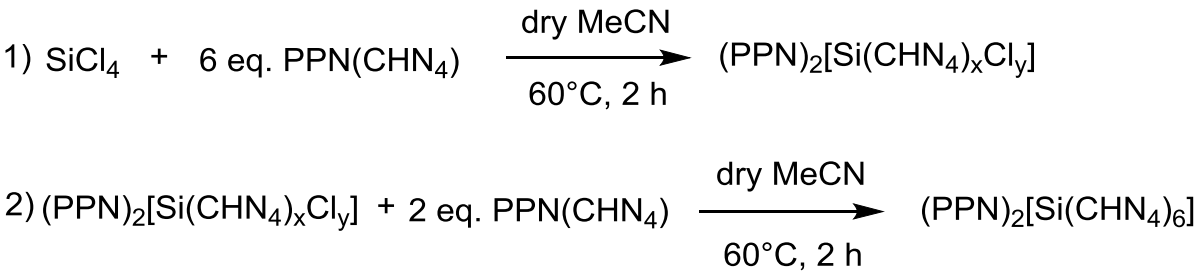

Scheme 14 – Preparation of $(PPN)_2[Si(CHN_4)_6]$.

The colourless crystals were analysed initially using IR and ^1H NMR spectroscopy.

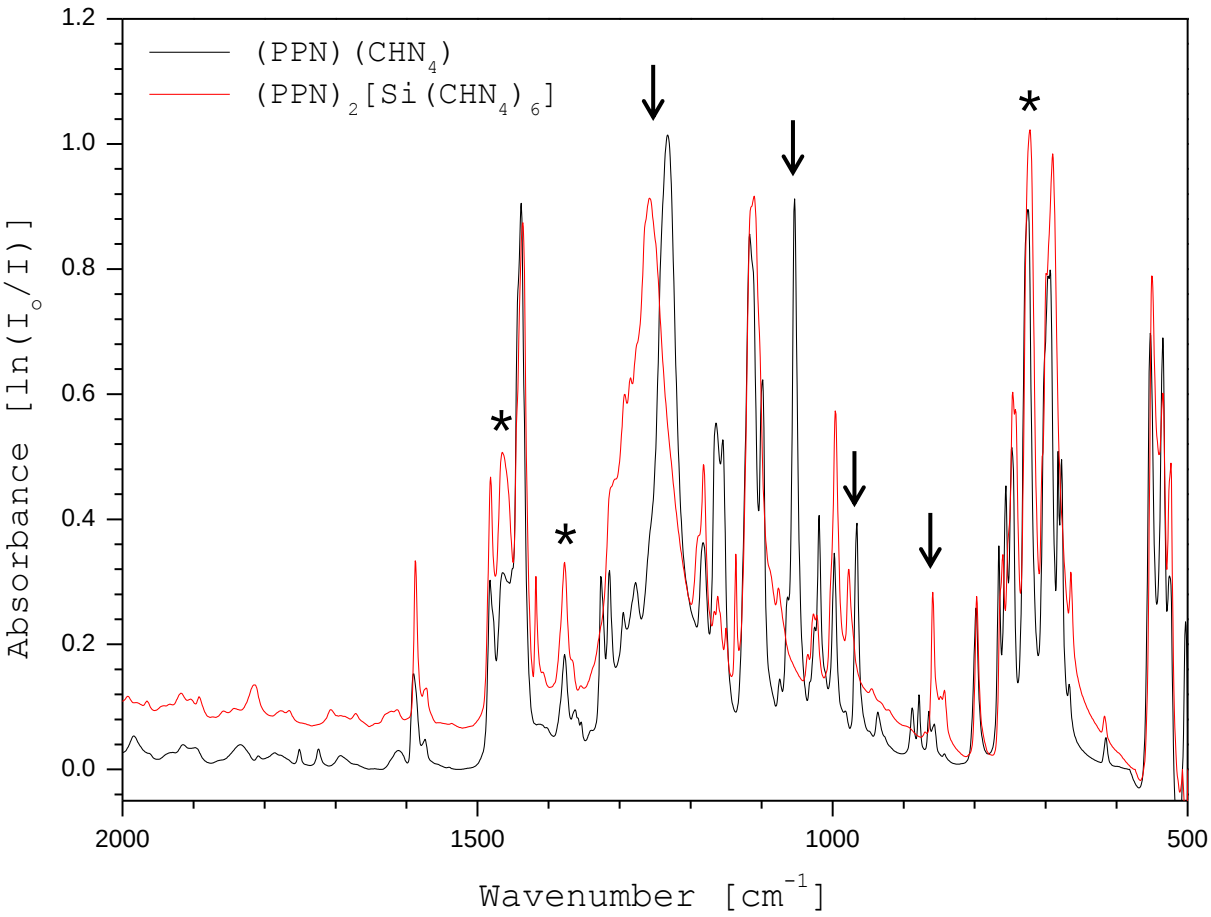

Figure 27 – IR spectrum showing the enlarged PPN fingerprint region between 2000 cm^{-1} and 500 cm^{-1} for the mulled $PPN(CHN_4)$ and $(PPN)_2[Si(CHN_4)_6]$. Nujol bands are denoted by asterisks (*).

The above spectral comparison highlights the difficulty in assigning the IR spectra produced by PPN salts; the PPN fingerprint region is only subtly changed when the anion is exchanged. In this case both spectra match apart from a broad band between 1357 cm^{-1} and 1228 cm^{-1}, in addition to bands at 1166 cm^{-1}, 1061 cm^{-1}, 964 cm^{-1} and 852 cm^{-1} (indicated by arrows). It is difficult to assign the individual bands as the region is crowded by absorption bands, but it is safe to assume that the new bands are caused by the co-ordination of the six tetrazolato ligands to the silicon. The ^{1}H NMR produced an unexpected result. The crystal structure of $(PPN)_2[Si(CHN_4)_6]$ as recorded by single crystal X-ray diffraction[70] shows that all six tetrazolato ligands bind in an *N*-1 fashion. This indicates that there should be just one hydrogen environment. However, the ^{1}H NMR spectrum displayed multiple tetrazolate peaks, of varying intensities (figure 28).

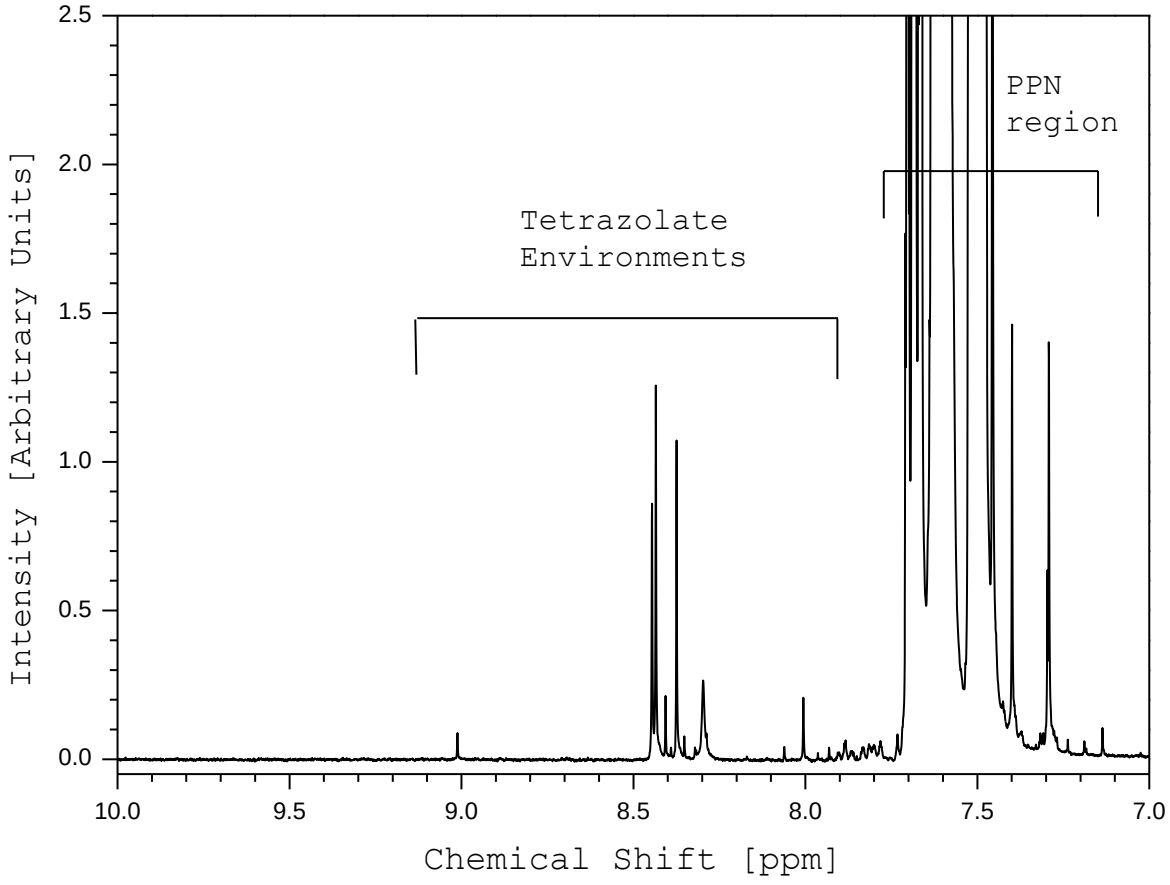

Figure 28 – Enlarged aromatic region of the $(PPN)_2[Si(CHN_4)_6]$ ^{1}H NMR spectrum.

It is possible that in solution, the tetrazolate ligands are exchanging their binding positions, a phenomenon commonly referred to as linkage isomerism. The binding change of just one tetrazolato ligand from the *N*-1 binding mode to *N*-2 creates a new proton environment,

and a new peak in the ^{1}H NMR spectrum. This can occur at each tetrazolato ligand, resulting in a highly fluxional system which could result in the multiple tetrazolate signals observed in the ^{1}H NMR spectrum.The purification of $(PPN)_2[Si(CHN_4)_6]$ also proved to be challenging. The by-product PPN(Cl), and the excess $PPN(CHN_4)$ can both easily precipitate out of the re-crystallisation solvent. To re-crystallise just pure $(PPN)_2[Si(CHN_4)_6]$ required meticulous control of the acetonitrile solution concentration. Using a warm solvent bath to slowly cool the reaction vessel was a convenient technique for the slow growth of pure crystals.

Element	Percentage expected [%]	Percentage found [%]	Variation [%]
Carbon	61.66	61.87	+0.21
Hydrogen	4.38	4.26	-0.12
Nitrogen	23.96	24.11	+0.15
Chlorine	0	<0.3 (detection limit)	0

Table 6 - Elemental analysis date obtained for $(PPN)_2[Si(CHN_4)_6]$.

The water-sensitive nature of the salt causes a certain amount of decomposition when determining the elemental concentrations in the microanalysis. However, it is apparent that the slow growth system yielded values within 0.3% of the expected carbon, hydrogen and nitrogen content. Also important is the absence of chlorine, proving the chloro- ligands have been completely exchanged with the tetrazolate ligands.

At this point it was necessary to question whether this purification method could be applied to the previously characterised $(PPN)_2[Ge(CHN_4)_6]$. However, preparation of the germanate analogue required a longer reaction time of 48 total hours instead of four, to drive the reaction to completion. In a similar fashion to the silicate, the crude product was re-crystallised extremely slowly from hot acetonitrile, which was cooled in a Dewar cylinder containing warm solvent. The Dewar cylinder was kept at -20°C, where it cooled slowly over 24 hours. The crystals obtained in this fashion were analysed using IR and ^{1}H NMR spectroscopy, and the spectra compared to the $(PPN)_2[Si(CHN_4)_6]$ data.

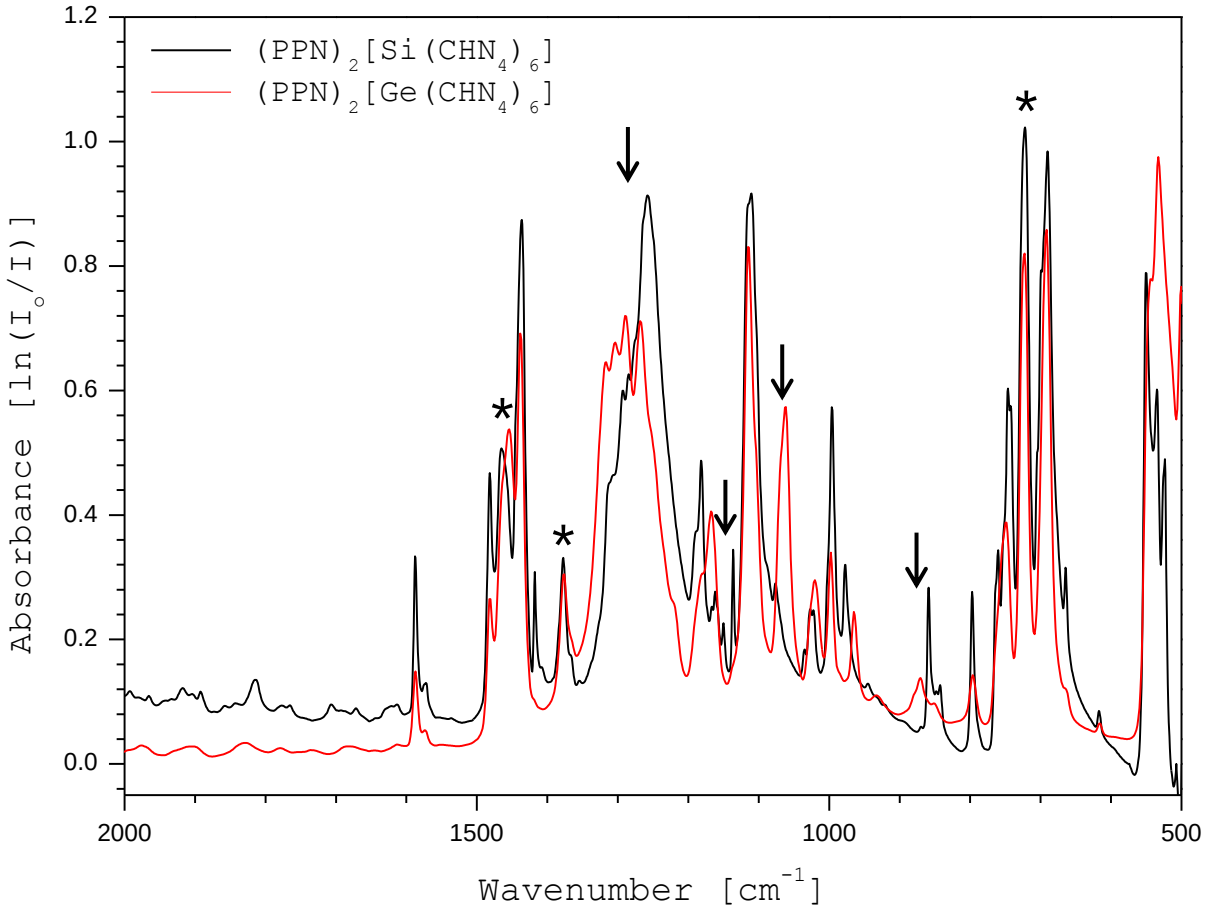

Figure 29 – IR spectral comparison of the respective fingerprint region of the mulled $(PPN)_2[Ge(CHN_4)_6]$ and $(PPN)_2[Si(CHN_4)_6]$. Nujol bands are marked by asterisks (*).

The comparison above illustrates the difficulty associated with assigning the crowded IR region of interest. The characteristic PPN bands are present in both complexes: with bands at 1589 cm^{-1}, 1436 cm^{-1}, 996 cm^{-1}, 798 cm^{-1}, 722 cm^{-1} and 690 cm^{-1} occuring in both spectra. However, there are observable differences between the two spectra. A broad series of bands between 1350 cm^{-1} and 1200 cm^{-1} in the germanate is instead a series of smaller bands and one large, broad band in the silicate. Variations at approximately 1170 cm^{-1}, 1060 cm^{-1} and 870 cm^{-1} (marked by arrows) also highlight the presence of a different metal centre. These differences are subtle, emphasising the difficulty of distinguishing between different PPN salts using IR spectroscopy.

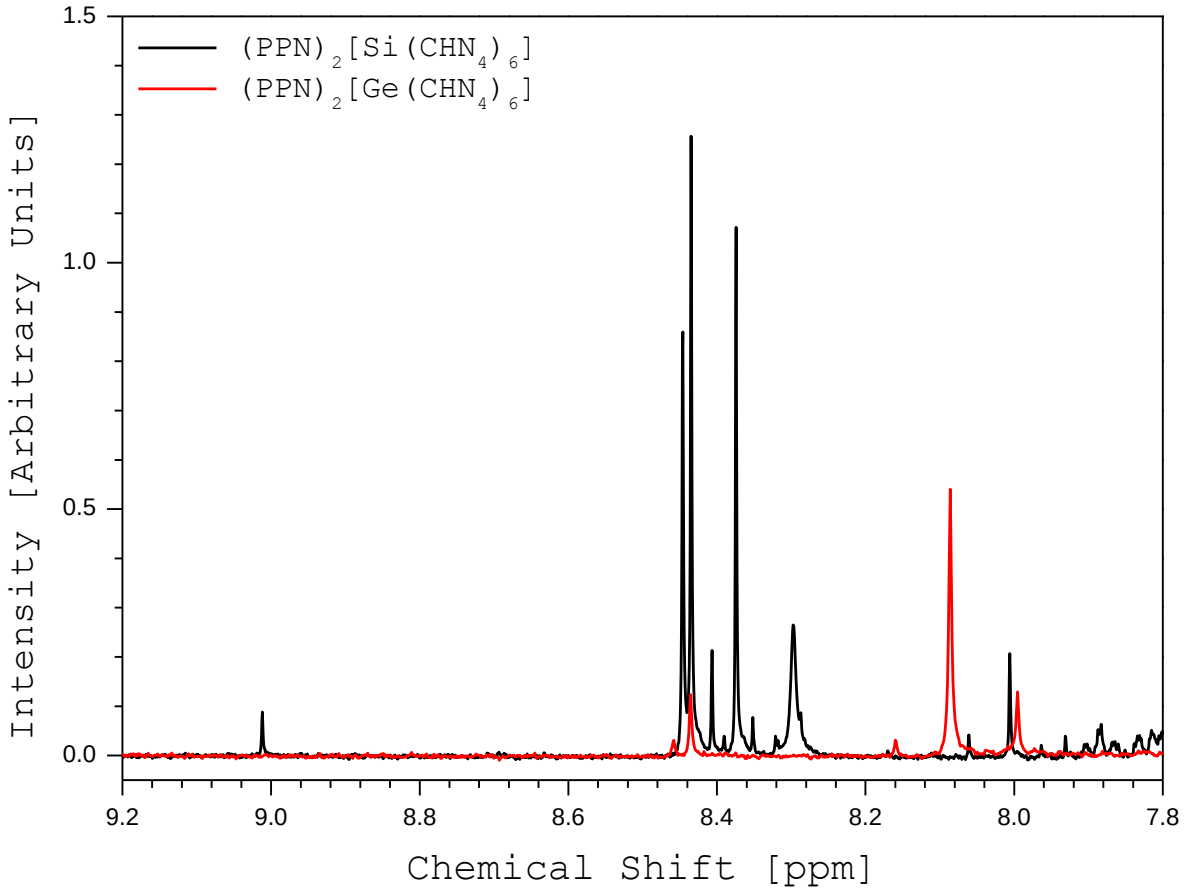

Figure 30 – ^{1}H NMR spectral comparison of the $(PPN)_2[Si(CHN_4)_6]$ and $(PPN)_2[Ge(CHN_4)_6]$ tetrazolate proton environments in the range between 9.20 ppm and 7.80 ppm.

The $(PPN)_2[Ge(CHN_4)_6]$ again possesses evidence of linkage isomerisation, but a smaller number of peaks, in comparison to $(PPN)_2[Si(CHN_4)_6]$. The different co-ordination centre is the likely cause of this discrepancy. To evaluate the purity of the compound, elemental analysis was utilised (table 7). The result of this analysis highlighted the purity of the isolated $(PPN)_2[Ge(CHN_4)_6]$ with all found values for carbon, hydrogen and nitrogen falling within 0.2%. In addition there was no detectable chlorine content, supporting the hypothesis that the fully exchanged product had been obtained, in a highly pure fashion.

Element	Percentage expected [%]	Percentage found [%]	Variation [%]
Carbon	59.90	59.72	-0.18
Hydrogen	4.25	4.12	-0.13
Nitrogen	23.28	23.23	-0.05
Chlorine	0	<0.3 (detection limit)	0

Table 7 – Elemental data for $(PPN)_2[Ge(CHN_4)_6]$.

Initial attempts to make the $(PPN)_2[Sn(CHN_4)_6]$ have had mixed results. The initial reaction between $PPN(CHN_4)$ and $SnCl_4$ in dry acetonitrile was first attempted at 60°C, with stirring for five days. The reaction progress was monitored using ^1H NMR spectroscopy.

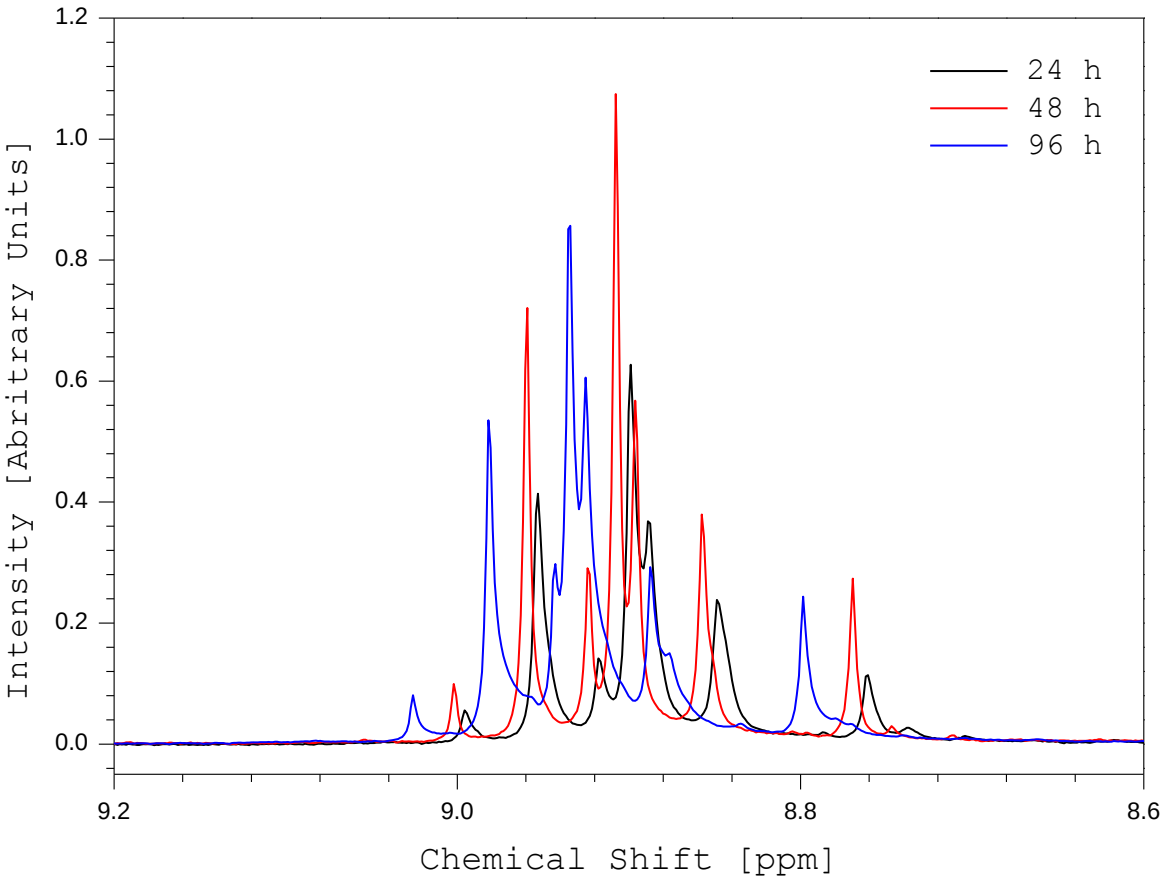

Figure 31 - ^1H NMR spectral comparison in the range between 9.20 ppm and 8.60 ppm of the $(PPN)_2[Sn(CHN_4)_6]$ reaction after prolonging reaction times.

Over the course of the reaction, the general peak pattern of the *in situ* complex remains the same. As the reaction time increases the peak pattern progressively shifts downfield. However, the shift is minor, with the peak maximum at δ = ~8.85 ppm after 24 h moving to δ = ~8.87 ppm after 96 h. The slight shift could be explained by small, unavoidable variations, such as the temperature and concentration of the sample. The peak pattern suggests that, as previously observed, linkage isomerisation is prevalent in solution. The reaction solution volume was reduced under dynamic vacuum until the onset of crystallisation, at which point the reaction vessel was stored overnight at -20°C, producing crystals. These crystals were collected by filtration and re-dissolved in acetonitrile, and a second batch of PPN(CHN_4) was added. Analysis of the resulting new crystals revealed that the obtained product was in fact the triply exchanged $(PPN)_2[Sn(CHN_4)_3Cl_3]$.

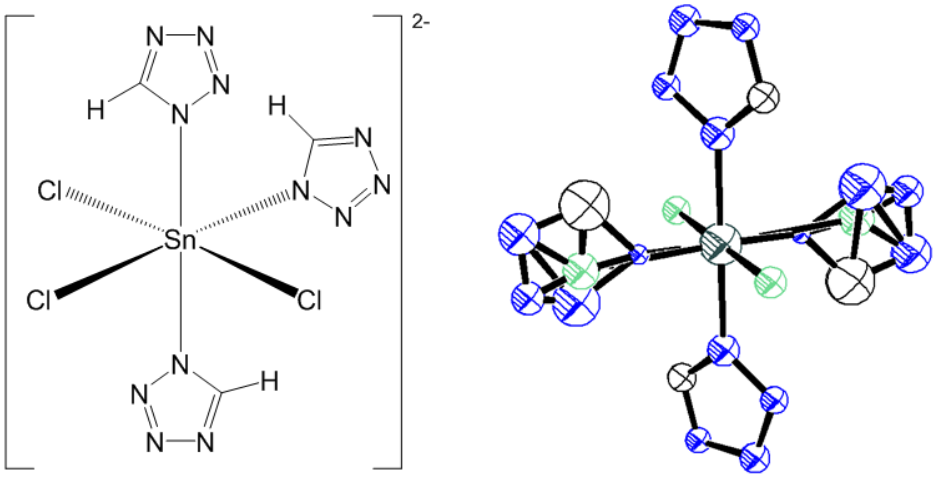

Figure 32 – Disordered ellipsoid diagram for $(PPN)_2[Sn(CHN_4)_3Cl_3]$ (right), with hydrogen atoms omitted for clarity. The Lewis structure (left) provides a simple representation of the dianion.

As shown in the above ellipsoid diagram, the $[Sn(CHN_4)_3Cl_3]^{2-}$ anion is disordered through the vertical plane, with the axial tetrazolato rings and the equatorial chloro ligands remaining 100% occupied. The remaining equatorial chloride and tetrazolato group are heavily disordered, each ligand present approximately 50% of the time. With hindsight, a reactivity trend becomes obvious when looking back at the preparation of all three complexes: $(PPN)_2[Si(CHN_4)_6]$, $(PPN)_2[Ge(CHN_4)_6]$ and $(PPN)_2[Sn(CHN_4)_3Cl_3]$. The production of the silicate required two steps, each of which takes two hours. On descending to germanium, the time needed for complete reaction in each step increased to 24 hours.

This trend continues down the group, with the preparation of $(PPN)_2[Sn(CHN_4)_3Cl_3]$ taking a full 10 days of stirring at 60°C, split over the two steps. This reduced reactivity towards $PPN(CHN_4)$ is the probable cause of the partially exchanged nature of the obtained product. It is evident from the partially exchanged nature of the product that using $PPN(CHN_4)$ as a transfer reagent is not a viable route to the fully exchanged $(PPN)_2[Sn(CHN_4)_6]$ system. This is partly due to the weak nucleophilic nature of the tetrazolate anion. Another reason could be that the formation of the salt by-product of the reaction, PPN(Cl), is a weak driving force in comparison to the NaCl salt which is generated in the final step of the production of the analogous $(PPN)_2[Sn(N_3)_6]$.[71] What is required is a transfer reagent that can force the reaction forwards, using the formation of a strong bond to ensure that the barrier to the fully exchanged product can be breached. This could be achieved through the use of trimethylsilyl-tetrazole ($TMS\text{-}CHN_4$).[17] This can be generated by the reaction of TMS-Cl and 1*H*-tetrazole in dry toluene, in the presence of dry Et_3N (scheme 15).

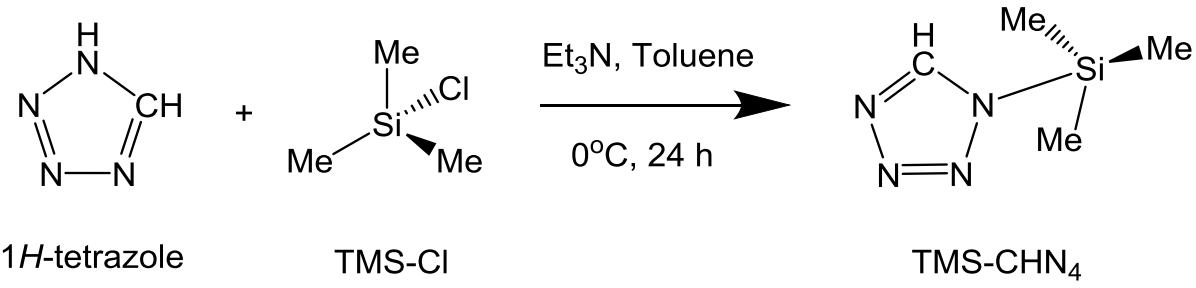

Scheme 15 – Preparation of trimethylsilyl-tetrazole[17]

The above reaction results in a thick, yellow liquid. This can be analysed using ^1H NMR spectroscopy and compared to the expected literature values (figure 33). The proton environments caused by the TMS group and the tetrazole ring are immediately obvious, at 0.63 ppm and 8.64 ppm, in an approximate 9:1 ratio. Small impurities are present, assignable as residual Et_3N and toluene. Exposing the $TMS\text{-}CHN_4$ to a dynamic vacuum could remove these trace impurities; however, this would also affect the yield of $TMS\text{-}CHN_4$, as it would also evaporate. The utility of the $TMS\text{-}N_4CH$ reagent arises when combined with fluoride-containing compounds. The formation of the strong Si-F bond in the TMS-F by-product results in a large driving force for reactions to progress.

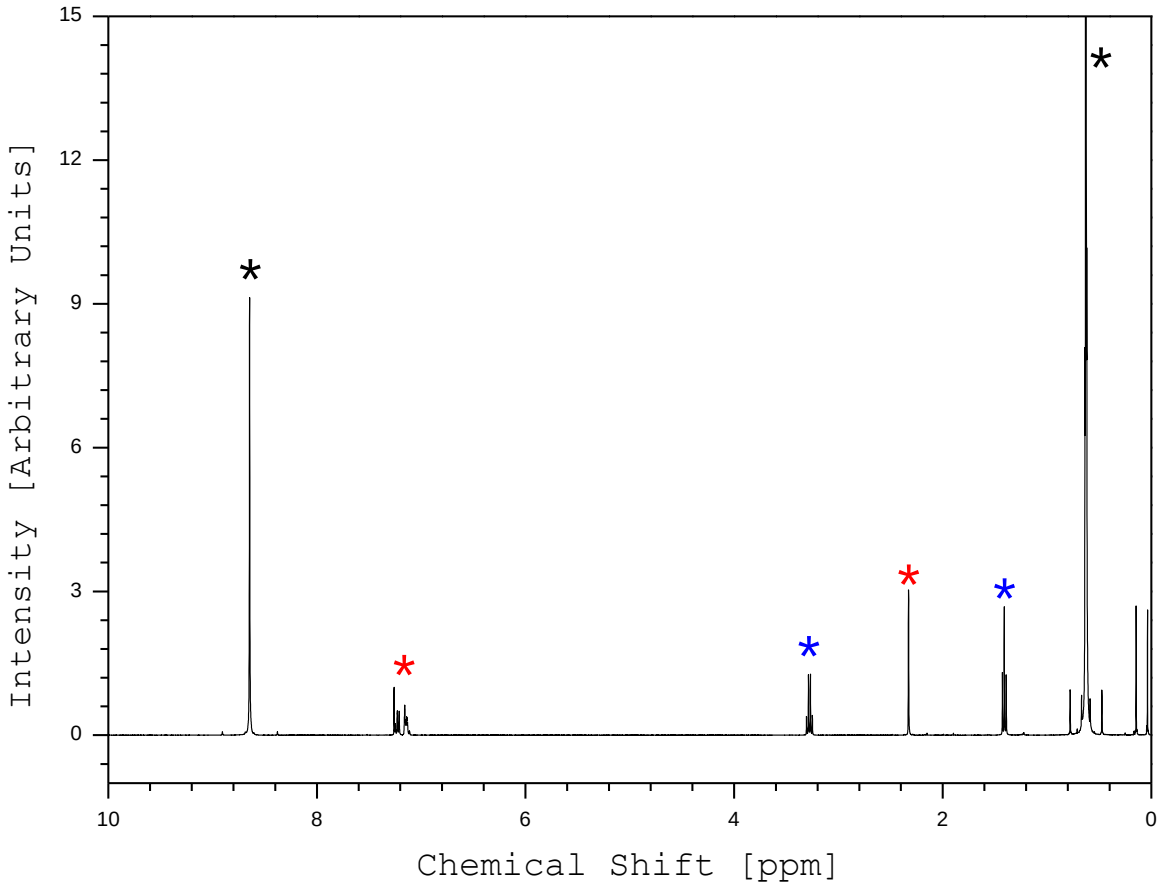

Figure 33 – ^{1}H NMR spectrum of TMS-CHN_4 in $CHCl_3$-*d*, with the trimethylsilyl and tetrazole proton environments marked (*). Small impurities due to toluene (*) and Et_3N (*) are also present.

The one-pot combination of PPN(CHN_4), TMS-CHN_4 and SnF_4 in dry acetonitrile (scheme 16) illustrated the improved effectiveness of the TMS-CHN_4 transfer reagent, resulting in a crystalline white solid. The reaction progresses at room temperature and reaches completion after two hours. This is a much gentler reaction environment in comparison to using PPN(CHN_4), which requires days of stirring at high temperature. Another advantage is that it is a much more economic reaction, both in the monetary sense and the use of material. Only a small excess of TMS-CHN_4 is required and the expensive PPN(CHN_4) reagent can be used in a stoichiometric fashion.

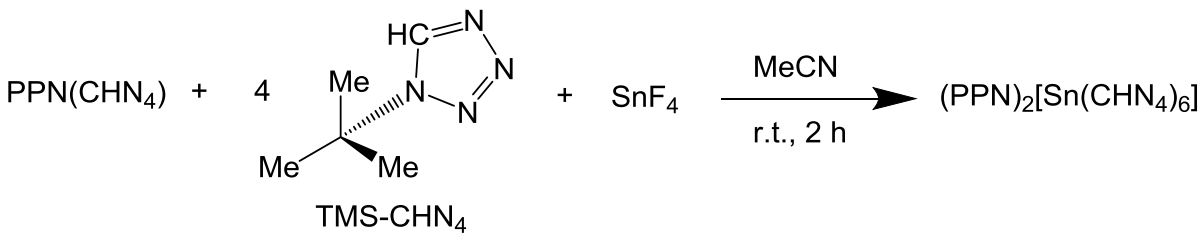

Scheme 16 – Alternative preparation of $(PPN)_2[Sn(CHN_4)_6]$.

When compared to the previously synthesised $(PPN)_2[Si(CHN_4)_6]$ and $(PPN)_2[Ge(CHN_4)_6]$, the ^1H NMR spectrum shows the characteristic peak pattern in the expected tetrazolate region between 9.20 and 8.00 ppm approximately. Whilst an encouraging piece of spectral evidence, an intermediary species could potentially exhibit similar signals, as seen in $(PPN)_2[Sn(CHN_4)_3Cl_3]$.

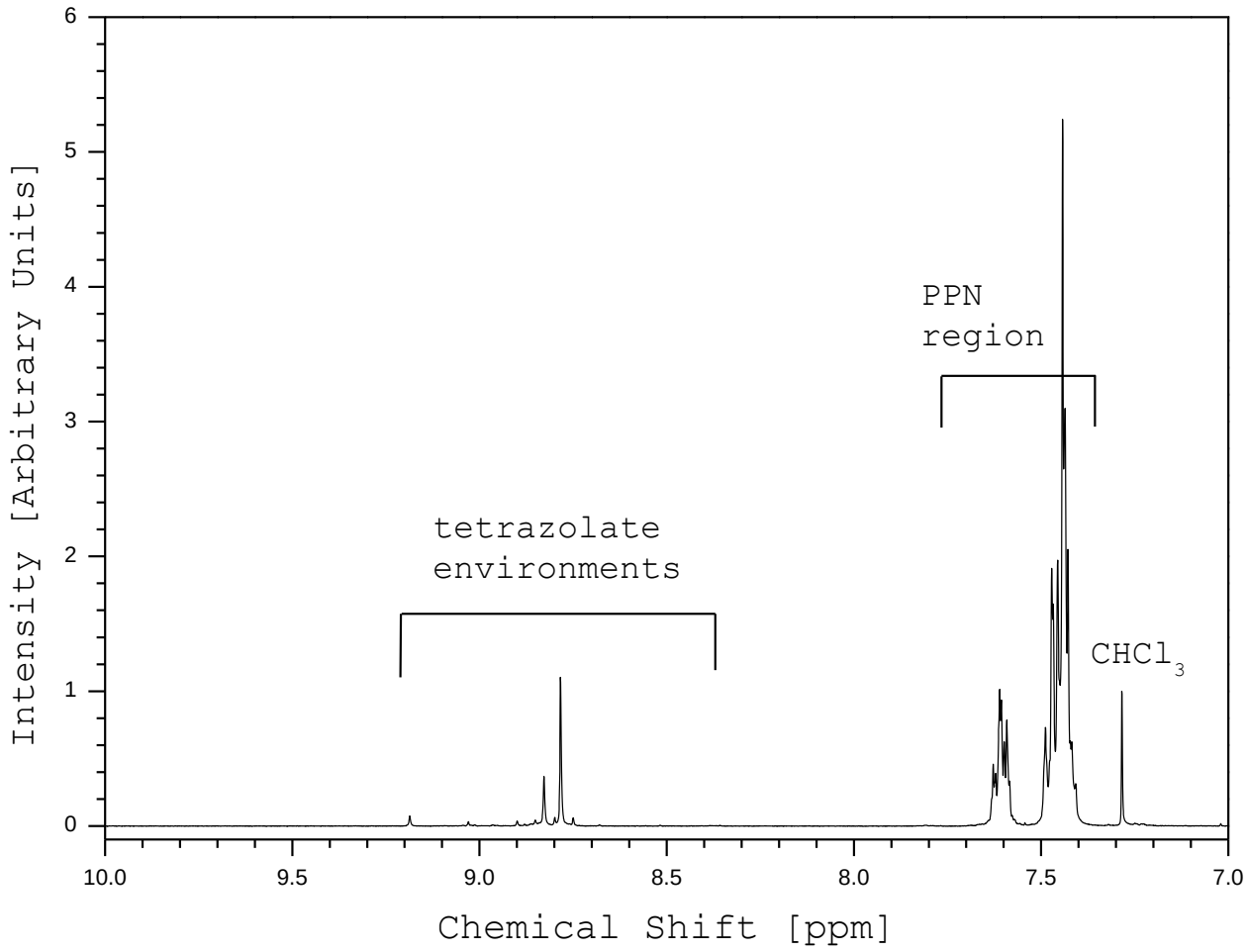

Figure 34 – ^1H NMR spectrum of $(PPN)_2[Sn(CHN_4)_6]$ in $CHCl_3$-*d* between 10.00 ppm and 7.00 ppm.

The IR spectrum affords more analytical data, but again cannot be used to formally designate the nature of the product. The majority of the peaks overlap due to both the PPN and tetrazolate peaks that occur in the observed region of the IR series. The major discrepancies occur at the broad peaks between 1330 cm^{-1} and 1218 cm^{-1} (marked by an arrow). Utilising this peak region it is possible to distinguish between different PPN salts. However ^{1}H NMR spectroscopy is a much more accurate tool for characterising tetrazolate-containing complexes.

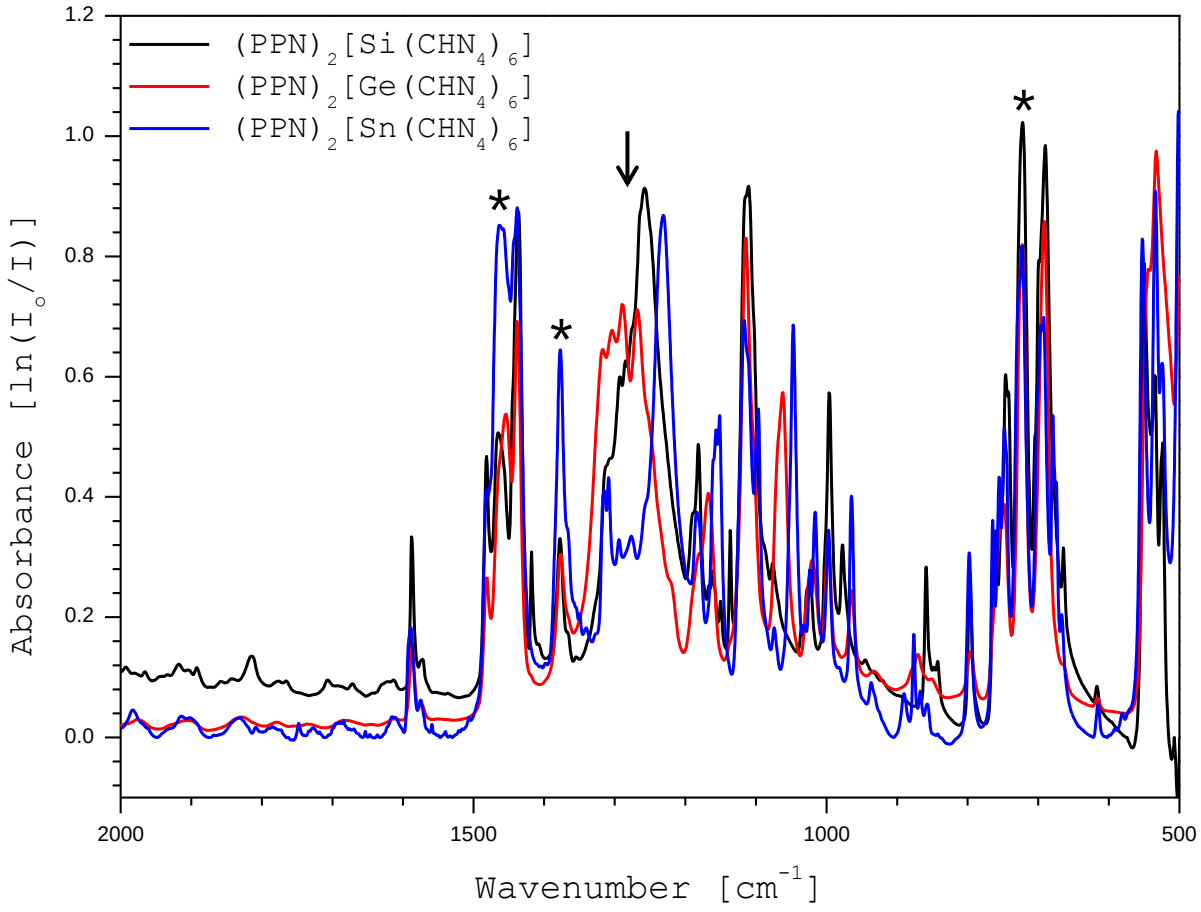

Figure 35 –IR comparison of the respective fingerprint region of the $(PPN)_2[Sn(CHN_4)_6]$ and the previously synthesised $(PPN)_2[Si(CHN_4)_6]$ and $(PPN)_2[Ge(CHN_4)_6]$. Nujol bands are marked by asterisks (*).

The white solid was re-crystallised from hot acetonitrile and upon cooling to −25°C, colourless block crystals were isolated. Upon analysis using single crystal X-ray diffraction studies, the crystals were shown to be the fully exchanged $(PPN)_2[Sn(CHN_4)_6]$.

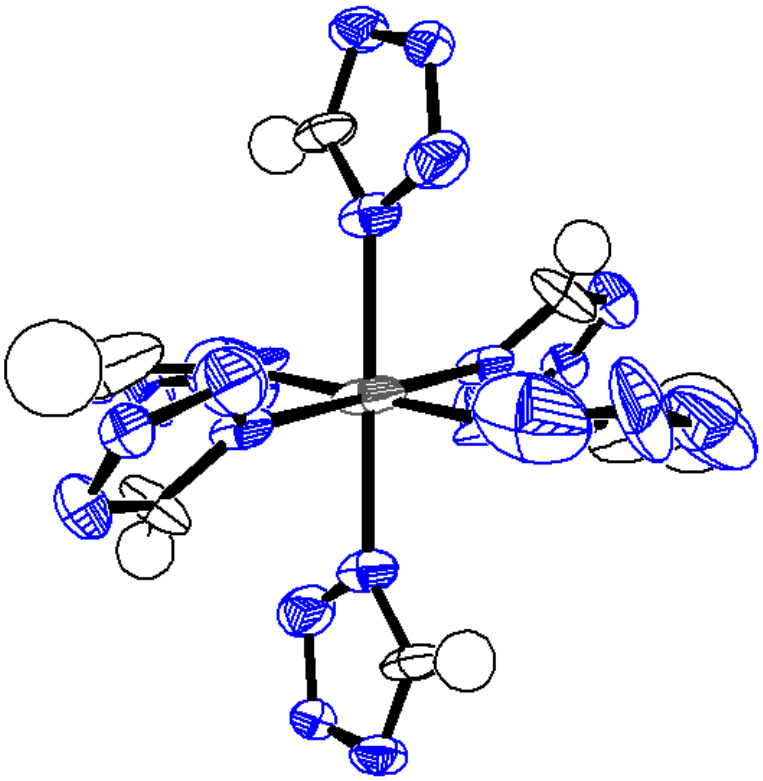

Figure 36 – Ellipsoid Diagram of $(PPN)_2[Sn(CHN_4)_6]$. Diagram produced using Ortep®.

The salt presents itself within a monoclinic unit cell, with the $P21/_n$ space group. This contrasts what has been reported previously for this class of complexes, as both the $(PPN)_2[Si(CHN_4)_6]$ and $(PPN)_2[Ge(CHN_4)_6]$ crystallise in the space group $P21/_c$.[70] This could explain the difficulty in the attempted synthesis of the Sn analogue using the synthetic method that produced both the silicate and germanate complexes. An additional explanation could be the alternative use of TMS-CHN_4 as the tetrazolate transfer reagent forces the crystallisation in the $P21/_n$ space group. Examination of the crystal data for the intermediate $(PPN)_2[SnCl_3(CHN_4)_3]$ species shows that this complex also crystallises in the $P21/_n$ space group, which indicates that the observed variation could simply be due to the increased size of the tin co-ordination centre. The asymmetric unit contains a single PPN cation and a $Sn(CHN_4)_3$ unit. This is due to the highly symmetrical nature of the $Sn(CHN_4)_6$ dianion, which possesses a plane of reflection that lies between each three co-ordinate pyramidal unit. In addition an inversion centre lies at the Sn metal centre, meaning that each tetrazolate ligand is symmetrically related. Upon investigation of the complete $Sn(CHN_4)_6$ system it was shown to exhibit an octahedral geometry, in a similar fashion to the Si and Ge analogues.

The bond distances of 2.028 Å, 2.148 Å and 2.127 Å for N1, N2 and N3 respectively are typical Sn – N bond lengths. All bonding angles are between 89° and 91° highlighting the undistorted nature of the geometry. The ability of the $[Sn(CHN_4)_6]^{2-}$ anion to exhibit typical bonding dimensions for an octahedral complex indicates each anion remain independent within the crystal lattice. Examining the packing of the crystal supports this hypothesis; the PPN cations occupy the internal volume of the unit cell, forcing the $Sn(CHN_4)_6$ units onto the faces of the cell. This ensures maximum separation of the anions. It is interesting to note that one cause for the inclusion of the PPN cation was its ability to dissipate the energetic nature of the salt. The below figure allows that to be visualised; the high carbon content of the PPN cations not only dilutes the overall nitrogen content but maximises the separation between the energetic anions.

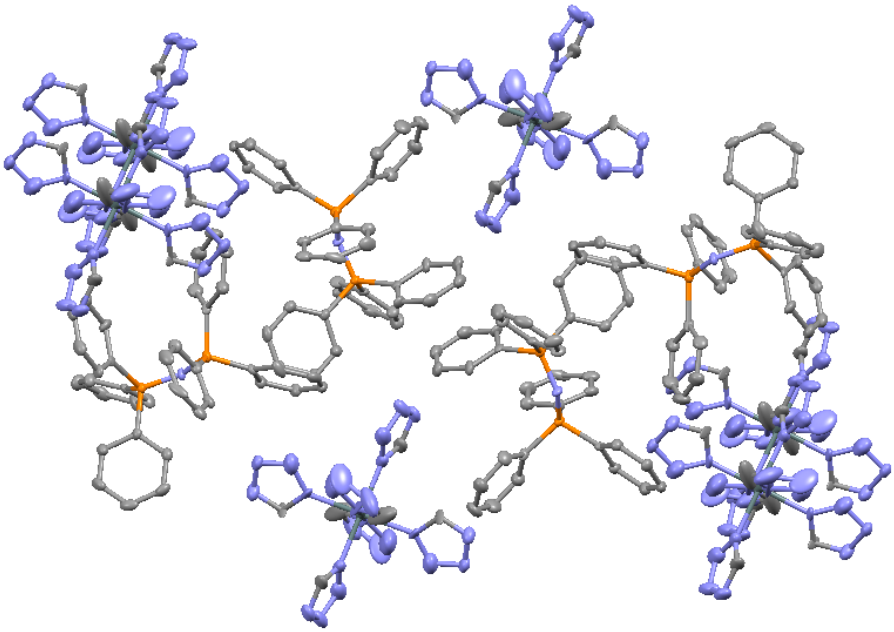

Figure 37 – Unit cell contents of the $(PPN)_2[Sn(CHN_4)_6]$ complex. The PPN cations occupy the internal volume, forcing the anionic $[Sn(CHN_4)_6]^{2-}$ species to the faces of the cell, maximising charge separation and minimising the energetic nature of the overall salt. Diagram produced using Mercury®.

The quality of the crystal was not perfect and this is can be observed in the size of the thermal ellipsoids. In addition the results of the elemental analysis also highlight the requirement for further re-crystallisation.

Element	Percentage expected [%]	Percentage found [%]	Variation [%]
Carbon	58.19	61.24	+3.05
Hydrogen	4.13	4.69	+0.56
Nitrogen	22.61	18.65	-2.96
Chlorine	0	0 (<0.3% detection limit)	-

Table 8 – Elemental analysis data for $(PPN)_2[Sn(CHN_4)_6]$.

Overall the replacement of $PPN(CHN_4)$ with TMS-CHN_4 represents a dramatic improvement in the accessibility of this reaction type. Numerous main group fluorides are available for investigation. Aluminium, boron and phosphorus must be excluded due to their E-F bonds being stronger than the Si-F bond, negating the driving force that forms the appeal of the TMS-CHN_4 reagent. This can also be extended to include SiF_4 as the reaction involves breaking four Si-F bonds then forming four Si-F bonds, meaning there is no net energy gain and no reaction. In addition both SiF_4 and GeF_4 are both gases, therefore difficult to work with without specialised equipment.

3.2.1 Synthesis and Characterisation of Various poly(tetrazolato)-poly(azido) main group complexes

An alternative route to homoleptic polytetrazolato main group complexes was investigated through the heating of the $(PPh_4)_2[Al(N_3)_5]$, $(PPN)_2[Si(N_3)_6]$ and $Na_2[Si(N_3)_6]$ complexes in dry acetonitrile. This procedure is based upon previous work within the group that synthesised neutral tetrazolato silicon complexes from $Si(N_3)_4(L)$ where L = 2,2-bipyridine and 1,10-phenanthroline.[72] Using high temperature and long reaction times it is possible to convert all azido groups into R-substituted tetrazolate ligands (R = CH_3, C_6H_5, 4-$C_6H_4CH_3$), dependent upon the nitrile that was utilised.

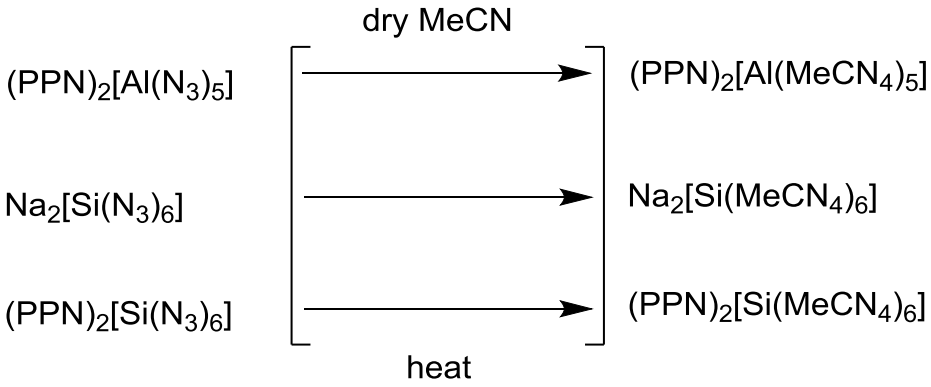

Scheme 17 – Attempted synthesis of various homoleptic methyltetrazolato- complexes.

The method was first attempted using $(PPh_4)_2[Al(N_3)_5]$. The progress was monitored using solution cell IR spectroscopy, which should indicate the extent at which the azide ligands have been converted. It was hypothesised before beginning the reaction that as azide-methyltetrazolate transformation occurred the observed azide bands should diminish.

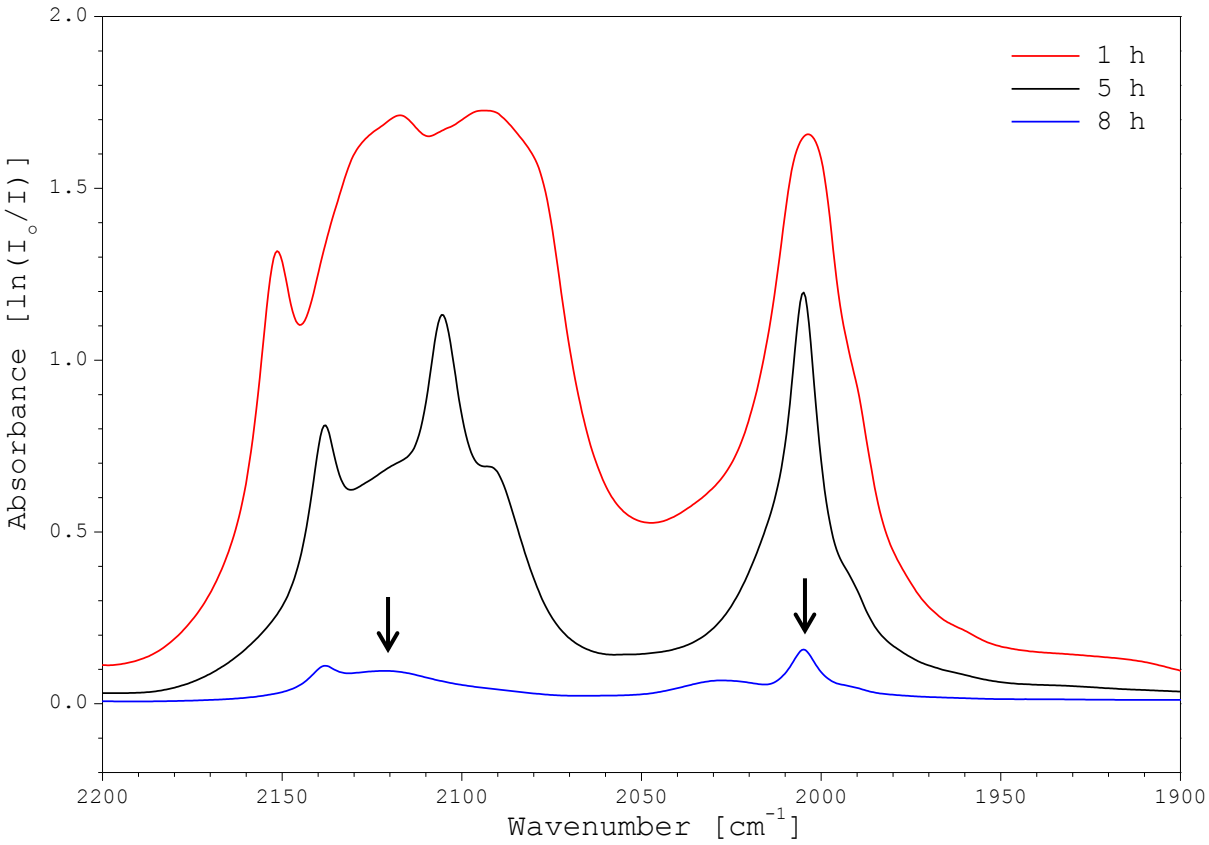

Figure 38 - Comparison of the solution cell IR spectra recorded whilst monitoring the $(PPh_4)_2[Al(N_3)_5]$ reaction. Figure is focussed upon the azide region of the spectra between 1900 cm^{-1} and 2200 cm^{-1}.

As the above figure shows, throughout the reaction, the azide signals were intensively weakened. This was taken as an indication that the azide-methyltetrazolate transformation was taking place. The solution was concentrated in an attempt to grow crystals. Small, orange needles were produced which were then investigated using single crystal X-ray crystallography. The unit cell matched that of $PPh_4(N_3)$. This suggests decomposition, yet the solution cell IR spectrum did contain azide bands at 2121 cm^{-1} and 2005 cm^{-1} (marked by arrows). The peak at 2137 cm^{-1} is due to HN_3, again supporting the idea that the reaction has resulted in, at the least, partial decomposition. It is unclear the extent at which the reaction progresses, and the isolation of the reaction product in a pure form is necessary for firm conclusions to be made. The preparation used for the previous reaction was extrapolated to other known poly(azido) main group compounds. The preparation is attempted using $Na_2[Si(N_3)_6]$. Again the reaction progress was monitored by solution-cell IR spectroscopy.

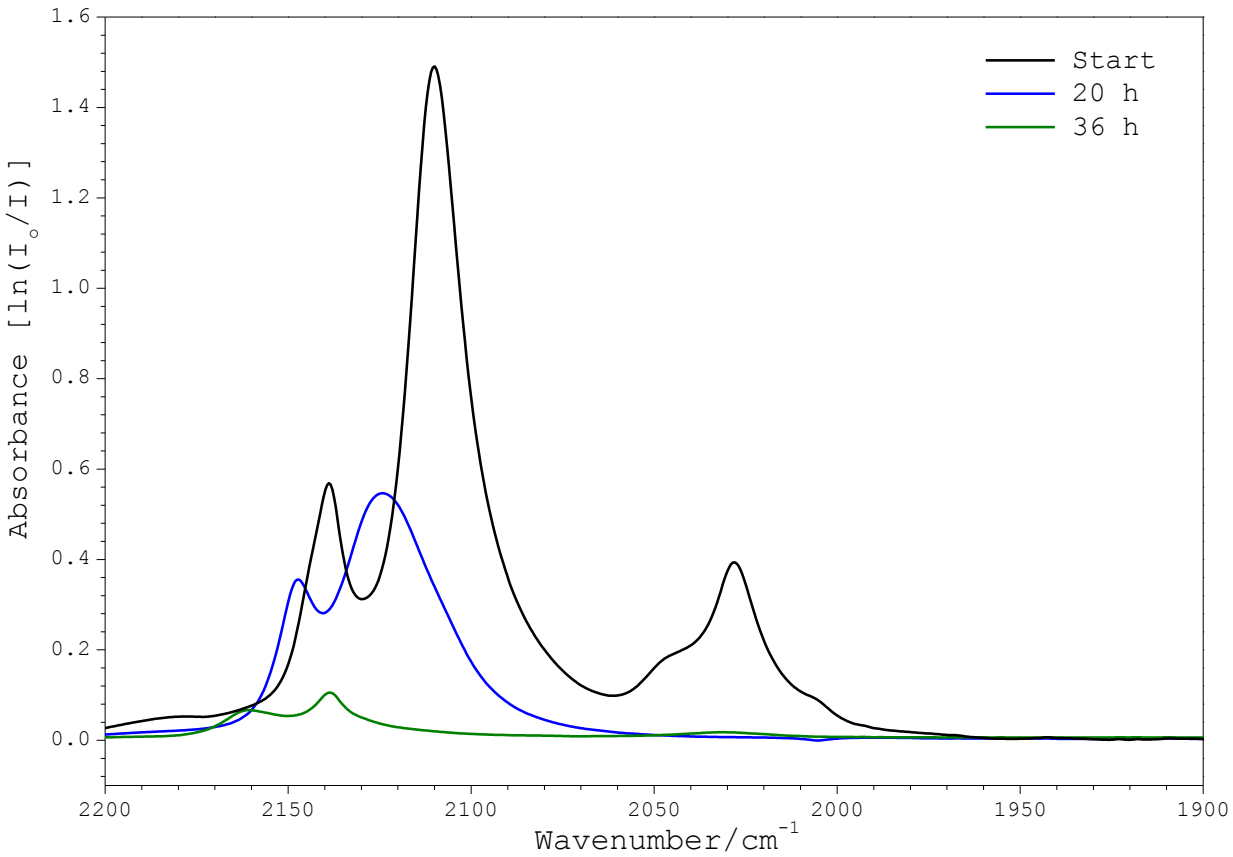

Figure 39 – Comparison of IR spectra obtained from the reaction between $Na_2[Si(N_3)_6]$ and acetonitrile.

The $Na_2[Si(N_3)_6]$ proved to offer more encouraging results than the analogous aluminium complexes. The change in the $Na_2[Si(N_3)_6]$ azide region as the reaction proceeded was more

pronounced than the comparable reaction with the $(PPh_4)_2[Al(N_3)_5]$. The azide bands shift completely to higher wavenumbers, with the peak maximum changing initially from 2110 cm^{-1} to 2124 cm^{-1} and then finally 2138 cm^{-1} after 36 h. The band maximum attributed to the measurement taken after 36 h is caused by HN_3, indicating that decomposition of the azido complex in solution had begun. In the initial IR spectrum an azide band at approximately 2020 cm^{-1} is not present after heating for 20 h. Hypothetically, the disappearance of the azide band at 2020 cm^{-1} could indicate the azide-methyltetrazolate transfomation taking place. The formation of a new azide band at 2160 cm^{-1} after 36 h is also indicative of a progressing reaction.

The gradual shift to higher wavenumbers indicates that as the reaction progresses, the *in situ* compound at 20 h and 36 h respectively are becoming increasingly more covalent. The neutral $Si(N_3)_4$ is highly covalent, with its azide band occurring at approximately 2170 cm^{-1}. At the opposite end of the spectrum, $PPN(N_3)$ is an ionic salt, and its azide band is at 1998 cm^1. Therefore the azide band at 2160 cm^{-1} present after 36 h shows that the Si-N bond associated with the *in situ* compound is highly covalent. Over the total 36 hours of stirring at 90°C, a large amount of white precipitate was produced, which on heating did not re-dissolve. The solution was removed by filtration and the slightly yellow solid was probed by IR spectroscopy of a Nujol mull suspension.

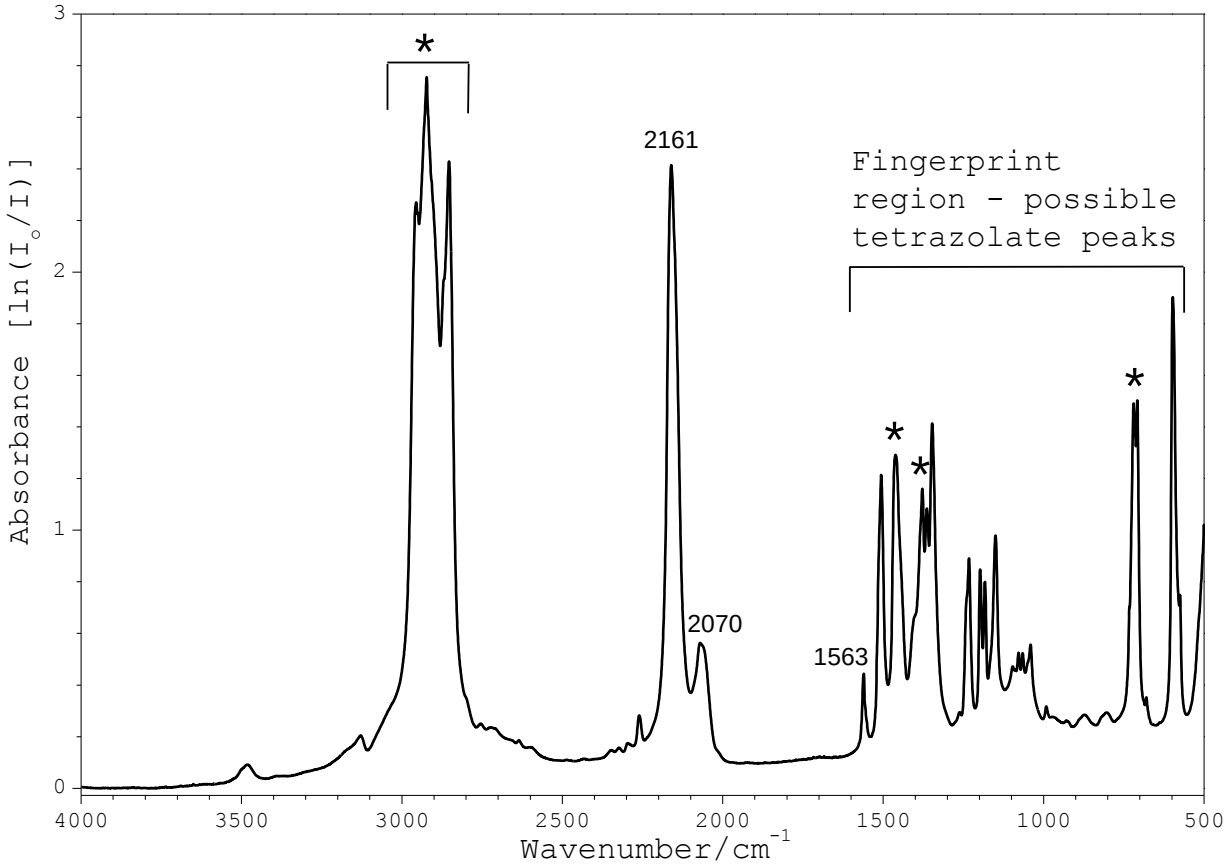

Figure 40 – Nujol mull IR spectrum of the white precipitate produced by the heating of $Na_2[Si(N_3)_6]$ in dry acetonitrile. Nujol bands are are asterisked (*).

The fingerprint region of the above spectrum contains numerous peaks which could indicate the present of methyltetrazolyl ligands. The small peak at 1563 cm^{-1} could be assigned to a C=N bond, further supporting the notion that a reaction has taken place.

The spectrum (figure 40) also shows two asymmetric azide bands at 2161 cm^{-1} and at 2070 cm^{-1}. A small band at 2260 cm^{-1} is due to residual acetonitrile, confirmed by comparison against a blank acetonitrile IR spectrum. The azide band for the original $Na_2[Si(N_3)_6]$ presents itself at 2119 cm^{-1} in the solution cell. This shift indicates that a reaction has taken place, and that there are two azide bands in the product. This would be possible if the azide-methyltetrazolate transformation had not occurred at all positions.

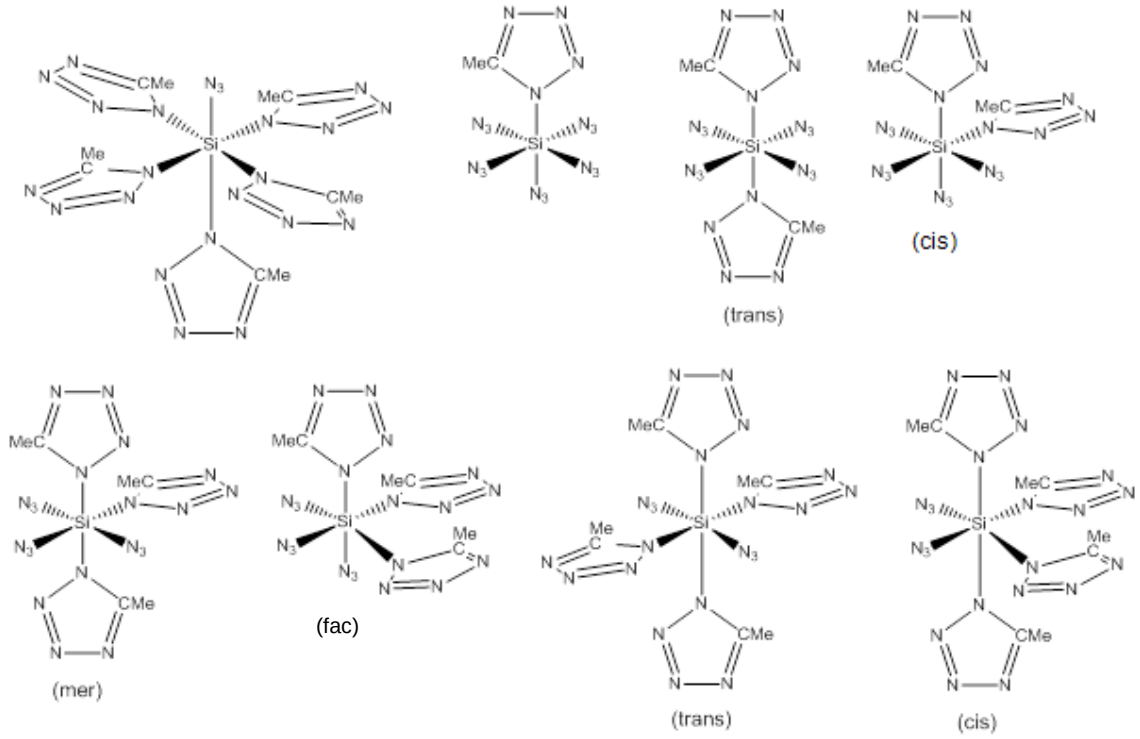

Figure 41 – Possible orientations of the $Na_2[Si(N_3)_x(MeCN_4)_y]$, ranging from one azide-methyltetrazolate transformation to five. Multiple environments show that it is possible to get more than one azide region. The κ(*N*-2) isomers have been omitted for clarity.

It was decided to repeat the $Na_2Si(N_3)_6$ reaction using an ampoule fitted with a Young's tap. The hypothesis was that the firmer seal would allow a higher temperature than a standard Schlenk tube. The shape of the ampoule also allows for further immersion in the heat source, in this case an oil bath. The combination of a higher temperature and a more uniform heating method could provide the conditions necessary to perform the azide-methyltetrazolate transformation at all six positions.

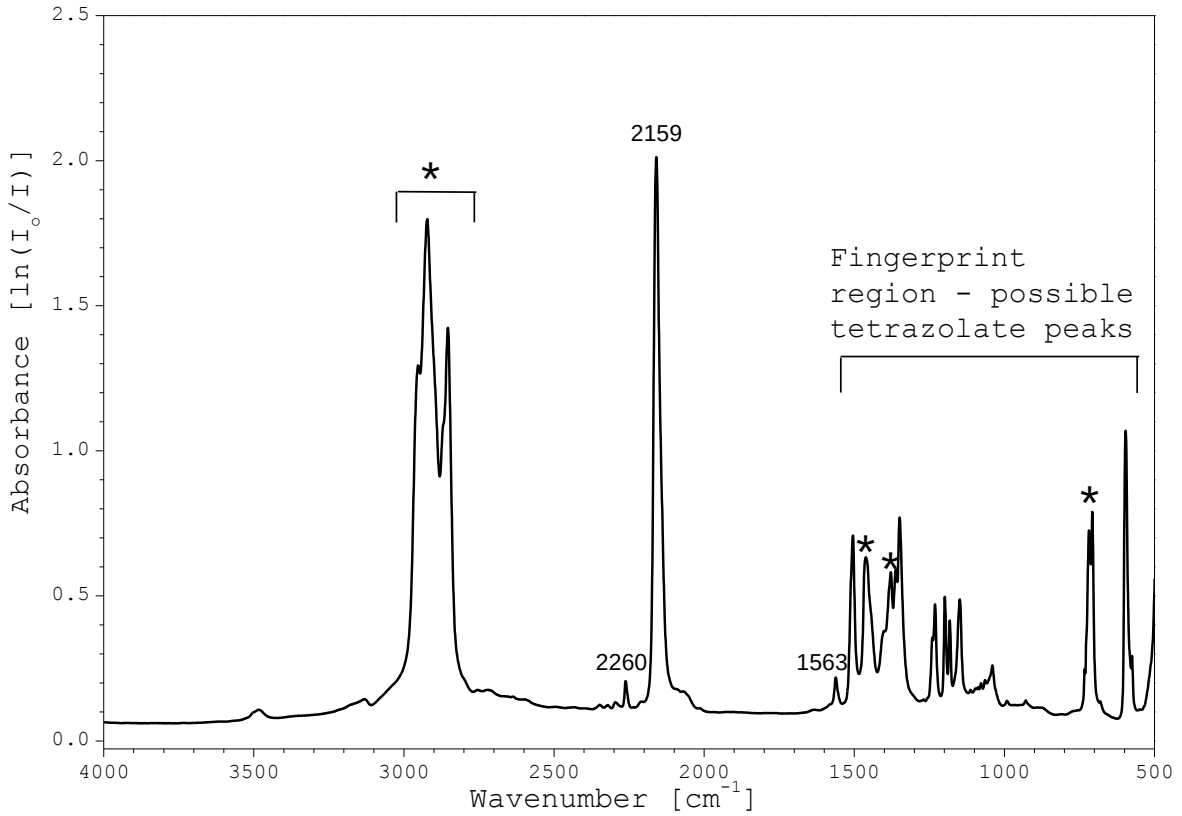

Figure 42 - IR spectrum of the repeat of the $Na_2[Si(N_3)_6]$ attempt, utilising an ampoule with a Young's tap. Nujol bands are asterisked (*).

The ampoule allowed for a higher temperature, and a further immersion into the oil bath, which meant a more uniform heating system. However, it seems as the resulting precipitate is similar to the previous attempt. Both precipitates have evidence of co-ordinated acetonitrile at 2260 cm^{-1}, and an intense azide band at approximately 2160 cm^{-1}. The second azide band found at 2070 cm^{-1} is less prominent on this occasion, allowing for the hypothesis that the reaction has progressed further than the previous attempt. The small C=N peak at 1563 cm^{-1} is still present, again indicating that the azide-methyltetrazolate reaction has occurred. Re-crystallisation was attempted from various dry solvents: acetonitrile, THF, DCM and diethyl ether. None proved to be able to dissolve the precipitate. It was theorised that it could contain a sodium salt of the methyltetrazole, which would explain the insolubility in organic solvents. This would however not explain the significant azide presence, therefore it must be a mixture of the $Na(MeCN_4)$ and an azide-containing decomposition product, possibly NaN_3. This would again be a result of decomposition, a disappointing result.

A flame test resulted in deflagration with a bright orange flame, but no audible report. The solid also dissolved in water, with no obvious reaction. This suggests that the product is likely a salt and gives no indication for the presence of silicon. The solution was left in air to slowly evaporate in an attempt to yield crystals. After one week the water had evaporated, leaving behind a ring of large, white crystals. However an attempt to probe the crystals by single crystal X-ray diffraction studies failed due to the inability of the crystalline material to rotate plane polarised light, meaning that no single crystalline specimen could be obtained. It is probable that the solution was left to evaporate in air for too long, resulting in the complete removal of the solvent. Changing the cation could aid re-crystallisation. The PPN cation can be used, making the salt much more soluble in most common solvents. Once in solution, re-crystallisation is possible. The experiment was therefore repeated, changing $Na_2[Si(N_3)_6]$ for $(PPN)_2[Si(N_3)_6]$. The $(PPN)_2[Si(N_3)_6]$ was dissolved in dry acetonitrile and heated to 90°C, as before. After eight hours, a solution IR spectrum was recorded.

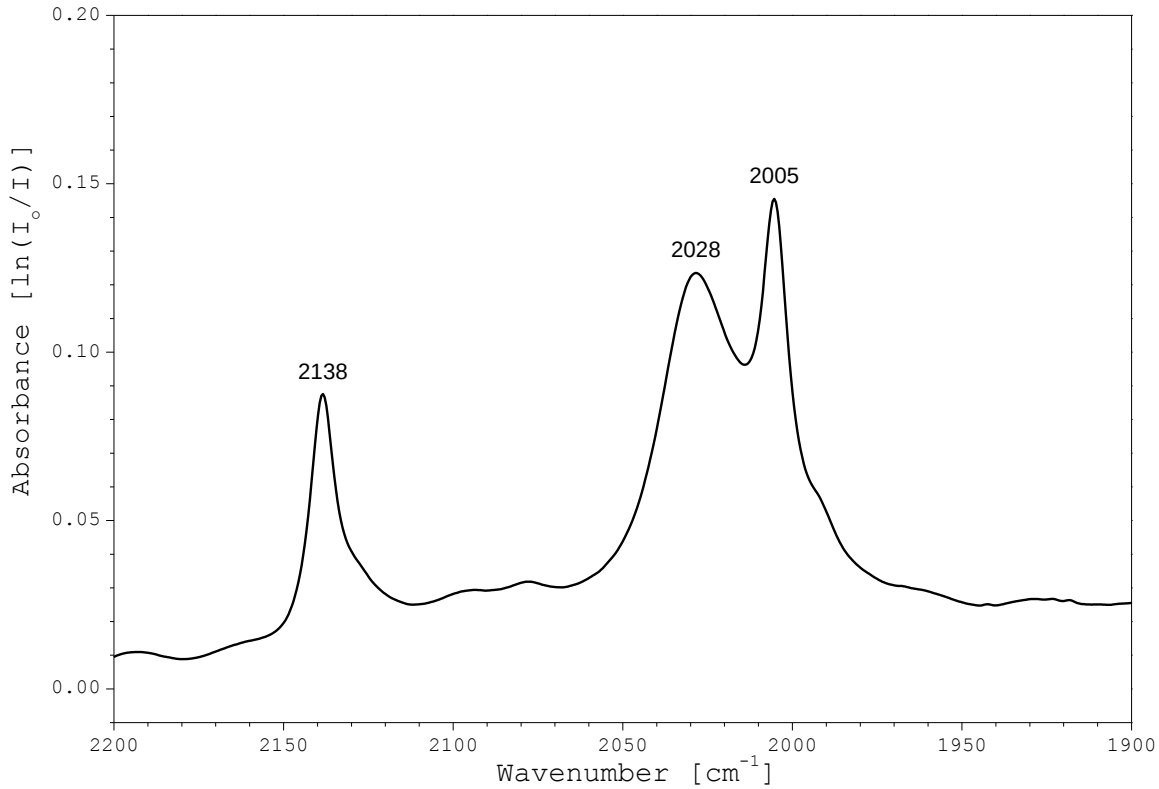

Figure 43 – Enlarged asymmetric N_3 stretch range of the IR spectrum for $(PPN)_2[Si(N_3)_x(MeCN_4)_y]$ in acetonitrile solution.

The azide band for the $(PPN)_2[Si(N_3)_6]$ occurs at 2104 cm^{-1} and its absence and the presence of new azide bands at 2028 cm^{-1} and 2005 cm^{-1} are evidence of a reaction taking place. The

band at 2005 cm^{-1} is possibly $PPN(N_3)$, which occurs in the region of 2000 cm^{-1}. The band at 2124 cm^{-1} indicates a covalent azide compound, possibly a neutal azide species. That could be either simply the $Si(N_3)_4$ or it could be evidence of the $Si(N_3)_x(MeCN_4)_y$ where x + y = 4. The peak at 2138 cm^{-1} is significant, as it corresponds to HN_3, which can only be explained by the decomposition of the $(PPN)_2[Si(N_3)_6]$ starting material. The solvent was removed under vacuum, and the resulting white solid was analysed using Nujol mull IR spectroscopy.

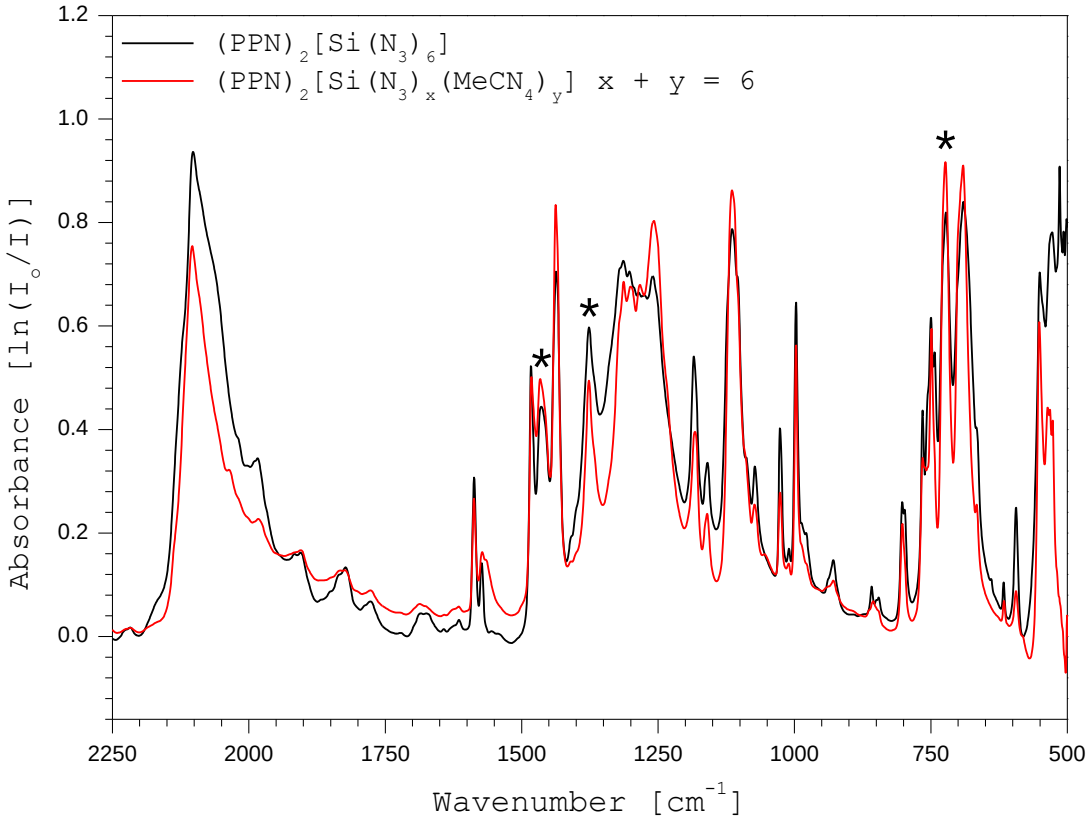

Figure 44 – Enlarged 2250 cm^{-1} to 500 cm^{-1} range of the Nujol mull IR. Comparison of the spectra for the expected $(PPN)_2[Si(N_3)_x(MeCN_4)_y]$ solid against the starting material $(PPN)_2[Si(N_3)_6]$. Nujol bands are labelled by asterisks. (*).

The spectrum obtained is essentially identical to the starting material $(PPN)_2[Si(N_3)_6]$. This result suggests that the reaction has not gone to completion, with the majority of the precipitate remaining as the $(PPN)_2[Si(N_3)_6]$. However, the solution cell indicated that there were new azide bands, at 2028 cm^{-1} and 2005 cm^{-1}. It is possible that the reaction had only progressed slightly, with the product compound forming in a low concentration.

A crystallisation was attempted to try and isolate the small amount of product. The solid was re-dissolved in ca. 2 mL dry acetonitrile, and was cooled to −20°C. The small, white block crystals that grew were analysed by single crystal X-ray crystallography. The diffraction data was solved to give PPN($MeCN_4$).

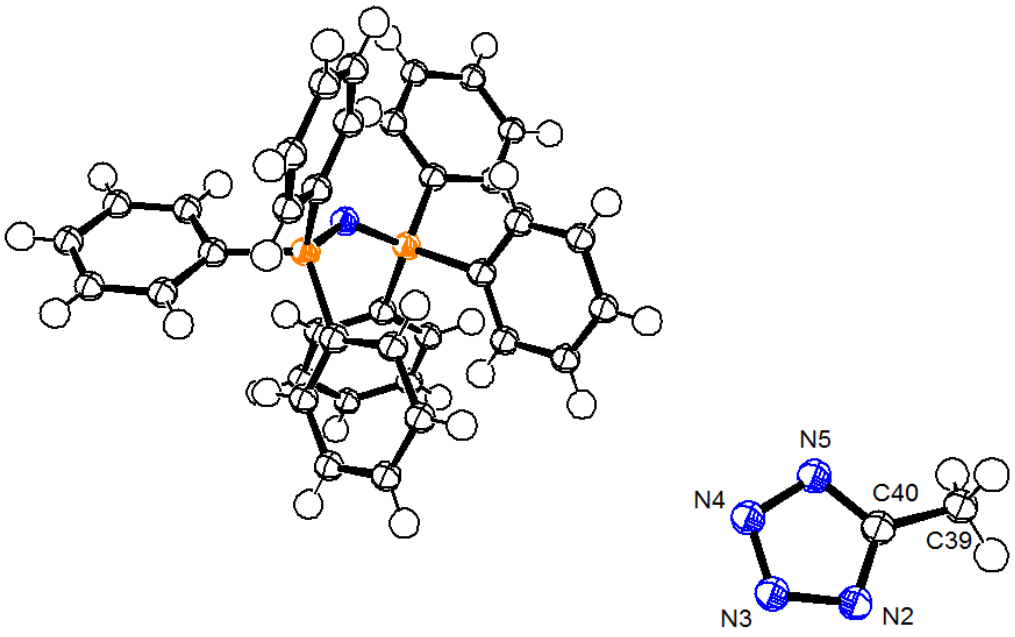

Figure 45 – Isotropic plot of PPN($MeCN_4$) with only the 5-methyltetrazolate labelled for clarity. Diagram produced using Ortep®.

While the X-ray diffraction data shows that the target compound has not been re-crystallised, the azide-methyltetrazolate transformation does occur within the reaction; an encouraging result. It remains unclear to what extent the reaction progresses; it could be that the azide-methyltetrazolate transformation causes dissociation from the main group centre, which would explain the presence of the PPN($MeCN_4$). This would seem to be the most likely explanation as all three investigations resulted in decomposition. The total azide-methyltetrazolate conversion can occur when using the neutral $Si(N_3)_4$(bipy) complex, which suggests that the charged nature of the utilised complexes could factor into the observed decomposition. The 2,2-bipyridyl ligand could also provide additional stability. Overall the observations from this investigation indicate that this method is not a suitable preparation of main group tetrazolato- complexes.

3.2.2 Attempted Synthesis of $Na_2[Si(CHN_4)_6]$

As the preparations for $(PPN)_2[Si(CHN_4)_6]$ and $(PPN)_2[Ge(CHN_4)_6]$ require large amounts of the expensive $PPN(CHN_4)$ reagent it was decided that it would be advantageous to attempt the preparation of a "stock" solution of $Na_2[Si(CHN_4)_6]$, which could be combined with a small amount of the $PPN(CHN_4)$ to yield the bis-PPN product. $Na(CHN_4)$ was suspended in dry acetonitrile, and under positive argon pressure, $SiCl_4$ was added via a volumetric pipette. The hypothesis was that the tetrazolate would be transferred to the silicon centre, and the by-product of NaCl would precipitate out of solution, driving the reaction forward. The mixture was stirred overnight and the colourless solution was separated from the precipitate by filtration.

$$SiCl_4 + \text{xs } Na(CHN_4) \xrightarrow[40^oC,\ 18\ h]{\text{dry MeCN}} Na_2[Si(CHN_4)_6] + 4\ NaCl$$

Scheme 18 – Attempted synthesis of $Na_2[Si(CHN_4)_6]$. Precipitation of NaCl provides the necessary driving force for the reaction to occur.

Crystals began to form once the solution was cooled to -20°C, and they were analysed using IR and ^1H NMR spectroscopies. Unfortunately the reaction's only isolable product was 1*H*-tetrazole. The $Na(CHN_4)$ forms as a hydrate, and previously it was not sufficiently dried, leaving H_2O associated to the Na^+ cation. For this reason, the $Na(CHN_4)$ was instead dried under dynamic vacuum at 100°C, rather than 40°C as used previously. This proved to be a suitable drying technique, with IR analysis indicating that all water has been removed.

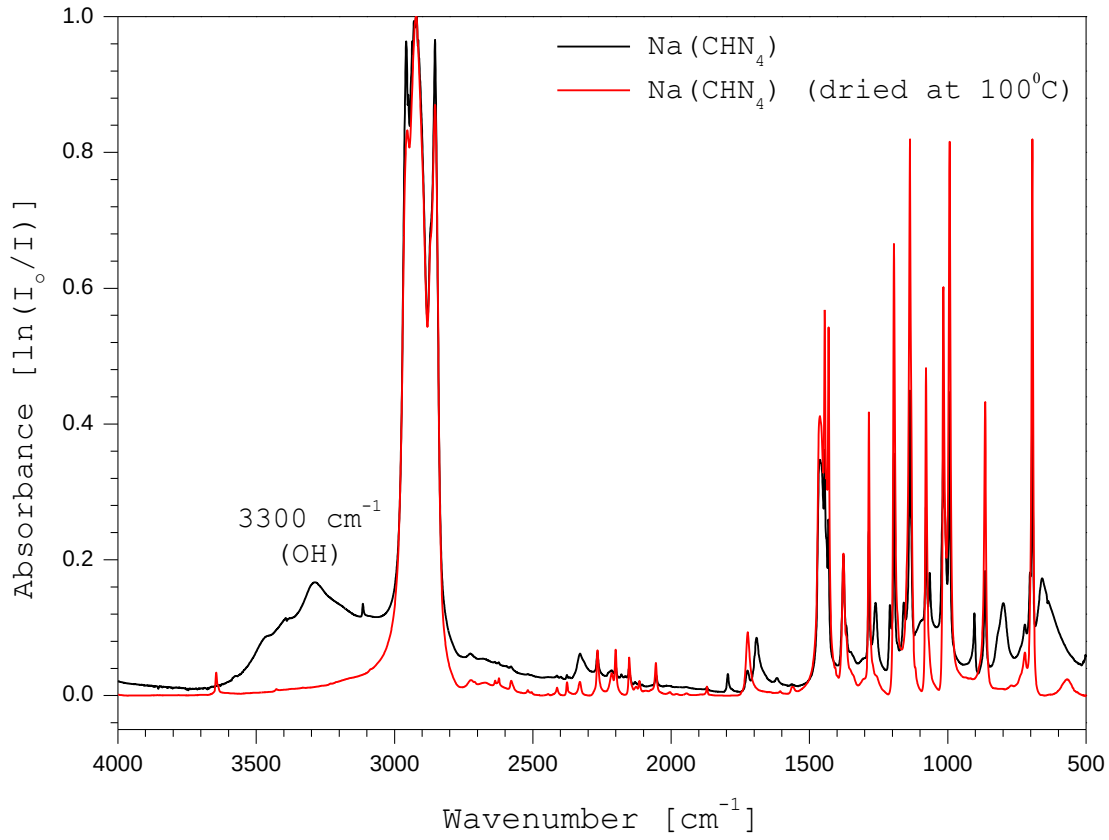

Figure 46 – Comparison of the IR spectra of the $Na(CHN_4)$ used initially and the $Na(CHN_4)$ dried at 100°C, which was used in the second attempt at synthesising $Na_2[Si(CHN_4)_6]$.

The removal of the broad band at approximately 3300 cm^{-1} shows the complete elimination of the water bound to the $Na(CHN_4)$. The attempted preparation of $Na_2[Si(CHN_4)_6]$ was repeated utilising the water-free $Na(CHN_4)$. An aliquot was used to record a ^1H NMR spectrum, which would immediately show evidence of the formation of the desired product $Na_2Si(CHN_4)_6$, or the decomposition to 1*H*-tetrazole. Unfortunately, the recorded spectrum showed the presence of 1*H*-tetrazole, indicating that again the reaction has resulted in decomposition.

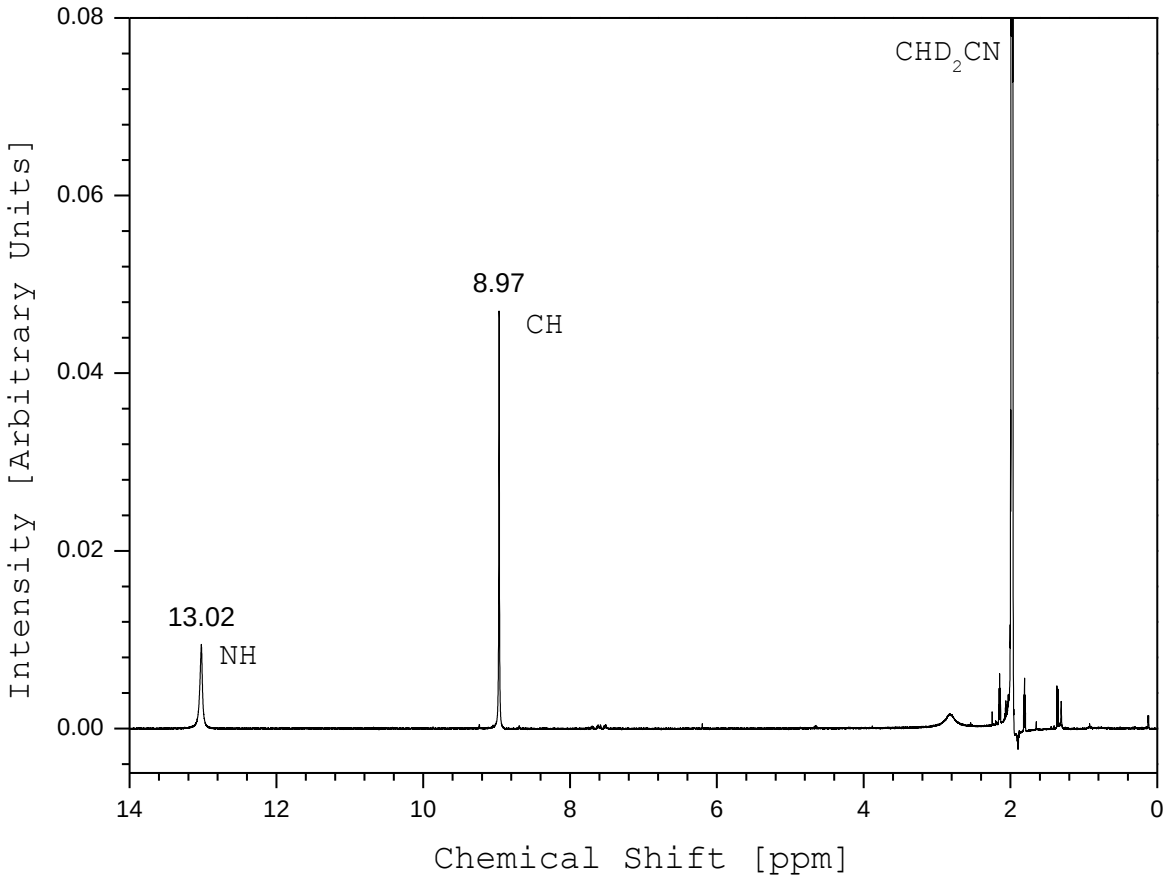

Figure 47 – ^{1}H NMR spectrum of 1*H*-tetrazole, a decomposition product resulting from the attempted synthesis of $Na_2[Si(CHN_4)_6]$.

It is unclear why the decomposition takes place. The refined drying procedure removed all residual water within the $Na(CHN_4)$ reagent, removing this as a cause for decomposition. It could be that the $Na_2[Si(CHN_4)_6]$ product is temperature sensitive and simply decomposes as it forms. The analogous $Na_2[Si(N_3)_6]$ solution is stable at room temperature and can be stored indefinitely at −25°C. It is unlikely that the exchange of the azide groups for tetrazolyl ligands would result in an unstable complex as the PPN salts have been isolated and shown to be stable. The complexity of this reaction requires further study to understand the behaviour of the product complex. In comparison, although the proven preparative routes of $(PPN)_2[Si(CHN_4)_6]$ and $(PPN)_2[Ge(CHN_4)_6]$ require large excesses of $PPN(CHN_4)$, their relative simplicity makes them much more suitable at present.

3.3 Conclusions

Building upon previous investigations, refined purification procedures for $PPN(CHN_4)$, $(PPN)_2[Si(CHN_4)_6]$ and $(PPN)_2[Ge(CHN_4)_6]$ resulted in the isolation of all three complexes in a highly pure yield. Extrapolation to tin proved difficult using $PPN(CHN_4)$ as a transfer reagent, and a new synthetic route to $(PPN)_2[Sn(CHN_4)_6]$ was developed. SnF_4, trimethylsilyltetrazole ($TMS\text{-}CHN_4$) and two equivalents of $PPN(CHN_4)$ were reacted in dry acetonitrile in a one-pot synthesis. Stirring overnight at room temperature followed by a simple purification resulted in crystals of $(PPN)_2[Sn(CHN_4)_6]$. The reaction conditions are gentle, and this route is highly economic, requiring cheaper reagents and smaller excesses.

An alternative route to polytetrazolato- main group complexes was also investigated by reacting the $(PPh_4)_2[Al(N_3)_5]$, $(PPN)_2[Si(N_3)_6]$ and $Na_2[Si(N_3)_6]$ complexes with dry acetonitrile. The resulting [3+2] cyclo-addition reactions have previously been shown to result in total azide-methyltetrazolate conversion.[73] However all attempts resulted in decomposition. It is probable that the charged complexes cannot be converted without dissociation of the product. Isolation and crystallisation of $PPN(MeCN_4)$ supports this conclusion, illustrating that the conversion does begin, but the intermediate product is not stable and results in decomposition.

A final investigation attempted to prepare $Na_2[Si(CHN_4)_6]$. In a similar fashion to the analogous $Na_2[Si(N_3)_6]$, if synthesised the $Na_2[Si(CHN_4)_6]$ could be kept as a stock solution in dry acetonitrile of known concentration. Simply adding two equivalents of $PPN(CHN_4)$ should result in cation exchange and precipitation of NaCl and $(PPN)_2[Si(CHN_4)_6]$. The initial attempt result in decomposition and isolation of 1*H*-tetrazole. It was concluded that this was due to residual water within the $Na(CHN_4)$ reagent. However upon removal of this residual water and the repeating of the reaction again resulted in 1*H*-tetrazole. The reason for this decomposition is unclear. The known preparative procedures to $(PPN)_2[Si(CHN_4)_6]$ and $(PPN)_2[Ge(CHN_4)_6]$ are comparatively simple and therefore their requirement for a large excess of $PPN(CHN_4)$ can be overlooked.

3.4 Further Studies – A Reactivity Investigation into the Homoleptic Tetrazolato- Main Group Complexes

The successful isolation and characterisation of the $(PPN)_2[Sn(CHN_4)_6]$ co-ordination complex in addition to the previous preparation of the Si and Ge analogues completed the objective of synthesising all three main group hypervalent homoleptic tetrazolato-complexes. The next step in the investigation would be the evaluation of the reactivity and energetic nature of this type of complex.

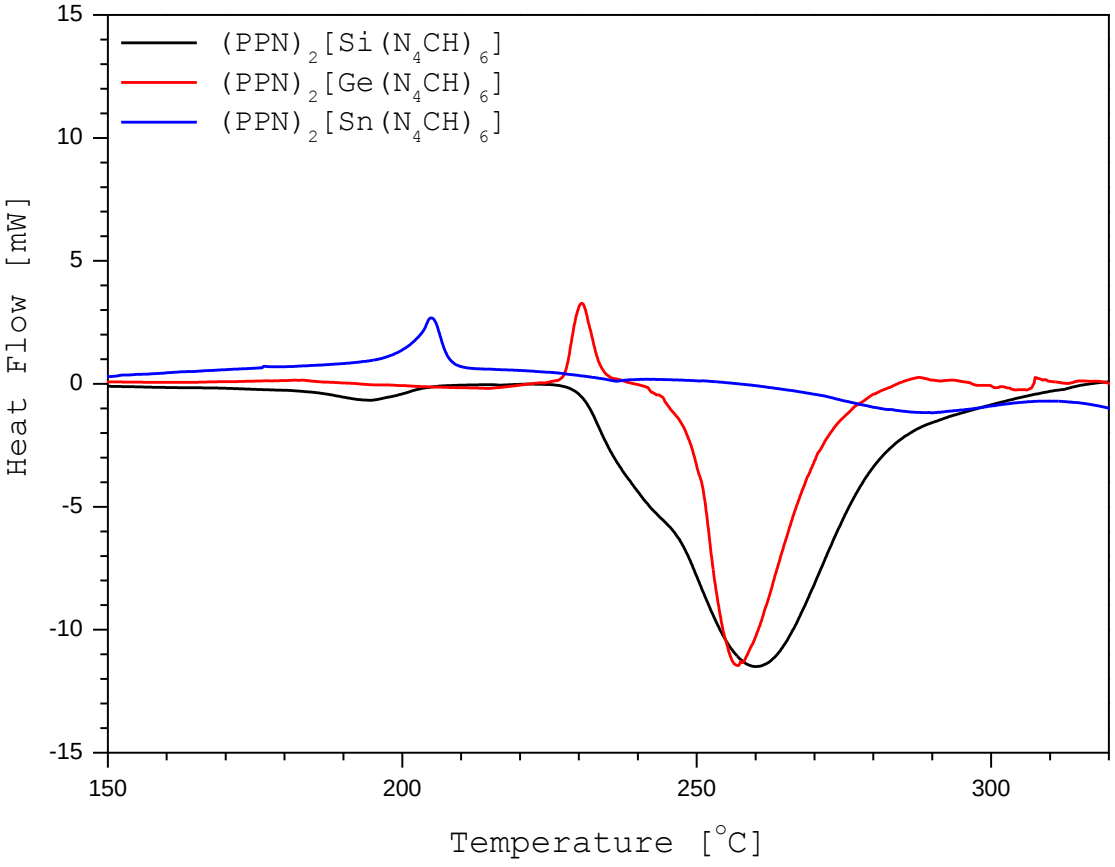

Figure 48 – Differential Scanning Calorimetry (DSC) traces for each $(PPN)_2[E(CHN_4)_6]$ complex.

The above figure illustrates how each complex behaves when exposed to high temperatures. The silicate does not melt but decomposes at approximately 225°C, whilst the germanate and stannate analogues both have distinct melting points. Interestingly the $(PPN)_2[Sn(CHN_4)_6]$ complex does not decompose, indicating that there is a trend; as the atomic mass of the co-ordination metal increases the thermal stability also increases.

A more detailed study would provide an excellent understanding of this novel series of complexes. Another necessary area of investigation would be the exchange of the PPN cation for a nitrogen-rich alternative, producing the first main group homoleptic tetrazolato-based energetic salt. A suitable candidate for this would be the guanidinium (Gd) cation. This high nitrogen molecule has previously been used within the research group and preliminary attempts to prepare the $Gd(CHN_4)$ transfer reagent have been promising, and it is hoped that simply substituting $Gd(CHN_4)$ for the previously used $PPN(CHN_4)$ could yield the hypothesised $(Gd)_2[E(CHN_4)_6]$ (where E = Si, Ge and Sn).

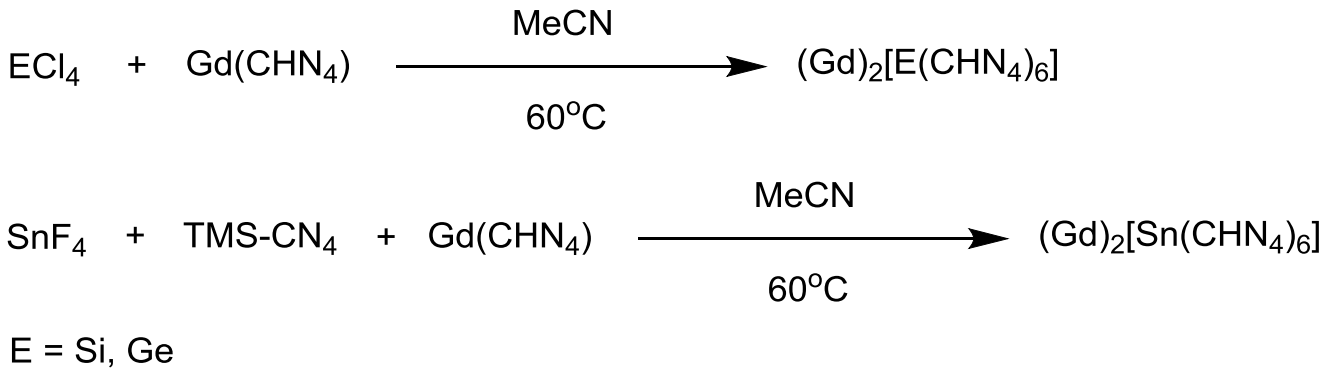

Scheme 19 – Potential preparative methods for the guanidinium containing analogues of the $(PPN)_2[E(CHN_4)_6]$ series.

4. Extension to Low Valent Main Group Centres: Synthesis of Novel Co-ordination Complexes

4.1 Overview

After the completion of the homoleptic tetrazolato-based $(PPN)_2[E(CHN_4)_6]$ series, the next step was to switch focus to the heavier main group elements. This is due to their ability to form low-valent complexes. This is controlled by the inert pair phenomenon which is described as a molecule that utilises a central atom of an element that exists in an oxidation state below its principal oxidation state. The effect was first hypothesised in 1928.[74] It was explained that for heavy main group elements the energy of the *s*-orbital is so low in energy that the gap to the *p*-orbitals is large enough to inhibit the *s*-orbital electrons from participating in bonding. It was predicted that by investigating the ionisation potential of main group elements it would explain the preference of the *s*-electrons of the heavier elements to abstain from bonding.[75] To explain the inert pair effect as a result of the increasing energy gap between the *s*- and *p*-electrons the ionisation potential is expected to increase down the group. The table shows that contrary to the predicted trend, the ionisation potential on descending the group decreases. The high ionisation potential of gallium can be explained by the *d*-block contraction; a completely full set of *d*-orbitals results in poor nuclear shielding, allowing the valence electrons to be held closer to the nucleus. This stronger attraction explains its higher ionisation potential.

Rather than having the lowest ionisation potential, thallium is significantly higher than indium. This is due to relativistic effects which become more prevalent as the atomic mass increases. Drago suggested that the thermodynamic behaviour of the compounds formed with a low valent main group centre can help explain the origins of the inert pair effect.[76] Through analysing the thermodynamic characteristics of the group 13 and 14 halides, Drago suggested that the preference for metal(II) halides for the heavier elements such as lead can be explained by the decreasing E-halide bond strength. The energy gained by forming four Pb-Cl bonds is not high enough to oxidise the co-ordination centre from +2 to +4, allowing the formation of a low valent compound.[77]

Lead(II) azide is an example of a main group homoleptic azide that has found commercial application as a primary explosive.[78] It is a non-hygroscopic solid, which is stored as a dextrinated solution to reduce its sensitivity. In the bulk, it has been shown that lead(II) azide exists in an erratic extended polymeric network.[79] For this reason it could be argued that lead(II) azide is not a simple inorganic compound, but a co-ordination polymer made up of $Pb(N_3)_2$ momomeric units.

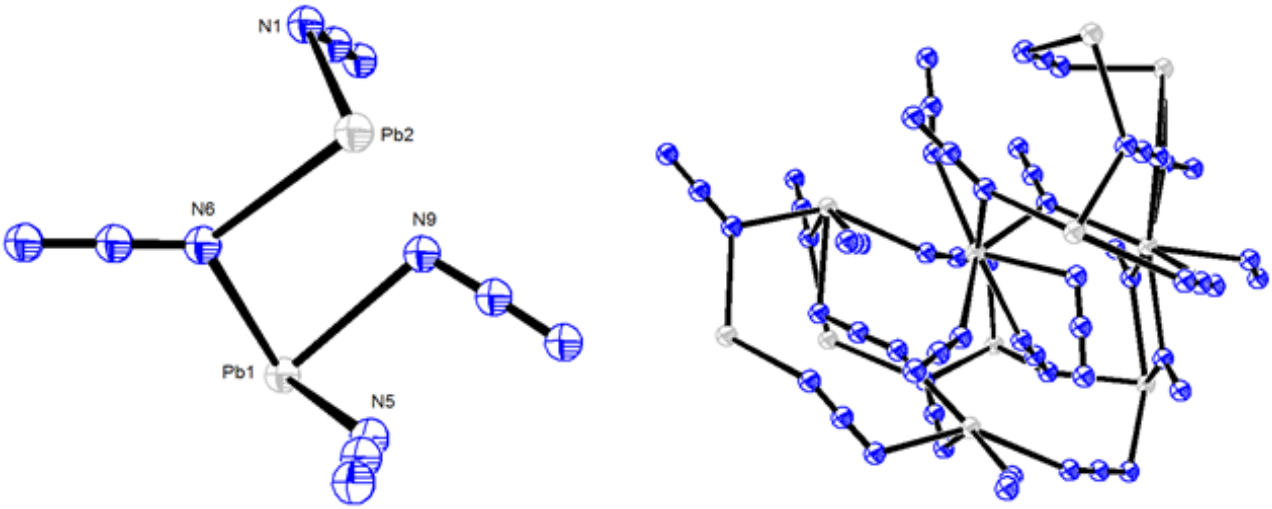

Figure 49 – Asymmetric unit of lead(II) azide (left) and its extended polymeric co-ordination network (right). Images generated using a CIF file from Ref. 80 using ORTEP®.

The widespread use of lead(II) azide leads to environmental damage as the lead cannot be consumed by its decomposition. Areas of extreme usage such as firing ranges and sites of military training will be contaminated by the build-up of heavy metal residues. These hazardous by-products can enter the groundwater and lead to serious health conditions. The preparation of low valent homoleptic azido complexes that utilise a more environmentally friendly co-ordination centre is of high interest. Within the Portius group the anionic species $[Sn(N_3)_3]^-$ and $[Ge(N_3)_3]^-$ have both been prepared.[80] Using the PPh_4 cation the nitrogen content can be reduced in both complexes, allowing for crystallisation and characterisation.

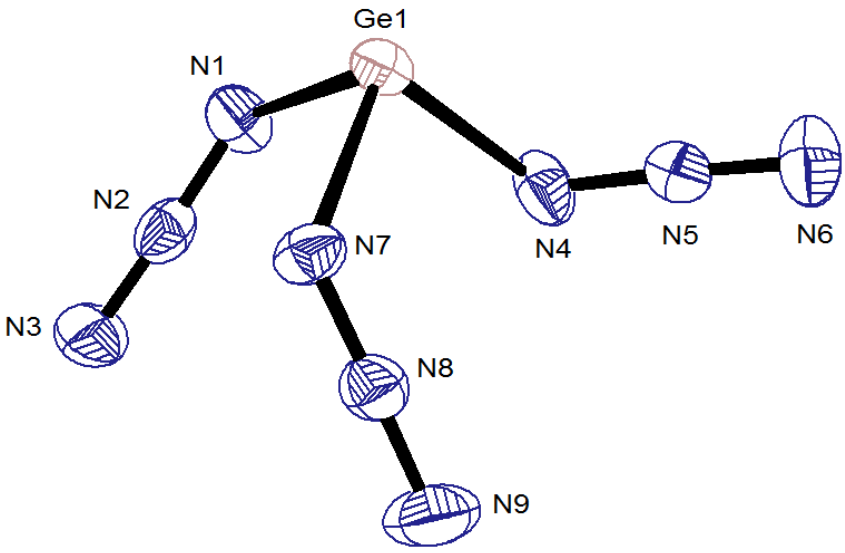

Figure 50 – Ellipsoid Diagram of the $[Ge(N_3)_3]^-$ anion. Images generated using a CIF file from Ref. 71 using ORTEP®.

Replacing the PPh_4 cation with a nitrogen-rich alternative would produce an energetic salt that could rival the energetic performance of lead(II) azide. The neutral $Sn(N_3)_2(py)_2$ complex has also been synthesised through the combination of trimethylsilyl (TMS) azide and SnF_2 using pyridine as a solvent.[71]

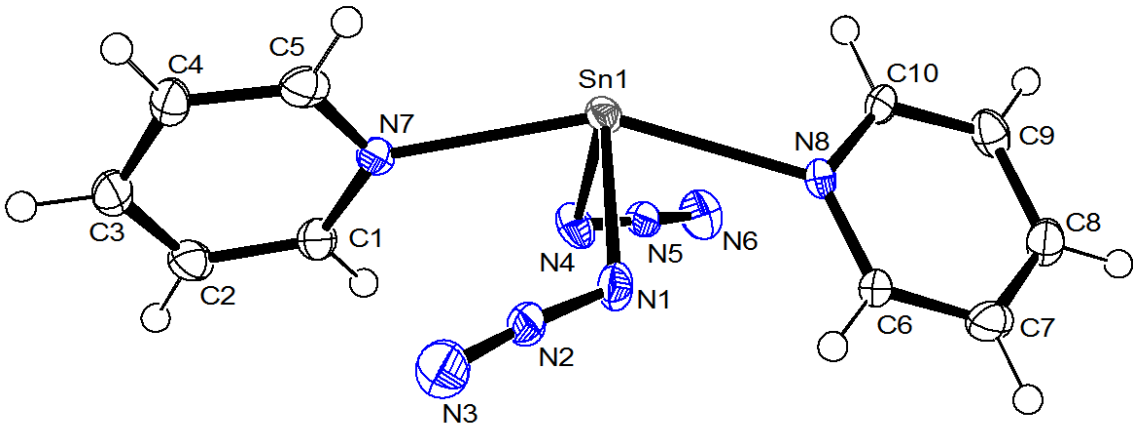

Figure 51 – Ellipsoid diagram of the $Sn(N_3)_2(py)_2$ complex.[71]

The structure of the complex is dictated by the repulsive power of the tin lone pair. The high electron density pushes all four bonds below the tin plane, forcing a "see-saw" orientation. The azido ligands are bound covalently, while the pyridine rings co-ordinate through the nitrogen, reducing the nitrogen content much like the bulky cations PPN^+ and PPh_4^+.

Bond	Bond Length (Å)
Sn_1-N_1	2.178(5)
Sn_1-N_4	2.195(6)
Sn_1-N_7	2.469(5)
Sn_1-N_8	2.472(5)

Table 9 – Comparison of bond lengths within the $Sn(N_3)_2(py)_2$ complex. N_1 and N_4 are both α-nitrogens of azide ligands, while N_7 and N_8 are the nitrogens within the pyridine ring.

The bond lengths support the conclusion that both pyridine rings are co-ordinating to the tin atom; their bonds are significantly longer than the covalently bond azido ligands. This illustrates the weaker nature of the co-ordination interaction. By stirring the co-ordination compound in dry acetonitrile the co-ordinated pyridine can be removed, resulting in the homoleptic neutral tin(II) azide.[71] This is an extremely sensitive material, with a highly explosive nature. However, further examination is necessary to evaluate its use as a replacement for lead(II) azide. There is no evidence in the literature for a homoleptic tetrazolate- based low valent main group compound. The replacement of the azido ligand with the tetrazolate ring would increase the stability of the resulting compound. This would be advantageous if the azido complex proved to be too sensitive, such as the neutral tin(II) azide. It is hypothesised that the analogous $[Sn(N_4CH)_3]^-$ and $[E(N_4CH)_4]^-$ (E = Sb, Bi) should be isolable. In addition, using co-ordination pyridine it should be possible to prepare $Sn(N_4CH)_2(py)_2$.

The co-ordinatively unsaturated nature of low valent systems also raises the possibility of the synthesis of low valent co-ordination polymers. These have been observed containing transition metal centres, but the main group analogues are much less common. The tetrazolate ligand would be the ideal organic linker as it has a variety of flexible binding modes, facilitating a higher geometric network. In addition tetrazolate groups have been successfully bound to main group atoms in previous investigations. The synthesis of a series of tetrazole main group co-ordination polymers would be a significant step in the development of energetic extended frameworks.

4.2 Results and Discussion

The viability of tetrazole-based low valent main group compounds was tested on the example of tin in the oxidation state 2+. The alkali tetrazolates, such as $Na(CHN_4)$, are effective as ionic tetrazole-transfer reagents provided a sufficient excess is employed. The latter requirement is critical since the exchange reaction is driven by only a comparably small thermodynamic advantage in favour of the E-CHN_4 bond making over E-X bond breaking. The previously used $PPN(CHN_4)$ was not suitable as the aim was to produce a neutral complex as opposed to a salt.

4.2.1 Attempted Synthesis of $[Sn(CHN_4)_2(py)_2]$

The reaction of $Na(CHN_4)$ and $SnCl_2$ was investigated in dry pyridine. On addition of the pyridine an immediate yellow suspension was produced. After the allowed reaction time the suspension was filtered, producing a clear yellow solution and a pale yellow solid.

$$Na(CHN_4)_{(excess)} + SnCl_2 \xrightarrow[\text{r.t., 46 h}]{\text{dry pyridine}} [Sn(CHN_4)Cl(py)_2]$$

Scheme 20 – Preparation of the $[Sn(CHN_4)Cl(py)_2]$ compound.

The solid was dried and probed using IR spectroscopy. It was shown to simply be mostly unreacted $Na(CHN_4)$, as expected. The discolouration is likely due to a small amount of the yellow solution remaining after filtration; once dried under vacuum the yellow colour stayed behind. The supernatant solution was concentrated and stored at -25°C. A small amount of yellow, block crystals were produced. The small amount of material did not allow a full characterisation, however upon investigation using X-ray diffraction it was shown that the a complex with a partially exchanged ligand sphere had been prepared with the rational formula $Sn(CHN_4)Cl(py)_2$.

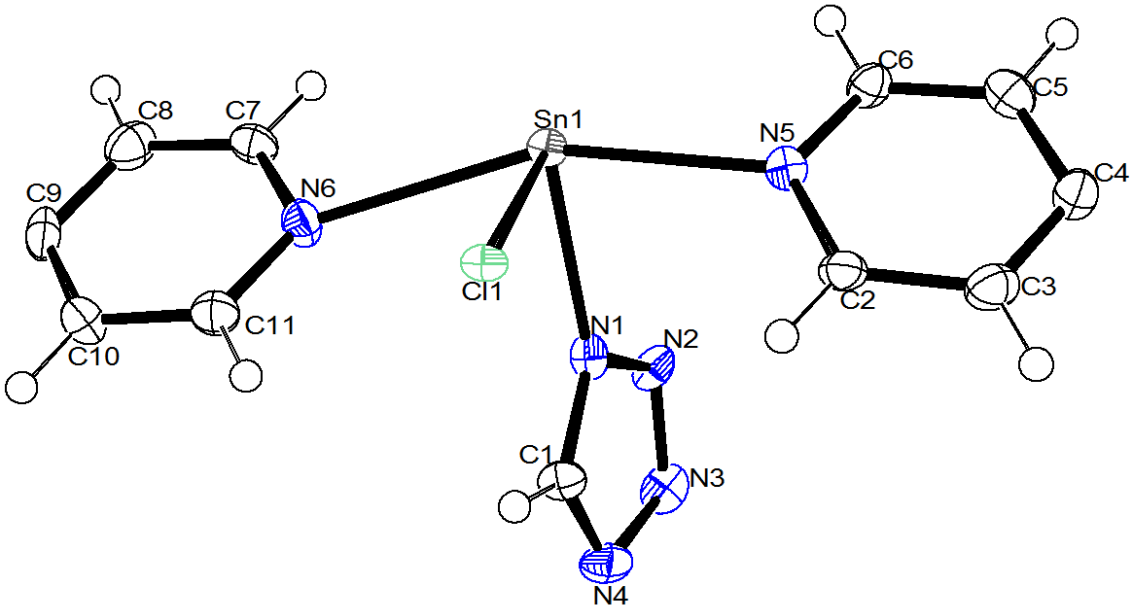

Figure 52 – Ellipsoid diagram of $Sn(CHN_4)Cl(py)_2$ Image using ORTEP®.

The asymmetric unit shown in figure 52 shows the structural nature of the molecule in question. It consists of a tetrazolato ligand, the unreacted chloride and two co-ordinating pyridine rings. All ellipsoids are sensible sizes, which suggest that the crystals were of a good quality, and the represented structure is correct. The tetrazolate ligand bonds via in N(1) fashion, as seen in the crystal structures for the previously prepared $(PPN)_2[E(CHN_4)_6]$ complexes, where E = Si, Ge and Sn. Both pyridines also co-ordinate via their respective N(1) atoms, as is typical for pyridine.

The orientation of the $Sn(CHN_4)Cl(py)_2$ does not appear as constricted compared to the analogous $Sn(N_3)(py)_2$. The chloride ligand remains in the tin plane, despite the repulsion experienced due to the tin lone pair. It seems the dominant effect upon the orientation of the complex is the steric bulk of the attached rings. The tetrazolate ring pushes the chloride into the tin plane, its large volume overcoming the electronic effect of the tin lone pair.

Bond	Bond Length (Å)
Sn_1-N_1	2.271(7)
Sn_1-N_5	2.408(4)
Sn_1-N_6	2.677(6)
Sn_1-Cl_1	2.4566(14)

Table 10 – Selected bond lengths within $Sn(CHN_4)Cl(py)_2$. N_1 is the tetrazolate nitrogen, while N_5 and N_6 are the nitrogens within the pyridine ring.

The table highlights the various bonding modes that are present within the complex. As seen in $Sn(N_3)_2(py)_2$, the exchanged ligand (in this case the tetrazolato ring) binds in a covalent fashion. At 2.271 Å the bond is longer than the analogous azido-tin bond (approximately 2.18 Å), indicating the decreased binding affinity of the tetrazolate ring. The ability of tetrazolate to resonant the electron density around the ring causes it to be significantly weaker nucleophile in comparison to the azide group.

The pyridine rings are again weakly co-ordinated to the tin centre. What is interesting is that one pyridine is considerably further from the tin atom, suggesting that it is an extremely weak interaction. When discussing the $Sn(N_3)_2(py)_2$ complex, both pyridine rings bind with a similar affinity. The central difference between the two complexes is the size comparison between the azido and tetrazolato ligands. The tin centre is substantially more sterically hindered in the $Sn(CHN_4)Cl(py)_2$ example and it is this that prevents both pyridine rings from binding in the same fashion.

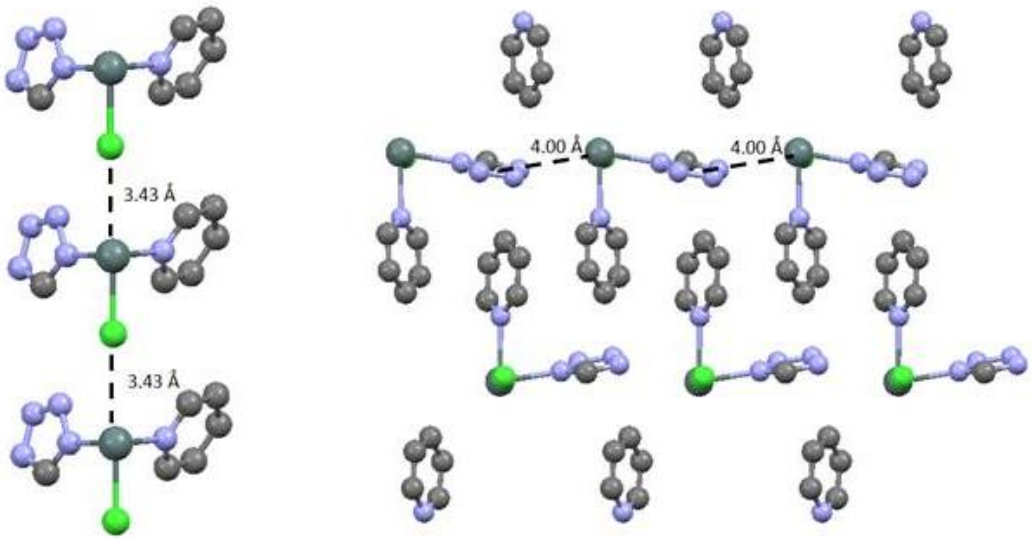

Figure 53 – Illustration of the interactions within the crystalline bulk of $Sn(CHN_4)Cl(py)_2$. There are significant Cl-Sn (left) and tetrazolate-Sn contacts (right). Images generated using Mercury®.

Within the crystalline bulk, the chloride ligand interacts via halogen bonding with the tin lone pair. In addition the tetrazolate ring is associated with the tin centre of an adjacent molecule. It is accepted that for a contact to be considered a true interaction the distance between the two centres must be less than the sum of the respective elements' Van der Waals radii.[47]

Atoms Involved	Sum of Van der Waal Radii (Å)	Distance of Interaction (Å)
Sn, N	4.24	4.000
Sn, Cl	4.08	3.433

Table 11 – Summary of the contacts within $Sn(CHN4)Cl(py)_2$ that are shorter than the Van-der-Waals radii. Interaction Distances calculated using Mercury®.

The halogen bond between the chloride and the tin lone pair is significant. The interaction distance is 0.65 Å than the sum of the Van der Waals radii of tin and chlorine. A halogen bond can be defined as a non-covalent interaction between a halogen atom, which can be considered a Lewis acid, and a Lewis base.[81]

The halogen atom acts as an electrophilic centre, forming a short contact with regions of high electron density. In this case, the inert lone pair at the tin centre acts as the Lewis base. The average bond length in tin(II) chloride is 2.58 Å, which compared to the halogen bond distance highlights its non-covalent nature. With respect to the Sn-Cl covalent bond and the Cl- -Sn halogen bond the angle across these interactions is 180°, typical of a halogen bond.[81] The tin-tetrazolate contact is much weaker, but can still be considered an interaction. The electropositive nature of the tin atom allows the formation of an ionic bond with the electronegative nitrogen atoms of the tetrazolate ring.

The $Sn(N_3)_2(py)_2$ complex by comparison does not form this "chain-like" (see figure 54) structure. It is instead dominated by a Sn-N interaction that forms a "pseudo dimer", in which the tin interacts with the nitrogen of an adjacent pyridine ring. This highlights an interesting discrepancy between the two compounds. The simple replacement of the azido ligand with the tetrazolyl group has a significant effect upon the bonding and shape of the resulting compound.

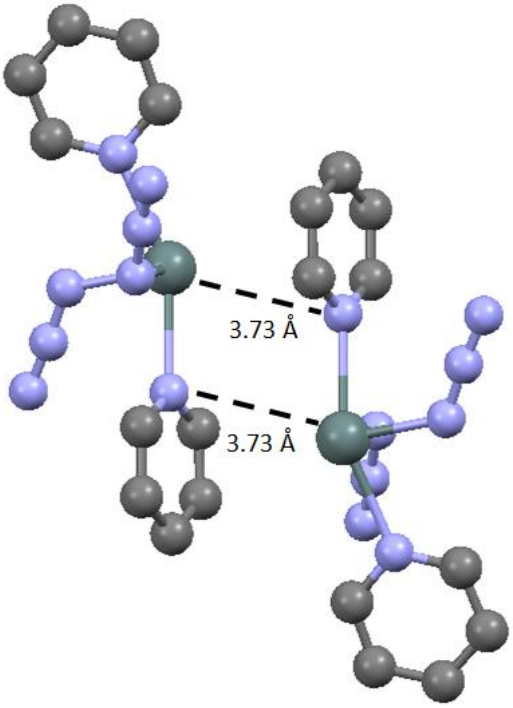

Figure 54 – Weak dimer structure of $Sn(N_3)_2(py)_2$. Image generated using a CIF file from Ref. 74 using Mercury®.

4.2.2 Alternative Synthesis of $[Sn(CHN_4)_2(py)_2]$

Pyridine has been utilised within the research group in the past to co-ordinate to main group centres, producing neutral main group complexes.[82] This is an alternative to using carbon-rich, bulky cations to produce salts. The pyridine has the advantage of being much cheaper, whilst still diluting the nitrogen content of the resulting complex sufficiently so that it is safe for manipulation. TMS-CHN_4 was reacted with various low-valent main group fluorides in an NMR tube, with deuterated pyridine as the solvent. The reaction progress was evaluated using the TMS proton as it changed from the reagent (TMS-CHN_4) to the product (TMS-F). First attempted was the combination of SnF_2 and TMS-CHN_4.

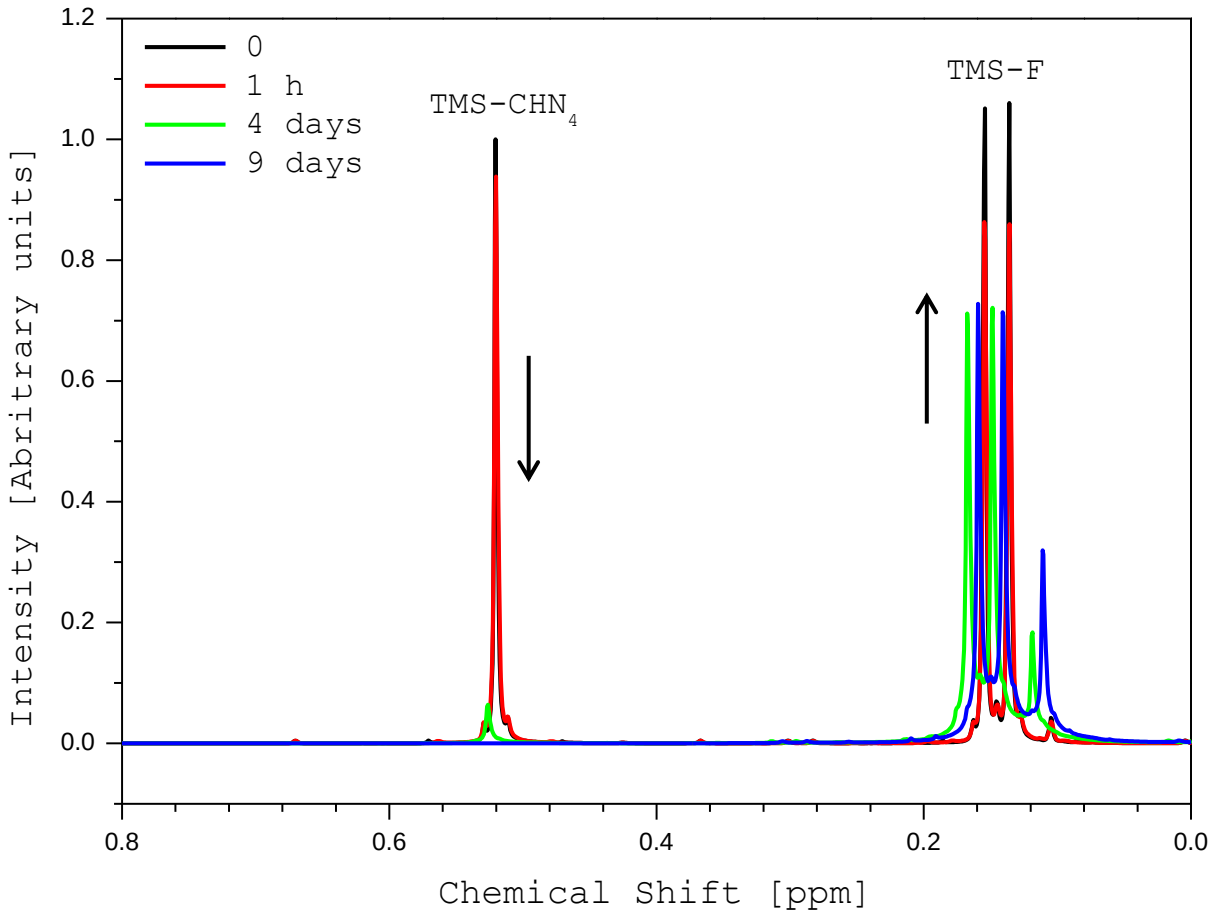

Figure 55 – ^{1}H NMR spectral study of the chemical shift in the reaction between TMS-CHN_4 and SnF_2 in *d*-pyridine in the range 0.80 ppm and 0 ppm.

As shown in the above spectrum, the TMS-CHN_4 peak at 0.52 ppm decreases over time showing its gradual removal from the reaction solution. The TMS(F) doublet at 0.22 ppm should increase at a similar rate. However it fluctuates unpredictably. This can be explained by the volatile nature of TMS(F); it boils at 15^{o}C and as a gas can escape the NMR tube. Also small fluctuations in ppm have been attributed to the nature of the investigation; there was a significant time difference between each measurement, resulting in differences in analytical conditions such as temperature. This can result in small changes in the observed ppm. Significantly, the observed peaks indicate that the combination of SnF_2 and TMS-CHN_4 does result in fluorine-tetrazolato exchange (figure 55). The NMR investigation was repeated using PbF_2, SbF_3 and BiF_3, all producing the same result. The TMS-CHN_4 peak can be followed as it decreases with respect to all metal fluorides explored.

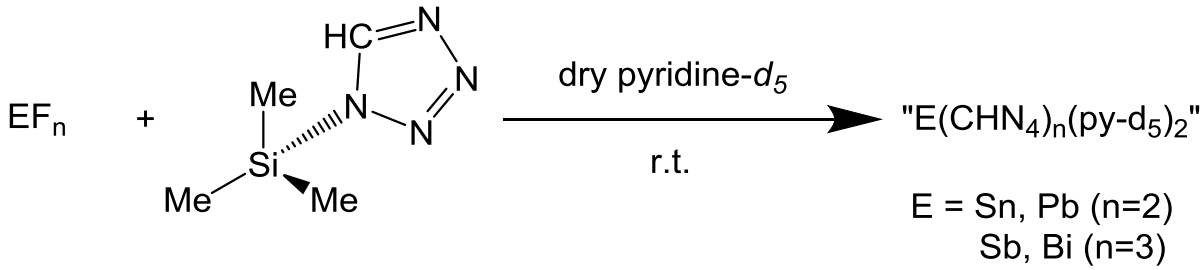

Scheme 21 – General synthetic procedure for the attempted preparation of the complexes "$E(CHN_4)_n(py)_2$" where E = Sn, Pb (n = 2) and Sb, Bi (n = 3).

The SnF_2 investigation results in the growth of crystals in the NMR tube. These were analysed using IR and ^{1}H NMR spectroscopy. The IR spectrum (figure 56) allows partial assignment of the product. The peak at 1593 cm^{-1} corresponds to co-ordinated pyridine. The fingerprint region between 1300 cm^{-1} and 500 cm^{-1} is crowded and therefore hard to assign. It is a similar peak pattern to previously prepared tetrazole containing compounds; however this does not allow assignment of the nature of the tetrazole's involvement.

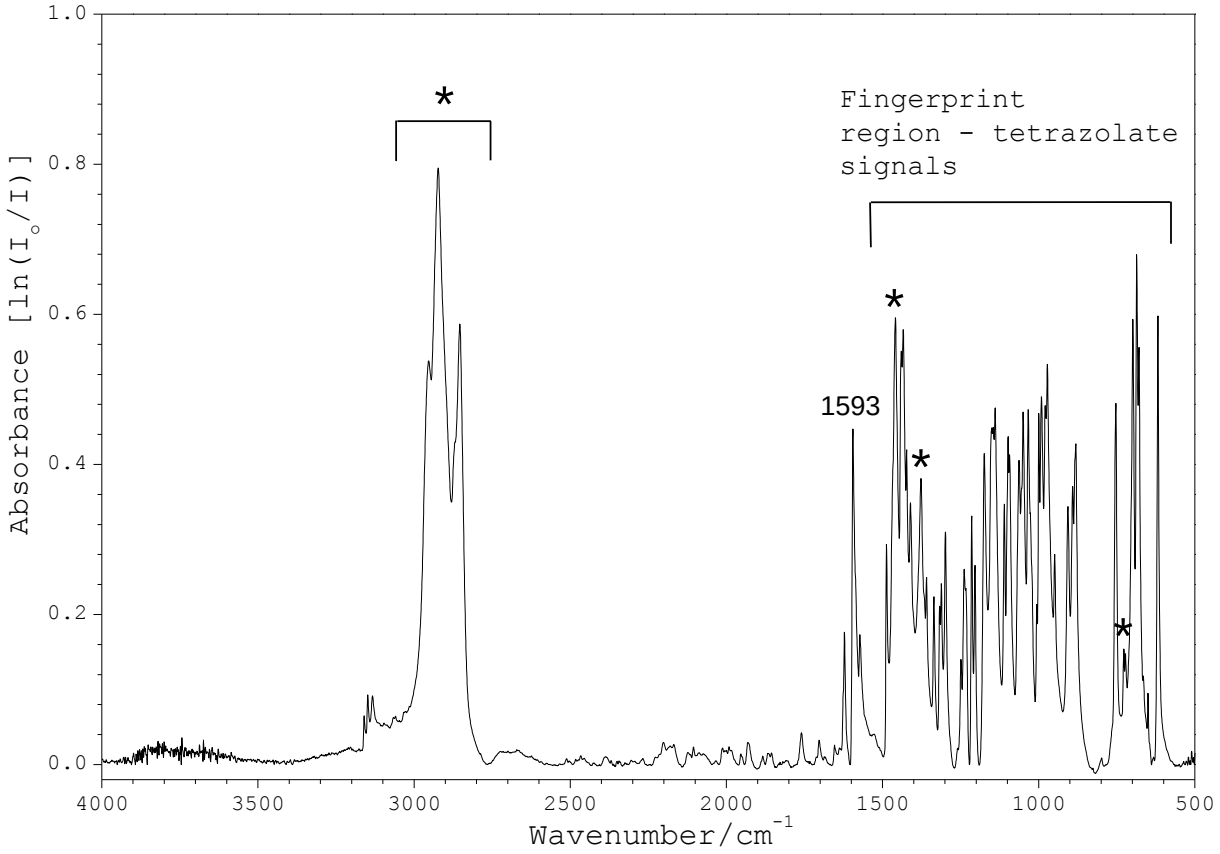

Figure 56 – Nujol mull IR spectrum of mulled "$[Sn(CHN_4)_2(py)_2]$". Nujol bands are marked by asterisks (*).

The ^{1}H NMR spectrum provides more information that, when combined with the data from the IR spectrum, allows tentative assignment. It exhibits four major product peaks, the three pyridine peaks at 7.35 ppm, 7.76 ppm, 8.59 ppm and the tetrazolate peak at 8.94 ppm. The tetrazolate peak is a singlet, indicating that there is either a single tetrazolate proton, or all tetrazolate protons are symmetrically equivalent. Its peak position is unique, different to all reagents and previously made tetrazolate-containing complexes. As the deuterated solvent used is pyridine-d_5, the position and nature of the pyridine peaks in the ^{1}H NMR spectrum are somewhat masked by the excess solvent and poor solubility of the white solid.

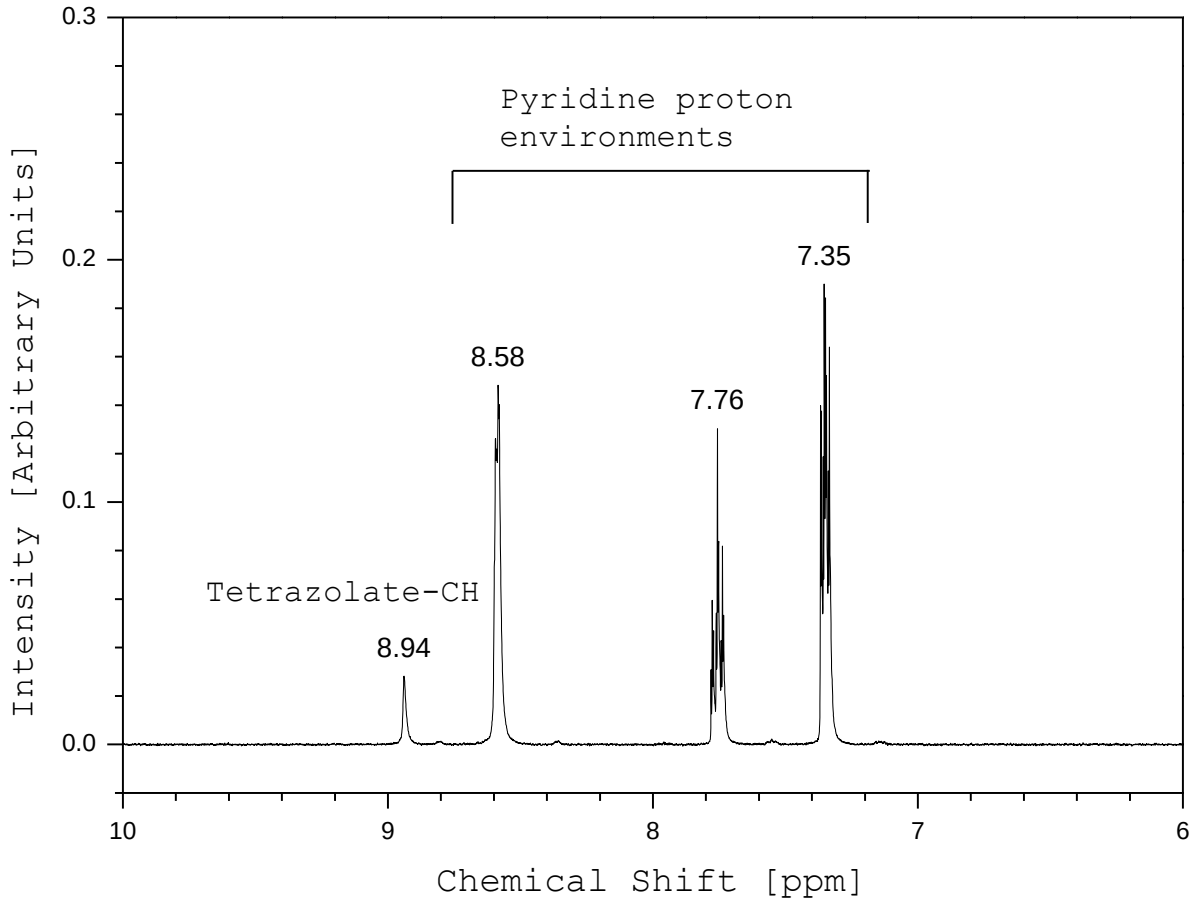

Figure 57 – ^{1}H NMR spectrum of "[Sn(CHN$_4$)$_2$(py)$_2$]" in pyridine-d_5 between 10.00 ppm and 6.00 ppm.

Using single crystal X-ray diffraction studies it proved that rather than the simple monomeric [Sn(CHN$_4$)$_2$(py)$_2$], a co-ordination polymer was produced. This was a surprising result as the crystals grew from a deuterated pyridine solution, therefore pyridine was available to co-ordinate in an analogous fashion to the [Sn(N$_3$)$_2$(py)$_2$]. Yet in the observed co-ordination polymer a single pyridine is bound to the metal centre, leaving a vacant site for further co-ordination of tetrazolato ligands. The tetrazolato ligands bridge in a N(1)-N(4) fashion in two dimensions, connecting each metal centre 2D planar network. The pyridine cannot bridge and it caps each repeating unit. This is the first example of such a polymeric system.

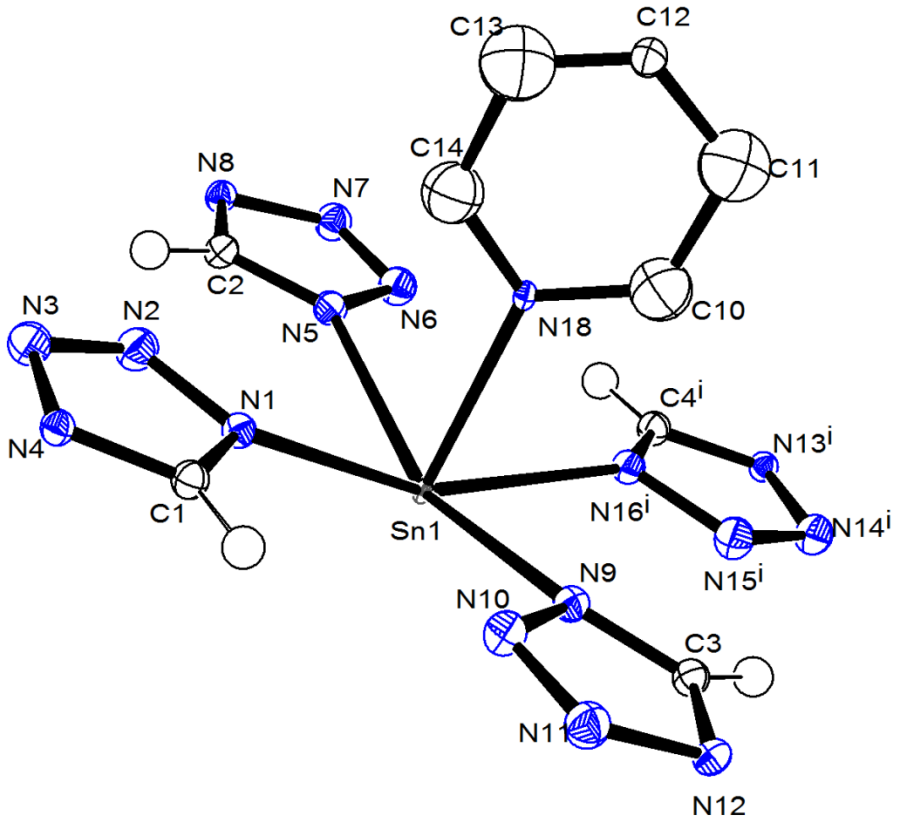

Figure 58 – Ellipsoid Plot highlighting the co-ordination geometry of the tin centre. The pyridine ligand is rotationally disordered, which has not been modelled for simplicity. This is the cause for the large ellipsoids. Image generated using ORTEP®.

Each tin centre is pentaco-ordinate and is orientated in a square-based pyramidal geometry. The bond lengths are summarised in table 12. It was expected that the Sn-tetrazolate bond lengths would be much shorter that the attached pyridine ring, as it has been shown using ^{1}H NMR spectroscopy to be a labile ligand. However what the crystal structure shows is that the bound pyridine has a shorter bond length, indicating a stronger interaction.

Bond	Bond length [Å]
Sn_1-N_1	2.535(8)
Sn_1-N_5	2.524(8)
Sn_1-$N_{16}{}^{i}$	2.537(8)
Sn_1-N_9	2.525(9)
Sn_1-N_{18}	2.366(9)

Table 12 – Summary of the bond lengths between Sn1 and the attached ligands detailed in figure 58.

The origins of this observation can be explained by the nature of the bonds within the network. The charge of each Sn(II) centre is balanced by the attached ligands, producing a charge neutral polymer. Ordinarily the tetrazolate ligand possessesing a (1-) charge. However as the polymer is neutral, each tetrazolate must contribute a (1/2-) charge to the complex. This could be explained by the bridging nature of the tetrazolate ligands within the polymer. Each tetrazolate ligand is bound to two tin centres, splitting its electron density between the two co-ordination centres. The four bridging tetrazolate ligands can then contribute a total of two electrons to each tin centre. The split nature of the bonding mode of the tetrazolate ring could explain a weaker interaction at each tin centre, therefore a longer bond. The pyridine binds via a co-ordination bond, and contributes no electron density. Alternatively, it could simply be due to the difference between axial and equatorial bond lengths. All the tetrazolate ligands are in the equatorial plane, whilst the lone pyridine ring occupies the single axial position. This represents a less hindered site to bond, allowing the pyridine ring to sit closer to the tin centre with minimal steric repulsion from the tetrazolate ligands. The typical bond angles for a square-based pyramidal geometry are 90^{o}. Table 13 shows that the co-ordination sphere at each tin centre is significantly distorted. This is attributed to the lone pair located at the tin centre; the high charge density resulting in a highly repulsive nature.

Bond	Bond Angle [^{o}]	Deviation from 90°
N_1-Sn_1-N_5	87.6(3)	-2.4
N_5-Sn_1-N_{16}^{i}	87.9(3)	-2.1
N_9-Sn_1-N_{16}^{i}	87.4(3)	-2.6
N_9-Sn_1-N_1	87.6(3)	-2.4
N_{ax}-Sn_1-N_{18}	78.18 (average)	-11.88

Table 13 – Summary of the bond angles within the neutral $\{Sn(CHN_4)_2(py)_2\}_n$ co-ordination centre.

The lone pair sits in an axial position and forces all equatorial bonds, i.e. the tetrazolate ligands, out of the plane. This can be observed by viewing the tin centre in the equatorial plane (figure 59). The repulsion is so strong that it overcomes the steric organisation for the typical square-based pyramidal orientation in preference for the relaxation of the electronic interaction. This gives rise to the unusual “umbrella” shape.

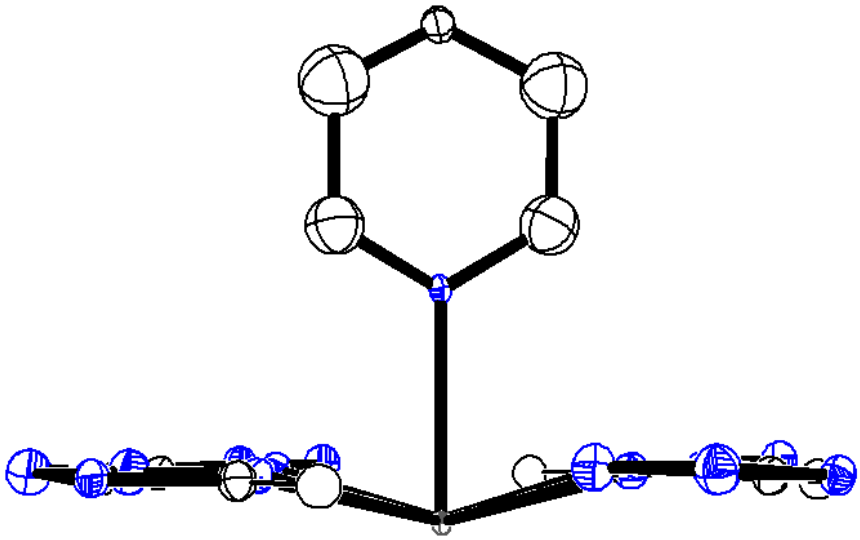

Figure 59 – Ellipsoid plot detailing the distorted square-based pyramid geometry that exists at each tin co-ordination centre within the $\{Sn(CHN_4)_2(py)_2\}_n$ co-polymer. Image generated using ORTEP®.

Although tetrazolate-containing co-ordination polymers are rare, $\{Cu_2(CHN_4)_2(OH)_2\}_n$ is a heteroleptic co-ordination polymer which contains copper co-ordination centres that exhibit a distorted square-based pyramid in a similar fashion to $\{Sn(CHN_4)_2(py)_2\}_n$[15] It is the similar co-ordination environment that allows direct comparisons to be made.

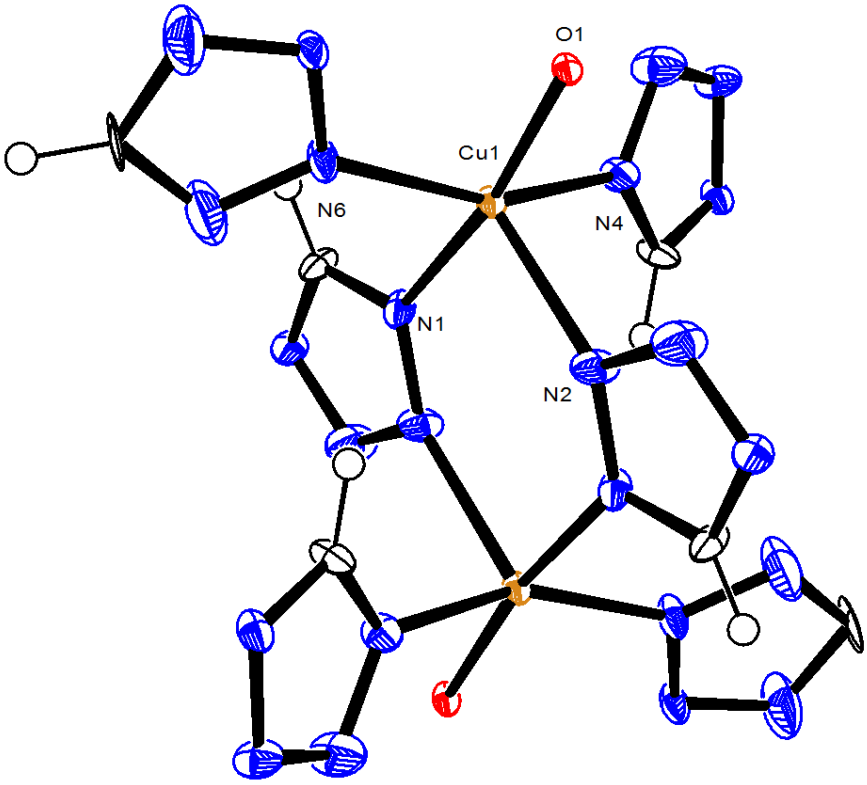

Figure 60 – Ellipsoid plot containing two symmetrical related Cu co-ordination centres within $\{Cu(CHN_4)_2(OH)_2\}_n$. Numbered atoms relate to the bond lengths detailed in table 14. Image produced from a CIF file from Ref. 16 using ORTEP®.

One notable difference is that the tetrazolyl ligands bridge in an N(1)-N(2) fashion within $\{Cu(CHN_4)_2(OH)_2\}_n$ rather than the observed N(1)-N(4) bridging for $\{Sn(CHN_4)_2(py)_2\}_n$. The distortion around the metal centre is also significantly different. For the Cu example, the distortion involves the equatorial bonds being pushed "away" from the axial ligand, whereas for $\{Sn(CHN_4)_2(py)_2\}_n$ the tin lone pair forces the equatorial bonds "towards" the axial bond. With respect to the copper metal centre, this distortion is much less uniform and likely caused by the steric requirements of the co-ordination polymer. This mirrors the $\{Sn(CHN_4)_2(py)_2\}_n$, in which the lone pair is dominant over steric repulsion, pushing the equatorial bonds towards the axial pyridine ring.

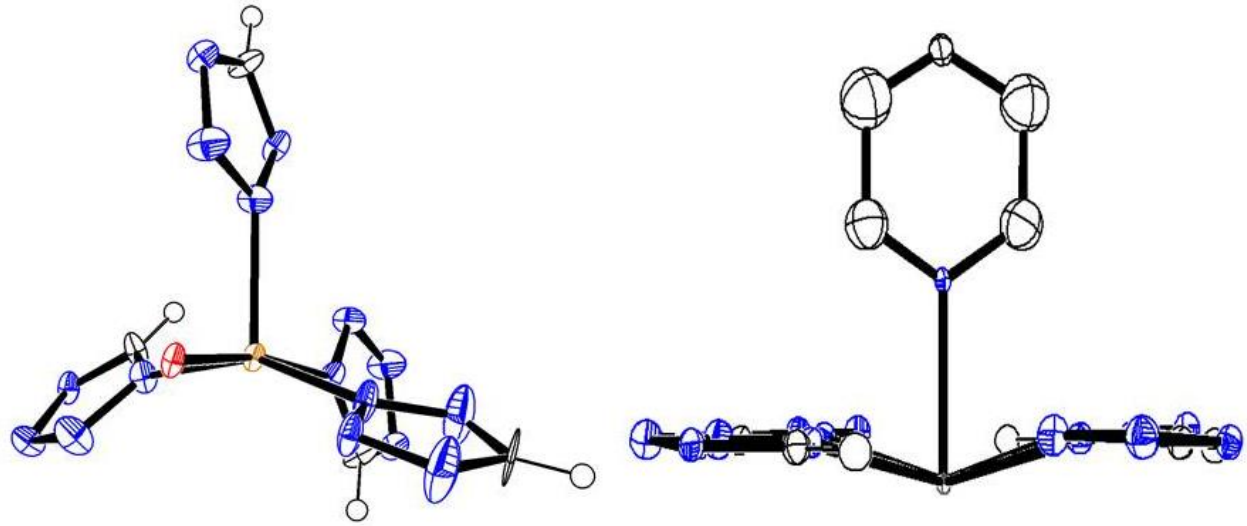

Figure 61 – Ellipsoid plot comparing the co-ordination geometries at $\{Cu(CHN_4)_2(OH)_2\}_n$ and $\{Sn(CHN_4)_2(py)_2\}_n$. Images produced using ORTEP®, the left image from a CIF file from Ref. 16.

$\{Cu(CHN_4)_2(OH)_2\}_n$		$[Sn(CHN_4)_2(py)_2]_n$	
Bond	Bond Length [Å]	Bond	Bond Length [Å]
Cu_1-N_1	2.004(4)	Sn_1-N_1	2.535(8)
Cu_1-N_2	2.246(4)	Sn_1-N_5	2.524(8)
Cu_1-N_4	2.020(4)	Sn_1-N_{16}^{i}	2.537(8)
Cu_1-N_6	2.033(4)	Sn_1-N_9	2.525(9)
Cu_1-O_1	1.900(19)	Sn_1-N_{18}	2.366(9)

Table 14 – Comparison of bond lengths within $\{Cu(CHN_4)_2(OH)_2\}_n$ and $\{Sn(CHN_4)_2(py)_2\}_n$.

The extended structure is highly interesting. Each tin centre is connected to the adjacent tin by the tetrazolate ligands bridging in a N_1,N_4 fashion. This yields an extended linear sheet in the equatorial plane, with the terminal pyridine ring bound in the axial position. The capping pyridine ligands on one layer participate in pi-pi stacking with axial pyridines on an opposing polymeric sheet. The result of this is a bilayer system (figure 62).

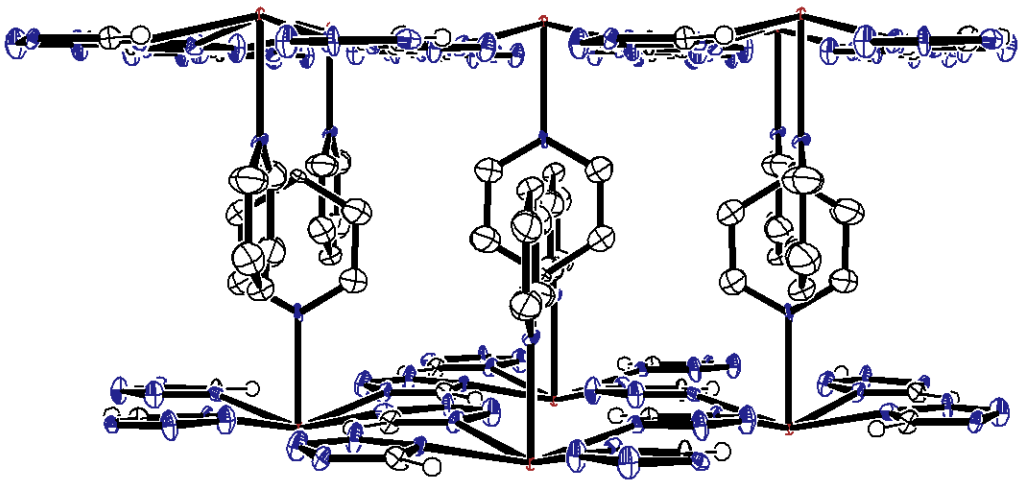

Figure 62 – Ellipsoid plot of a cross section of the extended bilayer network. This cross section is viewed through the xy plane. Note that the pyridine ligand is rotationally disordered, and it is the edge-to-face interaction that is represented here. This was to help distinguish between the two layers; also possible is a face-to-face interaction. Image generated using ORTEP®.

An electronic interaction can be deemed significant if its distance is less than the sum of the van der Waals radii of the respective elements. A pi-pi interaction can occur in three varieties: sandwich, T-shaped and parallel displaced.

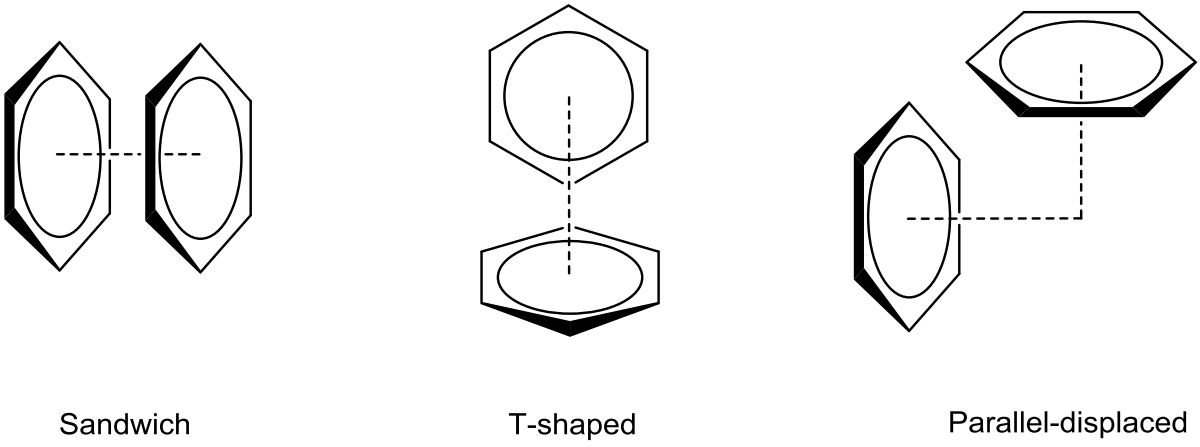

Figure 63 – Different types of π-π stacking interaction.

Both sandwich and T-shaped stacking can occur in this particular example, due to the disordered nature of the pyridine. In figure 62 the pyridine rings are orientated in an edge-face fashion, which corresponds to the T-shaped pi-pi stacking mode shown in figure 63. The distance for this interaction is 3.87 Å. This is higher than the sum of the respective van der Waals radii, which for two carbon atoms is 3.40 Å. This orientation cannot be the origin for the attraction. An edge-to-edge contact is instead 2.87 Å, which would satisfy the criteria for a pi-pi interaction. The rapid rotation about the tin-pyridine bond means that the true interaction could be a mix of the two orientations. Interestingly, the associated pyridine can be removed by stirring the white solid overnight in dry acetonitrile. This can be observed using IR spectroscopy. The IR comparison shown in figure 64 shows significant variation, in particular at the removal of pyridine illustrated by the absence of the strong absorption band at 1593 cm^{-1} (*). The tetrazolate bands for the $Sn(CHN_4)_2$ spectrum are poorly defined, but still present. It indicates that apart from the removal of the pyridine the compound seems unchanged.

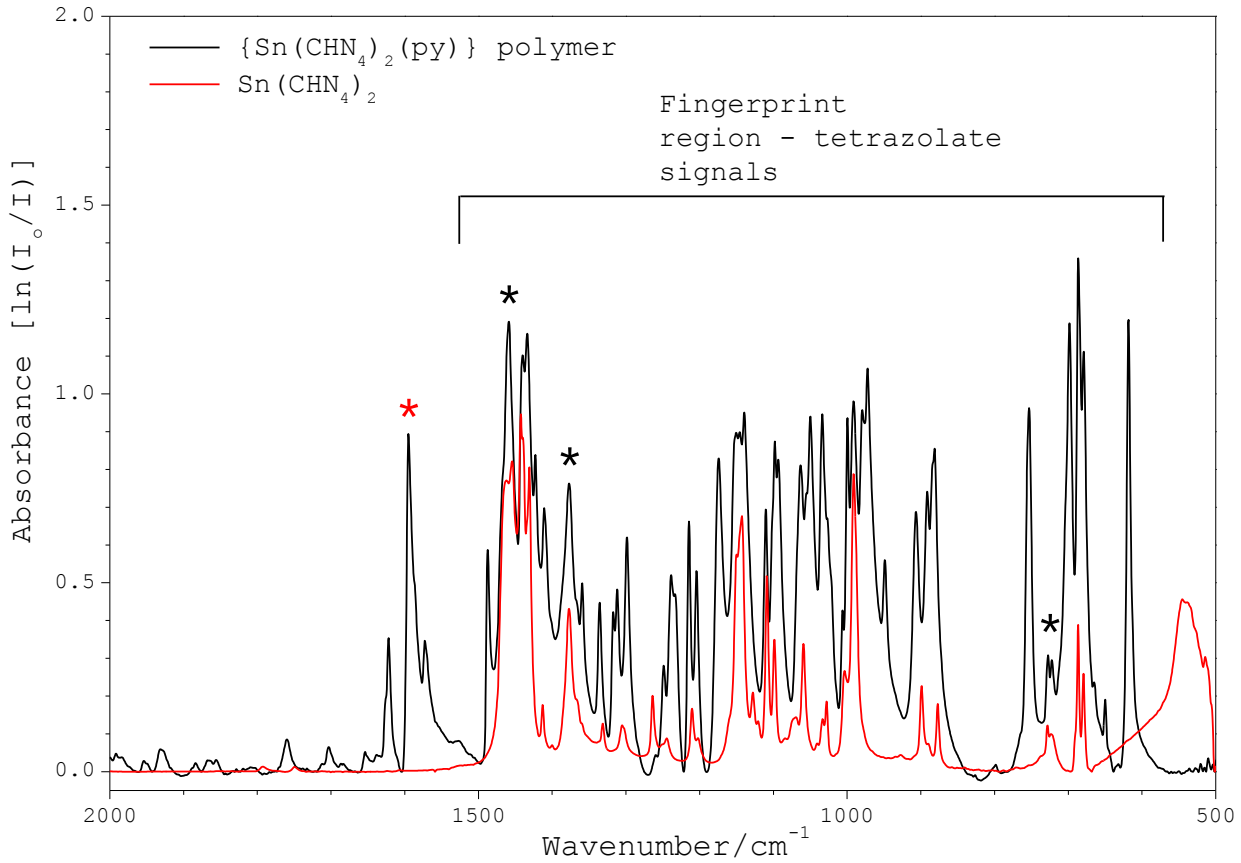

Figure 64 – Nujol mull IR comparison between $\{Sn(CHN_4)_2(py)\}$ and $Sn(CHN_4)_2$ between 2000 cm^{-1} and 500 cm^{-1}. Nujol bands are marked by asterisks (*).

The ^{1}H NMR spectra also support the hypothesis that the co-ordinated pyridine has been removed. The tetrazolate peak is shifted slightly in the $Sn(CHN_4)_2$ ^{1}H NMR spectrum from 8.94 ppm to 8.90 ppm, possibly due to the disassociation of the pyridine ligand. This could also be caused slight differences in the analytical environment. The most significant observation is that all pyridine peaks have been removed. The combination of the IR and ^{1}H NMR spectra strongly support the production of the neutral $Sn(CHN_4)_2$.

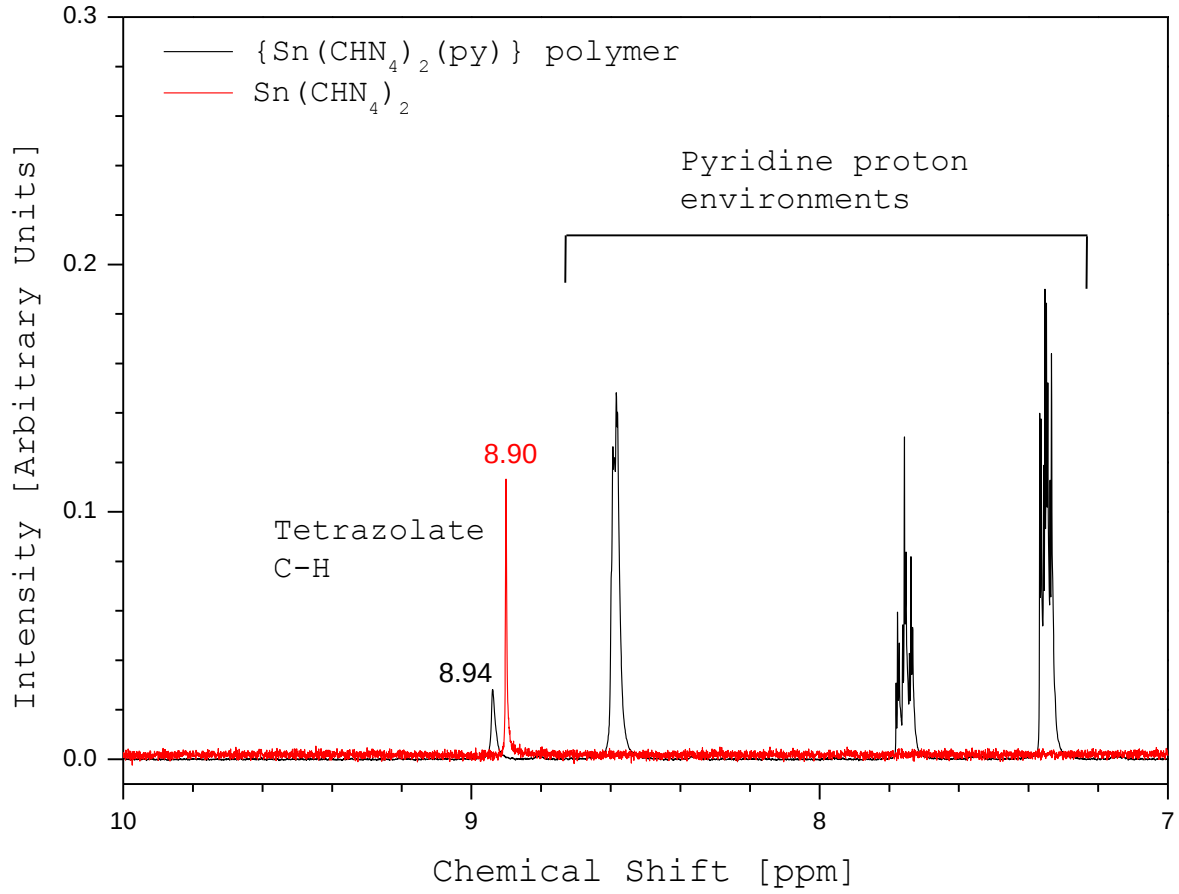

Figure 65 – ^{1}H NMR comparison of $\{Sn(CHN_4)_2(py)_2\}_n$ against $Sn(CHN_4)_2$, with both compounds dissolved in CH_3CN–d_3. Comparison focussed upon the product proton environments between 7 ppm–10 ppm.

However it is has poor solubility in all common solvents and therefore crystallisation is difficult. Nonetheless, this would represent a highly interesting result as it would be a direct tetrazolate-containing analogue to the commonly used lead(II) azide. It would contain 44% nitrogen, in comparison to 29% that is bound in $Pb(N_3)_2$.

4.2.3 Expansion of the new synthetic method to Lead Co-ordination Centres

The formation of an analogous Pb-based co-ordination polymer would be extremely interesting. In addition if the pyridine ligand proves to again be labile, its removal would result in the $Pb(CHN_4)_2$. The ^1H NMR investigation concerning PbF_2 suggested that F–CHN_4- exchange occurs, albeit at a reduced rate. As shown in figure 66 the TMS-CHN_4 peak at 0.54 ppm decreases as the reaction progresses. A significant reduction is achieved during a period in which the NMR tube was heated to 50°C (–). The NMR tube was subsequently left at room temperature for 3 days. The intensity of the observed TMS-CHN_4 peak remains at a similar level, which indicates that for the reaction to progress additional energy input is required.

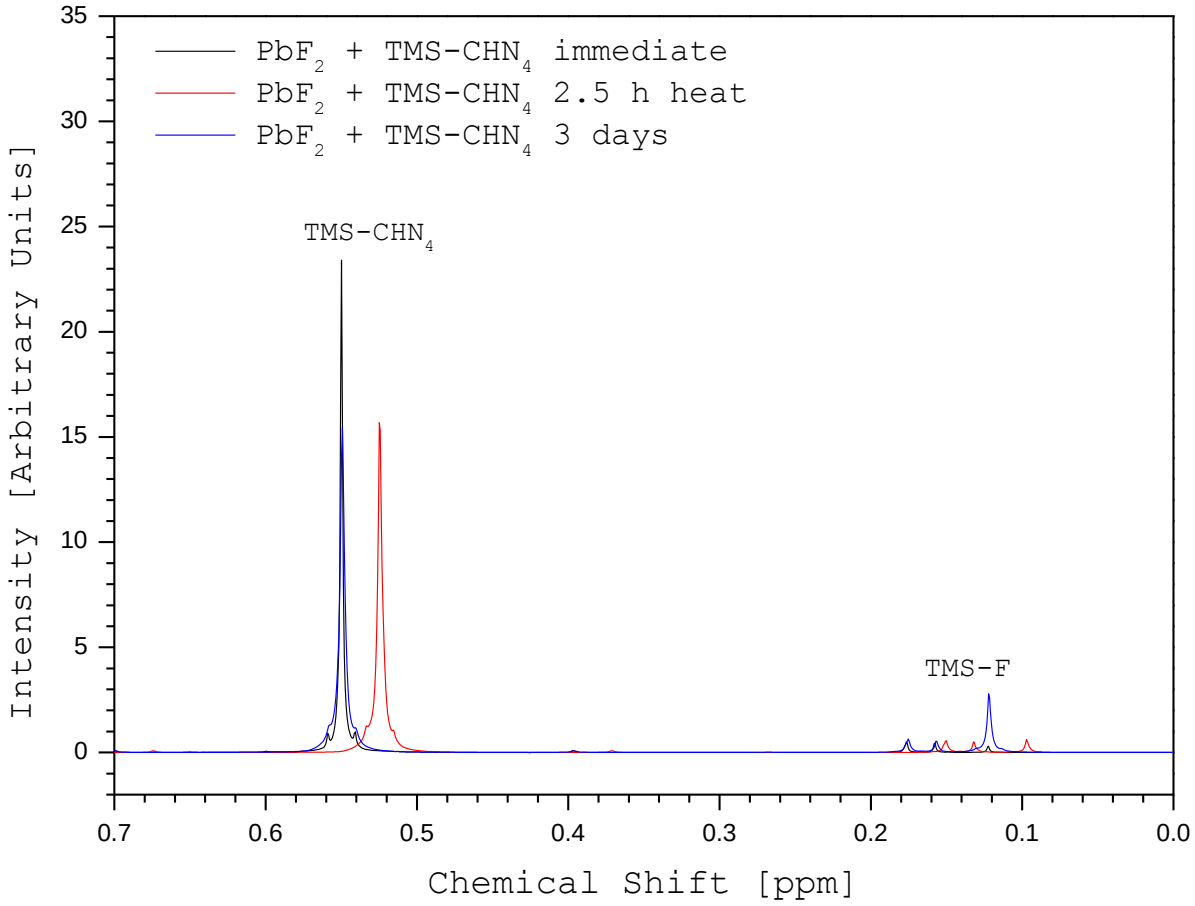

Figure 66 - ^1H NMR spectral series in the range 0.70 ppm and 0 ppm obtained by monitoring the reaction between PbF_2 and TMS-CHN_4. Small fluctuations in ppm have been attributed to the time difference between each measurement, resulting in differences in analytical conditions.

No crystalline material was recovered from the NMR tube so a full scale reaction was performed in an attempt to further understand the reaction and to characterise the products.

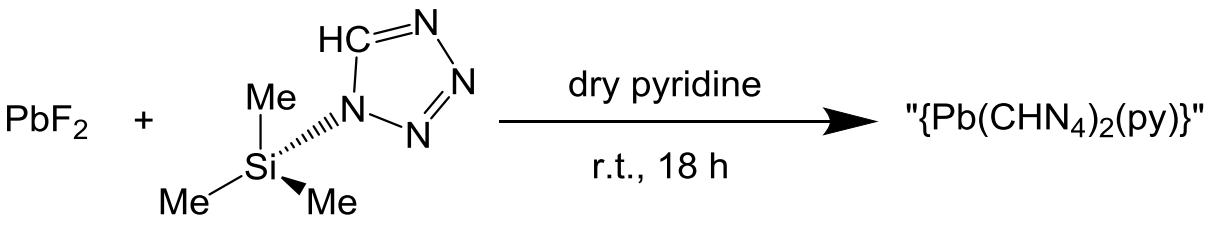

Scheme 22 – Attempted preparation of the analogous $\{Pb(CHN_4)_2(py)_2\}$ co-ordination polymer.

Both reagents are added to a single Schlenk tube and suspended in dry pyridine. After 18 h the white suspension was filtered to produce a white solid and a clear solution. The white solid was dried and analysed using IR and ^{1}H NMR spectroscopy.

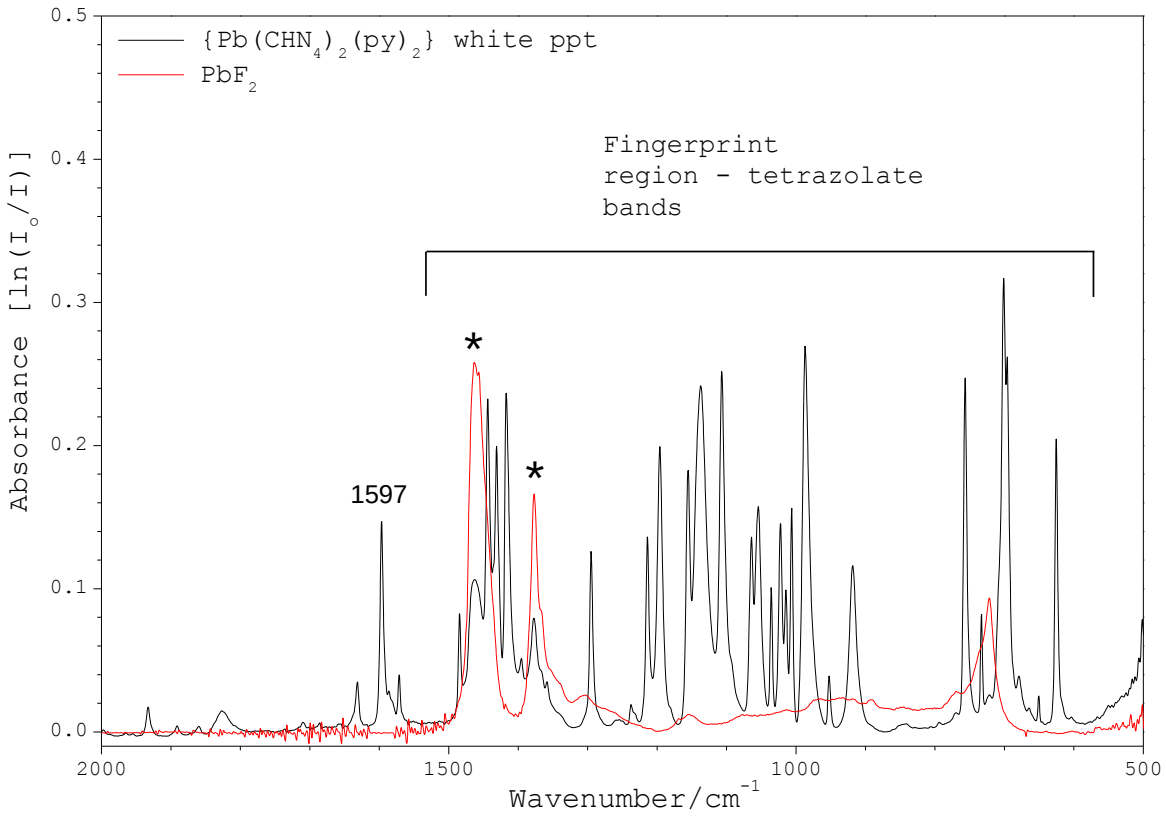

Figure 67 – Nujol mull IR comparison between the PbF_2 reactant and the resulting "$\{Pb(CHN_4)_2(py)_2\}$" white solid between 2000 cm^{-1} and 500 cm^{-1}. Nujol bands are marked by asterisks (*).

The comparison of IR spectra illustrates the difference between the PbF_2 reactant and the white solid isolated from the investigation (figure 67). The IR frequencies for PbF_2 all arise below 500 cm^{-1}, therefore the only observed peaks in the red spectrum are the Nujol bands at 1460 cm^{-1}, 1377 cm^{-1} and 721 cm^{-1}. The IR spectrum for the white solid possesses several characteristic regions. The peak at 1597 cm^{-1} represents co-ordinated pyridine, which supports the hypothesis that pyridine will co-ordinate to the lead centre. The crowded fingerprint region is completely unlike that shown in the PbF_2 spectrum also strongly suggests that the nature of the white solid is that of a tetrazolate-containing compound. These observations indicate that a reaction has indeed taken place, potentially leading to the analogous $\{Pb(CHN_4)_2(py)_2\}$ co-ordination polymer.

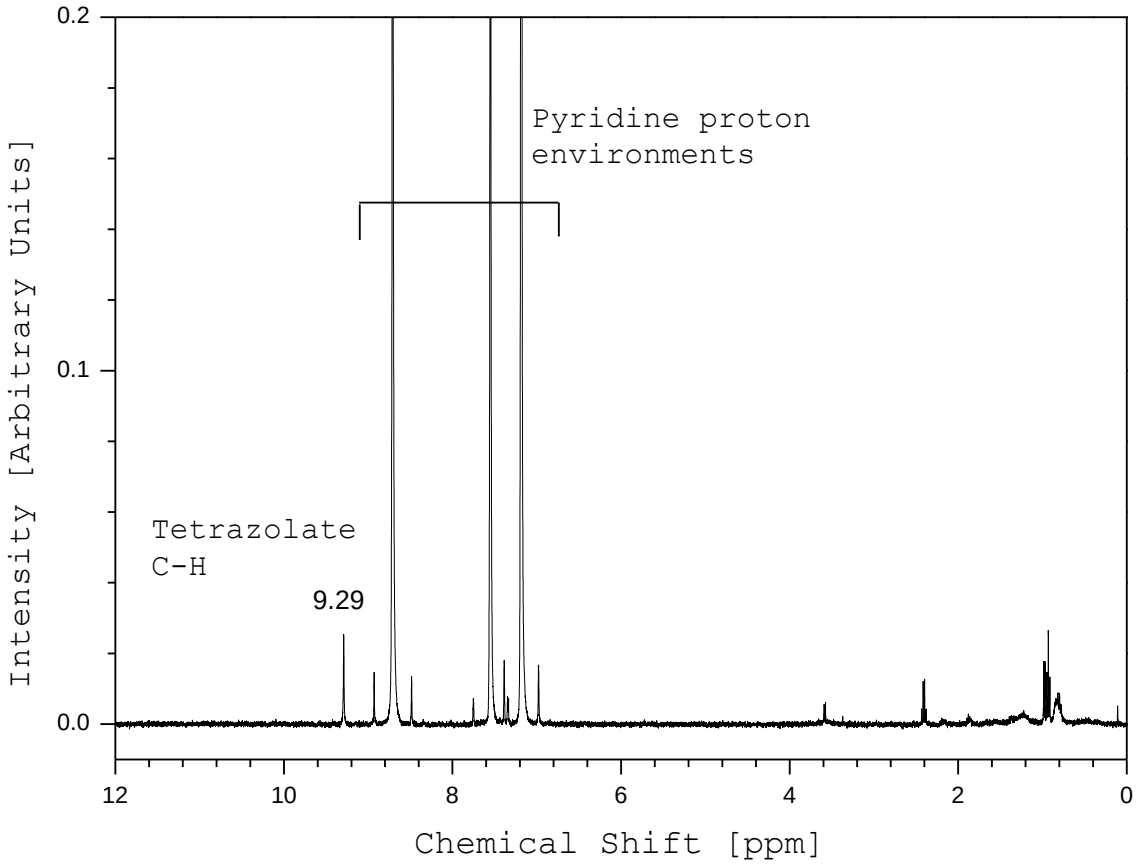

Figure 68 – ^{1}H NMR spectrum of the "$\{Pb(CHN_4)_2(py)_2\}$" white solid in pyridine-d_5.

The ^{1}H NMR spectrum contains a single tetrazolate proton environment at 9.29 ppm. As the deuterated solvent used is pyridine-d_5, the position and nature of the pyridine peaks in the ^{1}H NMR spectrum are somewhat masked by the excess solvent and poor solubility of the white solid.

The ^{1}H NMR analysis was repeated using CH_3CN-d_3; however the white solid was insoluble in the solvent and provided no useful information. Using the IR and ^{1}H NMR spectroscopic results it is a sensible suggestion that the F−CHN_4 exchange had, in the very least, begun to take place in the presence of co-ordination pyridine. Elemental analysis performed upon the white solid provided an unexpected, but interesting result. The found percentages are lower than expected, which indicated that the nature of the white solid is not the simple, fully exchanged product. The found values approximately corresponds to $Pb_2F_2(CHN_4)_2(py)$.

Complex	Carbon [%]			Hydrogen [%]			Nitrogen [%]		
	Exp.	Found	Variation	Exp.	Found	Variation	Exp.	Found	Variation
"$\{Pb(CHN_4)_2(py)\}$"	19.81	13.65	-6.16	1.66	0.96	-0.70	29.70	19.86	-9.84
"$Pb_2F_2(CHN_4)_2(py)$"	12.56			1.05			18.82		

Table 15 – Elemental Analysis of the "$\{Pb(CHN_4)_2(py)_2\}$" white solid. Predicted percentages of "$Pb_2F_2(CHN_4)_2(py)$" are included for comparison.

The presence of fluorine within the white solid can be evaluated using ^{19}F NMR spectroscopy. As predicted there are fluorine environments, at -70.32 ppm and -72.16 ppm. On initial inspection the small peak separation could be attributed to a single fluorine environment which has been split into a doublet. However a doublet should by definition possess the same intensity, which the two peaks within the ^{19}F NMR spectrum do not. This suggests that the peaks are caused by two distinct fluorine environments which are closely related. It is likely that both peaks are caused by intermediary $PbF_x(CHN_4)_y$ complexes; it is difficult to assign each peak to a particular intermediate due to the lack of crystallographic data or reference literature. The spectral and elemental data however did allow the conclusion that the isolated white solid contained both tetrazolate and fluorine, and it was likely a mixture of partially exchanged intermediates.

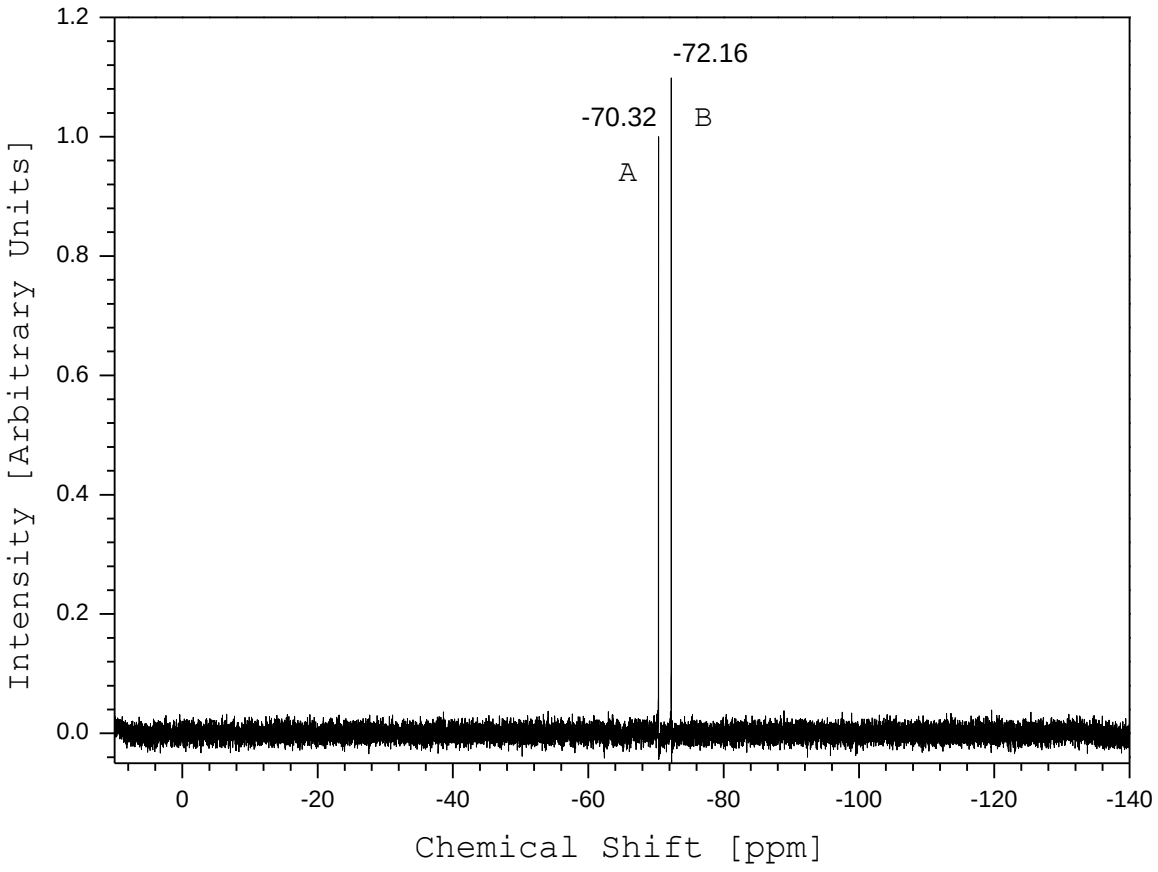

Figure 69 – ^{19}F NMR spectrum of the "{Pb(CHN$_4$)$_2$(py)$_2$}" white solid illustrating the two distinct ^{19}F environments.

The fully exchanged product could be dissolved in the supernatant solution. The pyridine solution was concentrated under dynamic vacuum and stored at -25°C. No crystals were produced and the pyridine was removed completely, leaving behind a small amount of a white solid. As pyridine seemed to be a poor crystallisation solvent for this reaction, dry acetonitrile was added and the white solid was heated into solution using a heat gun. After storage at -25°C crystals were produced; an intriguing result. Before probing the crystals with single crystal X-ray diffraction a ^{1}H NMR spectroscopic study was performed. Unfortunately the crystals proved to be 1*H*-tetrazole (figure 70). This is likely present due to decomposition of the TMS-CHN$_4$ reactant. It is possible that this occurred whilst heating the precipitate into solution during the crystallisation attempt. It is unfortunate that the fully exchanged product was not obtained, but the potential of the reaction is obvious. Tetrazolate-fluorine exchange does take place and a longer reaction time could result in the fully exchanged product.

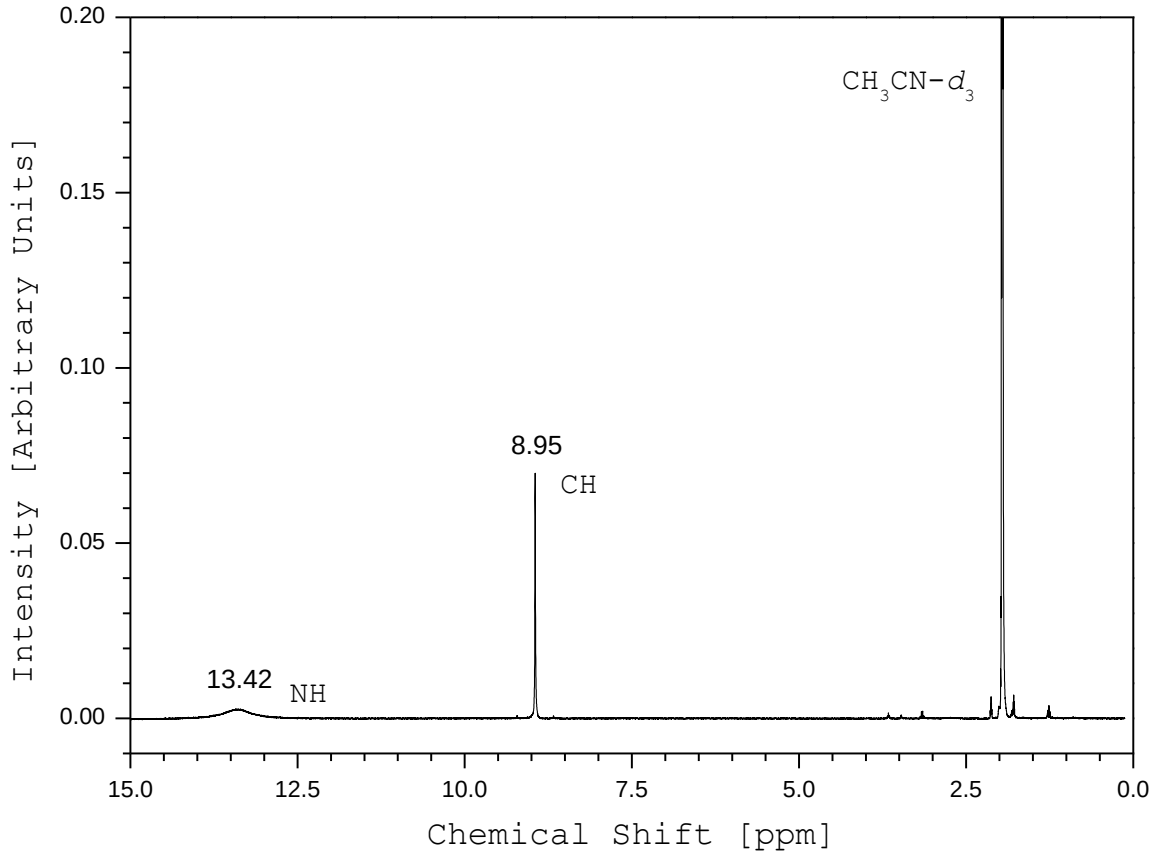

Figure 70 – ^{1}H NMR spectrum of the crystals isolated from the supernatant solution. Annotation of the proton environments indicates the crystals are 1*H*-tetrazole.

This significant result posed the question: could a homoleptic main group tetrazolato- co-ordination polymer be synthesised? The previously seen $(PPN)_2[E(CHN_4)_6]$ where E = Si, Ge and Sn all exist as monomeric systems. It can be inferred from this that these systems are co-ordinatively saturated. When the procedure is extrapolated to the low-valent main group fluorides, polymerisation occurs. This cannot be said for the recently synthesised low-valent $PPh_4[E(N_3)_3]$ where E = Ge, Sn.[80] This suggests that the azido ligand is much more effective at providing the necessary electron density to saturate the main group co-ordination centre. In addition, the tetrazole ring system is highly effective at bridging between metal centres due to its numerous modes of co-ordination.

With the three bound tetrazolato ligands, the tin centre is electronically and co-ordinatively deficient, which results in the tetrazolate rings bridging between tin centres, increasing the co-ordination number around each tin atom. This allows the electronic and co-ordinative saturation of the tin centres.

4.2.4 Low-Valent Tetrazolato- Tin and Lead Complexes

A strategy was devised to attempt the synthesis of low-valent $PPN[ECl_3]$ complexes, where E = Sn and Pb. This can be achieved through reacting PPN(Cl) with the $SnCl_2$ and $PbCl_2$ respectively. These intermediary complexes can be then reacted with an excess of $Na(CHN_4)$ in order to produce the fully exchanged $PPN[E(CHN_4)_3]$.

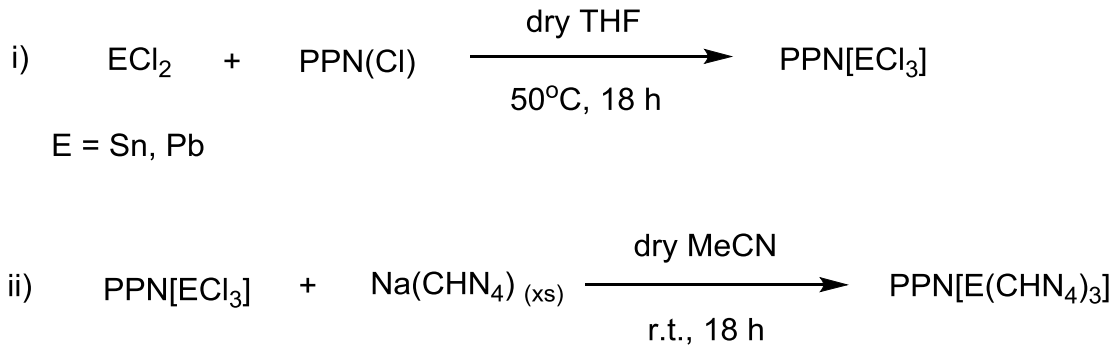

Scheme 20 – Two-step Preparation of $PPN[E(CHN_4)_3]$, where E = Sn, Pb.

Both the $PPN[PbCl_3]$ and $PPN[SnCl_3]$ were prepared in this manner. The white solids were isolated and characterised. The melting points (table 16) both suggested that a reaction has indeed occurred, as they melt at a significantly lower temperature than the PPN(Cl) and the corresponding ECl_2. In addition, both melting points are sharp transitions, which traditionally indicate the compound in question is pure. This is an important observation as the isolated solid could be simply a mixture of the two reagents.

Complex	M.p. [°C]
$PPN[SnCl_3]$	160-162(1)
$PPN[PbCl_3]$	235-237(1)
PPN(Cl)	270-272(1)
$SnCl_2$	247[83]
$PbCl_2$	501[79]

Table 16 – Comparison of melting points of $PPN[SnCl_3]$, $PPN[PbCl_3]$ and all involved reactants.

Both ^{1}H and ^{31}P NMR spectroscopy were used to further analyse the complexes. However the PPN proton environments do not observably change during the reactions, meaning that all NMR spectra show no assignable change. The absence of any other characteristic product peak results in NMR spectroscopy being unusable as an analytical tool. IR spectroscopy could identify the product when compared to the IR spectrum for the PPN(Cl) reagent.

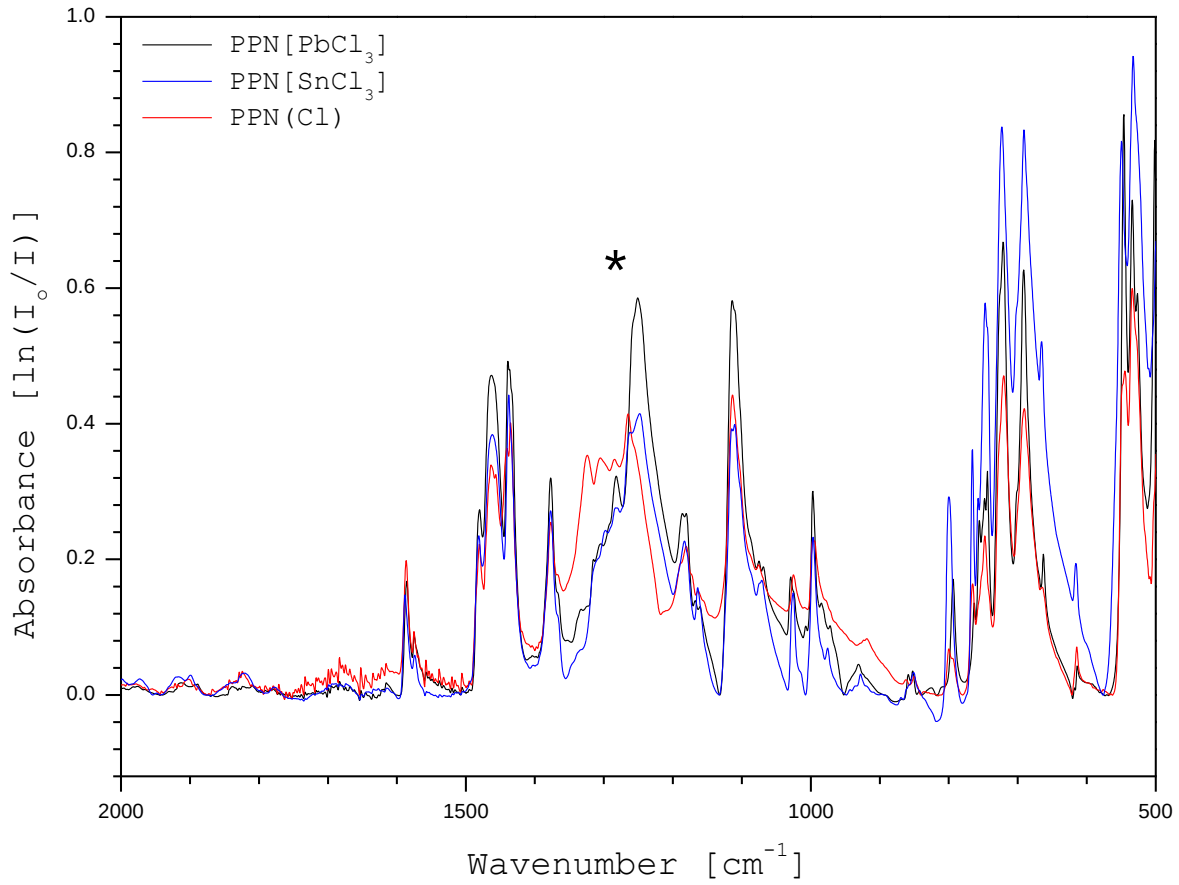

Figure 71 – IR spectral comparison between mulled PPN[$PbCl_3$], PPN[$SnCl_3$] and PPN(Cl). Figure focussed upon the IR region between 2000 cm^{-1} and 500 cm^{-1}.

However, both IR comparisons illustrate the difficulty encountered when trying to differentiate between the PPN(Cl) starting material and the expected PPN[$SnCl_3$] and PPN[$PbCl_3$] products. An obvious deviation is the broad peak represented in both products between approximately 1400 cm^{-1} and 1200 cm^{-1} (indicated by *). The PPN(Cl) peak in this region is slightly shifts to higher wavenumbers and exhibits a different peak pattern. Apart from this, the spectra are essentially identical.

The products PPN[$SnCl_3$] and PPN[$PbCl_3$] were both analysed using elemental analysis. Table 17 summarises these results. The percentages values all fall within, or very close, to the acceptable range of +/- 0.5%. The immediate reaction is to conclude that both products had been prepared in a pure fashion. Unfortunately both reactions do not have a by-product and a simple mixture of the two reactants could produce the same result. This, in combination with the previously recorded IR spectroscopy, results in a certain degree of uncertainty about the prepared (E = Sn, Pb) compounds. The only analytical evidence supporting the preparation of the PPN[ECl_3] products are their respective melting points, which cannot be solely relied upon as a diagnostic tool.

Complex	Carbon [%]		Hydrogen [%]		Nitrogen [%]		Chlorine [%]	
	Exp.	Found	Exp.	Found	Exp.	Found	Exp.	Found
PPN[$SnCl_3$]	56.62	56.29 (-0.33)	3.96	3.89 (-0.07)	1.83	1.61 (-0.22)	13.93	13.68 (-0.25)
PPN[$PbCl_3$]	50.74	50.98 (+0.24)	3.55	3.67 (+0.12)	1.64	1.71 (+0.07)	12.48	11.93 (-0.55)

Table 17 – Summary of elemental analysis data for PPN[$SnCl_3$] and PPN[$PbCl_3$].

The reaction with Na(CHN_4) was completed with both complexes in an attempt to isolate the individual PPN[$E(CHN_4)_3$] species. The first attempt was the reaction between PPN[$PbCl_3$] and an excess of the Na(CHN_4) (scheme 23)

$$\text{PPN}[ECl_3] \quad (E = Sn, Pb) \quad + \quad Na(CHN_4)_{(xs)} \xrightarrow[\text{r.t., 18 h}]{\text{dry MeCN}} \text{PPN}[E(CHN_4)_3]$$

Scheme 23 – Conversion of the trichloro- intermediates into the desired PPN[$E(CHN_4)_3$] complexes.

The reaction results in a white suspension, which is filtered to produce a white solid and a colourless solution. The white solid is analysed and shown to be the unreacted, remaining $Na(CHN_4)$ (figure 72). This is expected as it is only sparingly soluble in acetonitrile and was present in a large excess.

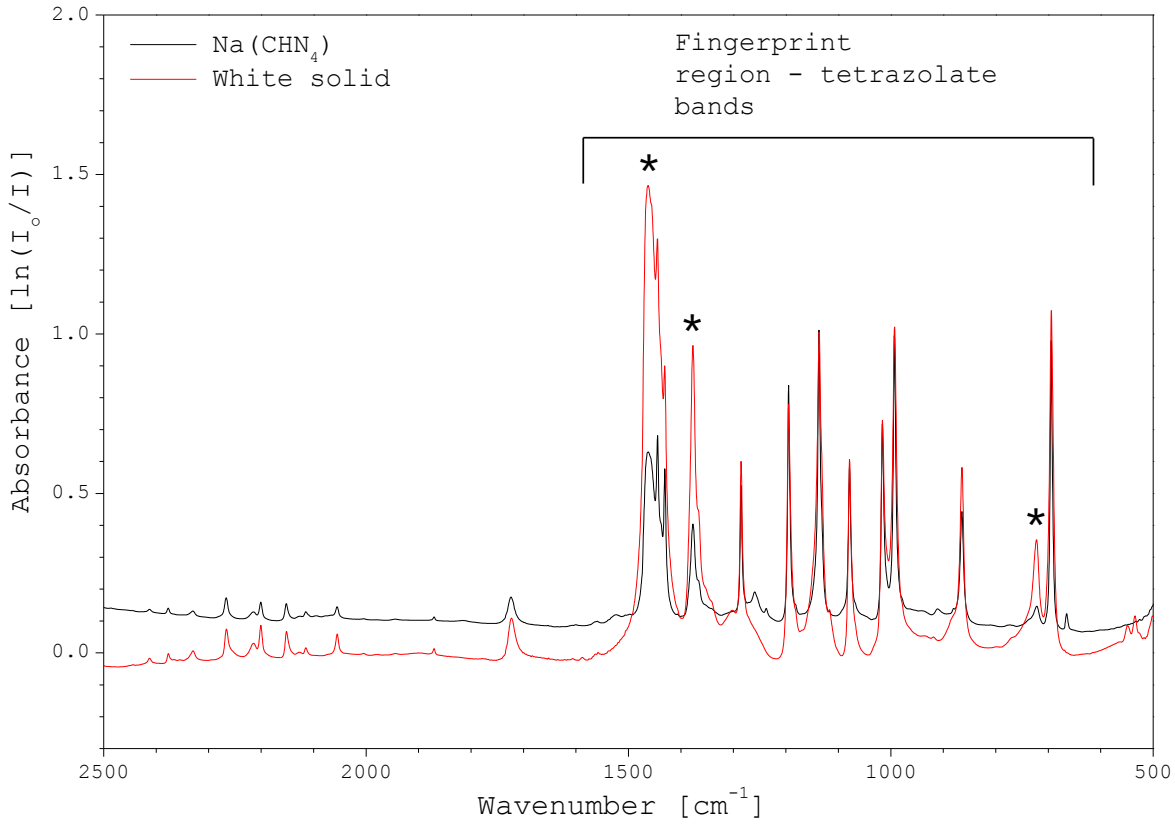

Figure 72 –IR spectral comparison of mulled $Na(CHN_4)$ and the mulled white solid between 2500 cm^{-1} and 500 cm^{-1}, illustrating that it is in fact excess $Na(CHN_4)$. Nujol bands are marked by asterisks (*).

The acetonitrile was removed from the colourless solution under vacuum, which left a white solid. This was analysed using IR spectroscopy and exhibits signs of promise (figure 73). The white solid was shown to be a definite PPN salt, which was determined by the characteristic peak at 1589 cm^{-1} (*). The IR comparison highlights that without a characteristic peak it is extremely difficult to give a definitive answer to whether the target has been produced. All PPN salts have a crowded fingerprint region which is unfortunate as the tetrazolate peaks are also found between 2000 cm^{-1} and 500 cm^{-1}.

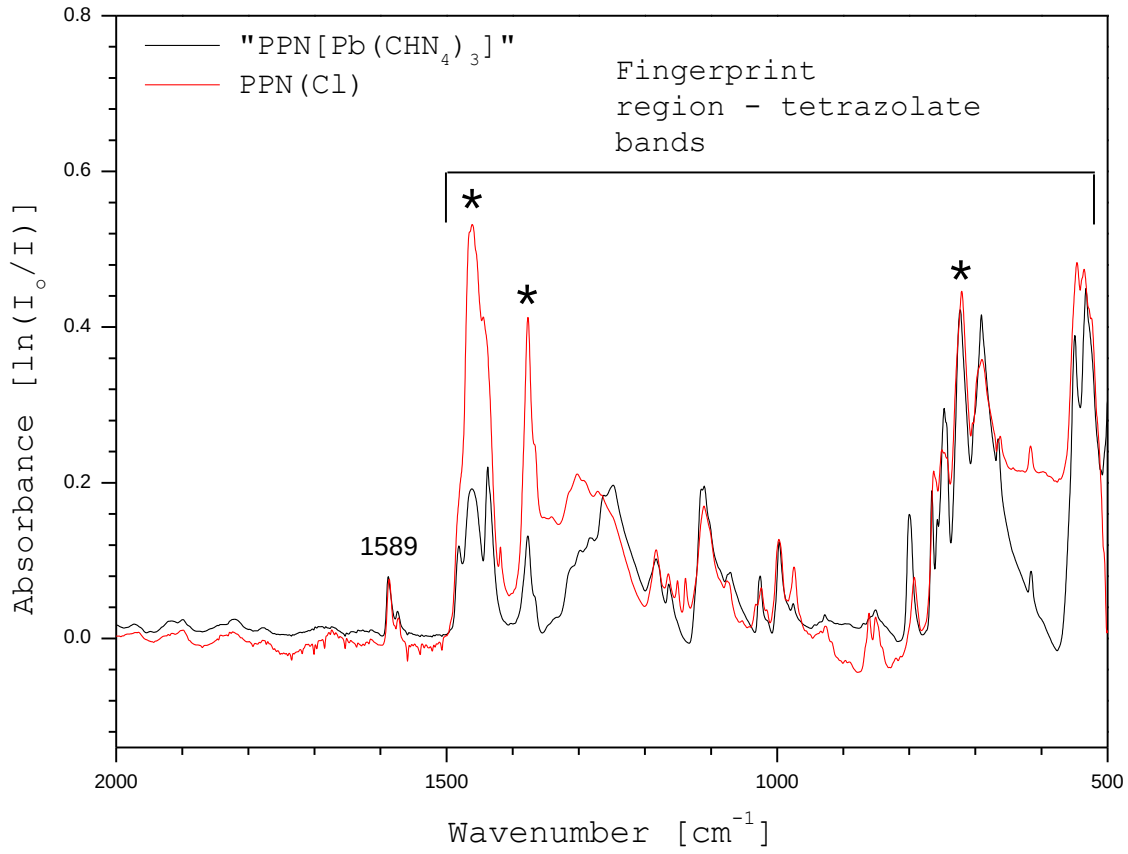

Figure 73 – IR spectra comparison of the mulled "PPN[Pb(CHN$_4$)$_3$]" and the PPN(Cl) starting material between 2000 cm^{-1} and 500 cm^{-1}. Nujol bands are marked by asterisks (*).

^{1}H NMR spectroscopy can be used as a diagnostic tool as the tetrazolate proton shifts dependent on its environment. As shown in figure 74 the tetrazolate environment has shifted from 9.00 ppm, which could correspond to the Na(CHN$_4$) starting material, to 8.37 ppm (*). Na(CHN$_4$) is insoluble in DCM therefore a direct comparison in the ^{1}H NMR spectrum is not possible. The "PPN[Pb(CHN$_4$)$_3$]" spectrum has just one tetrazolate environment despite there being three tetrazolato ligands present in the complex. This suggests that each proton is symmetrically related. It could also be explained by the single exchange of a tetrazolate ring for a chloride ligand, leaving the remaining two chlorides unreacted. This is possible but unlikely as the large excess of Na(CHN$_4$), in conjunction with the high temperature used, result in moderately extreme reaction conditions. This should result in the production of the fully exchanged product. A partially exchanged product could be explained by the poor solubility of lead-based reactants. This would limit the amount of PbCl$_2$ in solution, therefore slowing the reaction.

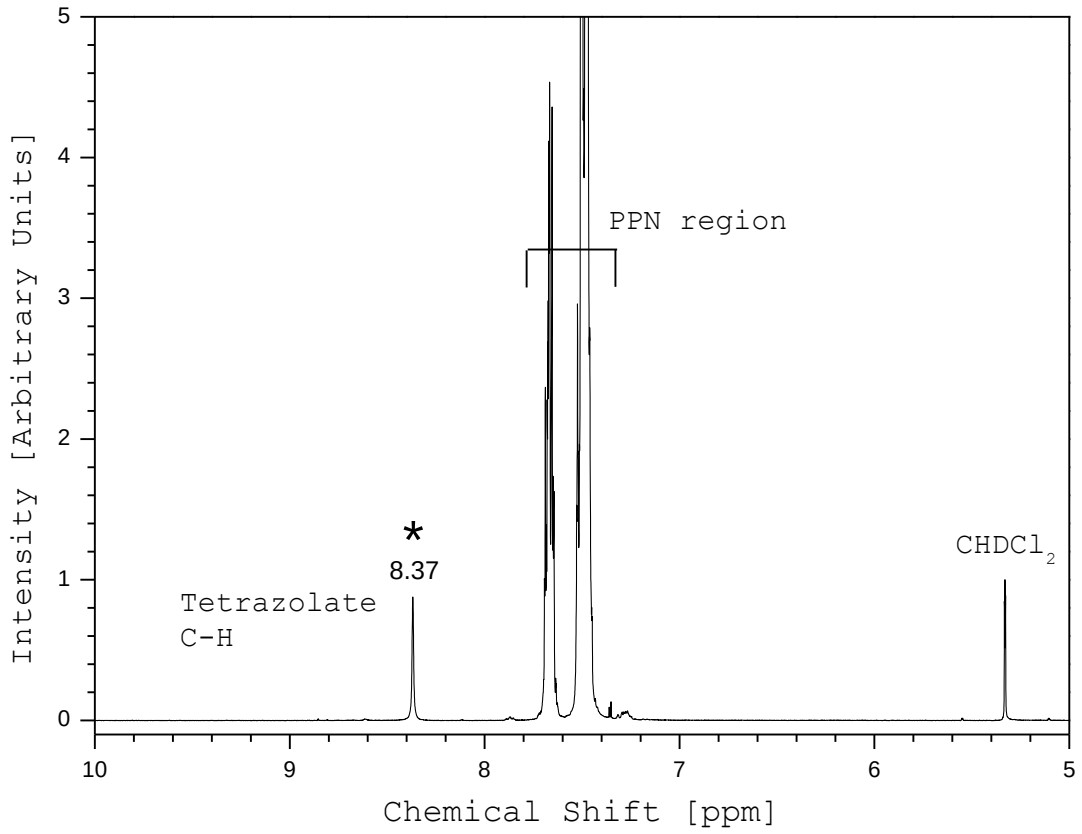

Figure 74 – ^{1}H NMR spectrum of "PPN[Pb(CHN$_4$)$_3$]" in DCM-*d$_2$* between 10.00 ppm and 5.00 ppm. New tetrazolate proton environment at 8.37 ppm (*) indicates a reaction had taken place.

A possibility is that the high concentration of unreacted PPN(Cl) in the "PPN[PbCl$_3$]" could react with the Na(CHN$_4$) to produce PPN(CHN$_4$). Comparison of the ^{1}H NMR spectrum of "PPN[Pb(CHN$_4$)$_3$]" and PPN(CHN$_4$) does not support this hypothesis (figure 75). The product peak is at 8.37 ppm (*) whilst the PPN(CHN$_4$) exhibits a peak at 8.21 ppm (*), illustrating the difference between the two compounds. This suggests that the chloride-tetrazolate exchange has occurred at least once, if not to completion. In order to fully characterise the prepared complex it is necessary to grow crystals to probe with X-ray diffraction.

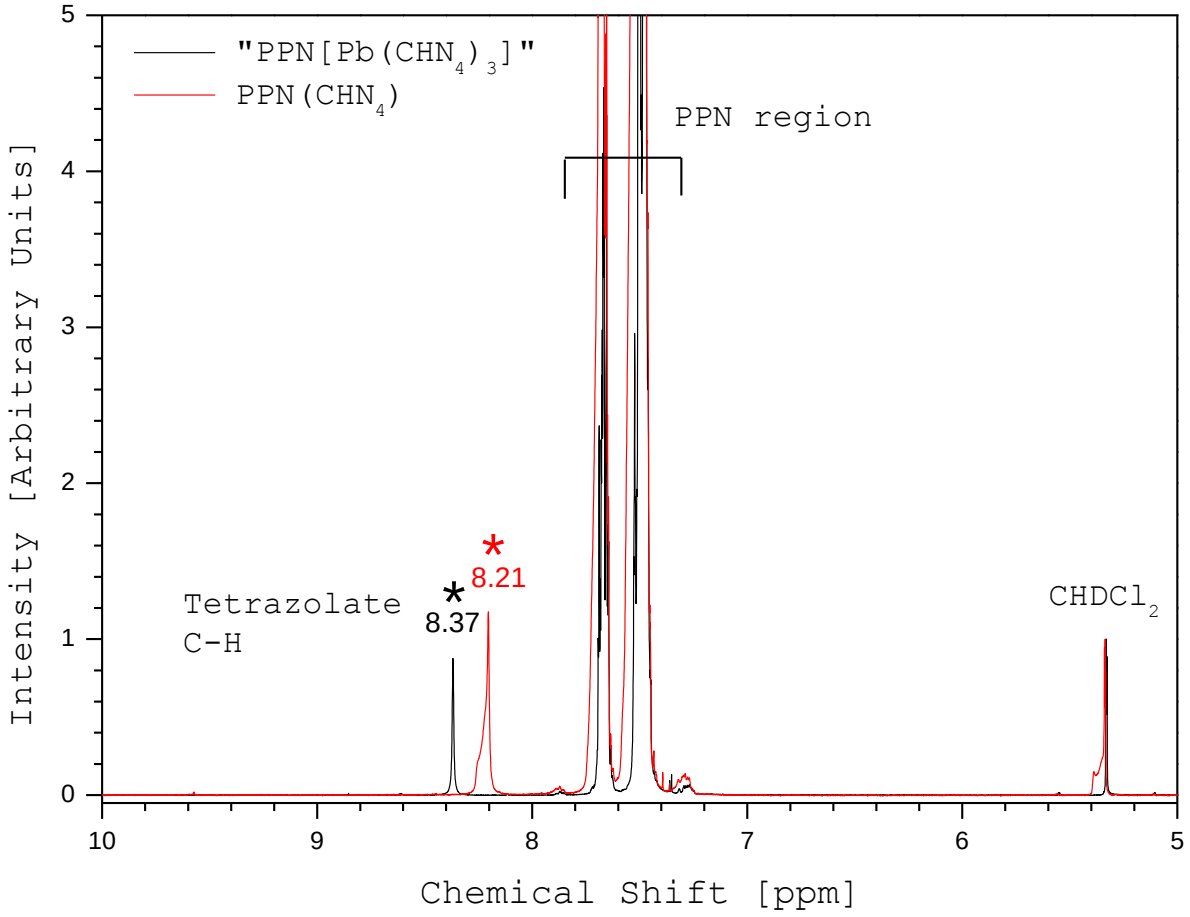

Figure 75 – ^{1}H NMR spectral comparison between "PPN[Pb(CHN$_4$)$_3$]" and PPN(CHN$_4$) between 10.00 ppm and 5.00 ppm.

Crystal growth was attempted in acetonitrile, THF and DCM solutions but no solvent system yielded the product in a crystalline form. This was again the case with the analogous preparation of "PPN[Sn(CHN$_4$)$_3$]". Similarly, the reaction proceeded via a white suspension that was filtered to separate the unreacted Na(CHN$_4$) from the product acetonitrile solution. On this occasion the acetonitrile was removed under vacuum to leave an oil. Freeze-thaw drying was attempted to dry the oil further but it was not successful. The oil was analysed using ^{1}H NMR spectroscopy.

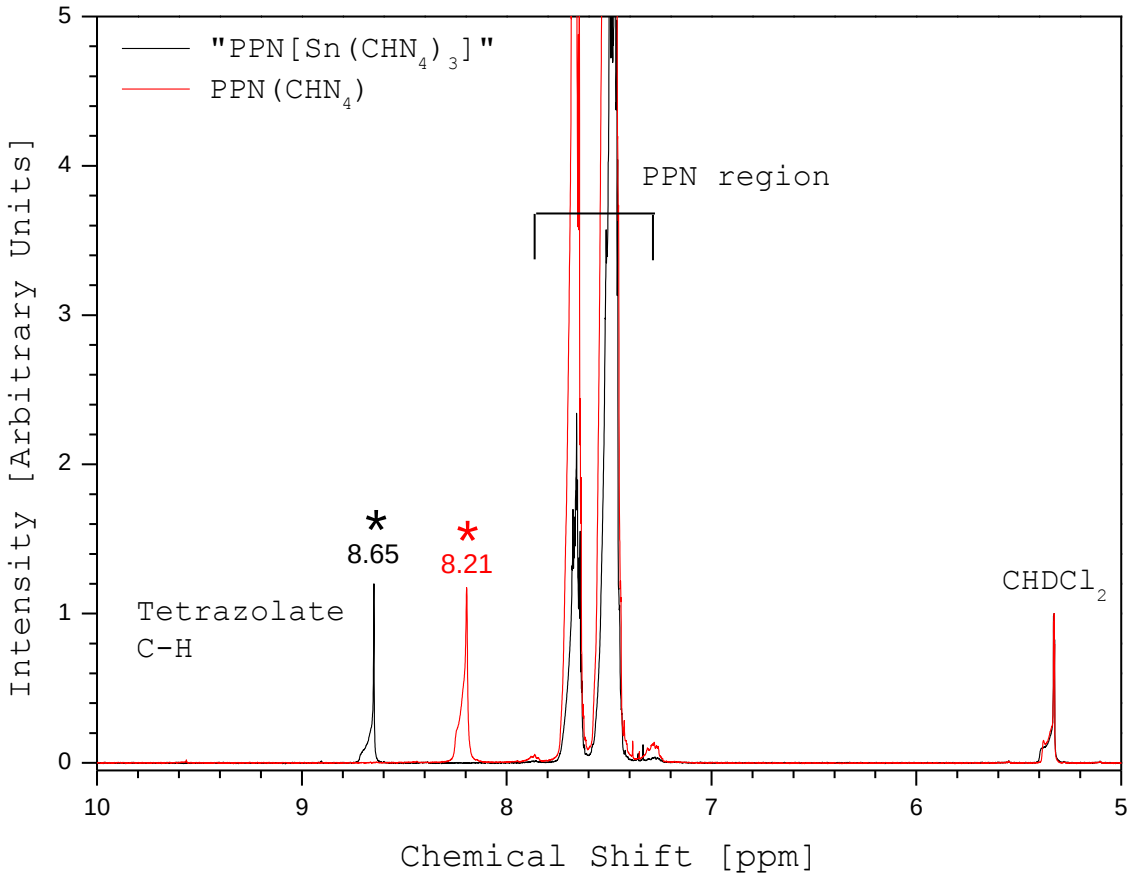

Figure 76 – ^{1}H NMR spectral comparison of "PPN[Sn(CHN$_4$)$_3$]" and PPN(CHN$_4$) between 10.00 ppm and 5.00 ppm. N.B asymmetric band deformation is due to the poor shimming of the magnetic field.

The "PPN[Sn(CHN$_4$)$_3$]" oil possesses a peak at 8.65 ppm. This is significantly further downfield in comparison with the "PPN[Pb(CHN$_4$)$_3$]" tetrazolate peak, and could indicate further exchange. It is different from both PPN(CHN$_4$) and Na(CHN$_4$), and is an intriguing result. However, again a problem arises with crystallisation. The inability to crystallise both products is due to the impurity and lack of characterisation of their reagents. Without the ability to assign the nature of each reagent conclusively, it is impossible to fully understand the nature of the reaction.

What is needed is a general preparation which begins with unequivocally pure reagents; that results in the synthesis of a product that is easily separated and purified, alongside a by-product that is easily removed. The successful use of TMS-CHN$_4$ during the preparation of (PPN)$_2$[Sn(CHN$_4$)$_6$] indicates that it could be the key tetrazolato ligand transfer reagent needed for the preparation of low-valent main group homoleptic tetrazolato complexes.

4.2.5 Preparation of a Homoleptic Low-Valent Tin Co-ordination Polymer

Using the serendipitous preparation of the {$Sn(CHN_4)_2(py)$} co-ordination polymer as a guideline, the synthesis of a homoleptic analogue was attempted. TMS-CHN_4, SnF_2 and $PPh_4(CHN_4)$ were reacted together in dry THF. The $PPh_4(CHN_4)$ transfer reagent replaced the previously used $PPN(CHN_4)$ due to the difficulty encountered crystallising the PPN salts of the analogous $[E(N_3)_3]^-$ complexes (where E = Sn, Ge).[80] The use of the PPh_4 cation ensured that the purified complex was easily isolated.

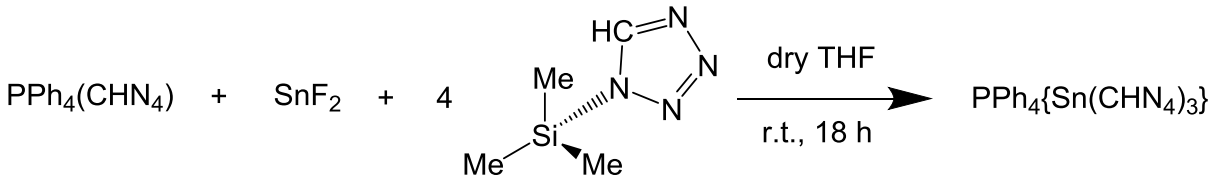

Scheme 24 – Preparation of the homoleptic $PPh_4\{Sn(CHN_4)_3\}$ co-ordination polymer.

The solvent was removed under vacuum which left the crude product as a white solid. This solid was analysed using ^1H NMR spectroscopy. The proton peak at 8.58 ppm (*) has deviated sufficiently from the proton environment of the tetrazolate transfer reagent $PPh_4(CHN_4)$ (*) that it can be attributed to a reaction having taken place. This was an encouraging analytical result, but a full data set required purification.

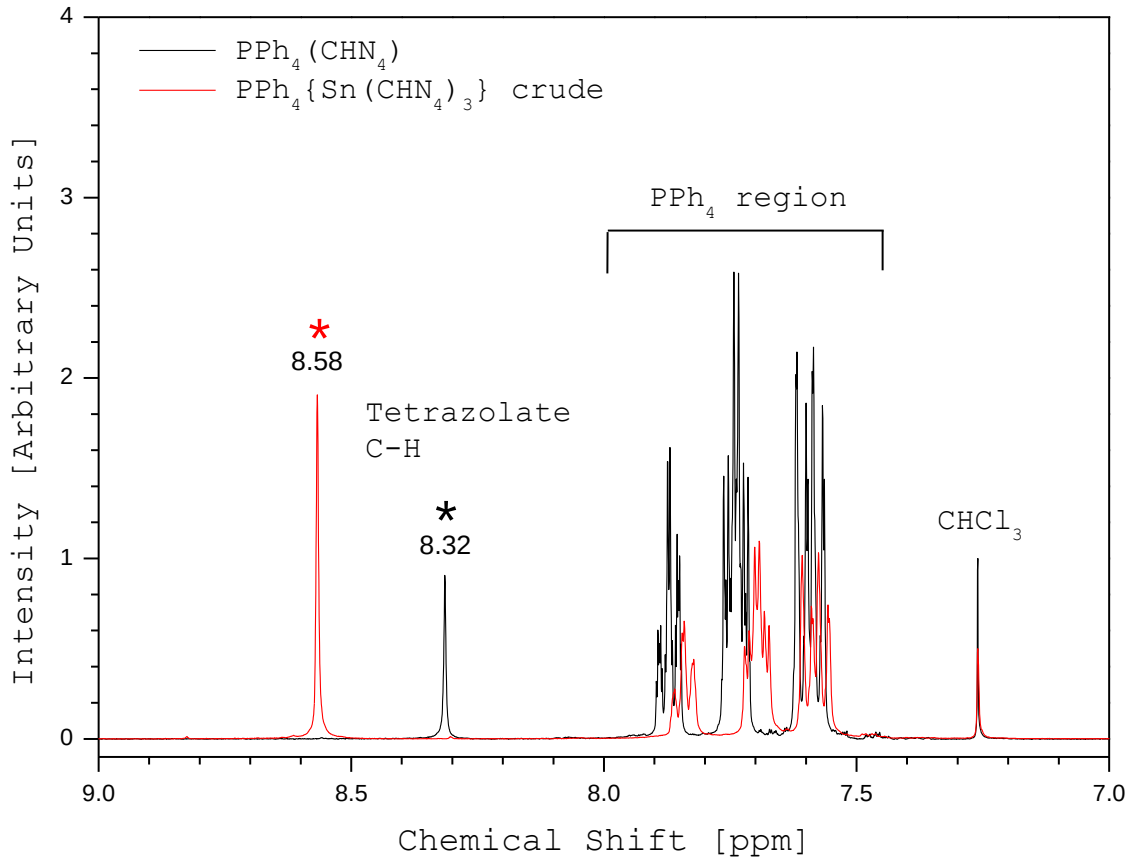

Figure 77 – ^{1}H NMR spectral comparison between the crude $PPh_4\{Sn(CHN_4)_3\}$ co-ordination polymer and the $PPN(CHN_4)$ starting material between 9.00 ppm and 7.00 ppm.

Crystallisation of the product was achieved using dry THF to dissolve the white solid, then adding a small amount of anti-solvent, in this case dry Et_2O. The colourless crystals were isolated and probed with IR and ^{1}H NMR spectroscopy. The IR spectrum (figure 78) shows that the obtained crystals are a PPh_4 containing salt, due to the peak at 1585 cm^{-1}. The fingerprint region shows significant variation from that of the tetrazolate reagent at 1452 cm^{-1}, 1224 cm^{-1}, 1043 cm^{-1} and 891 cm^{-1}. It is extremely difficult to assign these peaks to a particular bond vibration; however it is a strong indication that a reaction has taken place.

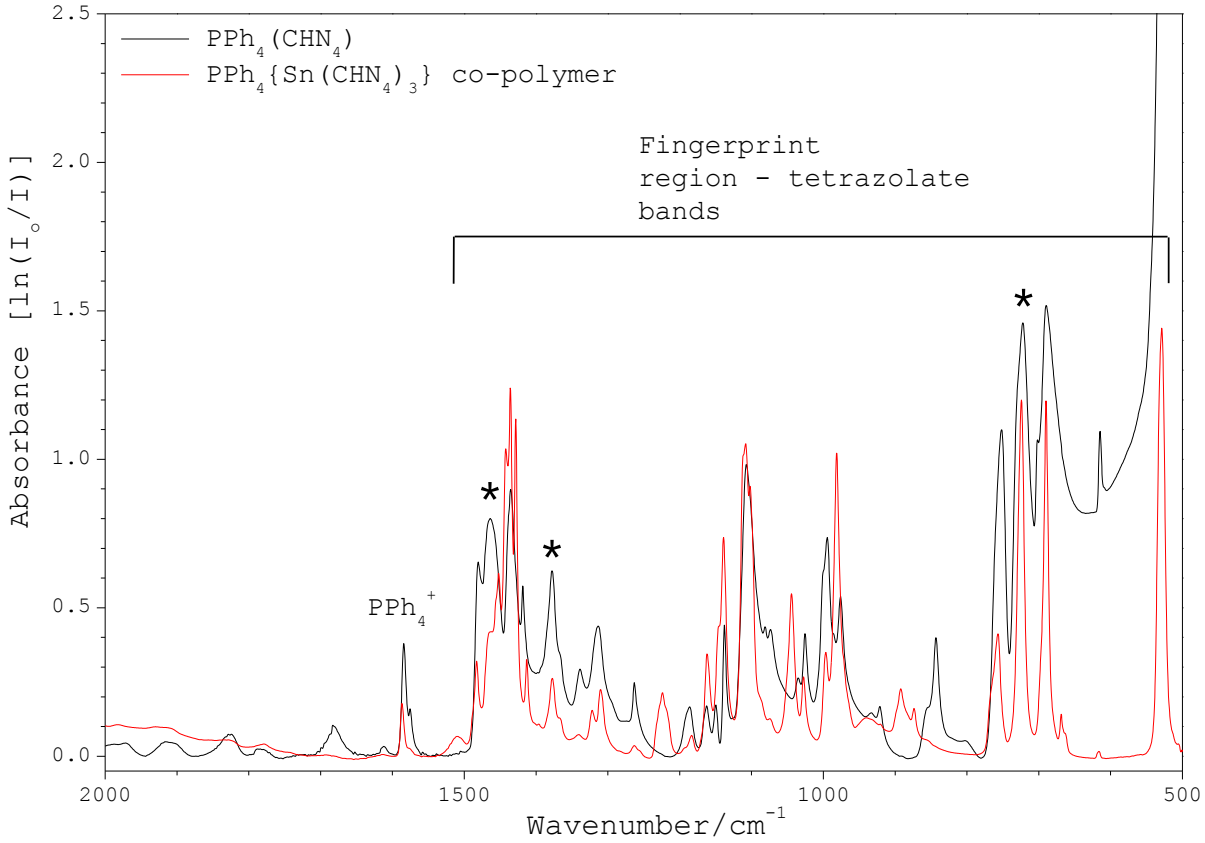

Figure 78 – Nujol mull IR comparison between the crystalline $PPh_4\{Sn(CHN_4)_3\}$ and $PPh_4(CHN_4)$ between 2000 cm^{-1} and 500 cm^{-1}. Nujol bands are asterisked (*).

The ^1H NMR spectrum also provides evidence for a reaction having occurred. It exhibits a single tetrazolate environment at 8.74 ppm, indicating that all tetrazolate ligands within the complex are equivalent. The peak position is unlike any previously prepared tetrazolate-containing compound, a further piece of evidence for the production of the desired complex. The ^1H NMR comparison spectrum shown in figure 79 illustrates the significant shift from the tetrazolate environment assigned to the reagent $PPh_4(CHN_4)$. An additional observation is the difference in peak position for $PPh_4(CHN_4)$ caused by the use of a different deuterated solvent (8.31 ppm in $CDCl_3$ compared to 8.10 ppm in CH_3CN-d_3). The effect of solvent upon the tetrazolate proton environment is substantial, and could indicate that the strict solvent control can influence the reaction in a considerable manner. The tetrazolate peak corresponding to the crystalline material differs from the crude product significantly; it is possible that the crude product contained a high concentration of intermediate complexes that were removed by crystallisation.

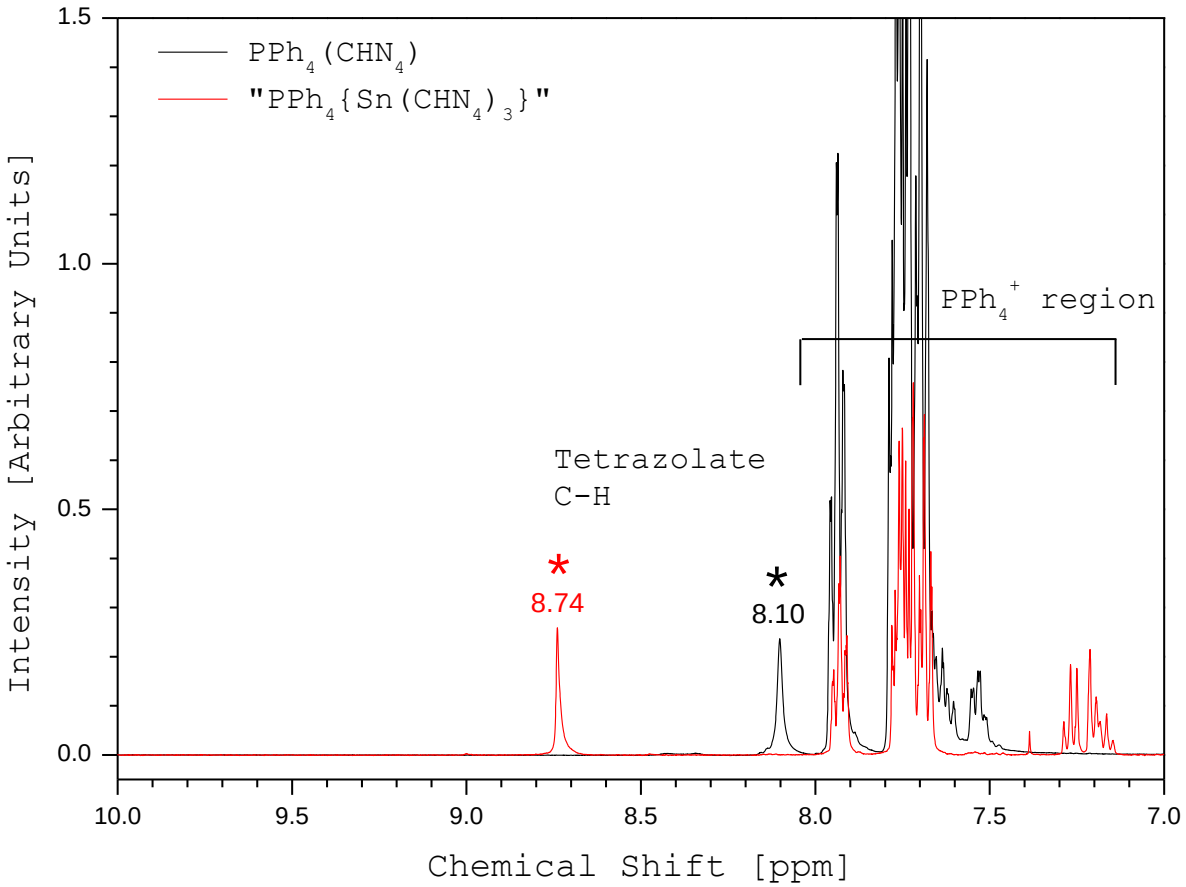

Figure 79 – ^{1}H NMR spectral comparison between 10.0 ppm and 7.00 ppm of the crystalline $PPh_4\{Sn(CHN_4)_3\}$ co-polymer and the $PPh_4(CHN_4)$ reactant.

The crystals were subsequently probed with single crystal X-ray diffraction. Again rather than the preparation of a monomeric species a co-ordination polymer had been synthesised. In this case it is a homoleptic $[Sn(CHN_4)_3]_n^-$ polymer, containing bridging tetrazolyl ligands that join adjacent co-ordination centres via a N(1)-N(4) bridging mechanism. This bridging occurs in two dimensions, forming a 2D polymeric sheet network. It is an anionic polymer, in which the charge is balanced by the PPh_4^+ cations. Also present in the asymmetric unit is a THF molecule. The extended packing shows the layers of the polymer separated by the PPh_4 cations and THF molecules (figure 80). This arrangement is almost certainly electronically driven in order to maximise the charge separation between the negatively charged polymer sheets.

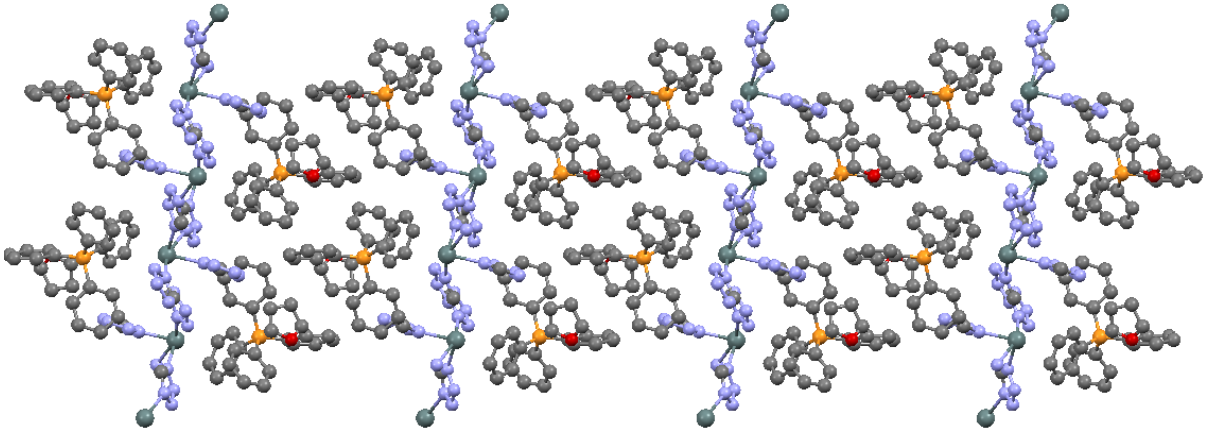

Figure 80 – Ball and stick diagram showing a projection of the packing of the $\{PPh_4[Sn(CHN_4)_3]\}_n$ co-ordination polymer along the *b* axis. Image generated using Mercury®.

Each tin co-ordination centre is co-ordinated by five tetrazolate ligands, four in the equatorial plane and one in an axial position (figure 81). The co-ordination centre again shows a distorted square-based pyramidal geometry. The high charge density of the tine lone pair forces the bonding electrons out of the plane, minimising the repulsion. Immediate inspection indicates that all five individual tetrazolate groups bind via the N_1 atom, which has been observed in all previously synthesised homoleptic tin complexes.

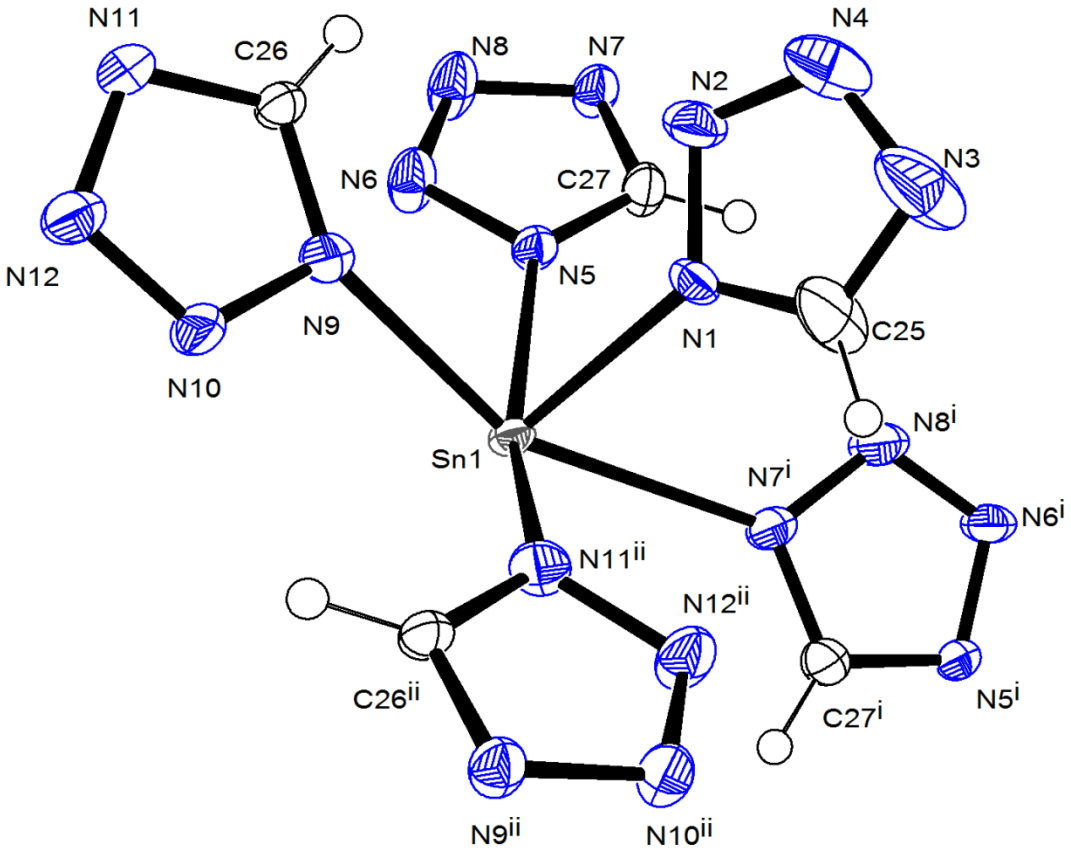

Figure 81 – Ellipsoid plot illustrating the co-ordination geometry at the tin centre of $\{PPh_4[Sn(CHN_4)_3]\}_n$. Image generated using ORTEP®.

As shown in table 18 the bond lengths within the co-ordination centre are highly flexible. It was expected that all equitorial bonds would be roughly similar, with the axial bond length (Sn(1)-N(3)) exhibiting some deviation due to its different binding position.

Bond	Bond Length [Å]
Sn_1-N_1	2.255(5)
Sn_1-N_5	2.405(5)
Sn_1-N_9	2.348(5)
Sn_1-N_{11}^{ii}	2.532(4)
Sn_1-N_7^{i}	2.532(4)

Table 18 – Bond lengths corresponding to each tin co-ordination centre within $\{PPh_4[Sn(CHN_4)_3]\}_n$ (see figure 81).

In a similar fashion to the bond lengths, the bond angles for the homoleptic co-ordination polymer are highly varied, in a similar fashion to the pyridine-containing analogue (table 13). The expected bond angles for a square-based pyramid geometry is 90°, and table 19 illustrates the extent of the variation. Whilst repulsive effects due to the tin lone pair were expected the flexibility observed was surprising. The origin of this flexibility is unclear.

Bond Angle	Angle [°]	Deviation from 90°
N_5-Sn_1-N_9	83.74(16)	-6.26
N_5-Sn_1-N_7^{i}	86.46(16)	-3.54
N_7^{i}-Sn_1-N_{11}^{ii}	94.44(16)	+4.44
N_9-Sn_1-N_{11}^{ii}	85.85(16)	-4.15
N_{ax}-Sn_1-N_1	78.41(average)	-11.59

Table 19 – Bond angles corresponding to each tin co-ordination centre within $PPh_4\{Sn(CHN_4)_3\}$ (see figure 81).

It could be due to the charged nature of the polymeric system. The pyridine analogue is charge neutral, which could result in a rigid system. It is possible that the anionic nature of the polymer causes the bridging tetrazolate bonds to be dynamic, stretching and bending to a further degree in comparison to the neutral pyridine network.

Another possibility is the difference observed in the extended packing. Rather than the bilayer orientation of the pyridine-containing polymer, the $[Sn(CHN_4)_3]_n^-$ example exhibits an undulated sheet in which the axial tetrazolate ligand alternates between being above and below the equitorial plane. This more flexible organisation could explain the observed variations in the bond lengths and bond angles.

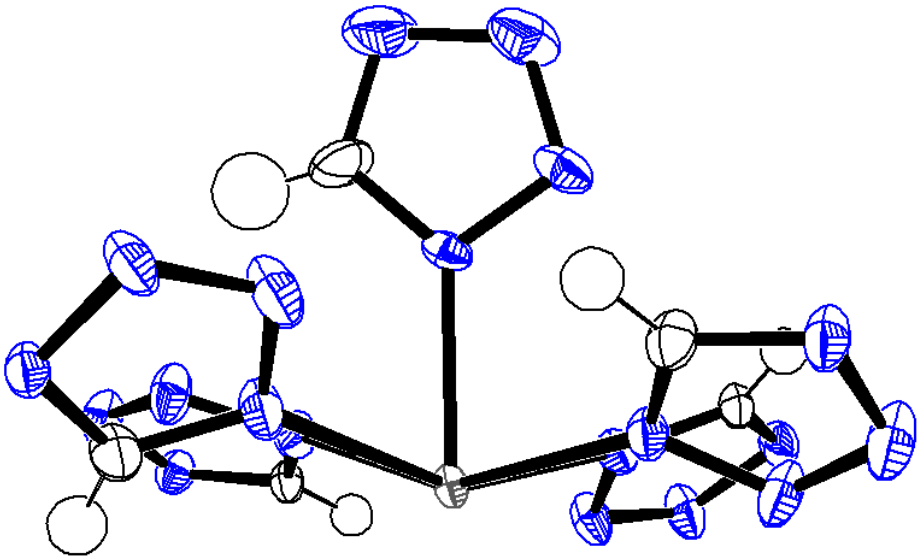

Figure 82 – Ellipsoid plot representing the distorted square-based pyramid geometry at each tin centre within $\{PPh_4[Sn(CHN_4)_3]\}_n$. Distortion is caused by the lone pair located at the tin centre. Image generated using ORTEP®.

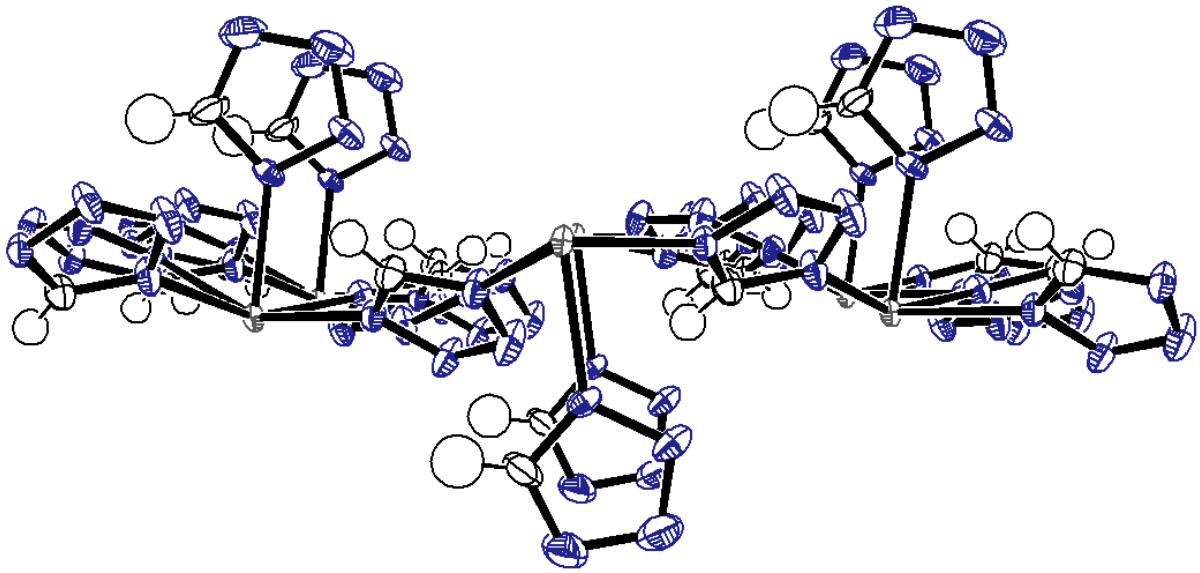

Figure 83 – Ellipsoid plot illustrating the undulating extended 2D sheet of the $PPh_4\{Sn(CHN_4)_3\}$ co-ordination polymer. The plot is viewed along the xy plane of the crystal lattice. Image generated using ORTEP®.

This is the first known example of an anionic homoleptic tetrazolato- main group co-ordination polymer. For this reason it is difficult to find comparative complexes in the literature. However neutral homoleptic examples are known, such as $[Zn(CHN_4)_2]_n$.[13] This co-ordination polymer also exhibits N(1)-N(4) bridging tetrazolyl ligands, but unlike $\{PPh_4[Sn(CHN_4)_3]\}_n$ it has a tetrahedral co-ordination geometry at each Zn centre. With no tin lone pair this geometry remains undistorted, with all bond angles at the co-ordination centre close to 109.5°. However the anionic nature of $[Sn(CHN_4)_3]_n^-$ and the influence of the Sn(II) centre requires a highly specific example for direct comparison, of which none exist.

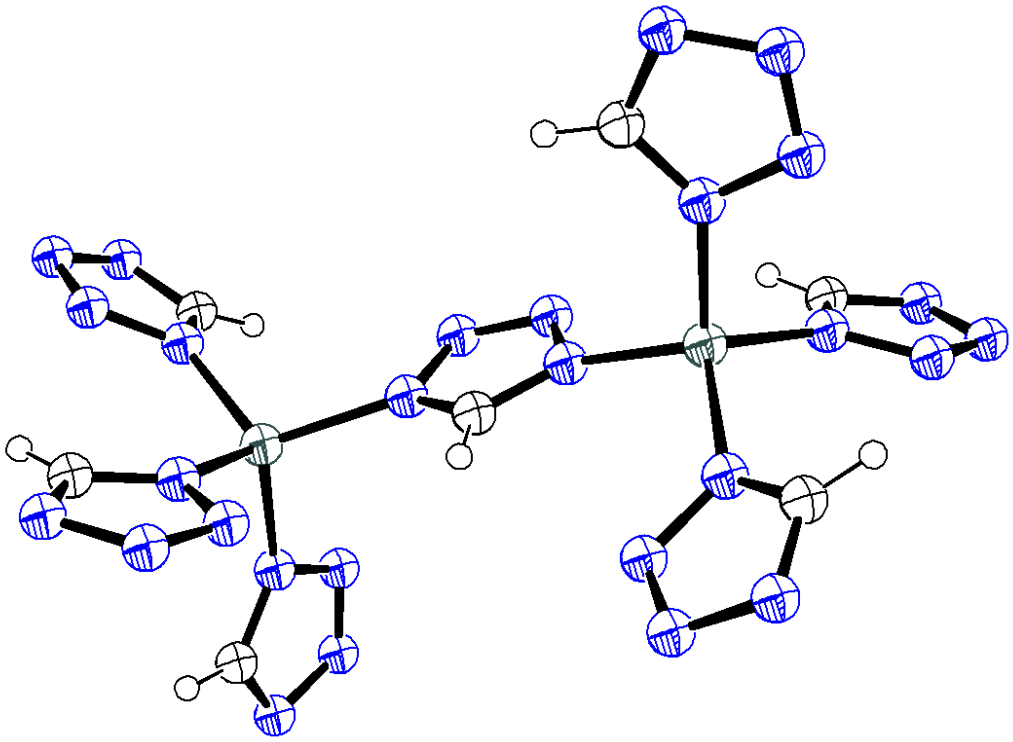

Figure 84 - Ball and stick plot illustrating two bridged tetrahedral co-ordination geometries within the $[Zn(CHN_4)_2]_n$ co-ordination polymer.

4.2.6 Extrapolation to Antimony(III) and Bismuth(III) Fluoride

This preparative method was subsequently applied to both antimony(III) and bismuth(III) fluoride.

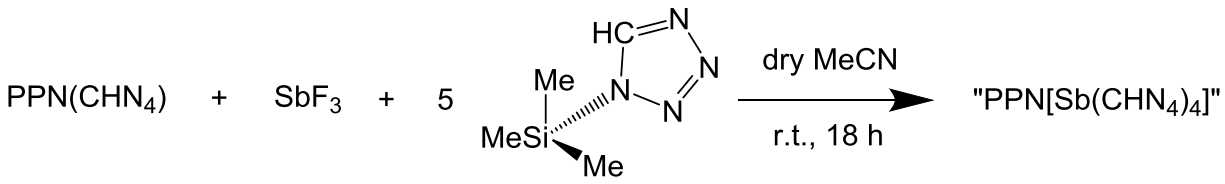

Scheme 25 – Attempted preparation of "PPN[Sb(CHN$_4$)]".

The first attempt utilised SbF_3. The reaction suspension was stirred overnight at room temperature, and then all solvent was removed under dynamic vacuum to leave a white solid. The crude product was analysed using ^{1}H NMR spectroscopy.

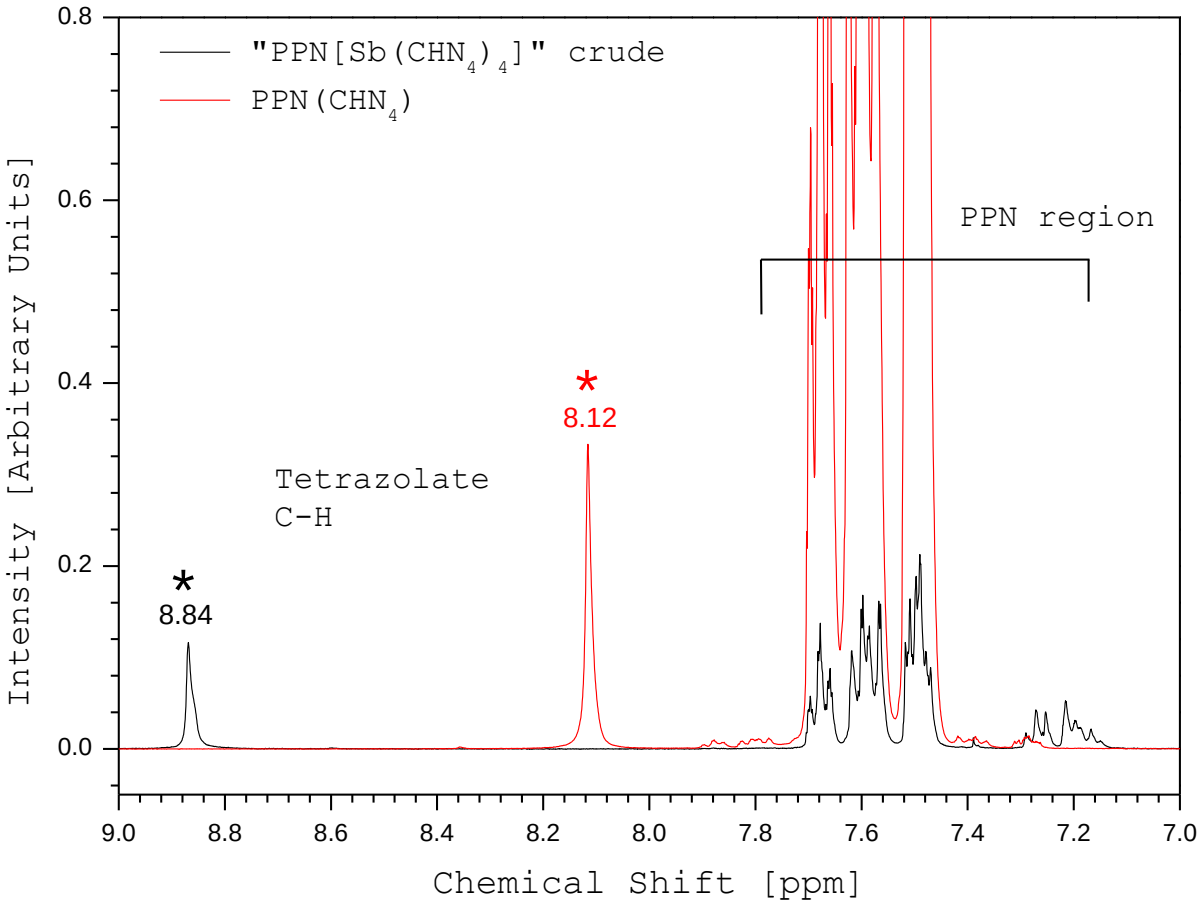

Figure 85 – ^{1}H NMR spectral comparison of the crude "PPN[Sb(CHN$_4$)$_4$]" and PPN(CHN$_4$) between 9.00 ppm and 7.00 ppm.

The ^{1}H NMR spectrum of the white solid has a single tetrazolate environment. The comparison to the $PPN(CHN_4)$ ^{1}H NMR spectrum shown in figure 85 indicates that a reaction has indeed taken place, with the proton environment shifting from 8.10 ppm to the crude product position at 8.84 ppm. The white solid was recrystallised using dry THF, producing colourless, block crystals. Under analysis, the crystals were shown to possess a unique IR spectrum, deviating considerably from the starting material. The immediately obvious difference is the broad peak located at 1323 cm^{-1} in the product. In comparison to the $PPN(CHN_4)$ reagent the entire peak system shifted to higher wavenumbers. In addition the peak pattern became more defined, presenting seven individual peaks. The product spectrum also deviates at 1191 cm^{-1}, 1149 cm^{-1}, 1043 cm^{-1} and 784 cm^{-1}. This is further evidence for the isolation of a product complex.

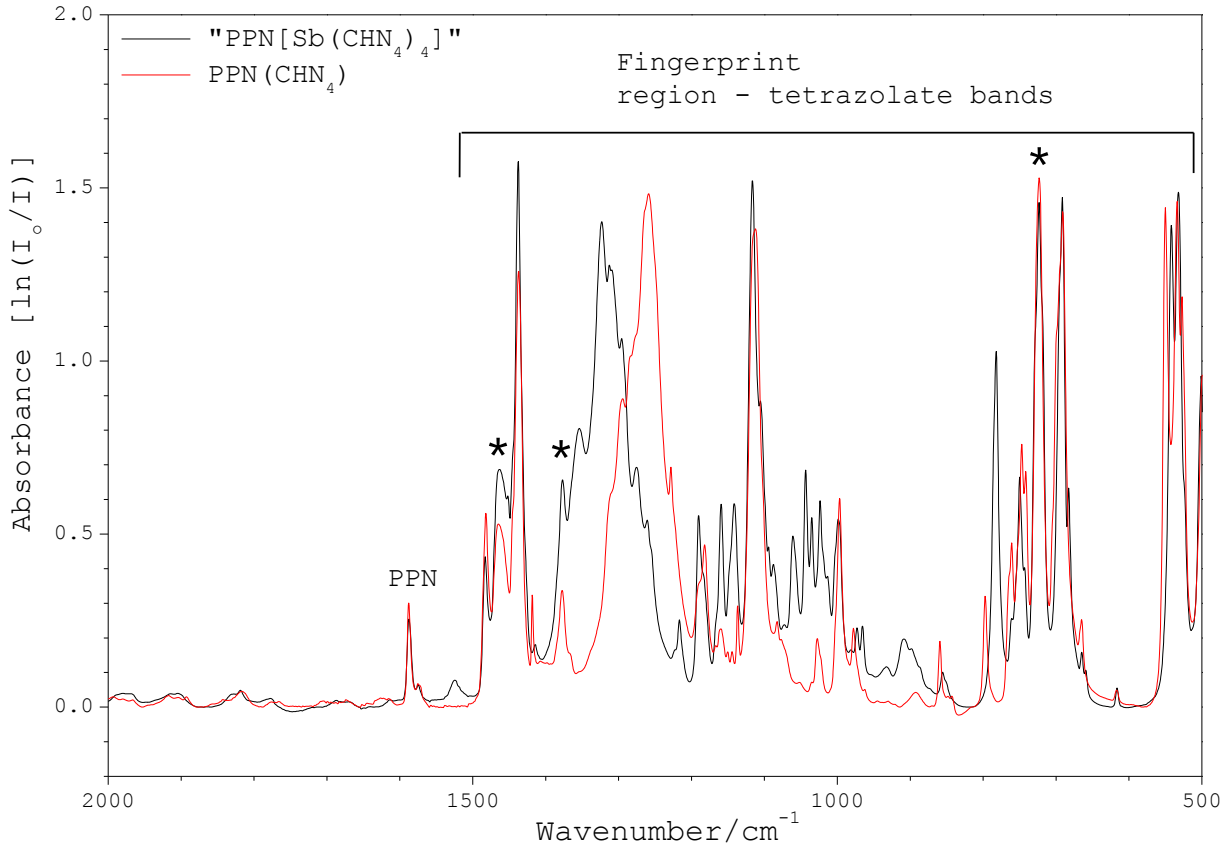

Figure 86 –IR spectral comparison of mulled "$PPN[Sb(CHN_4)_4]$" and the $PPN(CHN_4)$ starting material between 2000 cm^{-1} and 500 cm^{-1}. Nujol bands are marked by asterisks (*).

Further analysis using ^{1}H NMR spectroscopy revealed the true proton environment of the purified product is at 8.72 ppm (figure 87), rather than the 8.84 ppm as show by the ^{1}H NMR

spectrum for the crude solid. The cause for this displacement is likely the removal of all by-products and unreacted reactants. The presence of these could disrupt the tetrazolate protons sufficiently that it is observed in the spectrum.

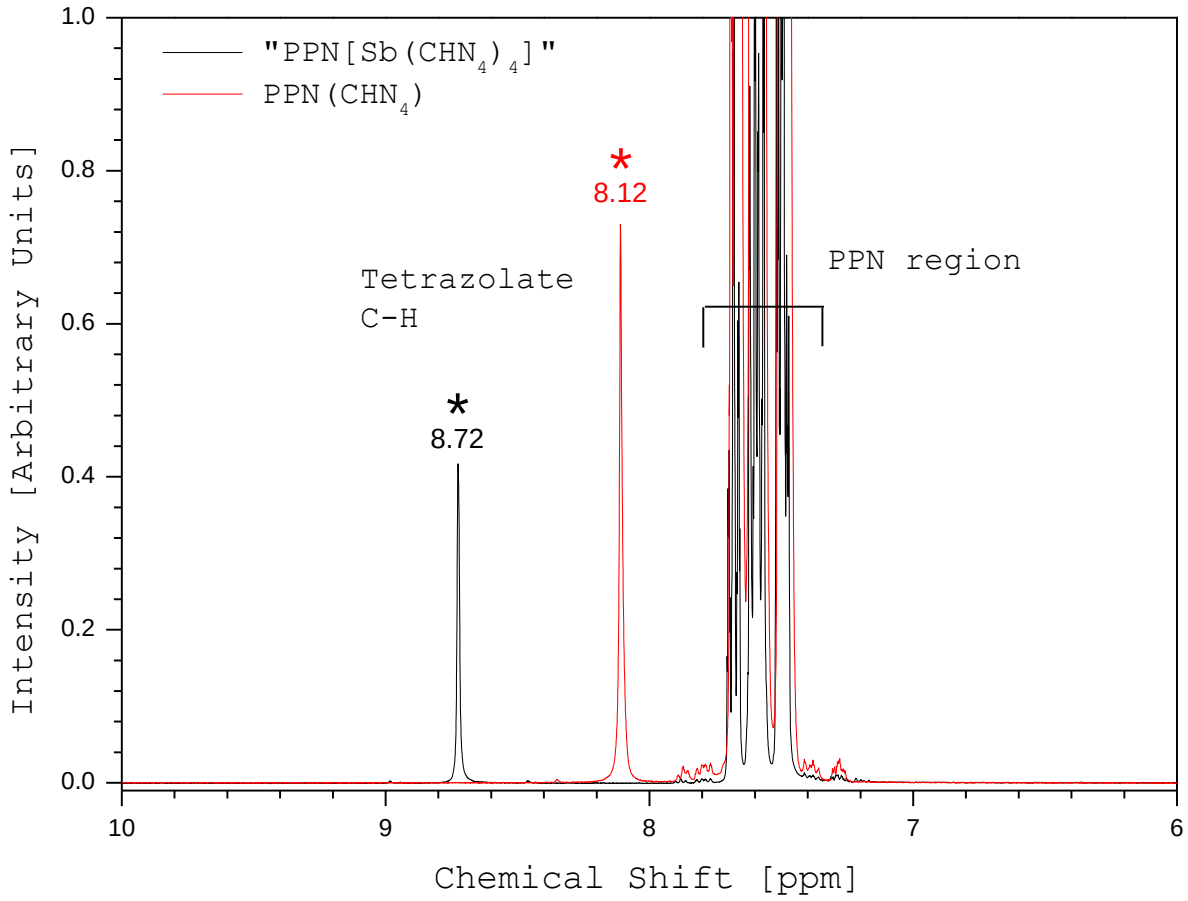

Figure 87 – ^{1}H NMR spectral comparison between 10.00 ppm and 6.00 ppm of the crystalline "PPN[Sb(CHN$_4$)$_4$]" and the PPN(CHN$_4$) starting material.

It has a single proton environment indicating that if multiple tetrazolate ligands are present, as expected, they are all symmetrically related. This aligns with what was observed when analysing the previously isolated PPh$_4${Sn(CHN$_4$)$_3$} polymeric network. This is highly encouraging as the synthesis of an antimony based co-ordination polymer would be a fascinating result. The crystals were subsequently probed using single crystal X-ray diffraction. What was found was highly surprising; a fluorine atom remained un-exchanged, allowing a unique complex to form.

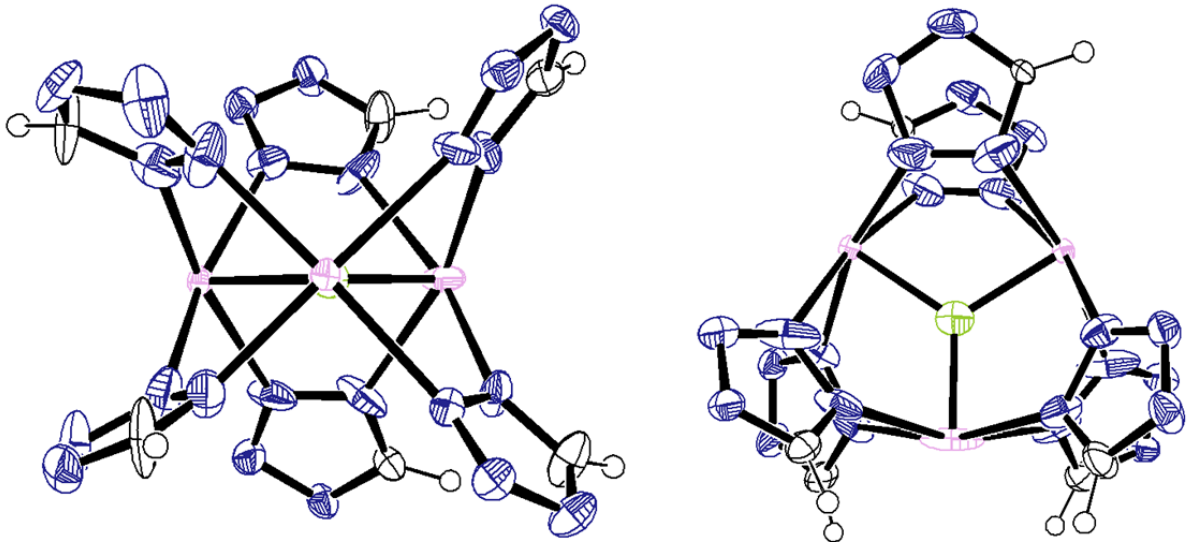

Figure 88 – Diagram illustrating the complexity of the $[Sb_3(CHN_4)_6F]^-$ anion structure. The PPN cation has been removed for clarity. Figure produced using ORTEP®.

As the above figure shows the anion contains three antimony atoms, bound around a single fluorine in a trigonal planar fashion. Each antimony atom forms a square-based pyramid, with the four equatorial bonds occupied by four tetrazolate ligands and the axial bond co-ordinated to the central fluorine. The 12 total equitorial bonds in the cluster are occupied by the tetrazolate ligands which bridge between the co-ordination centres via N_1, N_4 bridging. It is this ability of the tetrazolate group to bind to multiple metal centres that would provide the necessary flexibility to form an extended MOF framework. However, rather than its bridging nature facilitating the formation of a co-ordination polymer, the tetrazolate ligands bind together adjacent antimony atoms to result in the compact, symmetrical and cage-like anion. Each co-ordination centre possesses a (2+) charge.

This was a highly surprising result as the group 15 elements are commonly found in the E(III) and E(V) oxidation states, however the E(II) are not unknown. In fact, the synthesis of the first E(II) compound is often associated with the origins of organometallic chemistry. Tetramethyldiarsine ($Me_2AsAsMe_2$), commonly referred to as cacodyl due to its strong smell, was unknowingly prepared by Louis Claude Caset de Gassicourt in 1757.[84] Its structure was identified in a X-ray diffraction study undertaken in 1988, and the As–As covalent bond was found to possess a bond length of ca. 2.43 Å.[85]

The compound itself orientates into an antiperiplanar geometry. The two methyl groups bound to each arsenic atom result in an As(II) oxidation state, as the As−As covalent bond results in no electronic change, due to the identical nature of the arsenic atoms. Analogous compounds for antimony and bismuth have been synthesised.[86]

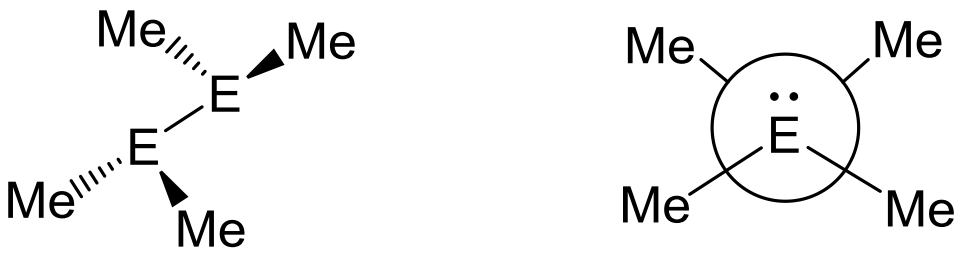

Figure 89 – Antiperiplanar arrangement of the $Me_2E{-}EMe_2$, where E = As, Sb and Bi.

The $PPN[Sb_3F(CHN_4)_6]$ is an antimony(II) trimer with an interstitial fluorine, unlike any previously synthesised complex in the literature. There are no Sb−Sb bonds as found in the $Me_2E{-}EMe_2$ compounds, instead the Sb(II) oxidation state arises from the total ligand bonds. There are six tetrazolate ligands which represent a total of (−6) and a fluoride which contributes (−1). The single PPN cation balances (+1) charge leaving (−6), which must be settled by the antimony centres, equating to (+2) for each Sb atom.

As shown by the bond angles and the orientation in figure 90 each antimony co-ordination centre has a distorted geometry caused by the antimony lone pair. The lone pair is located in the axial plane, which forces the four equitorial bonds out of the plane. It is this repulsive effect that reduces all bond angles at each co-ordination centre. It appears that the repulsive effect of the antimony lone pair is stronger than the comparable tin lone pair, resulting in further deviation from the 90° typical for a square-based pyramid. An alternative explanation for the increased deviation could also be caused by the cage-like framework. The large distortion could be necessary in order to appease the requirements for the rigid complex to form.

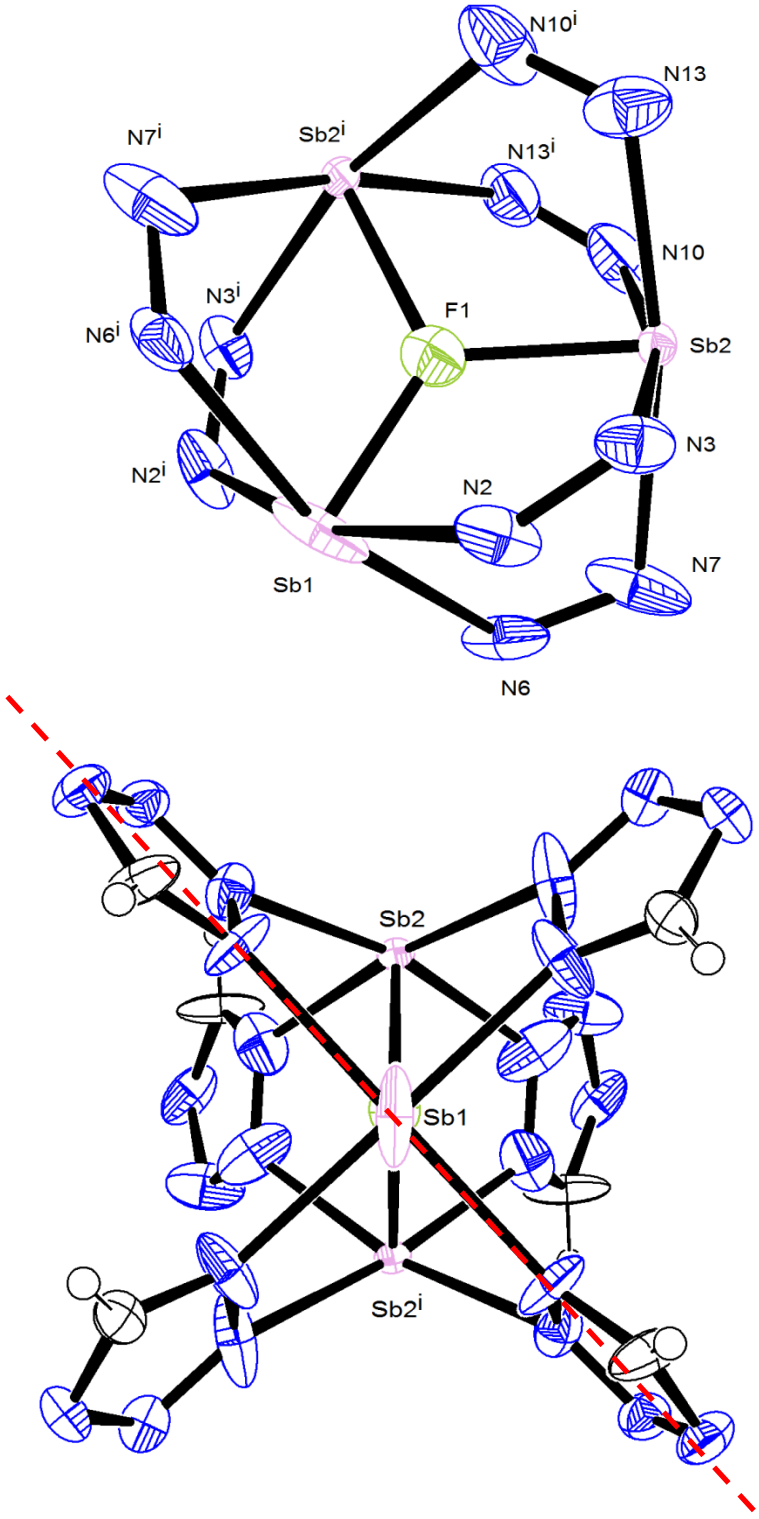

Figure 90 – Ellipsoid plot of the three Sb co-ordination centres within PPN[$Sb_3F(CHN_4)_6$] (top), with only the bound nitrogen atoms of the tetrazolyl ligands illustrated for clarity. Each Sb co-ordination centre is clearly a square-based pyramid. The dotted line indicates the mirror plane within the PPN[$Sb_3F(CHN_4)_6$] complex, making the Sb(2) and Sb(2^i) co-ordination centres equivalent. Figure produced using ORTEP®.

Bond	Bond Length [Å]
Sb_1-N_2	2.367(4)
Sb_1-N_6	2.350(4)
Sb_1-N_2^i	2.367(4)
Sb_1-N_6^i	2.350(4)
Sb_1-F_1	1.902(4)
Sb_2-N_3	2.378(4)
Sb_2-N_7	2.409(4)
Sb_2-N_{10}	2.269(5)
Sb_2-N_{13}	2.227(4)
Sb_2-F_1	2.011(2)
Sb_2^i-N_3^i	2.378(4)
Sb_2^i-N_7^i	2.409(4)
Sb_2^i-N_{10}^i	2.269(5)
Sb_2^i-N_{13}^i	2.227(4)
Sb_2^i-F_1	2.011(2)

Table 20 – Bond lengths for all three Sb co-ordination centres. Note that Sb(2) and Sb(3) contain identical co-ordination environments; this is due to the mirror plane indicated in figure 90.

A second crop consisting of semi-crystalline, white solid was isolated from the crystallisation solution. It was assumed that this material was again the $PPN[Sb_3F(CHN_4)_6]$ cluster, and its identity was checked using ^1H NMR spectroscopy.

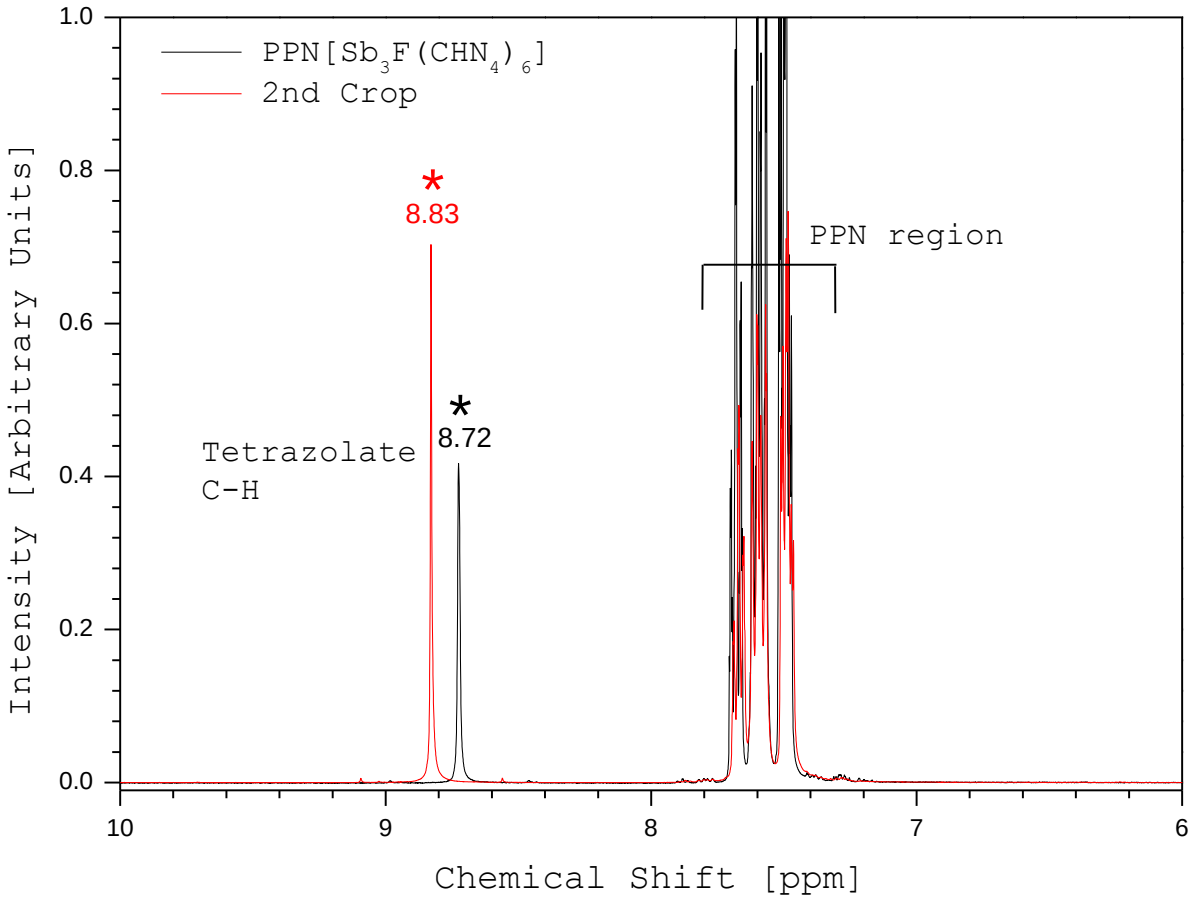

Figure 91 – ^{1}H NMR spectral comparison between the 1st crop (PPN[$Sb_3F(CHN_4)_6$]) and the 2nd crop illustrating the different proton environment.

Surprisingly, the 2nd crop exhibited a proton environment at 8.83 ppm, rather than the expected 8.72 ppm for the previously observed PPN[$Sb_3F(CHN_4)_6$]. The crystallisation solution did not change and was placed back into storage at −25°C. This suggests that the original solution contained a mixture of complexes: unreacted $PPh_4(CHN_4)$, the PPN[$Sb_3F(CHN_4)_6$] cluster and the unknown complex isolated in the 2nd crop of crystals. It is possible that the fluorine-containing cluster is an isolable intermediary species that has a lower solubility in THF than the unknown complex. It can be hypothesised that the nature of this unknown complex could be the fully substituted "PPN[$Sb(CHN_4)_4$]". The ^{19}F NMR of both the unknown complex and the antimony trimer were recorded in order to establish whether there is fluorine within the unassigned material.

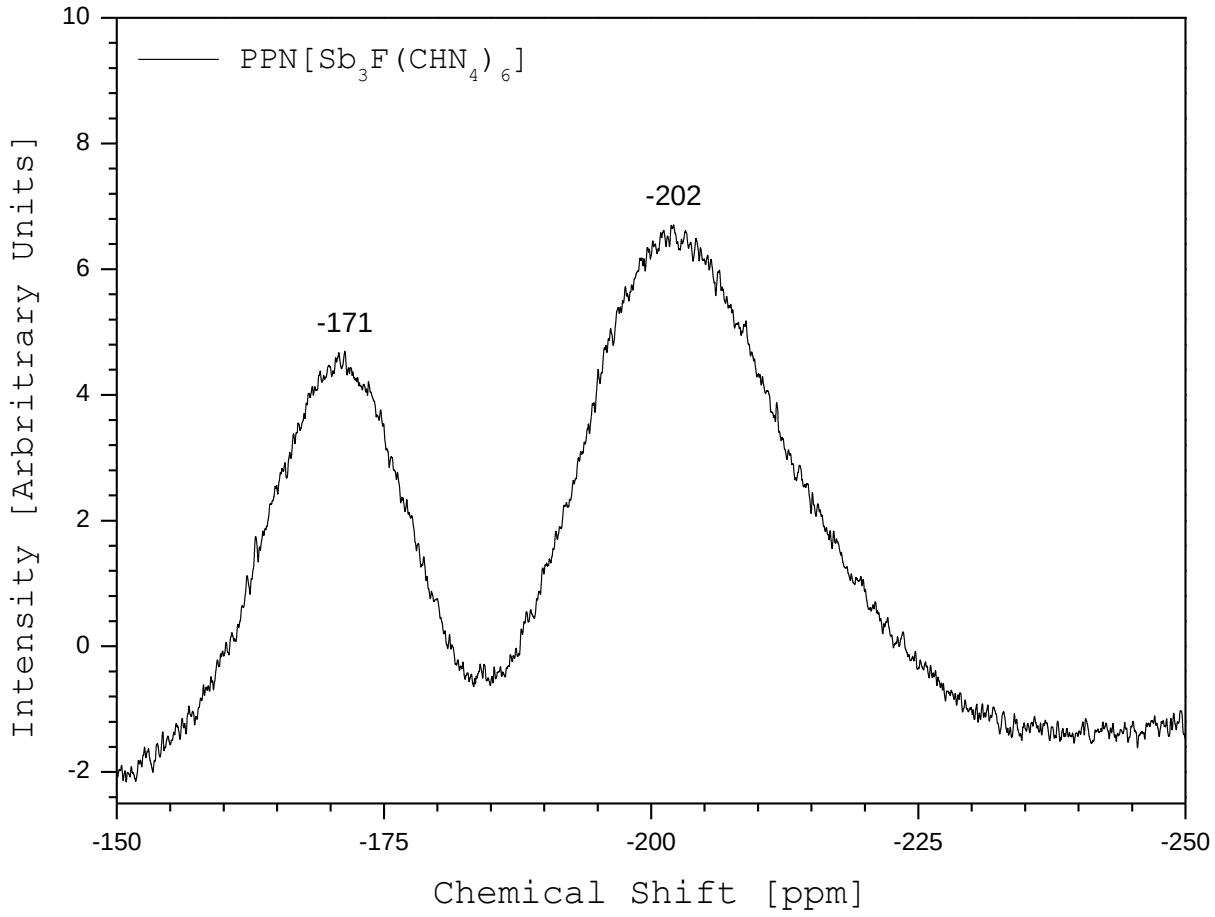

Figure 92 – ^{19}F NMR spectrum of PPN[$Sb_3F(CHN_4)_6$], expanded between -150 ppm and -250 ppm. Figure illustrates the two broad environments that can be found through expansion of the spectrum.

To produce the above spectrum required extensive manipulation as the peaks lay within the baseline. For this reason it cannot be used to form reliable conclusions, but does allow for speculative discussion. The PPN[$Sb_3F(CHN_4)_6$] does show evidence of fluorine content. However what was unexpected was that it produced two distinct peaks, at -171 ppm and -202 ppm. The symmetrical nature of the structure shown using X-ray diffraction dictates that only a single peak should be present. The intermediary nature of the trimeric species could explain this observation; the bulk solid could potentially contain two different intermediates, and it is just the trimeric species that can be crystallised. However the presence of two intermediates would be represented in the respective ^{1}H NMR spectrum as two different tetrazolate proton environments. As only one tetrazolate peak is present, this is unlikely to be the case.

Another possible explanation for the weak signals could be the cage-like nature of the complex which could "mask" the fluorine environment, preventing it from being detected in the ^{19}F NMR spectrum. The fluorine atom lies in a rigid position, attached to three antimony co-ordination centres. The influence of these centres could broaden the signal significantly. The ^{19}F spectrum of the second crop of material contained no fluorine environments. This is further evidence that the PPN[$SbF(CHN_4)_6$] is possibly an intermediary species, with the second crop containing the fully-exchanged species PPN[$Sb(CHN_4)]_4$. This explanation cannot be independently proven however and more data is required to make a concrete conclusion.

The preparation was then extended to bismuth(III) fluoride. The reagents were suspended in dry THF and stirred overnight at room temperature. THF was used as the reaction solvent rather than the MeCN that produced the PPN[$Sb_3F(CHN_4)_6$] as it was theorised that the less polar solvent could prevent the trimeric system from forming, resulting in the fully exchanged product. The suspension was filtered, leaving a small amount of white solid and a clear, colourless solution. The solvent is removed from this solution under dynamic vacuum to leave an oil. Dry MeCN is added to dissolve the oil, and the solvent volume was reduced until the onset of precipitation. The white solid was heated back into solution and the Schlenk tube was stored at −25°C in order to produce crystalline material.

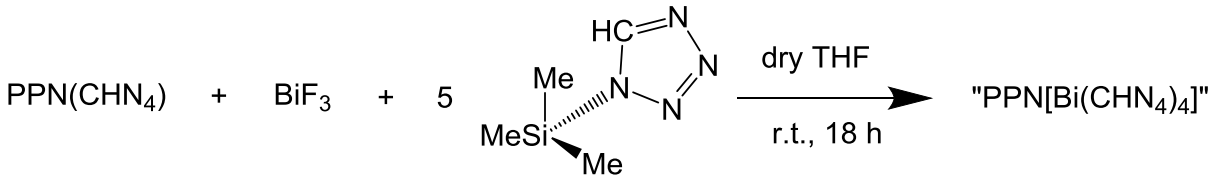

Scheme 26 – Attempted preparation of "PPN[$Bi(CHN_4)_4$]"

The solid residue was analysed only using IR spectroscopy as there was not enough material present for a more detailed inspection. Observing figure 93 it seems as though a small amount of a PPN salt is present, evidenced by the peak at 1588 cm^{-1}. The remaining spectrum is difficult to interpret accurately due to the weak concentration of solid present in the Nujol mull. It is possible that the majority of the solid is simply unreacted BiF_3. If the solid residue was indeed unreacted BiF_3 the presence of the PPN peak in the IR spectrum could be explained by any potential product remaining in solution.

When the white solid was dried under vacuum only the solvent would have been removed, leaving any dissolved PPN salt behind.

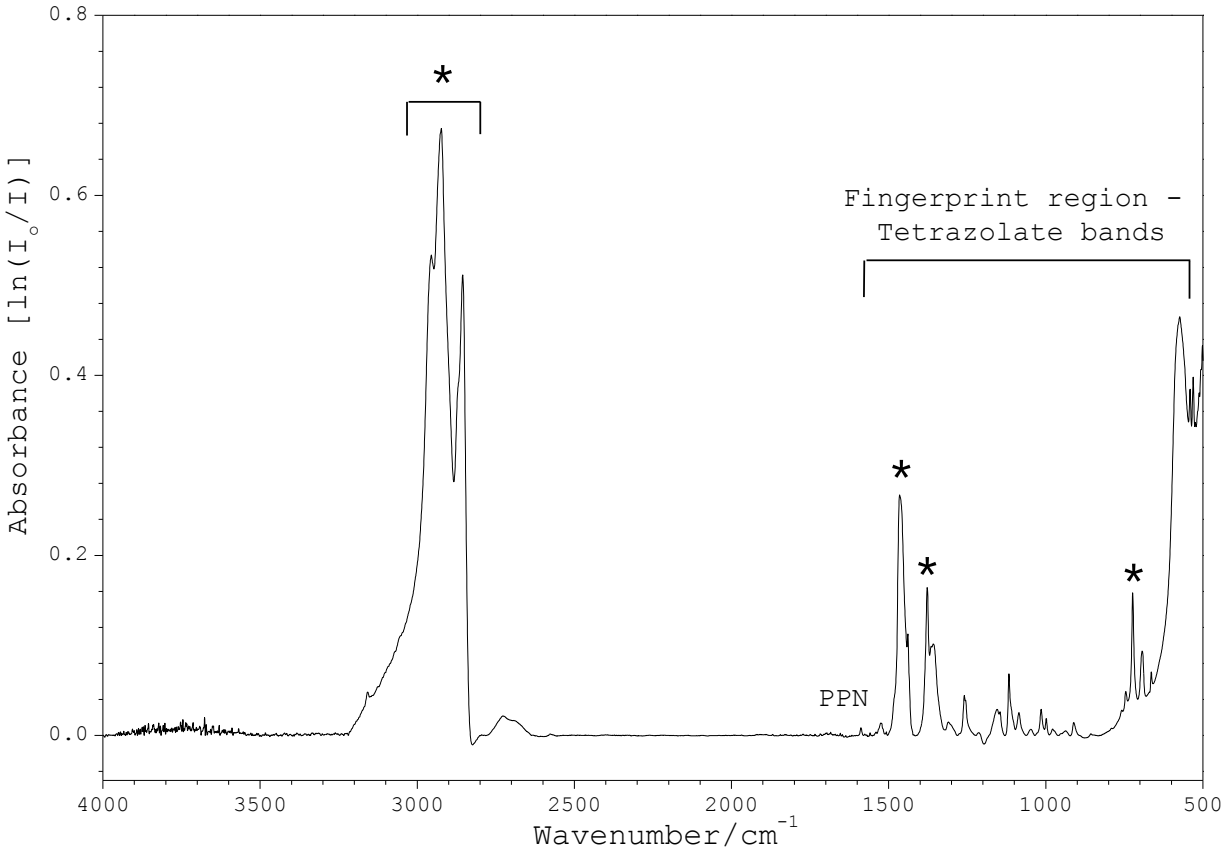

Figure 93 – IR spectrum of the mulled white solid residue from the attempted synthesis of "PPN[Bi(CHN$_4$)$_4$]" Nujol bands are marked by asterisks (*).

A semi-crystalline, white solid was isolated from the crystallisation solution and was dried briefly under vacuum. It was subsequently probed with IR and ^{1}H NMR spectroscopy in order to evaluate its identity.

As shown in figure 94 the white solid is a definite PPN salt, possessing a strong peak at 1588 cm^{-1}. The crowded nature of the fingerprint region is usually an indication that tetrazolate ligands are present. However these are difficult to separate from the peaks due to the PPN cation, therefore ^{1}H NMR spectroscopy provides further insight into the nature of the product.

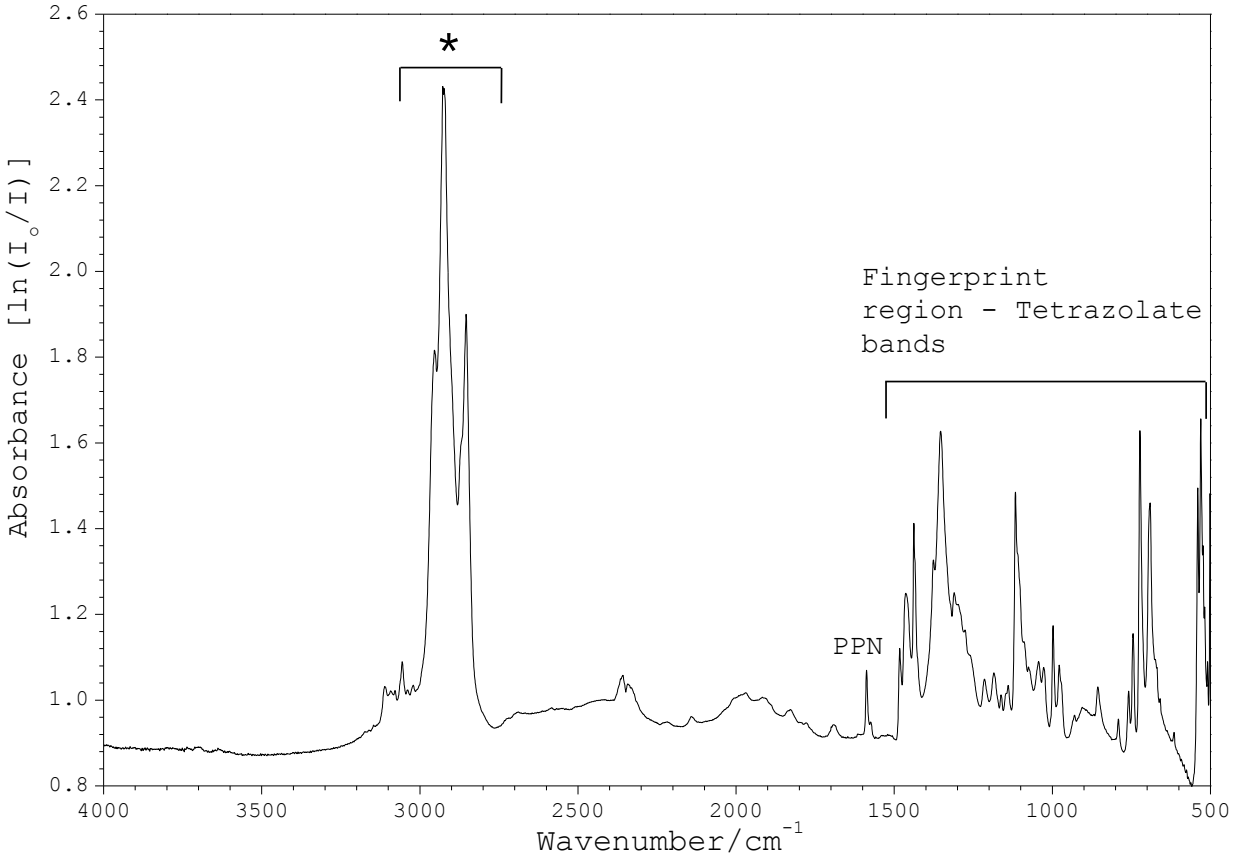

Figure 94 – IR spectrum of the mulled semi-crystalline "PPN[Bi(CHN$_4$)$_4$]". Nujol bands are marked by asterisks (*).

The ^{1}H NMR spectrum shown in figure 95 confirms that the isolated product contained tetrazolato ligands. Furthermore, the ^{1}H NMR spectrum is highly encouraging as the "PPN[Bi(CHN$_4$)$_4$]" proton environment at 8.70 ppm is very similar to that found for the previously prepared PPN[Sb$_3$F(CHN$_4$)$_6$] complex (8.72 ppm). This suggests that the isolated white solid could in fact be another trimeric cage-like system, the analogous "PPN[Bi$_3$F(CHN$_4$)$_6$]". If so, the 0.02 ppm deviation could be caused simply by the different co-ordination centre.

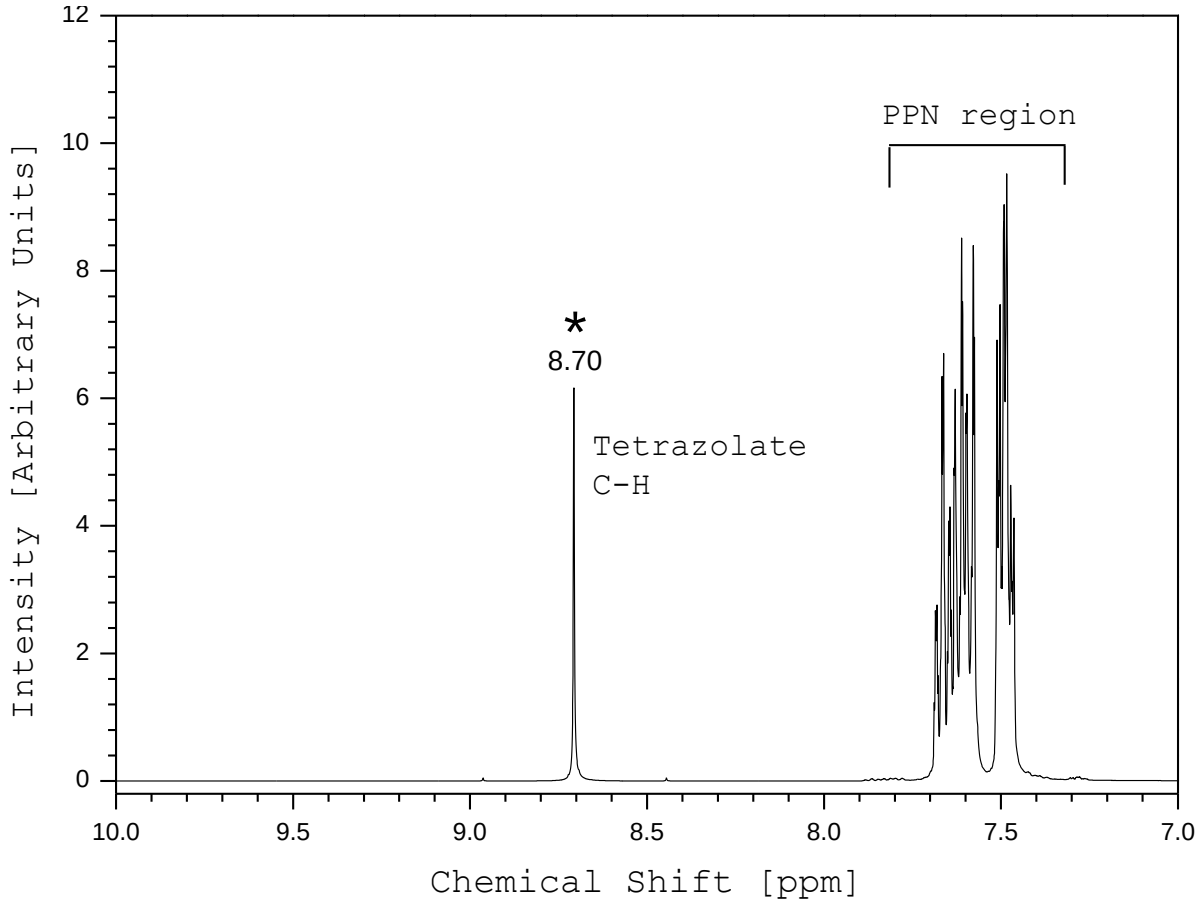

Figure 95 – ^{1}H NMR spectrum of the semi-crystalline "PPN[$Bi_3F(CHN_4)_6$]" in CH_3CN-d_3.

Comparing their respective IR spectra could provide a useful insight into the potential similarities between PPN[$Sb_3F(CHN_4)_6$] and the unconfirmed "PPN[$Bi_3F(CHN_4)_6$]". Figure 96 shown below focusses upon the crowded region between 1600 cm^{-1} and 500 cm^{-1}. Interestingly, the majority of the peaks found in both spectra align, suggesting that the complexes do possess structural similarities. The noticeable difference is at 1340 cm^{-1}, which is typical of variance in PPN salts. This is influenced by differences in the crystalline packing of PPN salts and also the ion ratios in the salt ie 1:1 salt compared to a 2:1 salt containing two PPN cations. Smaller differences at 970 cm^{-1} and 905 cm^{-1} support the hypothesis that the proposed "PPN[$Bi_3F(CHN_4)_6$]" and PPN[$Sb_3F(CHN_4)_6$] are of an analogous structural nature.

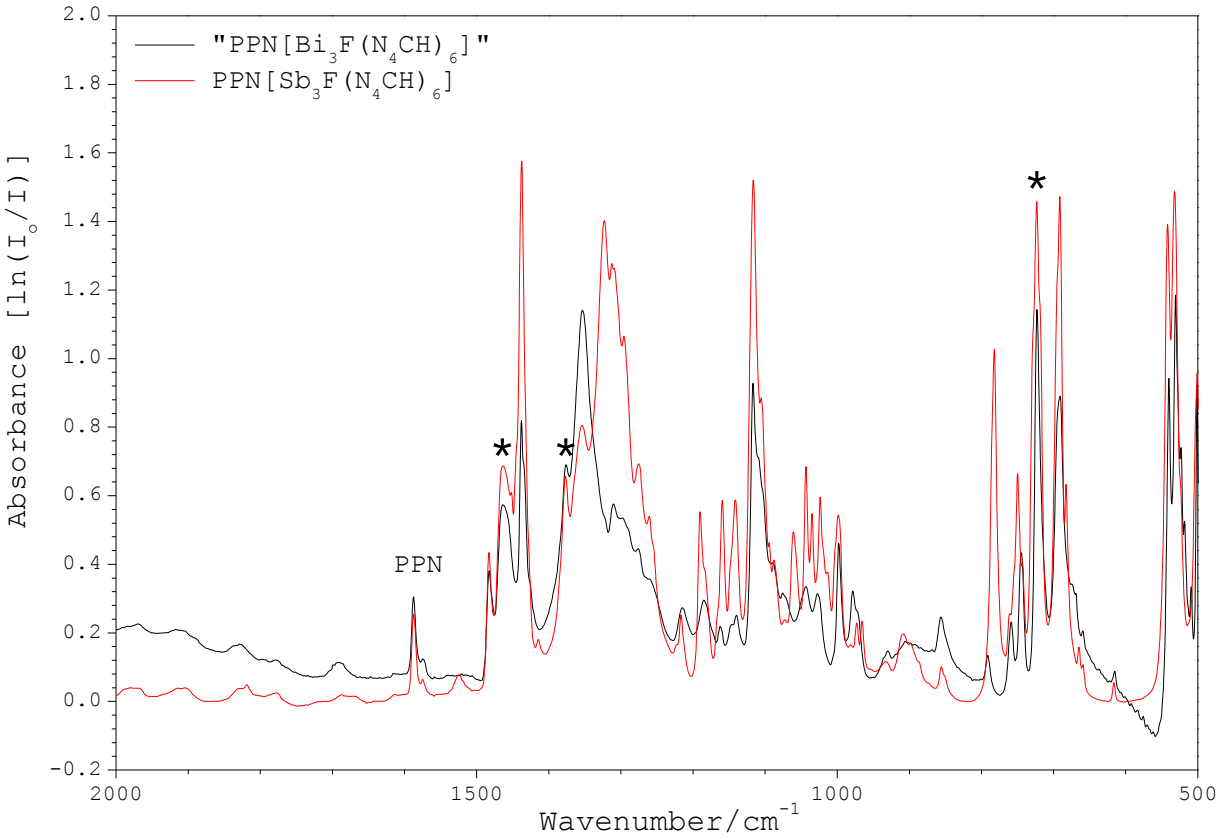

Figure 96 – Comparison of the fingerprint region in IR spectra of the mulled "PPN[$Bi_3F(CHN_4)_6$]" and PPN[$Sb_3F(CHN_4)_6$]. Nujol bands are marked by asterisks (*).

If, as the spectra suggest, the BiF_3 reacts to produce an analogous trimeric species the question arises as to why these complexes preferentially form. The preparation that utilises the group 14 compound SnF_2 results in the $PPh_4\{Sn(CHN_4)_3\}$ co-ordination polymer, so the cause of the variation must stem from the nature of the Sb and Bi co-ordination centres. Tin, antimony and bismuth all have two stable oxidation states: Sn(II) and Sn(IV), Sb(III) and Sb(V) and Bi(III) and Bi(V). Significantly antimony and bismuth can form stable compounds derived from both oxidation states with little electronic penalty. This is due to both E(III) and E(V) forms being able to possess a full octet of electrons easily. The variation could also be caused by the structural features of the starting materials. The SnF_2 possesses a trigonal planar geometry, with a lone pair occupying one of the three positions. With respect to the two bonding pairs the molecular shape is bent. The SbF_3 and BiF_3 both have a tetrahedral with respect to all electron pairs. Both again have lone pairs that take no part in bonding, therefore the bonding geometry is trigonal pyramidal.

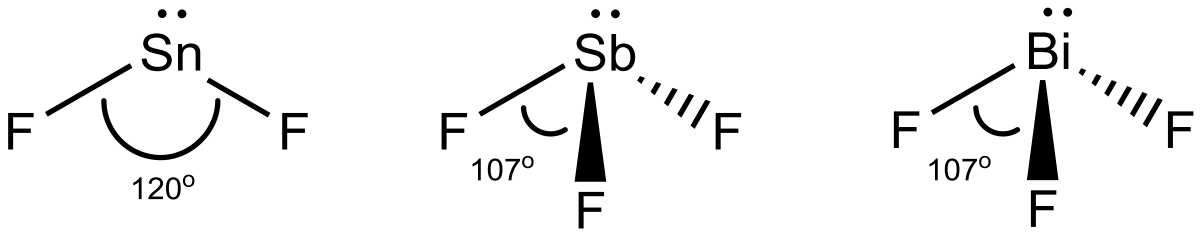

Figure 97 – Chemdraw representations of the respective geometries for SnF_2, SbF_3 and BiF_3. The bond angles for each compound are illustrated.

The crystalline structures of the above compounds will differ significantly from their hypothetical, individual geometries. In the crystalline structure of SnF_2 there are two distinct co-ordination centres (figure 98), each with a different bonding geometry. Sn1 and Sn3 are trigonal pyramidal, whilst Sn2 and Sn4 are both examples of distorted square-based pyramids. These co-ordination centres make up a four-membered system, with alternating Sn and F atoms forming a puckered ring.[83] The bridging fluorines within the ring are planar with respect to their tin co-ordination centre.

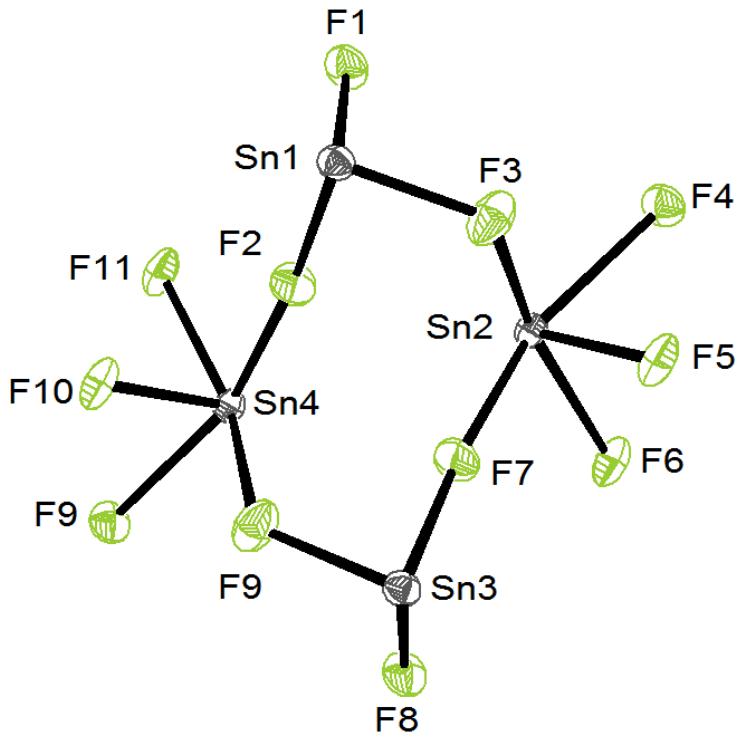

Figure 98 - Ellipsoid plot showing the extended network found within the crystal structure of SnF_2. Figure produced using a CIF file from ref. 84 using ORTEP®.

The remaining fluorines at each tin co-ordination centre are responsible for interacting with adjacent tetrameric rings. Specifically interesting is the co-ordination geometry at Sn2 and Sn4. The $PPh_4\{Sn(CHN_4)_3\}$ product also exhibits this distorted square-based pyramid geometry, which could indicate that the extended structure influences the structure of the resulting product. In addition, the preparation of $\{Sn(CHN_4)_2(py)_2\}_n$ co-ordination polymer uses the SnF_2 as a reactant, and the product also exhibits a square-based pyramid geometry at each SN centre. To add weight to this hypothesis it is necessary to extend this comparison to the SbF_3 and BiF_3 crystalline geometries.

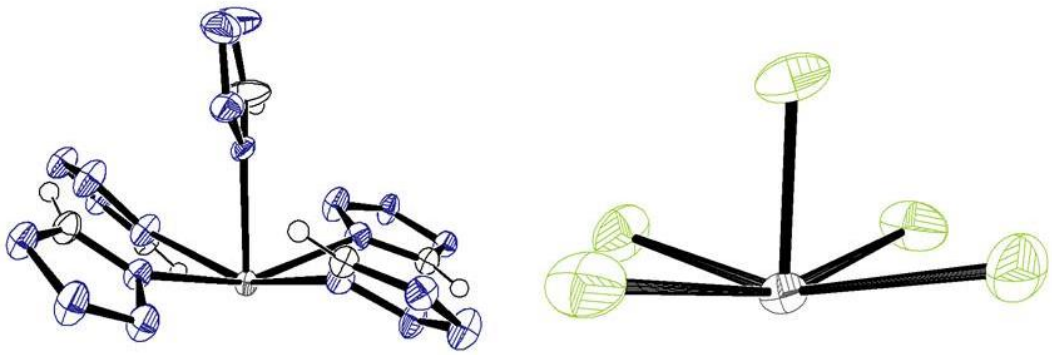

Figure 99 – Comparison of the tin co-ordination centres of $\{PPh_4[Sn(CHN_4)_3]\}_n$ (left) and SnF_2 (right). The distorted square-based pyramid geometry found for both complexes indicates that the crystal geometry of the starting material could dictate the crystal geometry of the resulting product. Images produced using ORTEP®, the right image using a CIF file from Ref. 84.

The crystal structure of SbF_3 was initially reported to consist simply of monomeric SbF_3 units.[87] However based upon the large variation in the melting point temperature between arsenic trifluoride (-8.5°C) and antimony trifluoride (292°C), it is believed that it could possess a more complex extended system. The crystal structure was reinvestigated in order to accurately determine the fluorine positions.[88] It was found that each Sb co-ordination centre is directly bound to three fluorine atoms, at an average distance of 1.92 Å. In addition to this, three additional fluorines are associated to each Sb at a longer average distance of 2.61 Å, giving an overall distorted octahedral arrangement.[88]

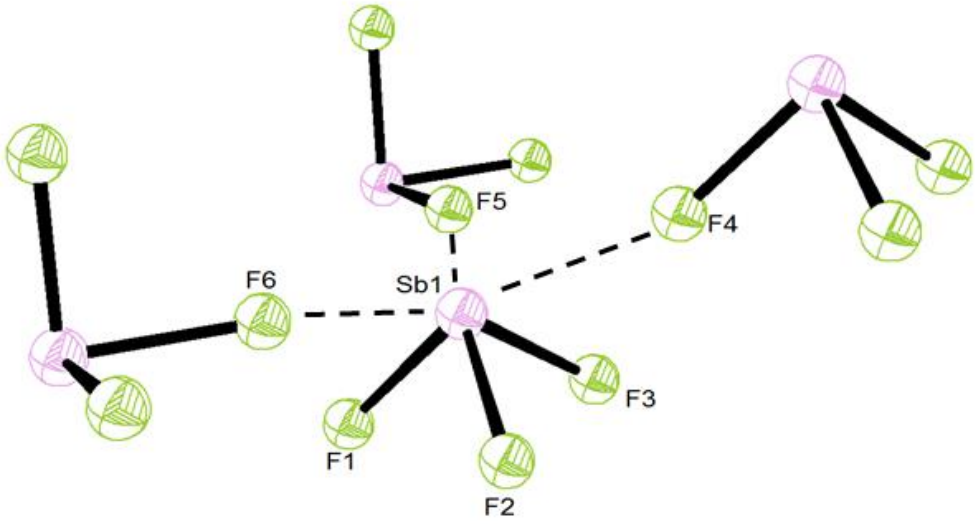

Figure 100 – Distorted octahedral antimony co-ordination centre found within the crystal structure of SbF_3. Ball and stick figure adapted from a CIF file from Ref. 89 using ORTEP®.

The $PPN[Sb_3F(CHN_4)_6]$ structure is built upon an interstitial fluorine, therefore it requires a knowledge of the fluorine co-ordination environment rather than the antimony itself. Examination of the X-ray data reveals that each F is co-ordinated in a planar, triangular fashion. In addition to the 1.92 Å bond length for the formal Sb1−F1 bond, the further associated Sb2 and Sb3 centres are at a length of 2.60 Å and 3.60 Å respectively. Whilst not possessing the strict trigonal planar geometry of the $PPN[Sb_3F(CHN_4)_6]$ complex, it could be an explanation for the preferential formation of the trimeric species.

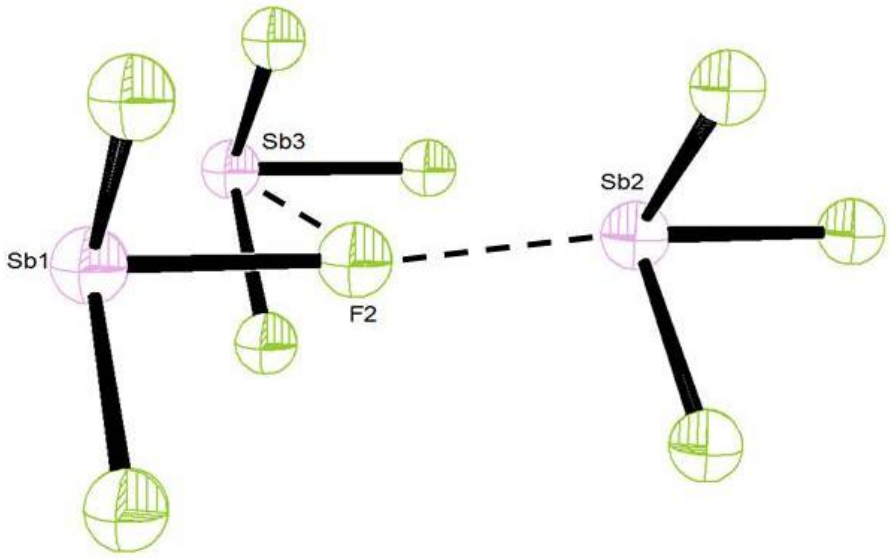

Figure 101 – Approximate trigonal planar fluorine environment found within the extended network of SbF_3. Ball and stick figure adapted from a CIF file from Ref. 89 using ORTEP®.

The final crystalline geometry to consider is that of BiF_3. An X-ray diffraction study found that each bismuth centre is bound to eight different fluorine atoms, with an average Bi–F bond length of 2.38 Å.[89] The geometry about the bismuth atom is a distorted square antiprismatic structure, which consists four fluorine atoms above and below the bismuth plane, each group of four forming an approximate square.

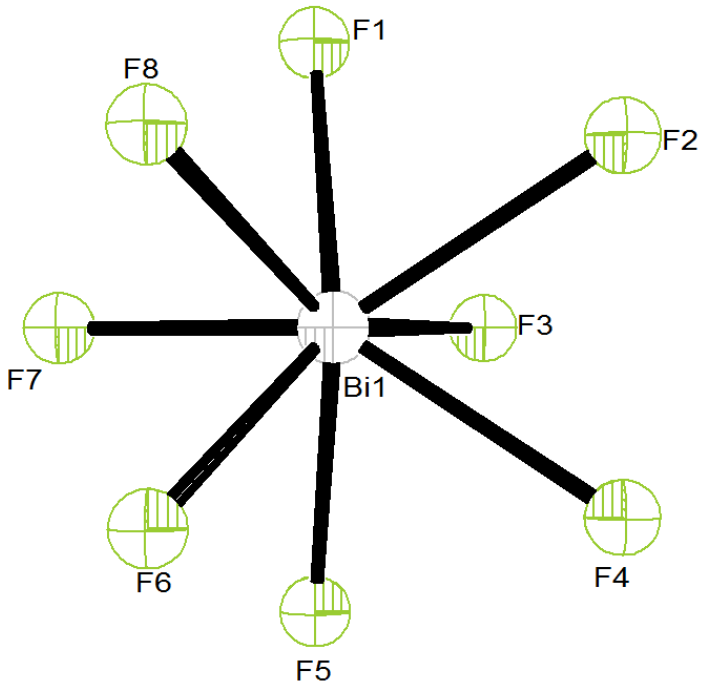

Figure 102 – Ball and stick plot illustrating the fluorine atoms that co-ordinate to the Bi metal centre in the BiF_3 crystal structure. Figure adapted from a CIF file from Ref. 90 using ORTEP®.

When examining the X-ray structure it is again possible to locate a pseudo-trigonal planar geometry with the extended crystal network of BiF_3. This particular example is a much more traditional example of the trigonal planar system, consisting of three bismuth atoms formally bound to the interstitial fluorine, at lengths of 2.39 Å, 2.50 Å and 2.34 Å for Bi1, Bi2 and Bi3 respectively.

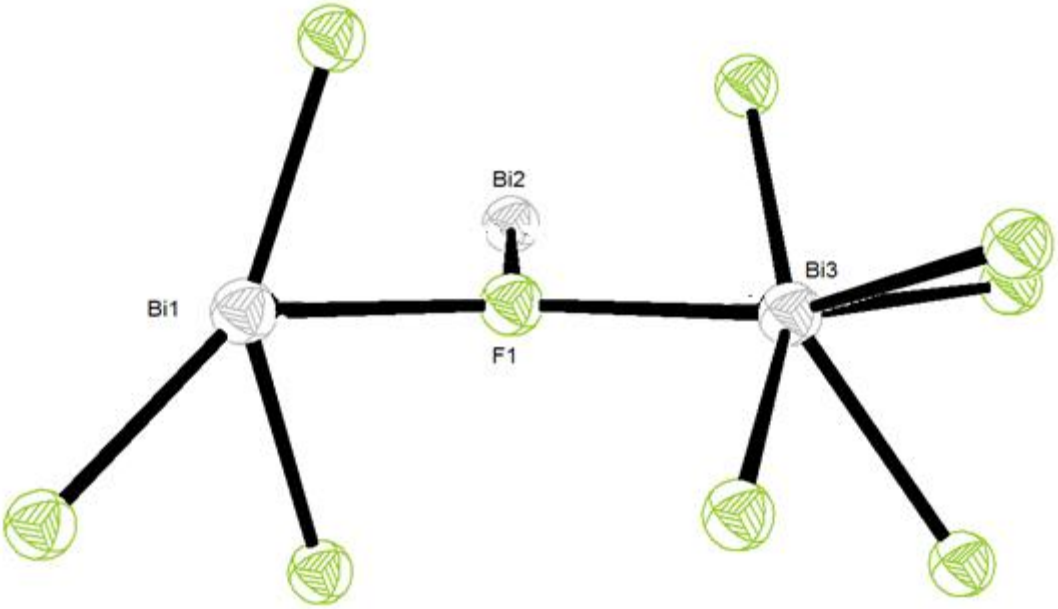

Figure 103 – Approximate trigonal planar fluorine environment found within the extended network of BiF_3. This is a much more obviously trigonal planar, which could indicate that the PPN[$Bi_3F(CHN_4)_6$] is even more likely that the observed PPN[$Sb_3F(CHN_4)_6$]. Ball and stick figure adapted from a CIF file from Ref. 90 using ORTEP®.

The results of investigating the crystalline structure of the reagents SnF_2, SbF_3 and BiF_3 in order to explain the unusual crystal structure of PPN[$Sb_3F(CHN_4)_6$] and the expected "PPN[$Bi_3F(CHN_4)_6$]" were highly enlightening. The SbF_3 and BiF_3 both contain approximate trigonal planar geometries about an interstitial fluorine atom, as illustrated in figure 101 and figure 103. This geometry is central to the observed PPN[$Sb_3F(CHN_4)_6$] and the hypothesised "PPN[$Bi_3F(CHN_4)_6$]" complexes. It appears that this fluorine is highly restricted and fluorine-tetrazolate exchange occurs first at the external, less hindered fluorine atoms. Once the exchange is complete, the interstitial fluorine is unable to react. The "PPN[$Bi_3F(CHN_4)_6$]" is a complex the evidence of which is only assumed tentatively, with only spectral evidence for its existence. However the BiF_3 crystalline structure possesses a much more typical trigonal planar geometry about a fluorine atom in comparison to SbF_3, suggesting that the trimeric species is likely to be produced in reality.

4.2.7 Attempted Synthesis of a Neutral Homoleptic Low-Valent Tin Co-ordination Polymer

The final experiment investigated whether a neutral, homoleptic tin-based co-ordination polymer could be synthesised. In an attempt to answer this question SnF_4 was reacted with TMS-CHN_4 in dry acetonitrile.

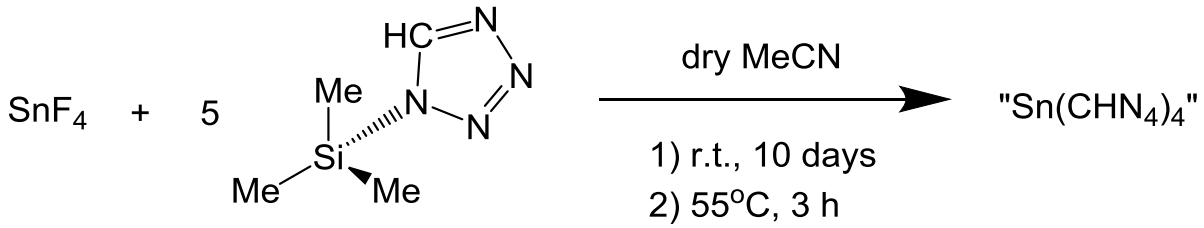

Scheme 26 – Attempted preparation of the neutral $[Sn(CHN_4)_4]_n$ co-ordination polymer.

The white suspension was stirred at room temperature for 10 days, and then to ensure the reaction had reached completion, the reaction mixture was heated to 55°C for 3 h. The suspension was filtered, resulting in a white solid and a slightly turbid solution. The white residue was probed using IR and ^{1}H NMR spectroscopy. The residue unfortunately was insoluble in the *d*-$CHCl_3$, even with heating. There is a strong acetonitrile peak at 1.98 ppm which indicates the residue is wet. Interestingly, due to the wet nature of the residue it is possible to observe a TMS(F) peak at 0.22 ppm. This is a strong indication that a reaction has, at the very least, begun to take place. A melting point analysis was attempted using the white solid. However it did not melt, even above 300°C. The starting material SnF_4 has a melting point above 700°C, therefore it is a sensible suggestion that this white solid is mostly unreacted SnF_4. This was disappointing, however the presence of TMS(F) suggests that a reaction had taken place, and that the product could be in the solution separated from the white residue.

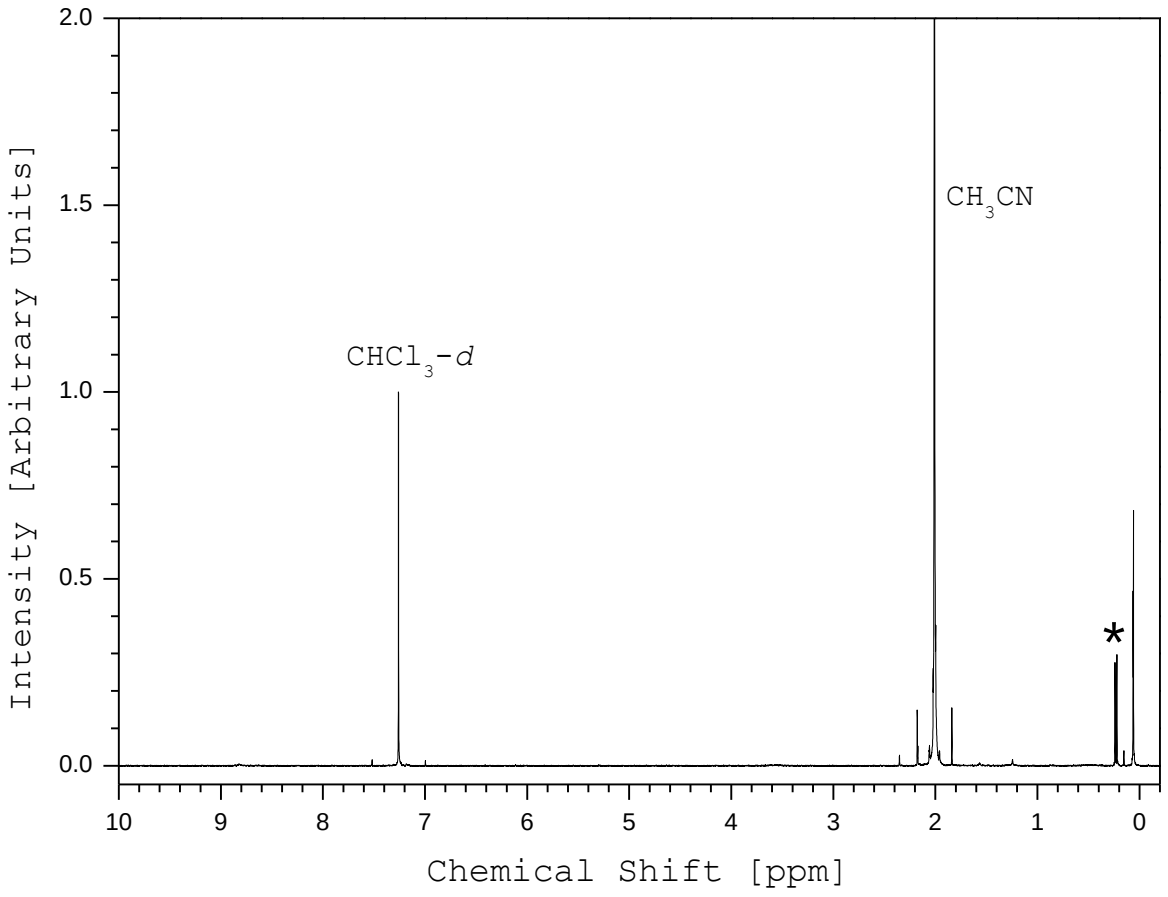

Figure 104 – ^{1}H NMR spectrum of the solid residue in *d*-$CHCl_3$. TMS-F ^{1}H environment at 0.22 ppm is marked (*).

The IR spectrum could not provide any conclusive information about the attempted reaction. The IR spectrum contains a crowded fingerprint region between 2000 cm^{-1} and 500 cm^{-1}, which often indicates the presence of tetrazole or tetrazolate ligands, an encouraging result. The hypothetical "$Sn(CHN_4)_4$" co-ordination polymer is a neutral complex therefore a PPN or PPh_4 cation peak at approximately 1590 cm^{-1} cannot be used for characterisation as seen in previous complexes. Comparison with the $\{Sn(CHN_4)_2(py)_2\}_n$ co-ordination polymer illustrates that the peak pattern is significantly different, with the $\{Sn(CHN_4)_2(py)_2\}_n$ spectrum containing many more fingerprint IR bands. It is evident that the residue is probably a combination of unreacted SnF_4, decomposition products and potentially a small amount of the hypothesised product that remained out of solution.

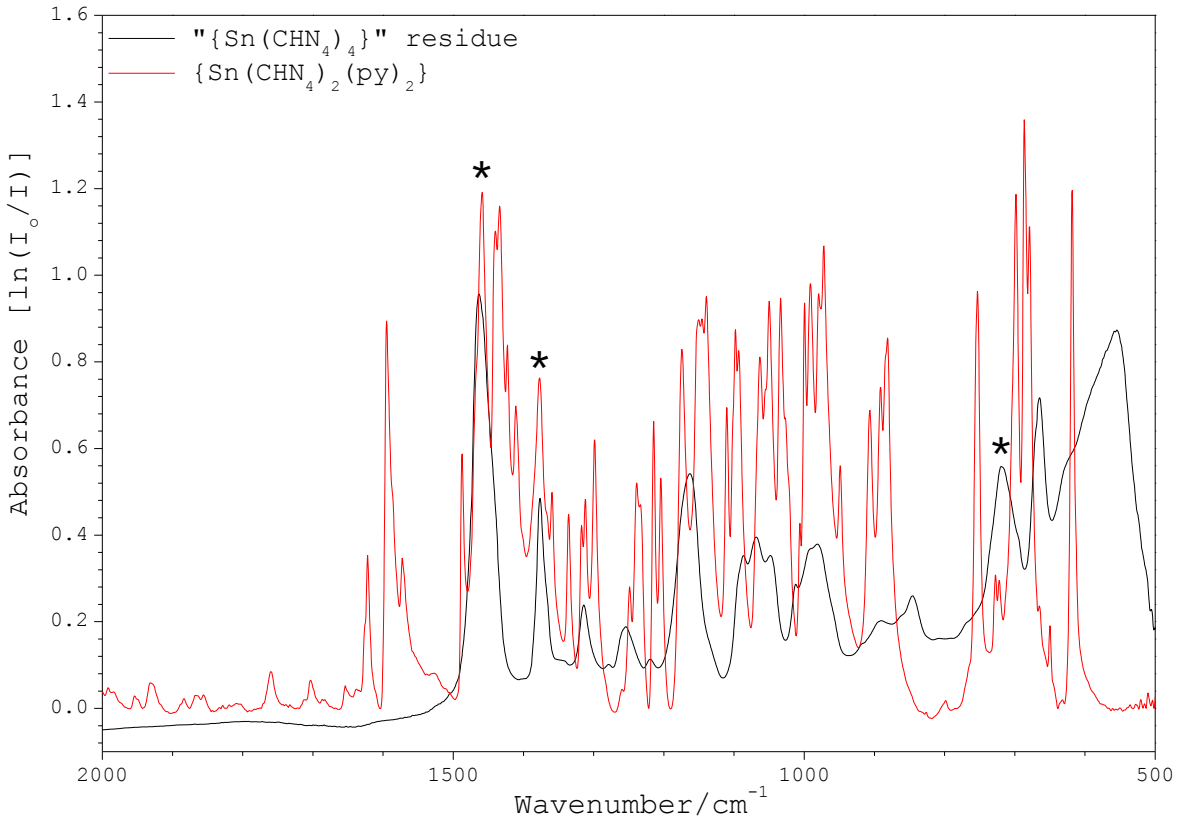

Figure 105 – Nujol mull IR spectral comparison between the $\{Sn(CHN_4)_2(py)_2\}_n$ co-ordination polymer and the potential "$\{Sn(CHN_4)_4\}_n$". Lack of fingerprint bands in "$\{Sn(CHN_4)_4\}_n$" indicate the white residue is not the target complex.

The turbid solution was concentrated under vacuum to approximately 2 mL and was subsequently stored at -25°C. A small amount of semi-crystalline material was isolated. This white solid was probed with IR and ^{1}H NMR spectroscopy in order to evaluate whether the target complex had been synthesised. The IR spectrum (figure 106) is similar to the white residue observed previously. This is expected due to the peaks observed in the IR spectrum for the white residue resulted from the removal of solvent depositing material that had been dissolved in solution. However there are marked differences. A large peak at 558 cm^{-1} observed in the IR spectrum for the white residue is not present in the purified solid. This could be due to the Sn–F bonds in the SnF_4 starting material, which would explain its absence. The peak at 1813 cm^{-1} falls within the region expected for a C=O stretch. This is puzzling as no solvents used during the reaction possess a carbonyl group, nor would the decomposition product be expected to contain such a bond. It could potentially have been caused by contamination of the plates.

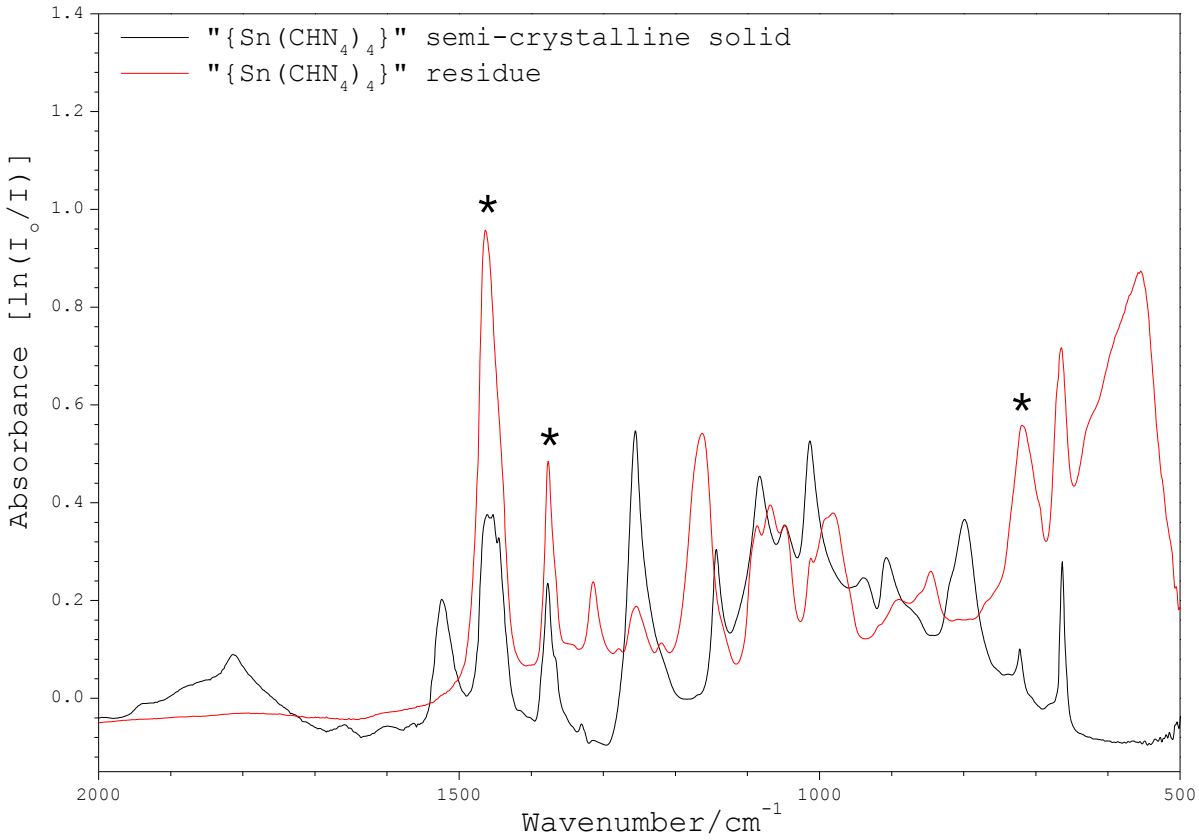

Figure 106 – IR spectral comparison of the respective fingerprint regions for mulled $\{Sn(CHN_4)_2(py)_2\}_n$ and the mulled "$\{Sn(CHN_4)_4\}_n$" semi-crystalline solid. Nujol bands are marked by asterisks (*).

The ^{1}H NMR spectrum (figure 107) can be attributed to free 1*H*-tetrazole by comparison with its known ^{1}H NMR spectrum. The peak at 13.70 ppm is due to the NH proton environment, whilst the peak at 8.94 ppm is attributed to the CH proton. This was highly disappointing, suggesting that the TMS-CHN_4 had decomposed during the reaction, leaving just SnF_4 (white residue) and 1*H*-tetrazole. TMS-CHN_4 does have a low decomposition temperature of approximately 135°C therefore it is probable that the 3 h of stirring at 55°C caused partial decomposition in solution.

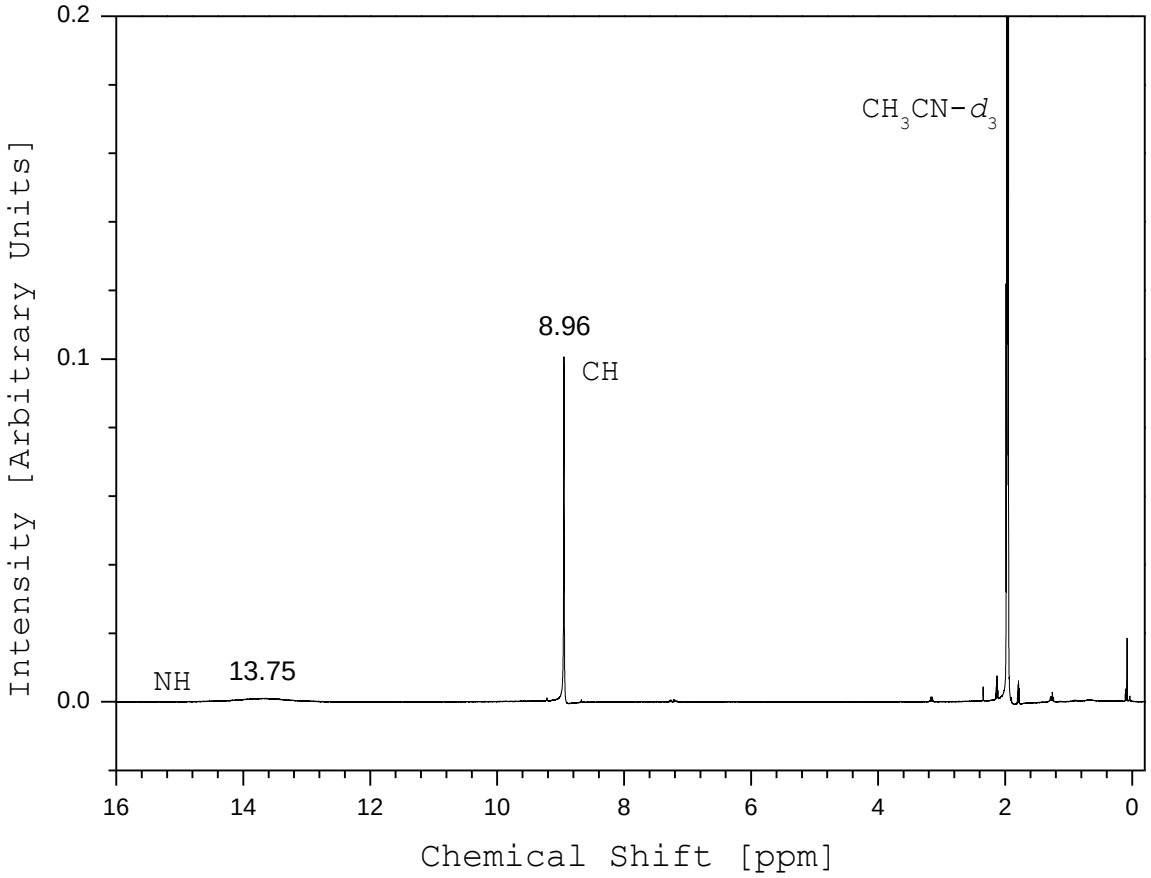

Figure 107 – ^{1}H NMR spectrum of the {Sn(CHN$_4$)$_4$} semi-crystalline solid. Analysis of the spectrum indicates the semi-crystalline solid is 1*H*-tetrazole, due to decomposition of the TMS-CHN$_4$ reactant.

Revisiting the IR spectrum of the semi-crystalline material supports this observation, as it overlays excellently with the IR spectrum of 1*H*-tetrazole. All peaks can be found in both spectra apart from a peak at 798 cm^{-1}, found in the semi-crystalline solid IR spectrum. It is unclear what the causes this peak, but it is doubtful that this single peak can be attributed to co-ordination to a tin centre. The previously unexplained peak at 1813 cm^{-1} can be explained by a strong C=N band caused by 1*H*-tetrazole.

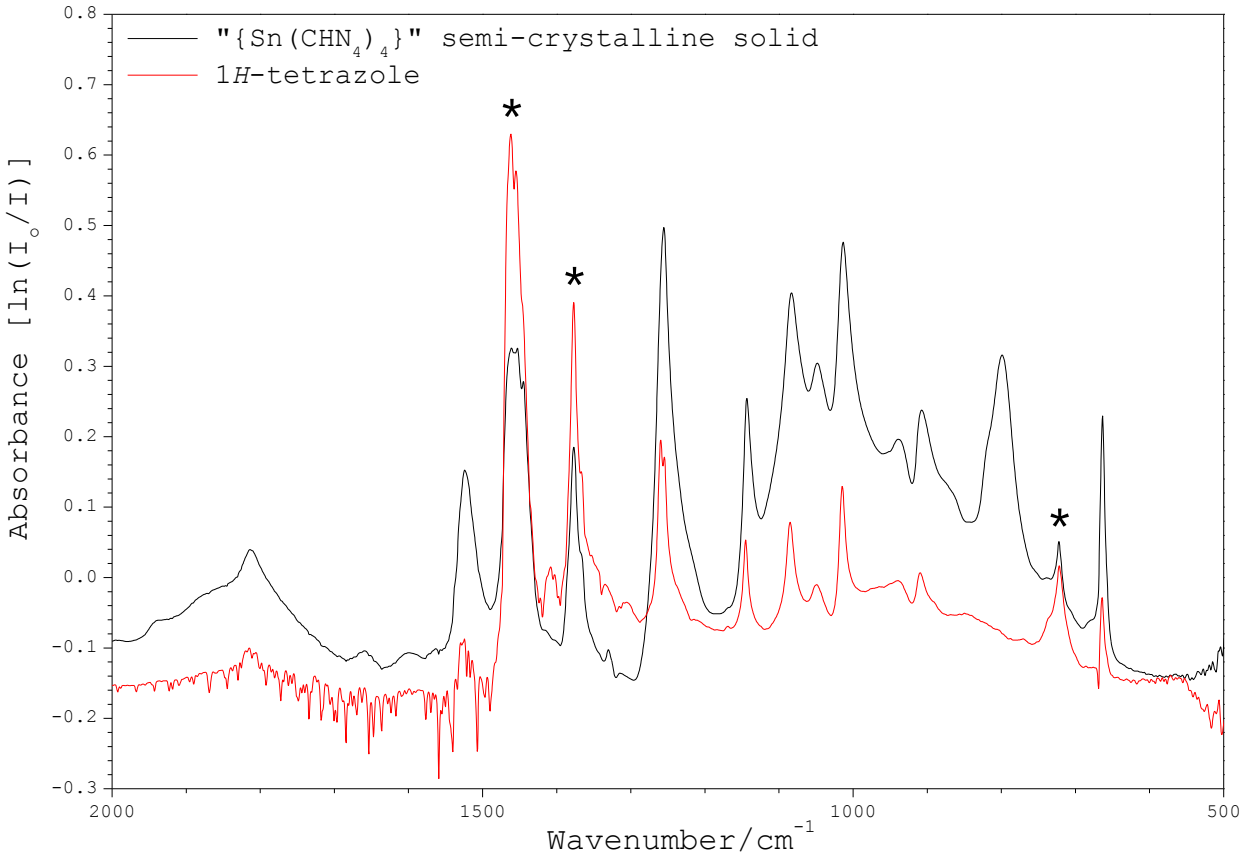

Figure 108 – Nujol mull IR spectral comparison of 1*H*-tetrazole and the semi-crystalline "{Sn(CHN$_4$)$_4$}". The matching spectra support the hypothesis that the semi-crystalline solid is 1*H*-tetrazole produced by decomposition.

Together the IR comparison and the recorded ^{1}H NMR spectrum matching that of 1*H*-tetrazole allows the conclusion that the reaction did not result in the production of the intended product, but rather resulted in decomposition of the TMS-CHN$_4$ reagent into 1*H*-tetrazole.

4.3 Conclusions

The initial experiment of this study focussed upon the synthesis of the monomeric $[Sn(CHN_4)_2(py)_2]$ complex, based upon the preparation for the reported $[Sn(N_3)_2(py)_2]$. What was instead isolated was $\{Sn(CHN_4)_2(py)_2\}_n$, a neutral tin-centred co-ordination polymer. This fascinating complex contains repeating five co-ordinate tin centres, with four tetrazolyl ligands bound in the equitorial plane and a single pyridine ring co-ordinating in an axial position. Overall this geometry can be described as a distorted square-based pyramid. This distortion is caused by the repulsive effect of the tin lone pair. The tetrazolate ligands bridge to adjacent tin centres in a N(1), N(3) fashion, resulting in a 2D polymeric sheet. The pyridine ligands are orientated out of the plane, and a second 2D sheet can "flip" to ensure that the pyridine rings are aligned. The formation of this bilayer structure was initially believed to have been driven by pi-pi stacking between the pyridine ligands. However the distances between them are too large, and it is likely to be simply due to sterics.

This preparation was adapted and resulted in the significant conclusion that can be taken from this investigation; the synthesis of the first homoleptic low valent tetrazolato-tin co-ordination polymer, $PPh_4\{Sn(CHN_4)_3\}$. Although homoleptic tetrazolate-based co-ordination polymers have been observed, examples from group 14 have until this study been overlooked. The polymer is built up again from repeating five co-ordinate tin centres, all exhibiting a distorted square-based pyramid geometry. Each tin centre is connected by bridging tetrazolate rings, which bridge in an N(1)-N(3) fashion. The result is an undulating 2D sheet polymer, with each sheet separated by a layer of the PPh_4 cations and THF molecules.

After the success using tin, the preparative method was subsequently extended to antimony and bismuth. Antimony was investigated first but rather than the expected co-ordination polymer an unusual cage-like system was isolated, consisting of three antimony centres bound to an interstitial fluorine, which was orientated in a trigonal planar fashion. Six tetrazolyl ligands are shared between the antimony centres, with each tetrazolate ring bridging between two Sb atoms in a N(1)-N(3) fashion. This results in each antimony co-ordination centre containing the previously observed square-based pyramid geometry, distorted by the Sb lone pair.

Extending to bismuth resulted in similar observations, but as yet no unequivocal structural data has been obtained. The reason for the preferential formation of the antimony (and likely bismuth) cage-like complex seems to stem from the crystal structure of the antimony(III) and bismuth(III) fluorides. Each crystal structure contains a fluorine environment that is associated to three metal centres in a roughly trigonal planar geometry. This highly restricted fluorine could be difficult to exchange, resulting in tetrazolate-fluorine substitution occurring at less hindered fluorine atoms. This would result in this interstitial fluorine being "trapped" at the centre of the newly formed complex. If true this indicates that the formation of homoleptic antimony and bismuth tetrazolato- co-ordination polymers in not possible using this particular preparative technique. Nonetheless the characterisation of a unique class of antimony complex is of extreme interest.

The significance of a tetrazolate-based co-ordination polymer is the potential for high-nitrogen content. This coupled with the high density of a polymer could result in a highly energetic material. In an attempt to produce such a material the preparation of the neutral homoleptic $\{Sn(CHN_4)_4\}$ co-ordination polymer was attempted. Tetrazolate-fluorine exchange does occur, as evidenced by the presence of TMS-F in the ^1H NMR spectrum of the crude material. A semi-crystalline material was isolated but upon spectral investigation this was found to be 1*H*-tetrazole. This is likely due to heating used during the reaction, which led to decomposition of the TMS-CHN_4, which has a relatively low decomposition temperature of 135°C. Despite this setback it is likely that the preparation of $\{Sn(CHN_4)_4\}$ is possible but requires gentle reaction conditions combined with a longer reaction time.

5. The Pentazole Ring: Investigations Concerning its Isolation, Metal Co-ordination and Purification

5.1 Overview

The arylpentazoles are a class of compounds that contain the pentazole ring and importantly are stable at low temperatures. Functionalisation at the *para*- position of the phenyl ring allows for some control over the sensitivity and reactivity of the arylpentazole, as does a suitable solvent system. The pentazole ring is attached to the aryl subunit by a C-N single bond. It was hypothesised that this bond could be prone to reduction, allowing for the removal of the pentazolate anion. If this free pentazolate anion could be stabilised it would represent a significant advancement in the field of high-nitrogen compounds. It is hoped that through the use of metal-based reducing agents, specifically sodium naphthalenide and the (^{mes}nacnac)Mg−Mg(nanac^{mes}) species the necessary reduction and stabilisation will be achieved. As it is theorised that the pentazolate anion could be stabilised by metal co-ordination it was also attempted to synthesise a rhodium-bound aryl pentazole through the reaction between the *p*-dimethylaminophenyldiazonium tetrafluoroborate salt[90] and $Rh(N_3)_2Cp^*$.[91]

As these investigations require pure starting materials the scope of the study is limited by the small number of crystalline arylpentazoles available.[36,92] It is an additional objective to design a re-crystallisation method for the *p*-hydroxyphenylpentazole so that it can also be used in analogous studies.

5.2 Results and Discussion

The synthesis of *p*-dimethylaminophenylpentazole (DMAP-pentazole) is not a trivial procedure, requiring a strict control over reaction temperature at all times. All reaction materials were kept below -40°C. Mixing the reactants above this temperature risked the decomposition of the product, which is thermally sensitive. The decomposition of DMAP-pentazole can easily be observed using IR spectroscopy.

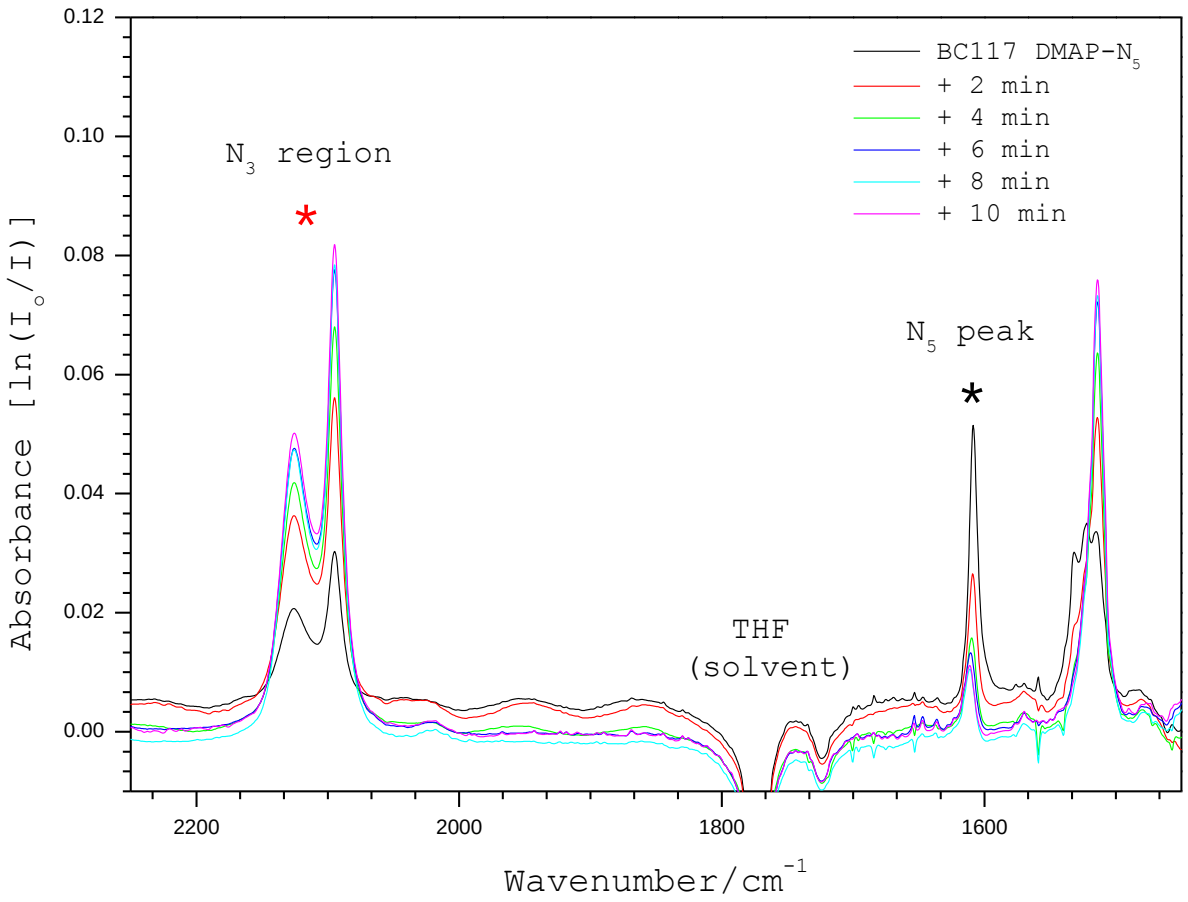

Figure 109 – Nujol mull IR series monitoring the thermal decomposition of DMAP-pentazole.

In the initial spectrum, the DMAP-pentazole peak at 1609 cm^{-1} (*) is intense, and is accompanied by smaller DMAP-azide peaks at 2125 cm^{-1} and 2095 cm^{-1} (*). The Nujol mull spectrum was recorded at room temperature; therefore the azide is present due to the decomposition of DMAP-pentazole. As sequential IR spectra are recorded the pentazole peak falls in intensity and is accompanied by an increase in DMAP-azide concentration. The DMAP-azide can be re-crystallised from DCM as a yellow crystalline solid. It is a light-sensitive compound and must be kept in the dark.

5.2.1 Attempted reduction of *p*-dimethylaminophenylpentazole

The first objective of this investigation was to attempt the cleavage of the C–N bond attaching the aromatic unit to the N_5 ring. Disputed evidence of the isolation of free pentazolate has been produced[32,93,94], but the extremely sensitive nature of pentazolate makes true characterisation near impossible at present.

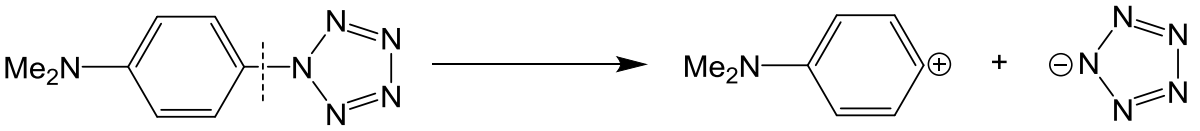

Scheme 27 – Chemdraw illustration of C-N bond cleavage for DMAP-pentazole.

It is possible that the C–N bond could be broken by a reducing agent and this was initially investigated using sodium naphthalenide.[95] It is a strong reducing agent produced through the reaction of sodium metal and naphthalene, in dry THF. The dark green solution is highly air sensitive and cannot be reliably stored longer than a few days at −25°C.

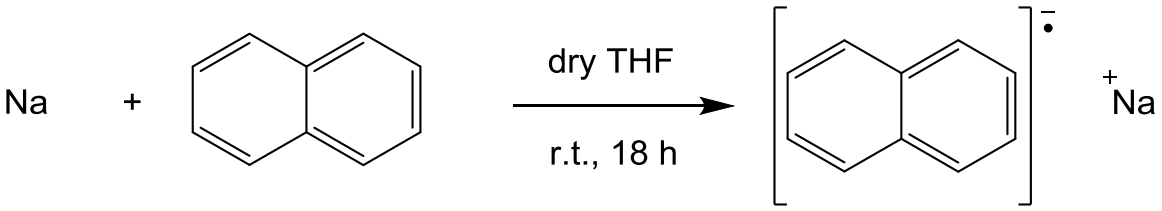

Scheme 28 – Synthesis of the sodium naphthalenide reducing agent.

Once the sodium naphthalenide stock solution had been prepared and the approximate concentration was known it could be reacted with DMAP-pentazole in an attempt to selectively cleave the C–N bond. The light brown DMAP-pentazole produced a light brown suspension upon addition of dry THF at –78°C, with crystalline material remaining undissolved. The corresponding amount of sodium naphthalenide was added via volumetric pipette. Upon addition an immediate purple colour was seen at the site of mixing, which was also accompanied by bubbling. The purple colour quickly dissipated leaving a yellow solution once the addition was completed, with all crystalline DMAP-pentazole that was previously suspended disappearing. After 5 minutes stirring at –78°C a solution cell IR spectrum was recorded.

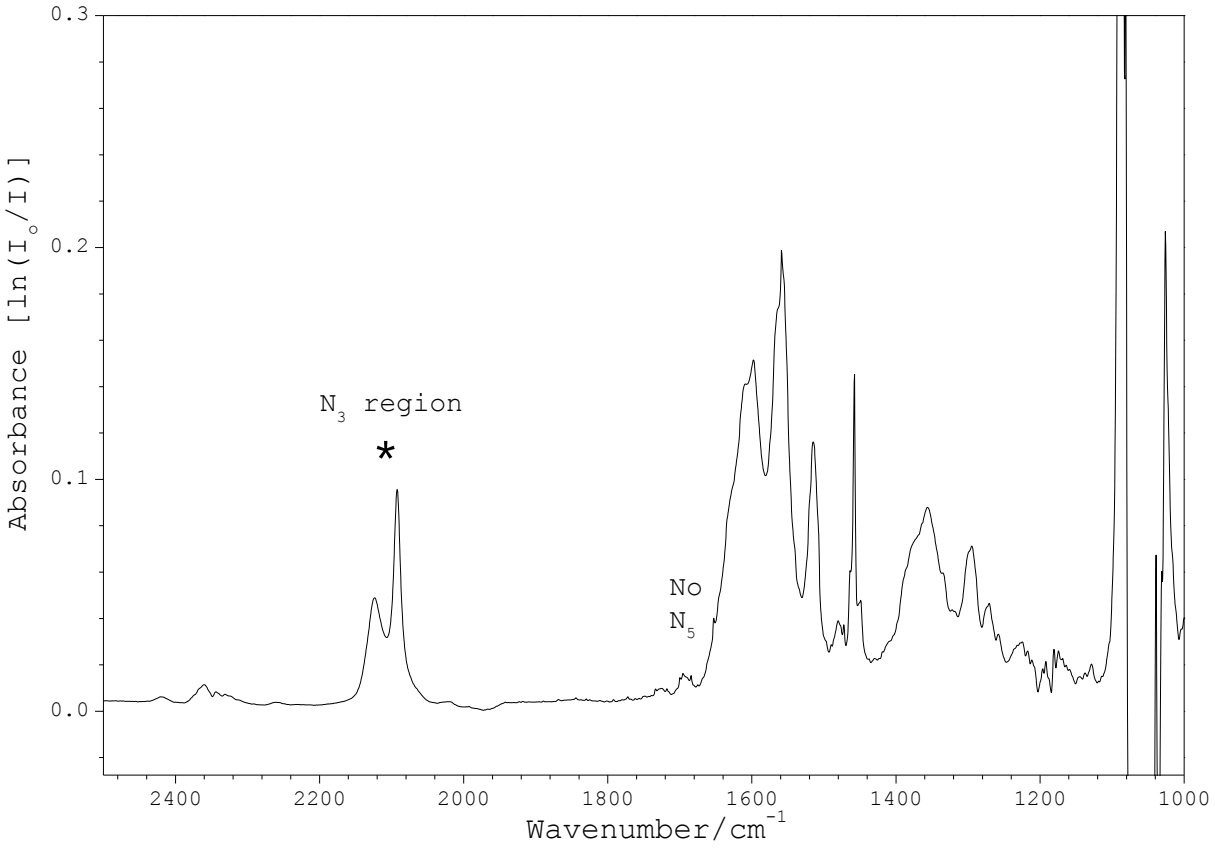

Figure 110 – Solution cell IR spectrum of the resulting solution from the reaction between sodium naphthalenide and DMAP-pentazole.

This indicates that the solution contains only DMAP-azide, the decomposition product. The decomposition would also result in the release of dinitrogen which would explain the observed bubbling. The stirring of the yellow solution was continued whilst it was allowed to slowly warm to room temperature.

Over the course of one hour the solution did not change in appearance. The solvent was subsequently removed and the yellow solid was analysed using IR spectroscopy.

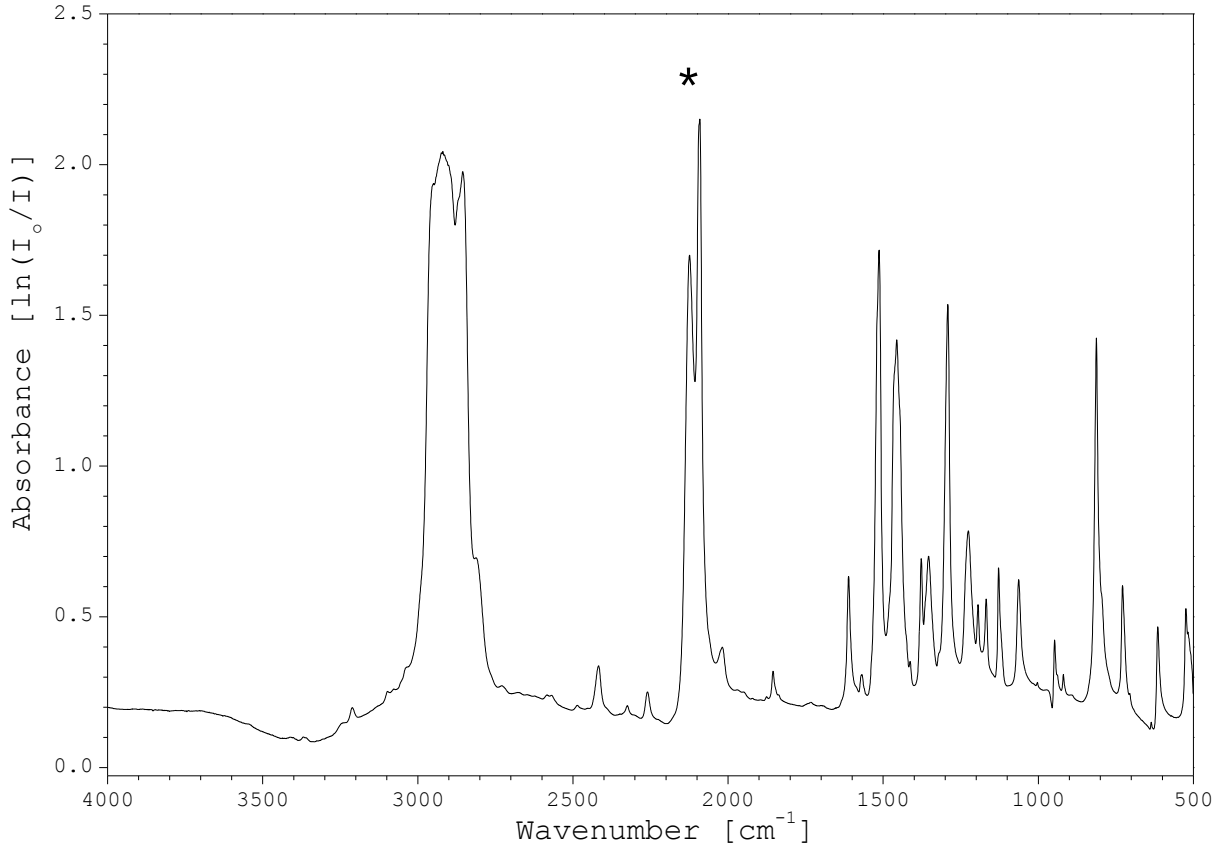

Figure 111 – Nujol mull IR spectrum of the yellow solid from the reaction between sodium naphthalenide and DMAP-pentazole. Strongly suggests that the reaction simply results in the production of DMAP-N_3.

This IR spectrum confirmed that the reaction resulted in the decomposition of the DMAP-azide. The significant problem with the use of sodium naphthalenide is that it is a stock solution. Although the concentration can be estimated, the calculation assumes 100% yield of sodium naphthalenide, which is unlikely. Also the highly sensitive nature of sodium naphthalenide means that within the stock solution there will be a certain amount of decomposition. Uncertainty about the concentration of the stock solution results in poor control of the stoichiometric ratio between sodium naphthalenide and DMAP-pentazole. The presence of DMAP-azide is indicative of the site of reduction; rather than the cleavage of the C–N bond the sodium naphthalenide instead breaks apart the pentazole ring, resulting in the arylazide. This highlights the importance of selectivity; the reducing agent must attack universally at the C–N bond.

This process would be exacerbated if the reducing agent was present in excess, which without strict control over the stoichiometry of the reaction is possible. What is required is a milder reducing agent that can be purified and easily used in a stoichiometric fashion. Mg(I) dimers have been shown to act as reducing agents[96] and it was hypothesised that these compounds could satisfy the above requirements. The first step toward the synthesis of the ([mes]nacnac)Mg–Mg([mes]nanac) dimer[97] was the preparation of the mesityl "nacnac" ligand. All steps leading to the dimer are published procedures, allowing the comparison of spectral data with the literature values.[98]

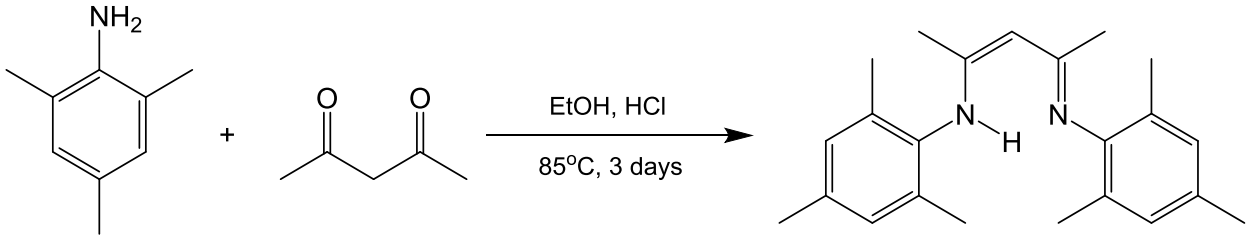

Scheme 29 – Preparation of [mes]nacnac-H

The crude product is a brown oil that under high vacuum results in an oily, semi-crystalline solid which is washed with cold methanol. Hot acetonitrile is a suitable crystallisation solvent and produced large, colourless crystals. The product is probed using ^{1}H NMR spectroscopy. There are several hydrogen environments in the product as illustrated in figure 115.

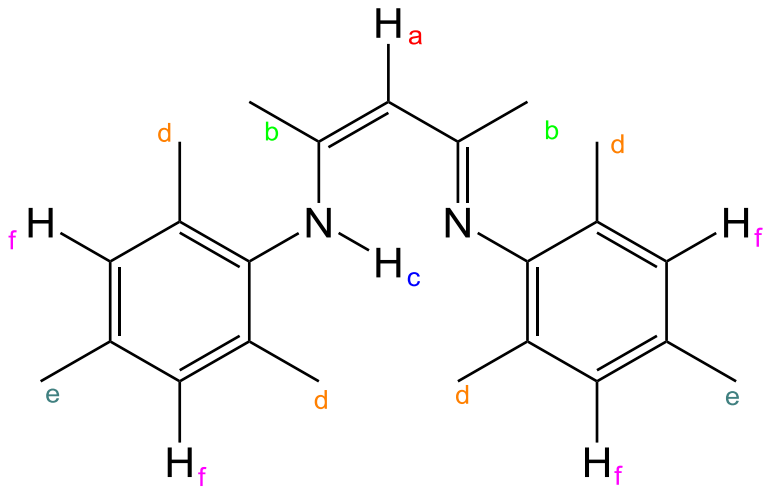

Figure 112 – Colour coded hydrogen environments found within [mes]nacnac-H.

The resulting ^{1}H NMR spectrum (figure 113) contains the expected proton signals, in their expected positions. Small amounts of impurities are present and a large acetonitrile peak can be observed at (*), present due to its use as a re-crystallisation solvent. The peak at 12.17 ppm (*) is significant as it is due to the amino proton designated as H_c in figure 112. This is a reactive position, and the extent of the next step of the preparation can be monitored using this characteristic peak.

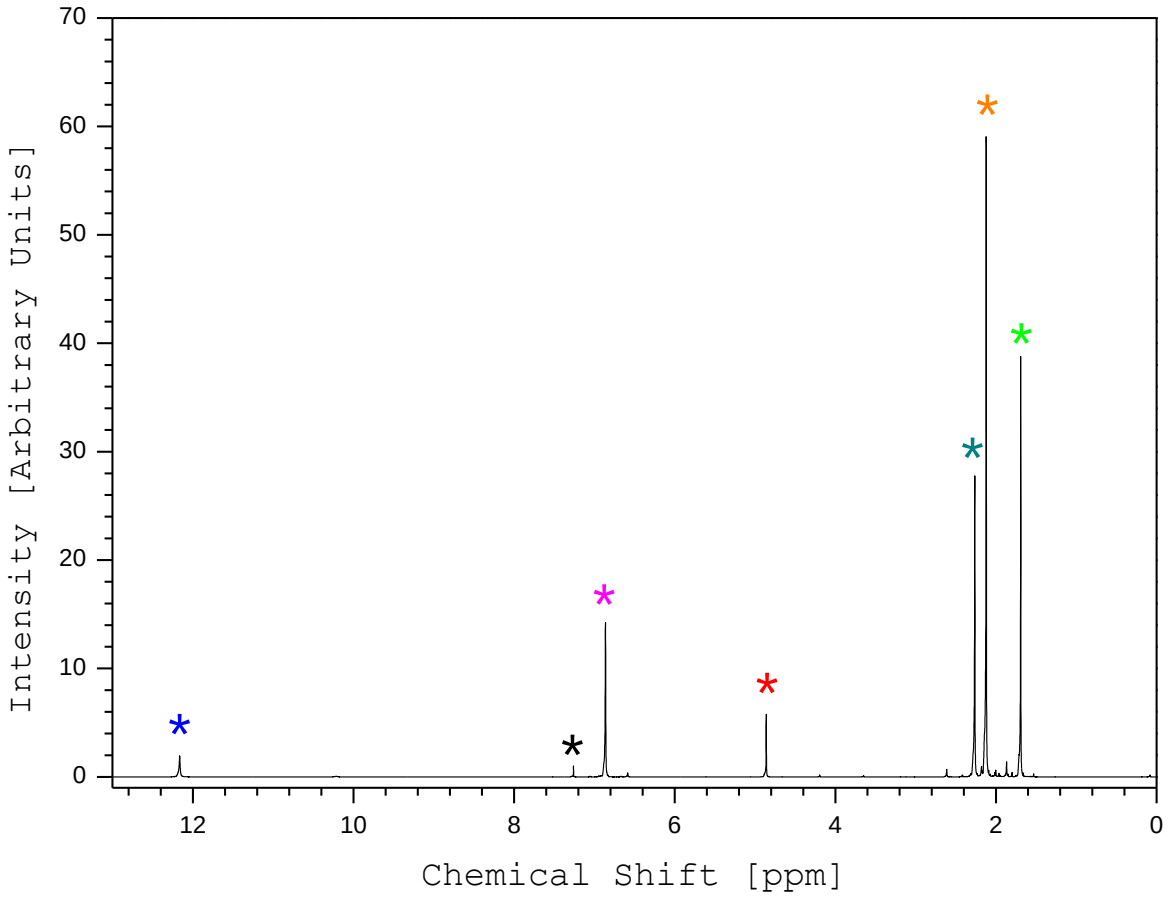

Figure 113 – ^{1}H NMR spectrum of ^{mes}nacnac-H in benzene-d_6. Colours refer to the hydrogen environments detailed in figure 112. Benzene-d_6 peak is marked by *.

Subsequently, the ^{mes}nacnac-H was lithiated using n-butyllithium to produce the required ^{mes}nacnac-Li. The yellow solid was washed with cold hexane to remove impurities (small, unmarked peaks remain in figure 113). The solid was analysed using ^{1}H NMR spectroscopy. It is expected that the amino proton will have been removed, due to its substitution for the lithium atom.

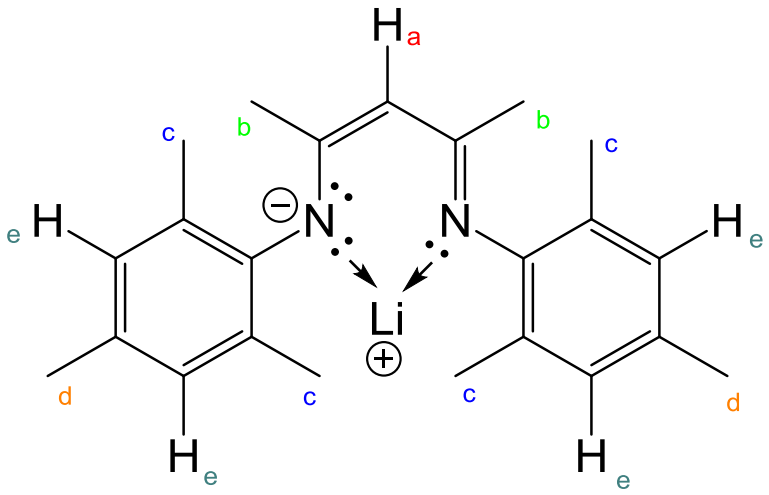

Figure 114 – Colour coded hydrogen environments found within the lithiated reagent ^{mes}nacnac-Li.

The ^{1}H NMR spectrum was disappointing (figure 115). Whilst it suggested that the majority of the yellow solid is the expected product, there are impurities present. A significant example is the presence of the ^{mes}nacnac–H starting material due to the small peak at 12.26 ppm. This hypothesis is supported by other peaks that can be attributed to the presence of the reactant, indicated by (*). A slight shift in ppm observed in comparison to figure can be explained by the use of a different NMR solvent, benzene-d^6 rather than deuterated chloroform. The product is not crystallised upon isolation, it is simply washed with cold hexane in an attempt to remove all impurities. The long, thin nature of a Schlenk tube coupled with the large amount of solid that was produced is the likely cause of the presence of impurities; the washing solvent was unable to penetrate the entirety of the solid, therefore could not effectively remove the impurities. It is of the upmost importance that these impurities are removed. This could be achieved through the use a more efficient washing procedure, or ideally a method for re-crystallisation. As seen in the next step the ^{mes}nacnac-Li is soluble and stable in dry Et_2O. It is therefore logical that a concentration solution of ^{mes}nacnac-Li in dry Et_2O could produce pure crystalline material upon cooling to −25°C.

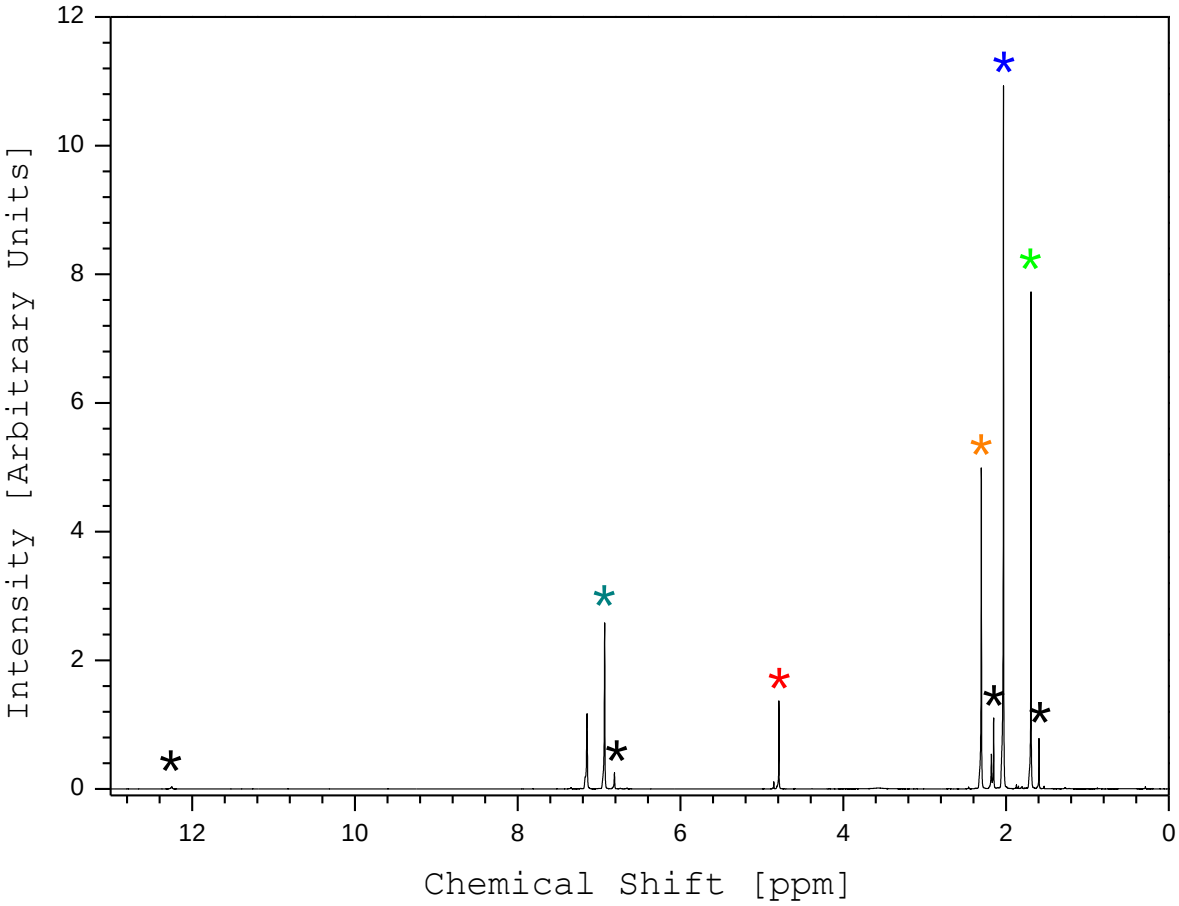

Figure 115 – ^{1}H NMR spectrum of ^{mes}nacnac-Li in benzene-d_6. Coloured asterisks refer to the hydrogen environments detailed in figure 114. Peaks due to impurities marked by *.

The next step was the reaction between the ^{mes}nacnac-Li and MgI_2 in dry Et_2O to produce the Mg(^{mes}nacnac)I·OEt_2. The MgI_2 can simply be produced by combining magnesium turnings with sublimed iodine. This produced the MgI_2·$2Et_2O$ dietherate as white crystals. The Et_2O can be removed under dynamic vacuum to yield the pure MgI_2.

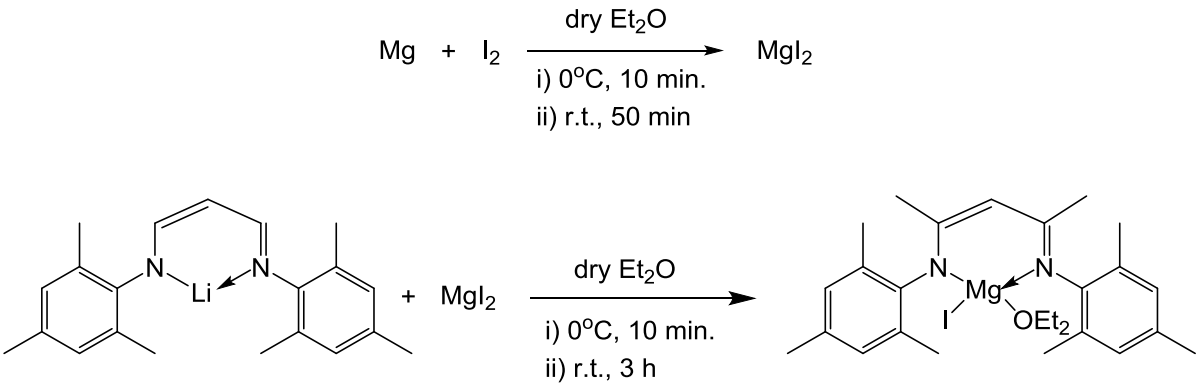

Scheme 30 – Preparations of MgI_2 and the Mg(^{mes}nacnac)I·OEt_2 precursor.

The crude Mg(^{mes}nacnac)I·OEt_2 was re-crystallised from toluene to give colourless crystals. It is paramount that this product is pure as it is the direct precursor to the (^{mes}nacnac)Mg–Mg(nanac^{mes}) dimer. The crystals were characterised using ^{1}H NMR spectroscopy. There should be five individual proton environments corresponding to the purified Mg(^{mes}nacnac)I·OEt_2, as indicated below. In addition, will be additional proton peaks attributed to the associated Et_2O.

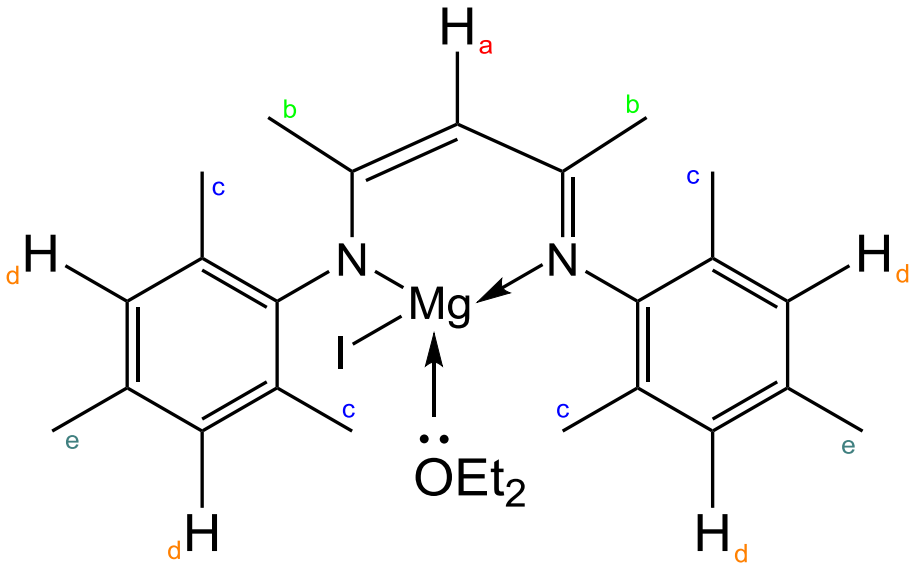

Figure 116 – Colour coded hydrogen environments found within the lithiated reagent Mg(^{mes}nacnac)I·OEt_2.

The Mg(^{mes}nacnac)I·OEt_2 was of high purity, containing very little visible impurities. This was an excellent result. All expected peaks are present in their expected positions and relative ratios, as indicated by the colour co-ordinated markers. The associated Et_2O (*) forms broad peaks rather than the expected triplet and quartet. It is possible that its presence also broadens the peaks at 2.19 ppm (*, 12H) and 2.59 ppm (*, 6H) attributed to Mg(^{mes}nacnac)I·OEt_2. This broadening caused their respective peak heights to be much smaller than the narrow peak at 1.60 ppm (*, 6H). Considering the peak areas the ratio was found to be 2:1:1, the expected ratio when considering the number of hydrogens at each symmetrically independent environment.

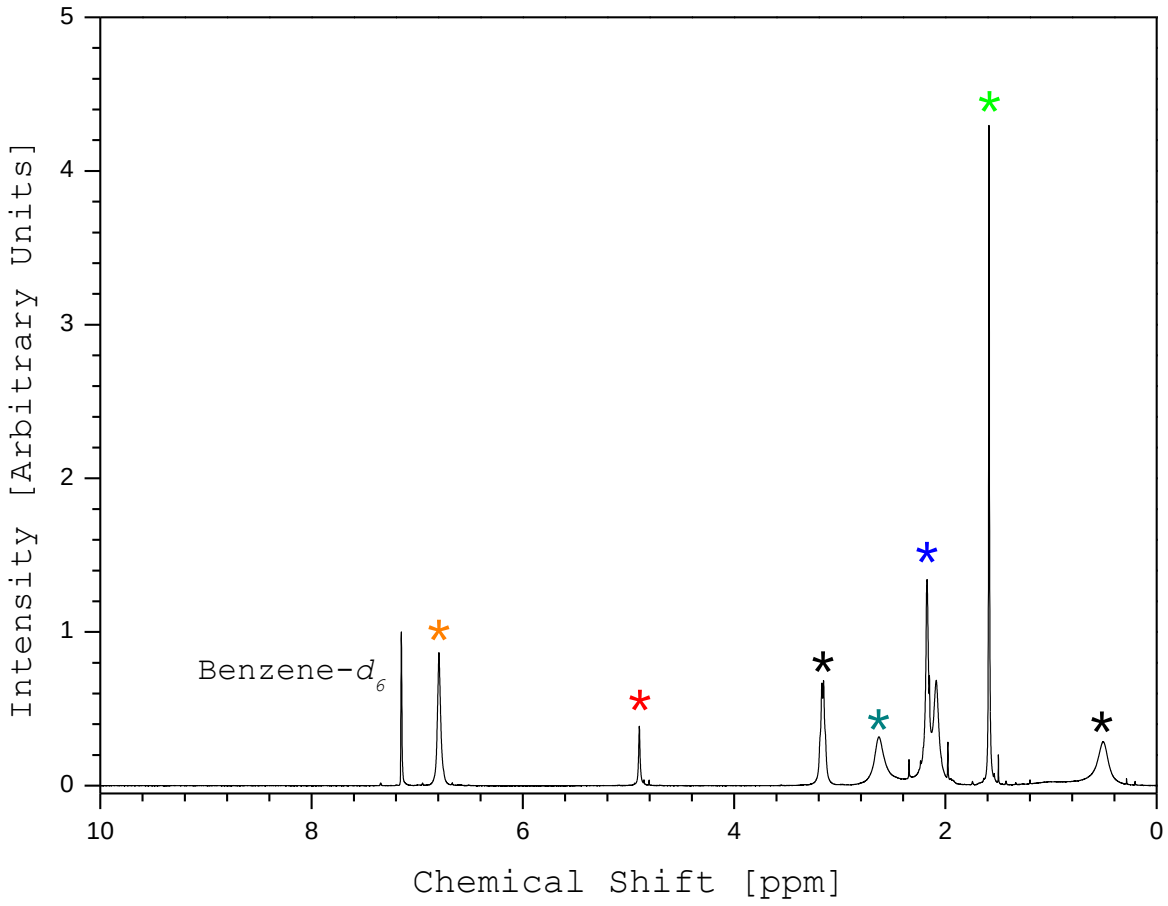

Figure 117 – ^{1}H NMR spectrum of Mg(^{mes}nacnac)I·OEt$_2$ in benzene-d_6. Colours refer to the hydrogen environments detailed in figure 116. Et$_2$O peaks are marked by (*).

The final step required the use of a sodium mirror to reduce the Mg(^{mes}nacnac)I·OEt$_2$ precursor into the desired (^{mes}nacnac)Mg–Mg(nanac^{mes}) dimer. The sodium mirror was prepared by heating sodium metal in a Schlenk tube whilst it is under dynamic vacuum. The sodium sublimes and re-solidifies upon contact with colder surfaces of the Schlenk tube. The advantage of a sodium mirror is the large surface area available for reaction.

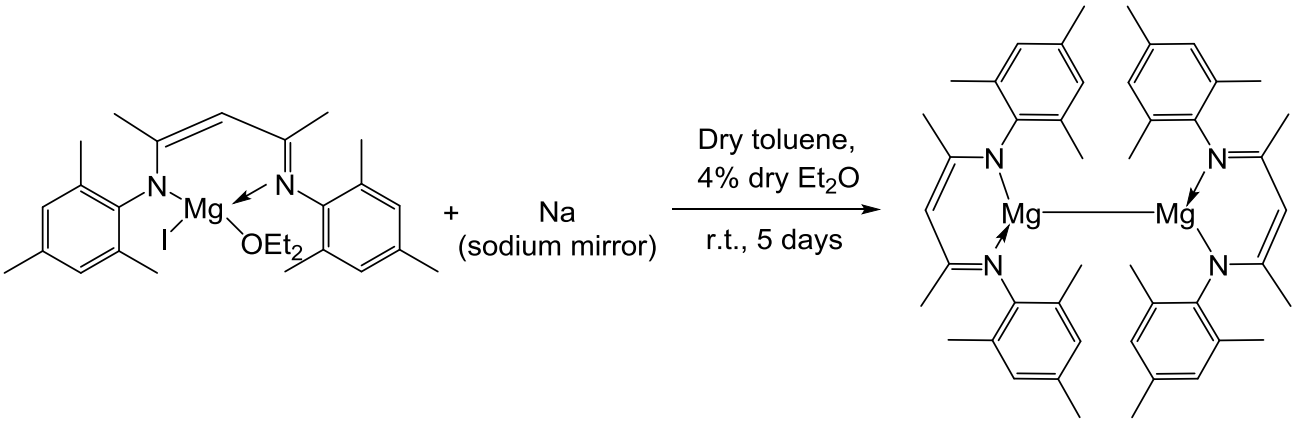

Scheme 31 – Final step in the preparation of the (^{mes}nacnac)Mg–Mg(nanac^{mes}) dimer.

A yellow solution resulted from the reaction, which was concentrated and cooled to -25°C to produce yellow crystals. These were washed with cold, dry toluene and dried under dynamic vacuum. ^{1}H NMR spectroscopy was used to confirm the presence of the (^{mes}nacnac)Mg–Mg(nanac^{mes}) dimer.

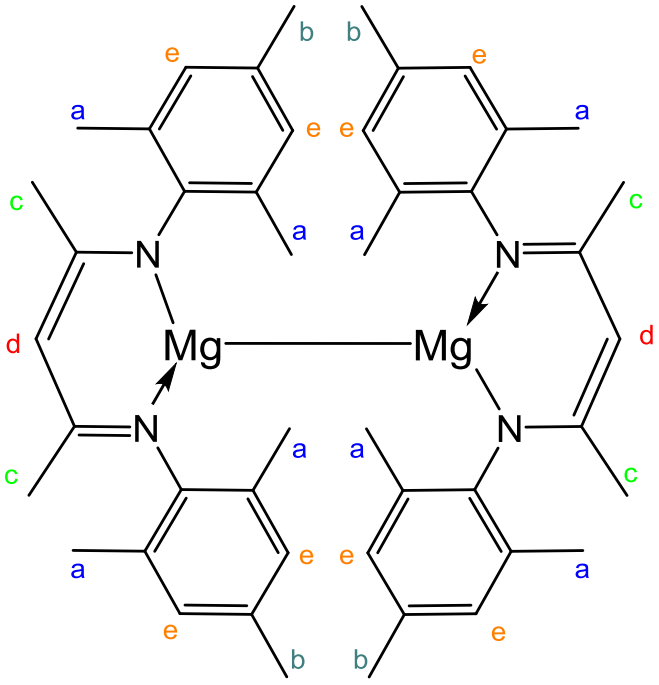

Figure 118 – Colour coded hydrogen environments found within the lithiated reagent (^{mes}nacnac)Mg–Mg(nanac^{mes}) dimer.

The highly symmetrical product possesses five different proton environments. These are all found in the identifying ^{1}H NMR spectrum (figure 119), as indicated by the appropriately coloured labels.

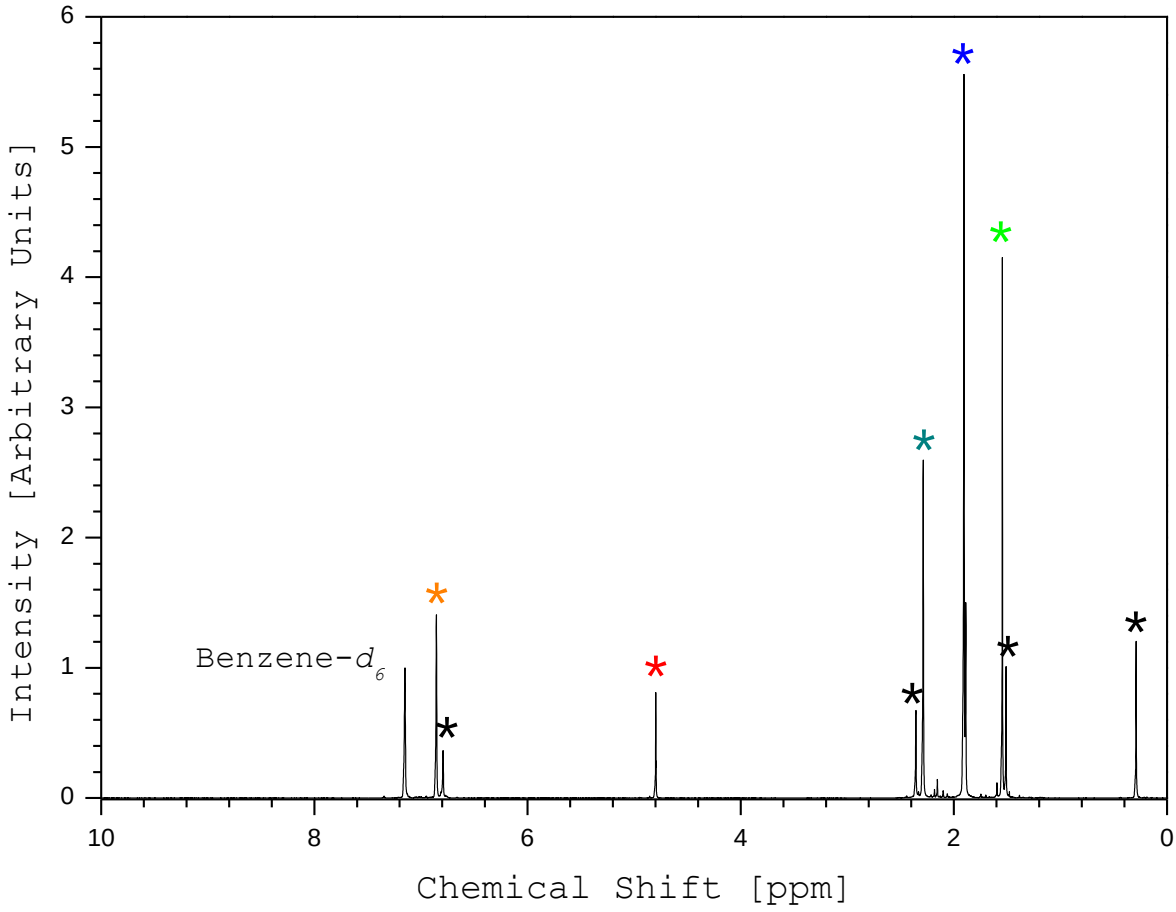

Figure 119 – ^{1}H NMR spectrum of (^{mes}nacnac)Mg–Mg(nanac^{mes}) dimer in *d*-benzene. Colours refer to the hydrogen environments detailed in figure 118.

Figure 119 indicates that the isolated (^{mes}nacnac)Mg–Mg(nanac^{mes}) dimer was of high purity. All expected peaks are present in their expected positions. There is no evidence for remaining solvent, with the absence of peaks that can be attributed to toluene or Et_2O. The Mg(^{mes}nacnac)I·OEt_2 starting material is present, indicated by the marked peaks (*). While the isolated product was crystalline, it is possible that a small amount of the reactant remained unreduced. The product was washed numerous times with cold, dry toluene, however it seems that this was insufficient, leaving behind the unmarked peaks that correspond to impurities. A second re-crystallisation would produce a product of increased purity, but at the expense of yield. Upon the isolation of the crystalline (^{mes}nacnac)Mg–Mg(nanac^{mes}) dimer it could be subsequently combined with DMAP-pentazole in order to evaluate the possibility of C–N cleavage, in addition to the stabilisation of the resulting free pentazolate ring.

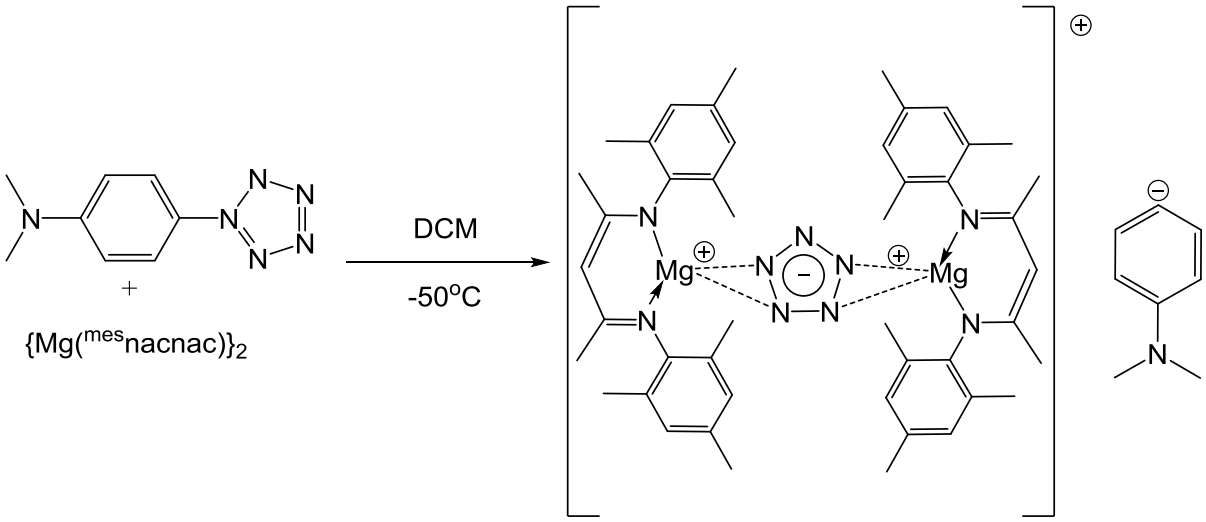

Scheme 32 – Scheme illustrating the possible reduction of DMAP-pentazole, producing a magnesium stabilised free pentazolate anion.

The hypothetical product is not likely to remain as represented above for a long period of time. Interaction with the proposed counter-ion could result in the separation of the product and the formation of a magnesium dimer with bridged pentazole rings. However this has not been observed experimentally; it is simply a prediction that is chemically possible.

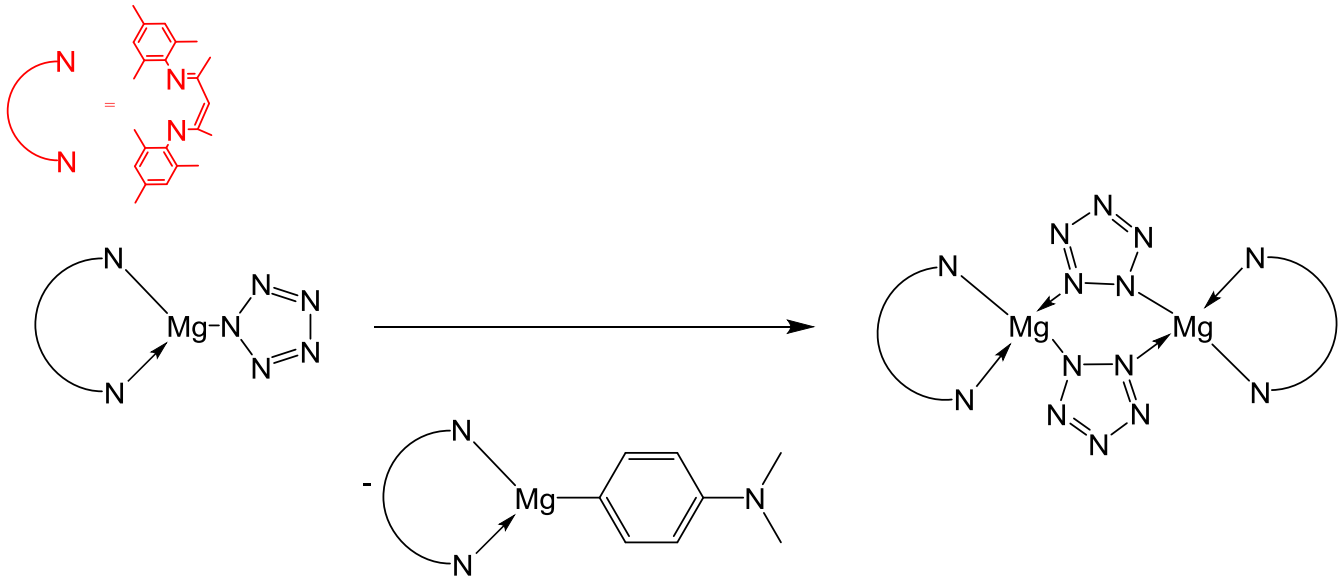

Scheme 33 – Possible dimerisation of a Mg-bound pentazole species.

The progress of the reaction was monitored using solution-cell IR spectroscopy. After four hours the concentration of pentazole in solution (*) remained constant. The time taken to record the sample unfortunately required exposure to room temperature, which could result in unreliable results. A high level of attention and control was maintained in order to minimise this effect.

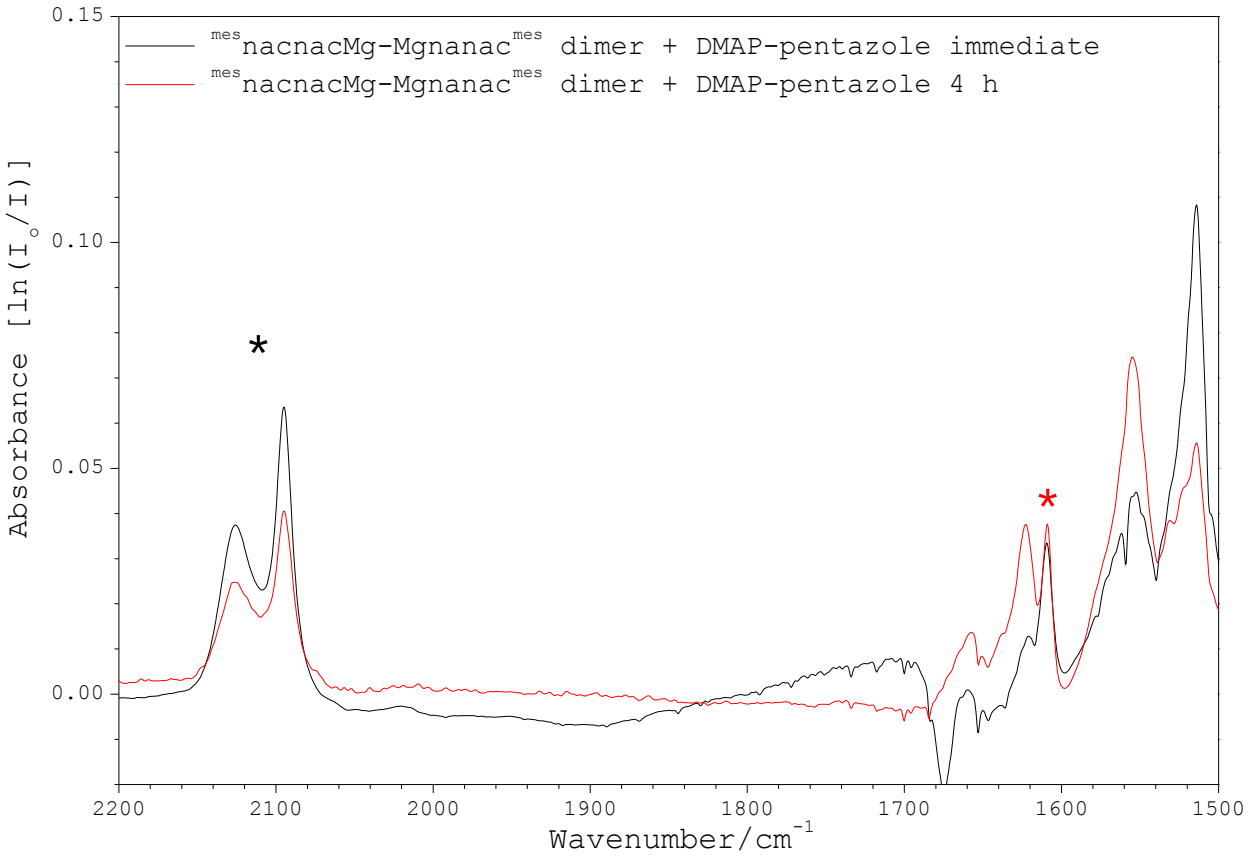

Figure 120 – Solution cell IR comparison illustrating the reaction progress after 4 h at -50°C.

After four hours the IR sample was allowed to decompose within the IR cell. This allowed in-situ observations of the decomposition process. This could help identify the nature of the reaction, if any had taken place. What is shown is that as the DMAP-pentazole remains in solution, evidenced by the rise in DMAP-azide (*) and loss of DMAP-pentazole (*). These peak positions are unchanged from free DMAP-pentazole, indicating that the attempted reduction did not take place.

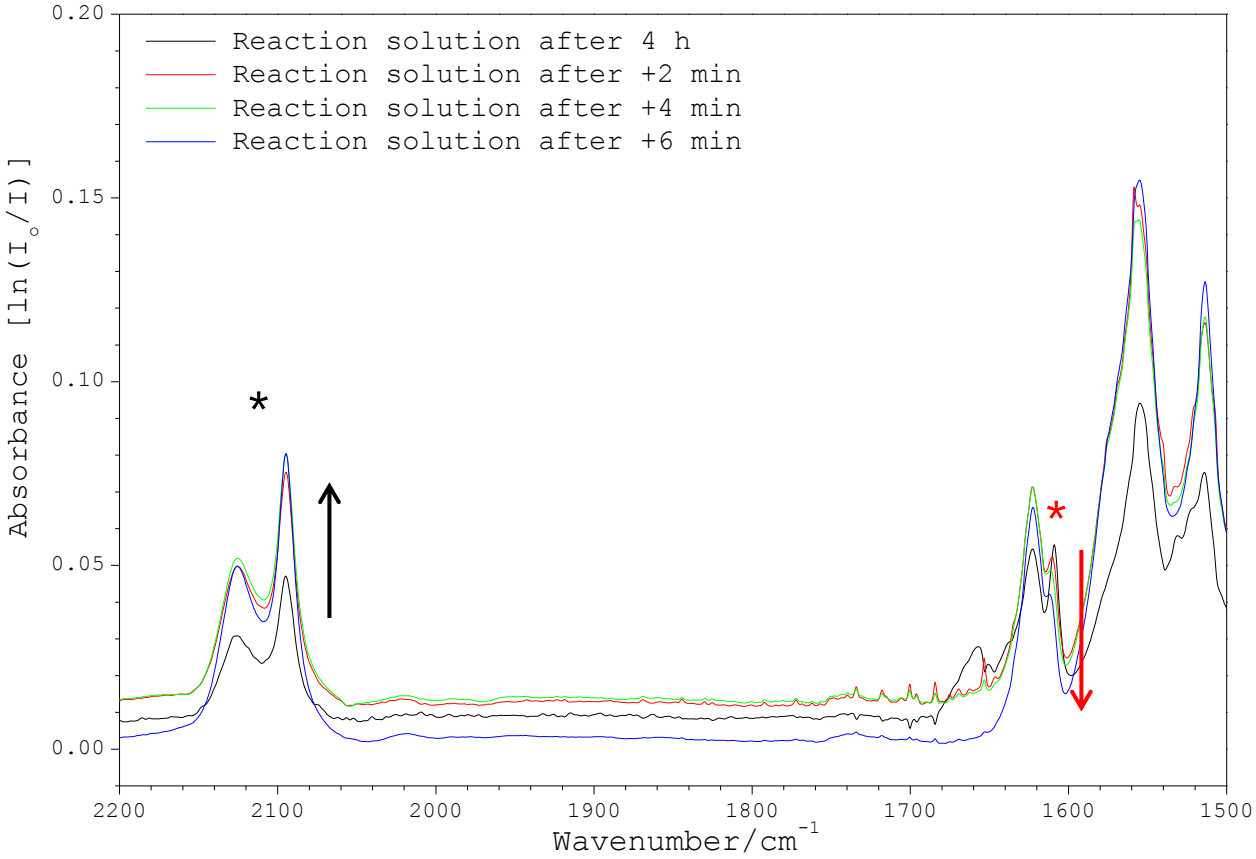

Figure 121 – Solution cell IR spectral comparison showing the decomposition of the 4 h solution as it warms to room temperature.

It is possible that at low temperature the (^{mes}nacnac)Mg–Mg(nanac^{mes}) dimer is not reactive enough to act upon the DMAP-pentazole. The reductions studied from the literature[96] begin at −80°C but are universally warmed to room temperature. If this is a requirement for a successful reduction of a reactant it is not suitable for reaction with arylpentazoles; the pentazole ring will decompose before the reduction can be achieved. This was evaluated by allowing the reaction solution to warm to room temperature whilst using IR spectroscopy to monitor the behaviour of the reaction. If reduction occurs it would be observable in the IR series (figure 122).

However as expected only decomposition of the DMAP-pentazole was observed, evidenced by the diminishing pentazole peak (*) and growing azide peak (*). This is the typical decomposition pattern, unaffected by any interaction with the (^{mes}nacnac)Mg–Mg(nanac^{mes}) dimer reducing agent. If reduction had taken place one would expect shifting of the pentazole peak indicating the unbound nature of the pentazole ring. The absence of reduction is further evidenced by the release of DMAP-azide; decomposition of the reduced "free" pentazole would produce hydrazoic acid (HN_3), which is not present in the below IR series.

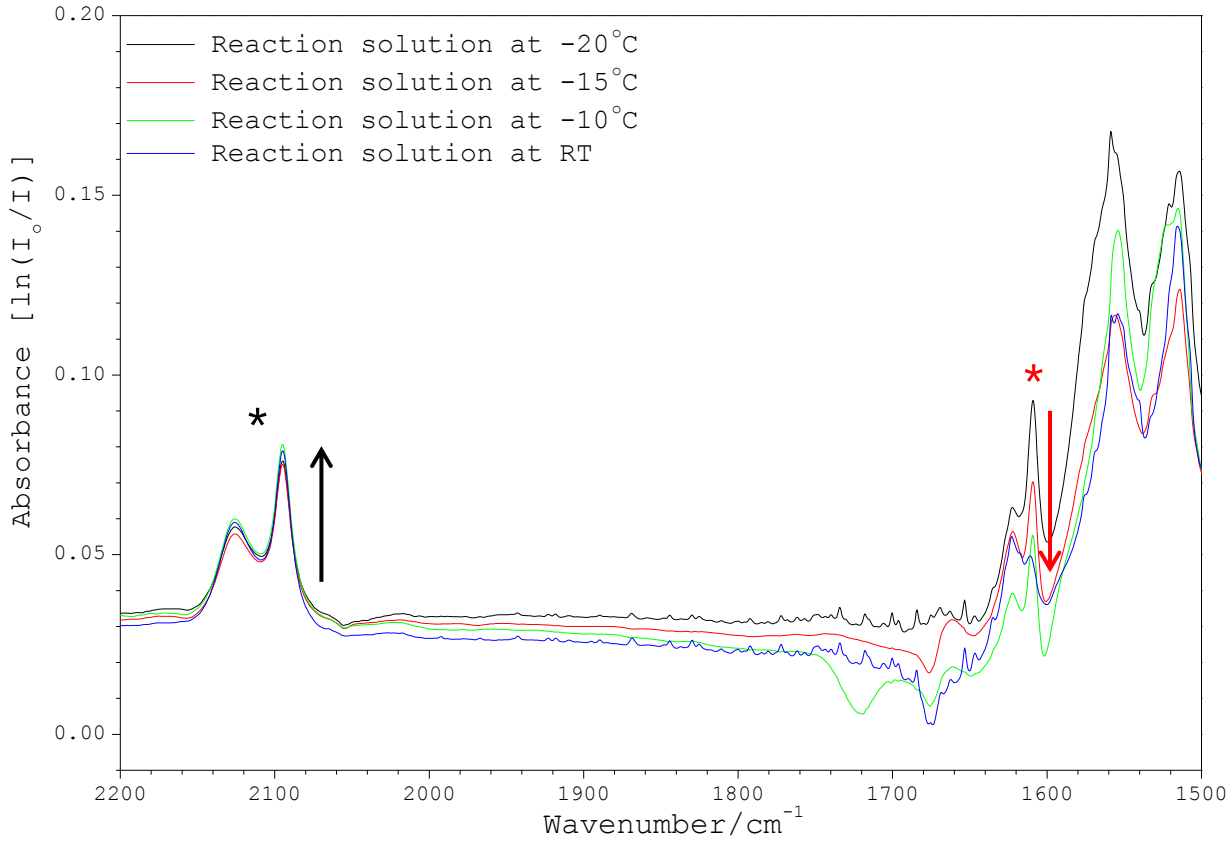

Figure 122 – Solution cell IR series following the reaction solution as it is allowed to warm to room temperature with stirring. This graph supports the hypothesis that no reaction with the reducing agent is observed as the decomposition profile matches that of free DMAP-pentazole.

The combined observations produce only one logical explanation; the (^{mes}nacnac)Mg–Mg(nanac^{mes}) dimer does not reduce DMAP-pentazole at low temperature. It is possible that prolonged time at higher temperatures could result in C–N cleavage; however this is not suitable for the temperature sensitive arylpentazole.

5.2.2 Combination of an aryldiazonium tetrafluoroborate salt and a Rhodium-bound azide

A second line of investigation focussed upon the possibility of the in-situ generation of a metal-bound pentazole ring. There is no precedent for a metal-bound pentazole system in the literature therefore the successful synthesis of such a system would be highly interesting. In addition, it has been calculated that if it was possible to cleave the C–N bond of an arylpentazole to yield a free pentazolate ring, it could be stabilised through the formation of a "sandwich-like" complex, in a similar fashion to ferrocene.[99] It would be advantageous to produce a metal-bound arylpentazole in order to study the bonding nature of such an attachment in addition to the effect on the stability of the pentazole ring.

The general procedure for synthesising an arylpentazole is the reaction between an ionic azide compound, such as NaN_3, and an aryldiazonium salt ($Ar–N_2^+X^-$). The diazonium salt is usually generated in situ due to its low stability. However if the diazonium intermediate could be synthesised in a pure fashion, and was stable enough for storage, this could provide the foundation for a spectroscopic study of the hypothetical formation of a metal-bound aryl pentazole. The use of a large stabilising anion could result in a diazonium salt with an increased stability. Tetrafluoroboric acid (HBF_4) was used in place of HCl in order to prepare the DMAP-$N_2^+BF_4^-$ diazonium salt.[100]

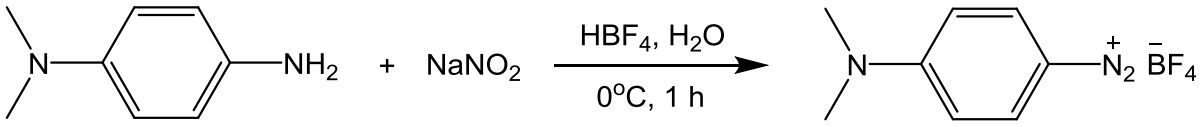

Scheme 34 – Synthesis of *p*-dimethylaminophenyldiazonium tetrafluoroborate (DMAP-$N_2^+BF_4^-$).

On addition of the HBF_4 the purple aniline solution quickly turns red. The addition of the sodium nitrite aqueous solution produced a brown-green foam. This can be quickly filtered using a simple sinter in order to minimise the time at room temperature. The crude product is washed with cold methanol and hexane, leaving an orange solid. The purified product was assessed using IR spectroscopy. The IR spectrum contained the expected N_2^+ peak at 2160 cm^{-1} (*), the assignment of which is supported by previously published reports on this

diazonium species.[100] This peak confirmed that the desired product had been synthesised, in a somewhat pure fashion.

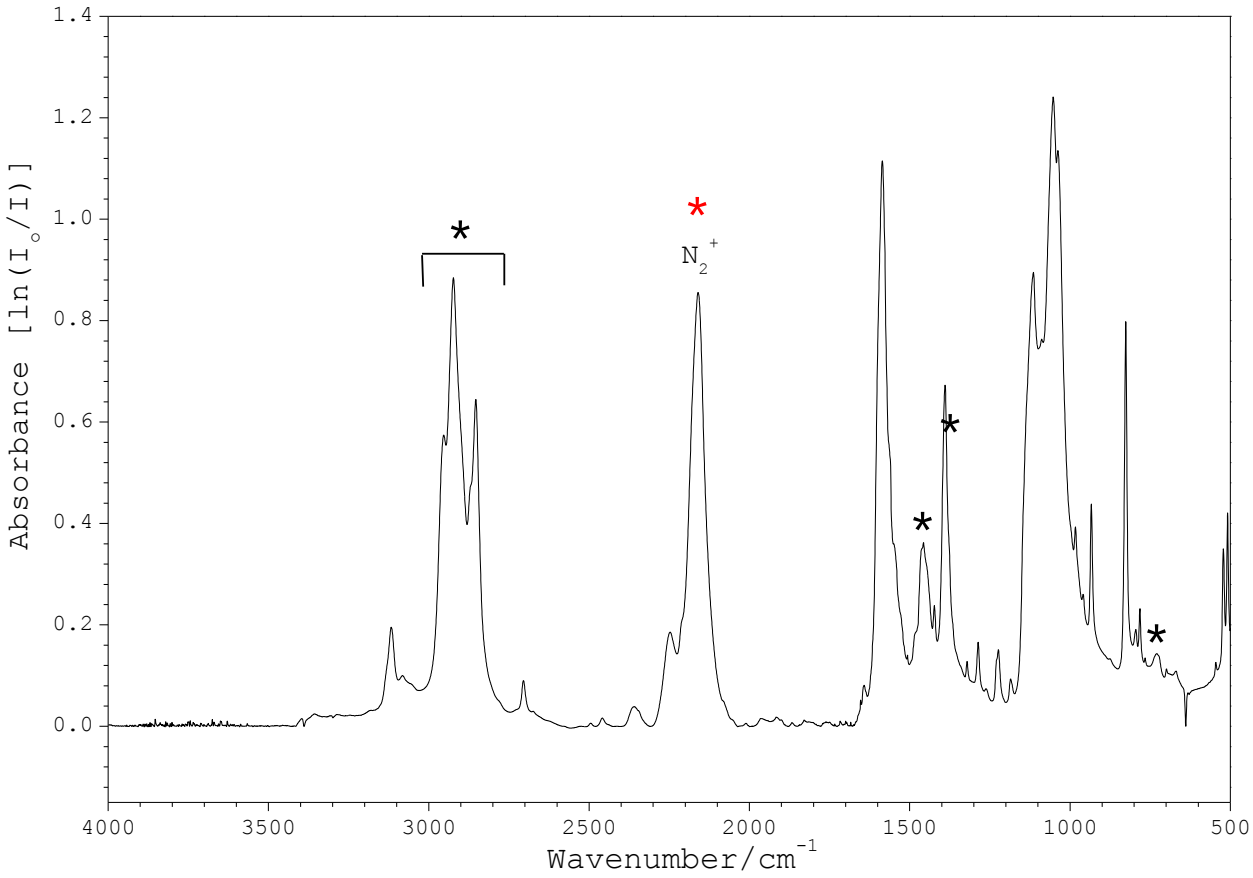

Figure 123 – Nujol mull IR spectrum of DMAP-$N_2^+BF_4^-$ with the N_2^+ band highlighted (*). Nujol bands are marked by asterisks (*).

The extent of the purity can be investigated using ^{1}H NMR spectroscopy. It is expected that there should be three proton environments, with a singlet caused by the methyl protons at environment a, and two doublets corresponding to environments b and c respectively.

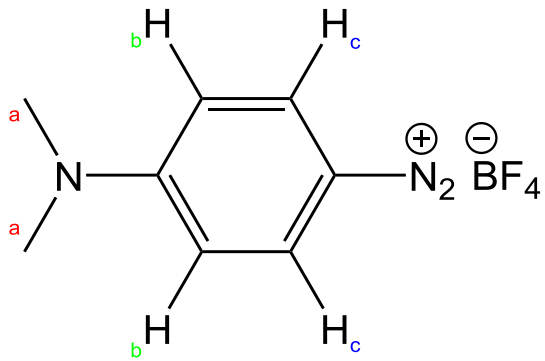

Figure 124 – Various hydrogen environments of DMAP-$N_2^+BF_4^-$.

As shown in figure 125 the resulting ^{1}H NMR spectrum indicates a high purity. The three expected proton environments are present, in the approximate ratios. There are small peaks present (*) but they are of such low concentration that they can be ignored.

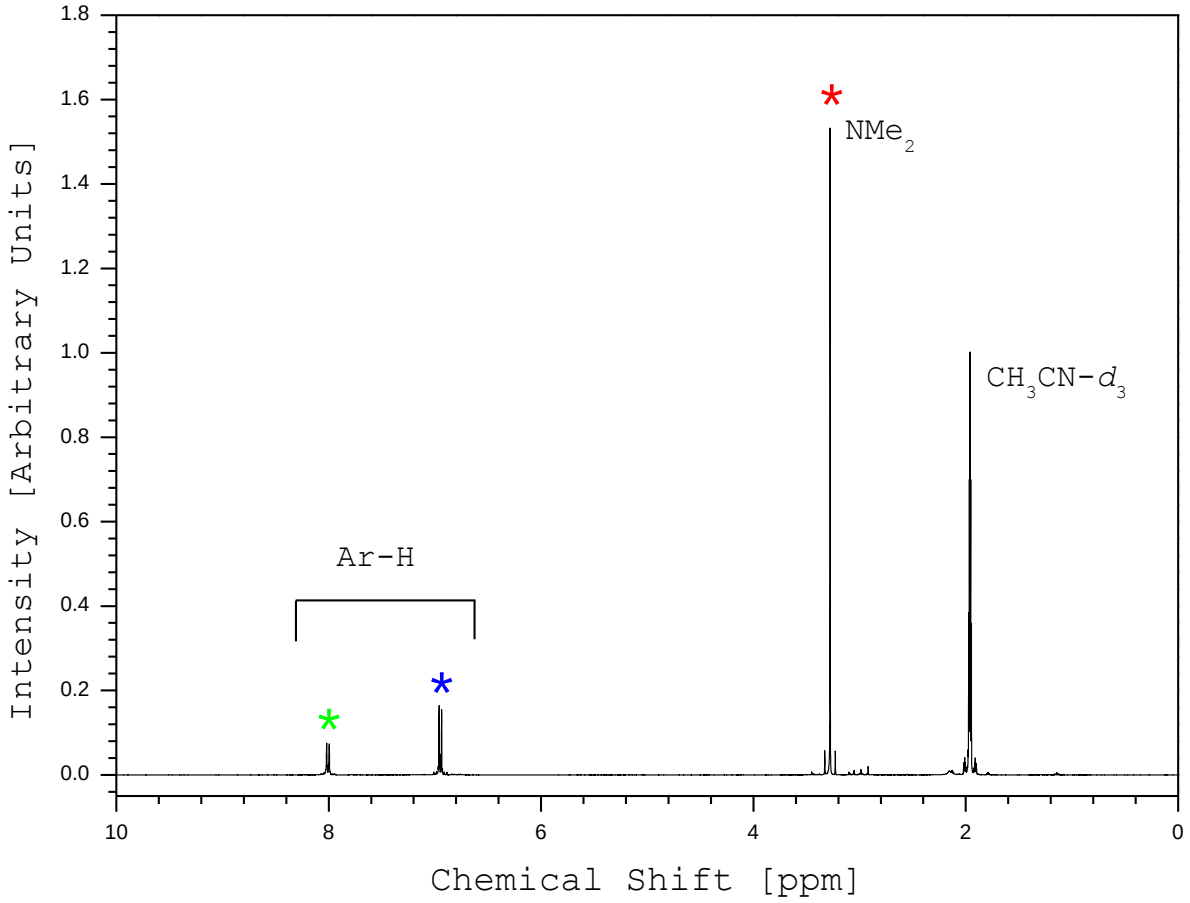

Figure 125 – ^{1}H NMR spectrum of DMAP-$N_2^+BF_4^-$ in CH_3CN-d_3. Colour coded hydrogen environments refer to figure 124.

The material is air stable and can be stored indefinitely at −25°C. In fact this synthesised material was still viable 12 months after synthesis. This is an extreme improvement in the stability of the diazonium salt, and the isolation of a pure product allows accurate control over the stoichiometry of future reactions. The metal-containing reactant used was $RhCp^*(N_3)_2$. This compound had been previously synthesised for a past investigation[92], and therefore was initially chosen due to the convenience of its availability. However in addition to this $RhCp^*(N_3)_2$ contains numerous NMR-active atoms, as well as the Cp* functional group which will give rise to a characteristic peak. It should be therefore straightforward to follow the reaction between $RhCp^*(N_3)_2$ and DMAP-$N_2^+BF_4$ using in-situ ^{1}H NMR spectroscopy.

The first reaction attempted concerned DMAP-$N_2^+BF_4$ and RhCp*$(N_3)_2$ Initial mixing was performed at −20°C and the first ^{1}H NMR spectrum was immediately recorded. The sample was warmed within the NMR spectrometer to with subsequent spectra being recorded at −10°C, 0°C, 10°C and 20°C. These can be overlaid in order to evaluate the change illustrated in the ^{1}H NMR series.

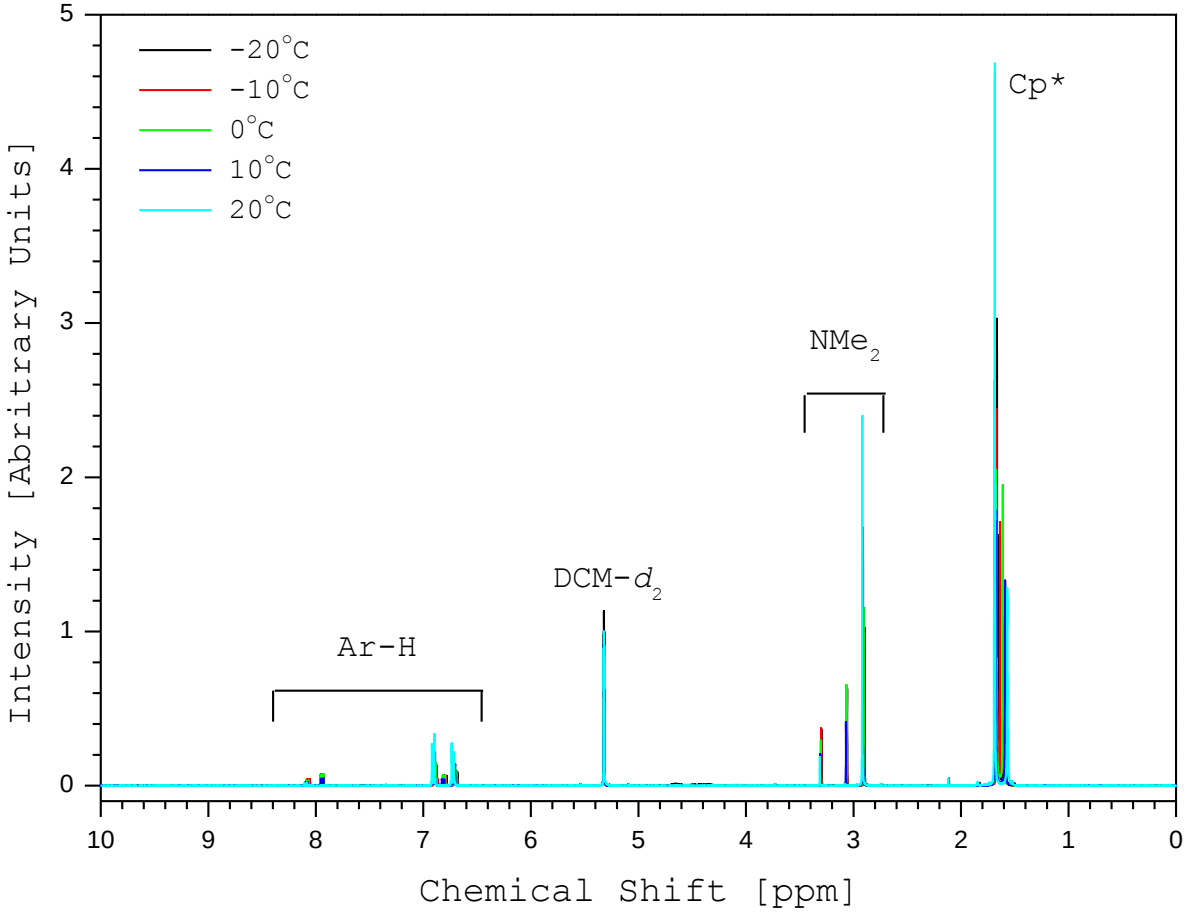

Figure 126 – ^{1}H NMR series of the reaction between DMAP-$N_2^+BF_4^-$ and RhCp*$(N_3)_2$ in DCM-d_2.

There will be multiple hydrogen environments present in the ^{1}H NMR series, caused by the presence of the DMAP-$N_2^+BF_4^-$, the potentially Rh-bound DMAP-pentazole and the DMAP-azide that is unavoidably produced alongside the DMAP-pentazole.

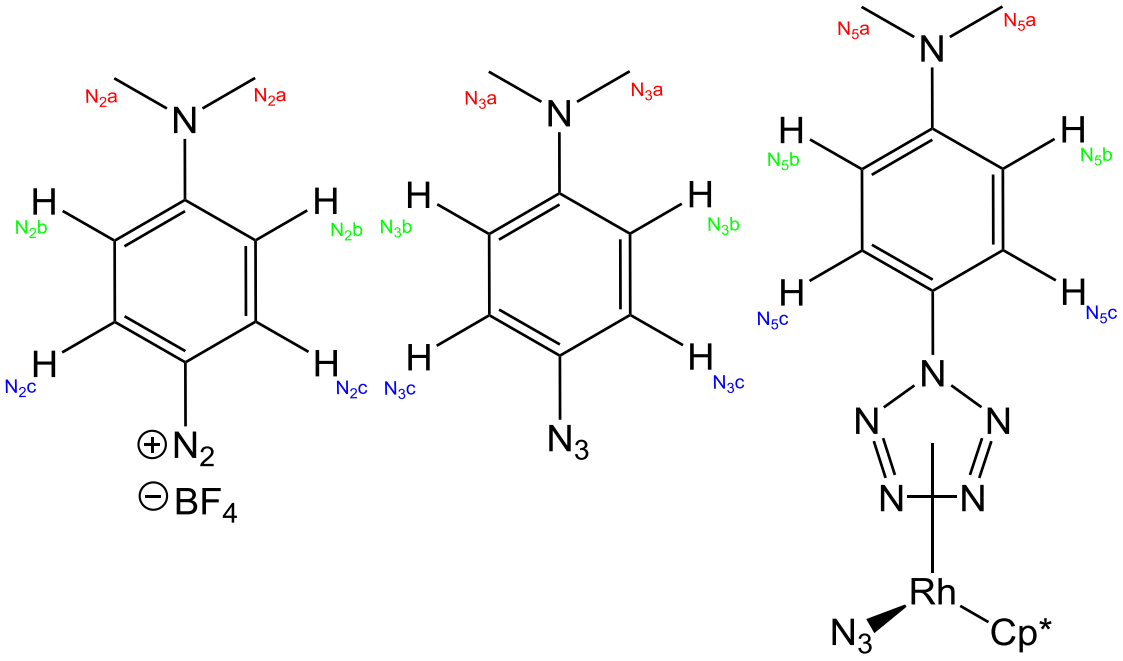

Figure 127 – H environments present in the reagents and potential product.

The overall ^{1}H NMR series contains all expected peaks, at all temperatures, and is therefore difficult to interpret. There are also certain unknowns within the investigation, such as the role of the BF_4^- anion and the possible binding mode of the pentazole ring to the metal centre. Only the η^3 bonding mode is possible whilst conforming to the 18 electron rule.

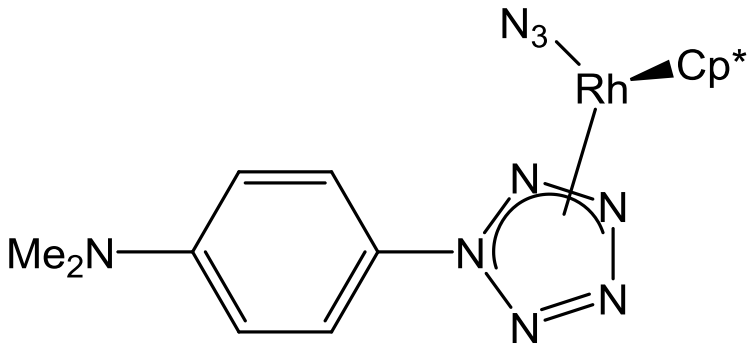

Figure 128 – Possible Rh binding mode for the potential product of the reaction between DMAP-$N_2^+BF_4^-$ and $RhCp^*(N_3)_2$.

In order to fully understand the results of the investigation it is necessary to focus upon the three relevant sections of the ^{1}H NMR series: the aryl proton region (figure 129), the NMe_2 region (figure 130) and the Cp* region (figure 131). Figure 129 illustrated that at −20°C, there is evidence for the presence of DMAP-pentazole due to the peaks at 6.78 ppm and 7.97 ppm. This was extremely exciting. This suggests that under the conditions used the

diazonium salt can react with the Rh-bound azide to form the desired arylpentazole. This is confirmed upon the warming of the NMR sample. As the temperature increases the DMAP-pentazole peak intensities drop, whilst the peaks corresponding to DMAP-azide at 6.72 ppm and 6.92 ppm both increase. This phenomenon is due to the temperature sensitive nature of the produced DMAP-pentazole, and can be the only explanation for this observation. The diazonium peaks at 6.92 ppm (overlaps with the DMAP-azide peak) and 8.08 ppm are present due to the ongoing nature of the reaction. An NMR tube is a poor reaction vessel and for this reason any reaction taking place will occur at a slow rate. In addition it is possible that the diazonium salt is present in a slight excess.

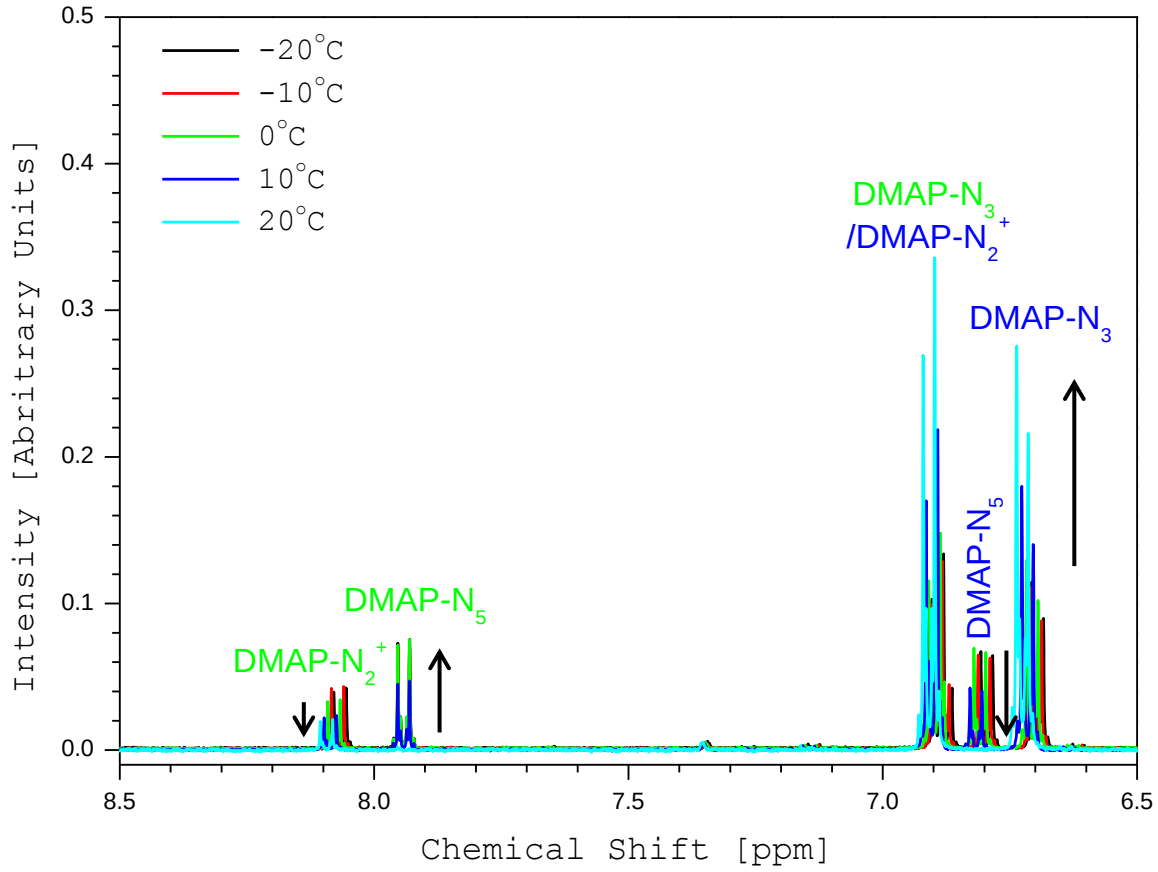

Figure 129 – Aryl region of the ^{1}H NMR reaction. This graph will contain the aryl proton environments of the unreacted DMAP-$N_2^+BF_4^-$, the "Rh-bound" DMAP-pentazole product and the DMAP-N_3 decomposition product. Small fluctuations in the position of the observed peaks are due to a change in solvent dielectric constant as temperature increases.

The methyl-amino proton region of the ^{1}H NMR series illustrated a similar observation (figure 130). There are three independent singlets present, one for each of the present compounds. The DMAP-$N_2^+BF_4^-$ peak is the furthest downfield at 3.30 ppm, DMAP-pentazole is at 3.05 ppm and the DMAP-azide is at 2.90 ppm. As the temperature increased the DMAP-$N_2^+BF_4^-$ intensity dropped, indicating the on-going state of the reaction. At 20°C the DMAP-$N_2^+BF_4^-$ peak remains, again an indication of either the reaction not proceeding to completion, or its presence in excess. Between −20°C and 0°C the "DMAP-pentazole" peak remains at its highest intensity, and quickly drops upon further warming. At room temperature "DMAP-pentazole" is completely absent from the reaction ^{1}H NMR solution. This corresponds with an increase in the concentration of DMAP-azide, an observation mirrored in the previously discussed section of the ^{1}H NMR series.

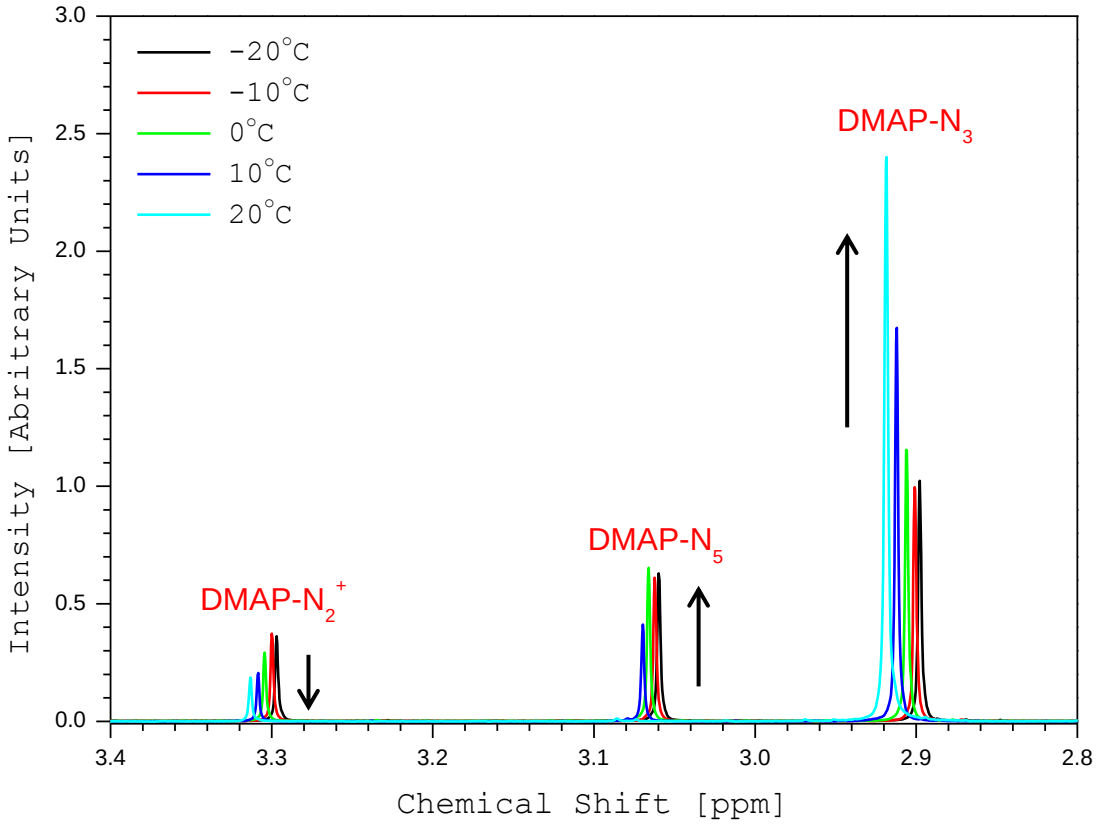

Figure 130 – Methyl amino region of the ^{1}H NMR series. This graph will contain the dimethylamino- proton environments of the unreacted DMAP-$N_2^+BF_4^-$, the "Rh-bound" DMAP-pentazole product and the DMAP-N_3 decomposition product. Small fluctuations in the position of the observed peaks are due to a change in solvent dielectric constant as temperature increases.

The final section of the ^{1}H NMR series that must be considered is that for the Cp* protons. These environments can be caused by the $RhCp^*(N_3)_2$ starting material, the possible Rh-bound pentazole product or the $[RhCp^*(N_3)]^+$ centre left by decomposition. Unfortunately this region is complex, and difficult to interpret accurately. At −20°C there are two distinct proton environments present, two rough doublets at 1.59 ppm and 1.65 ppm. In addition there is a shoulder upon the left peak of the doublet at 1.65 ppm. The two doublets could be attributed to the two possible Cp* containing compounds, $RhCp^*(N_3)_2$ and the Rh-bound pentazole product. The shoulder could indicate the small concentration of $[RhCp^*(N_3)]^+$ due to decomposition. At −10°C the doublet at 1.59 ppm is significantly weaker, whilst the doublet at 1.65 ppm has split, with the right peak moving to 1.64 ppm and the left peak moving slightly downfield to 1.67 ppm. In addition the shoulder on the left peak at 1.67 ppm has grown. This supports that below 0°C there are three individual Cp* environments, the weak doublet at 1.59 ppm, the singlet at 1.64 ppm and the singlet with a growing shoulder at 1.67 ppm.

At 0°C the doublet at 1.59 ppm is no longer present, leaving two proton environments; a singlet at 1.61 ppm and an approximate doublet at 1.68 ppm. The disappearance of the weak doublet a 1.59 ppm could be assigned to the disappearance of Rh-bound DMAP-pentazole. At 10°C the shoulder previously discussed has grown significantly, producing an almost perfect doublet at 1.68 ppm, in addition to a singlet at 1.59 ppm. The shoulder growth indicates that at this particular environment there is an increasing amount of splitting due to coupling to a spin-active nucleus. Finally once at 20°C there is now present a triplet at 1.69 ppm and a singlet at 1.57 ppm. The triplet could be caused by the splitting of the Cp* singlet by coupling to two ½ spin-active nuclei.

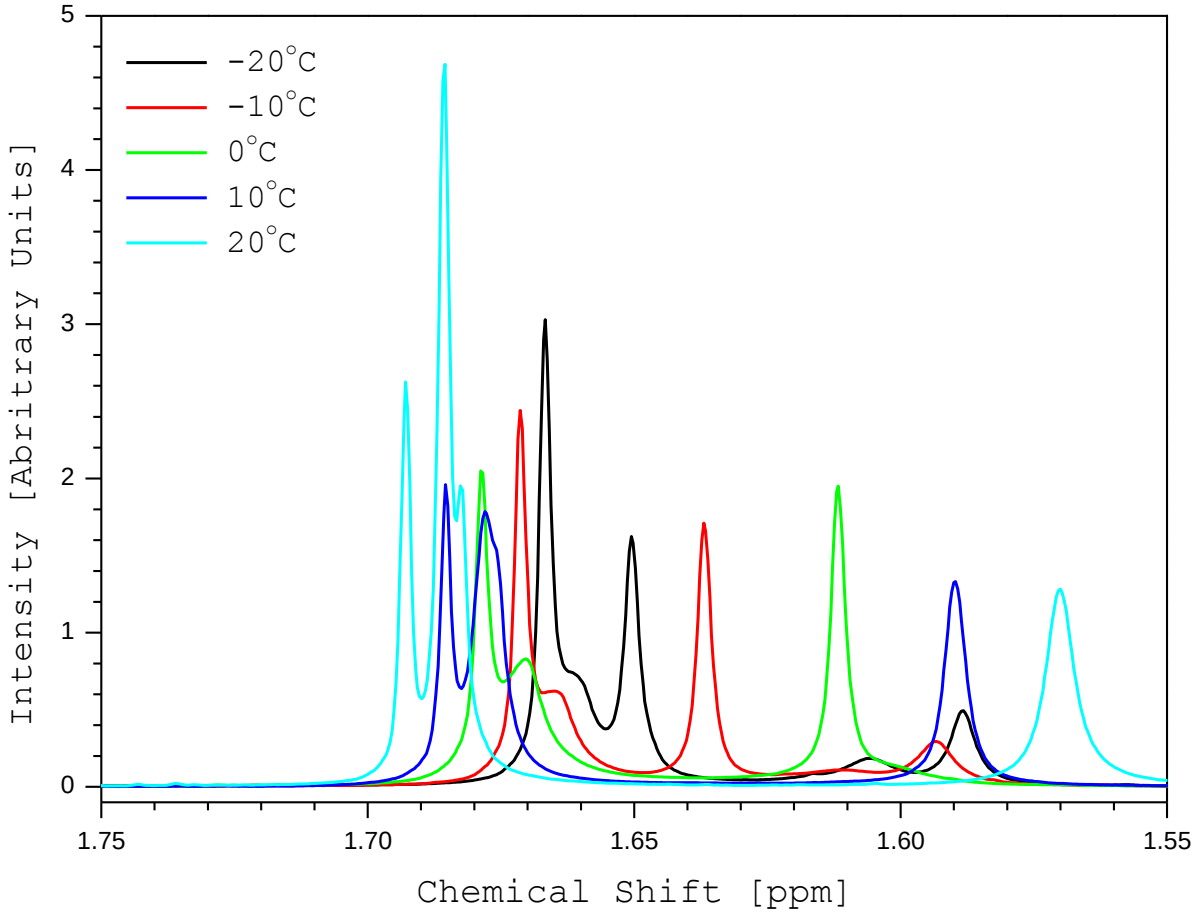

Figure 131– Cp* region of the ^{1}H NMR spectral series. This graph refers only to the RhCp*$(N_3)_2$ starting material, the potentially Rh-bound DMAP-pentazole and any Cp* containing decomposition products. Small fluctuations in the position of the observed peaks are due to a change in solvent dielectric constant as temperature increases.

Overall this is a highly complicated ^{1}H NMR pattern and required further discussion to form a sensible suggestion for the cause of the above observations. The presence of the triplet could be explained by the Rh centre abstracting a hydrogen atom upon decomposition of the Rh-bound DMAP-pentazole. Decomposition of the N_5 ring would lead to free DMAP-azide, and a $[RhCp^*(N_3)]^+$ centre, which is electron deficient.

This deficiency would be balanced by the abstraction of a hydrogen atom, which would also justify the presence of the observed triplet. To add to the complexity, the role of the BF_4^- anion is unclear. It is possible that the constant presence of this anion in solution could interfere with the expected path of the reaction, making all observations incorrect. It is possible that the $[RhCp^*(N_3)]^+$ could abstract a fluorine atom from the BF_4^- anion, producing

$RhCp^*(N_3)F$ and the neutral BF_3. This could also result in the observed triplet as ^{19}F has a nuclear spin of I = ½. The nature of the singlet remains unclear. For all expected compounds there should be splitting due to Rh coupling, ruling out the presence of a singlet. Free Cp* could explain the presence of a singlet, but the peak position does not match the expected value. In addition the mechanism for the release of Cp* from the Rh centre is not obvious. However, unforeseen reaction pathways could result in an unpredictable Cp* environment that gives rise to the singlet. Nonetheless this is a highly encouraging reaction, which proves that a metal-bound azide can be combined with an aryldiazonium salt to produce an arlypentazole. The question of whether this arylpentazole remained bound to the Rh centre or was released upon formation remains unclear.

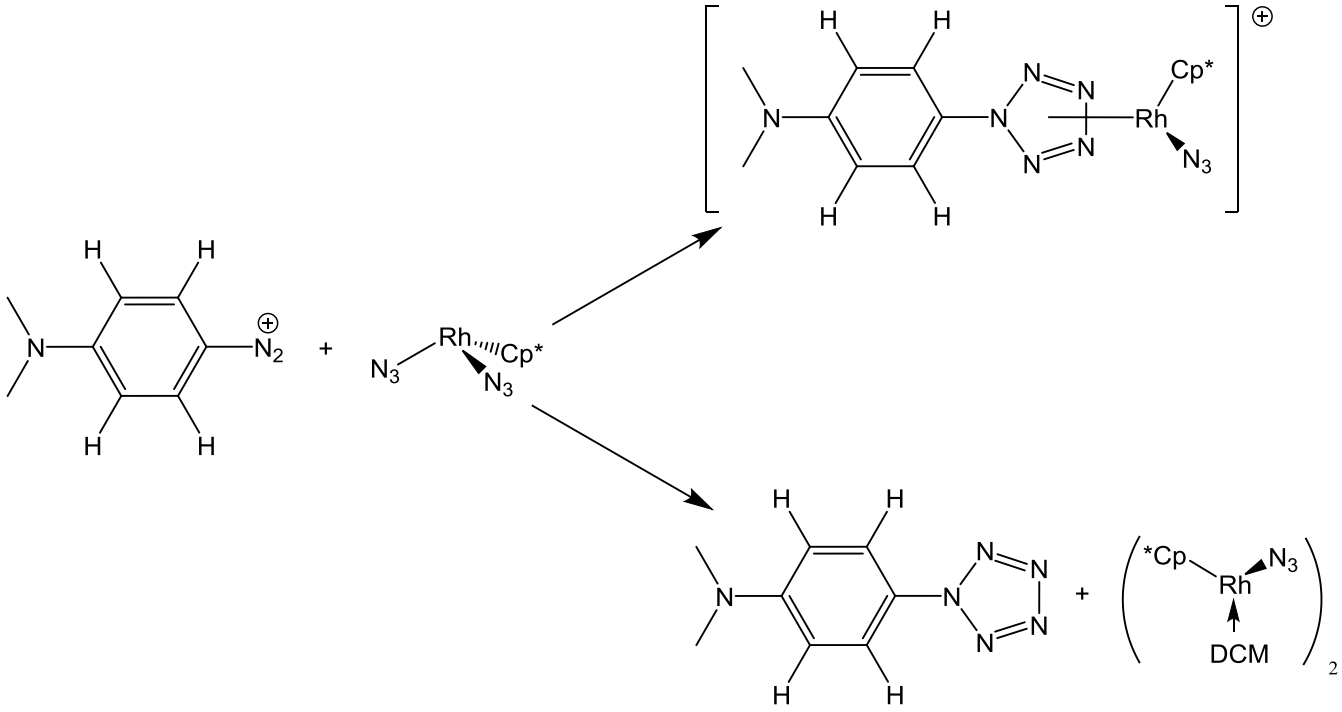

Scheme 35 – Possible reaction pathways for the observed reaction between DMAP-$N_2^+BF_4^-$ and $RhCp^*(N_3)_2$.

5.2.3 Re-crystallisation of arylpentazoles

A feature that is neglected within the field of arylpentazoles is their crystallisation. To date the crystal structure of only two arylpentazoles are known: phenylpentazole[36]and *p*-*d*imethylpheylpentazole (DMAP-pentazole).[92] Due to the nature of their preparation, in which the presence of the aryl-azide due to decomposition is unavoidable, crystallisation is vital in order to isolate the pure arylpentazole.

Many are washed to remove the majority of the impurities, but this is insufficient; without the pure arylpentazole any results from further studies would be skewed due to the contaminating presence of other compounds. Therefore deriving crystallisation procedures for other arylpentazoles would permit a more in depth approach to studying arylpentazoles, allowing analysis upon a wider range of crystalline compounds.

The first crystallisation attempt focussed upon hydroxyphenylpentazole.[101] This compound was chosen due its ability to form salts through deprotonation of the hydroxyl proton using base. The oxophenylpentazole salts[101] are amongst the most stable arylpentazoles, and the crystallisation of such a salt would be an interesting starting point for a range of studies. The preparation of *p*-hydroxyphenylpentazole follows an analogous procedure to the previously synthesised DMAP-pentazole, via the appropriate aniline.

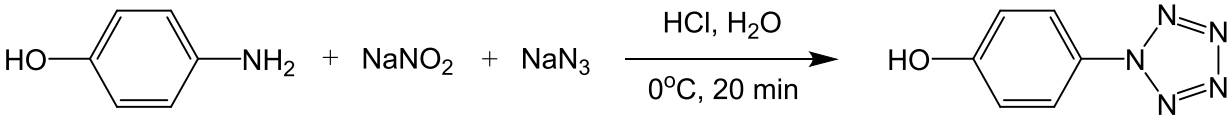

Scheme 36 – Preparation of *p*-hydroxyphenylpentazole.

The preparation resulted in a grey-green solid, which was analysed using IR spectroscopy. The IR spectrum confirmed that the preparation was a success, containing both strong pentazole and azide peaks. Without the crystallisation step, the azide peak at 2114 cm^{-1} (*) is much larger than the previously synthesised DMAP-pentazole. However, the *p*-hydroxyphenylpentazole is still present as evidenced by the peak at 1597 cm^{-1} (*).

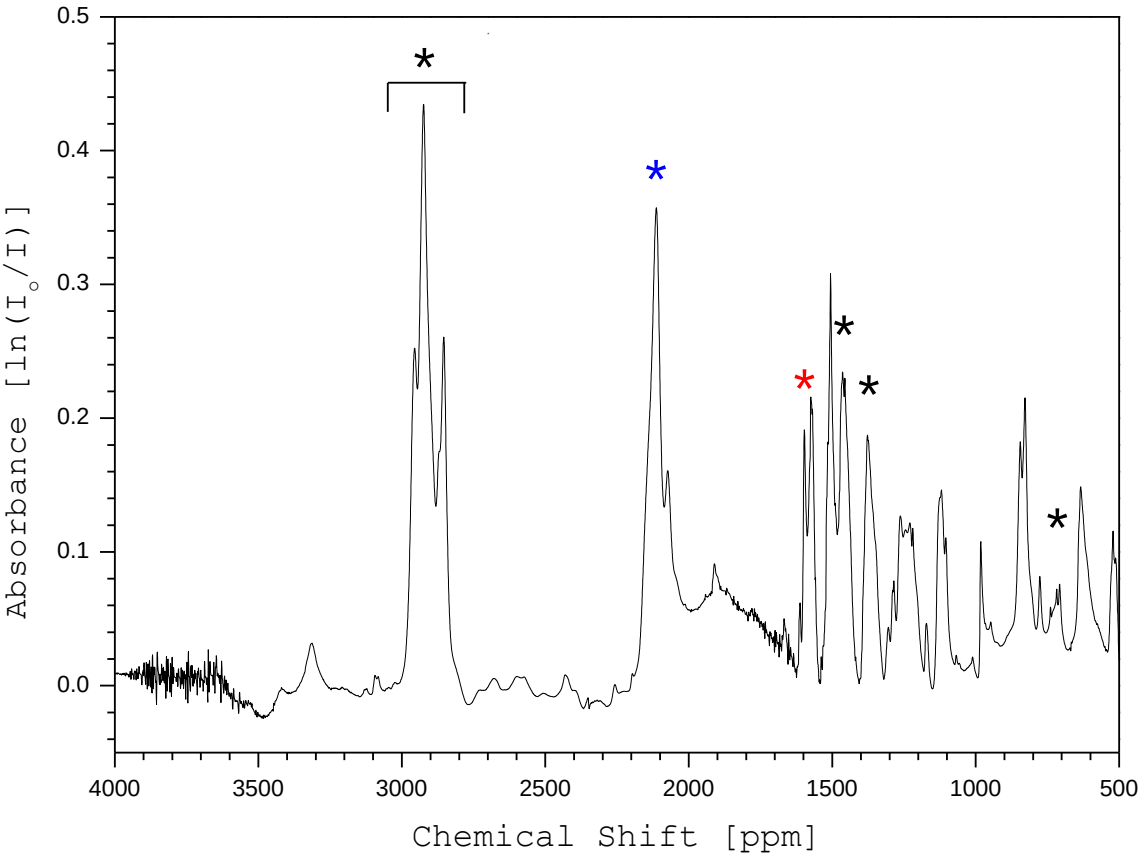

Figure 132 – Nujol mull IR spectrum of *p*-hydroxyphenylpentazole. The azide region (*) and the pentazole peak (*) are both indicated. Nujol bands are asterisked (*).

The presence of *p*-hydroxyphenylpentazole was strengthened by performing an IR decomposition study. The extent of decomposition can be monitored using the peak intensity at both the azide (*) and pentazole (*) positions.

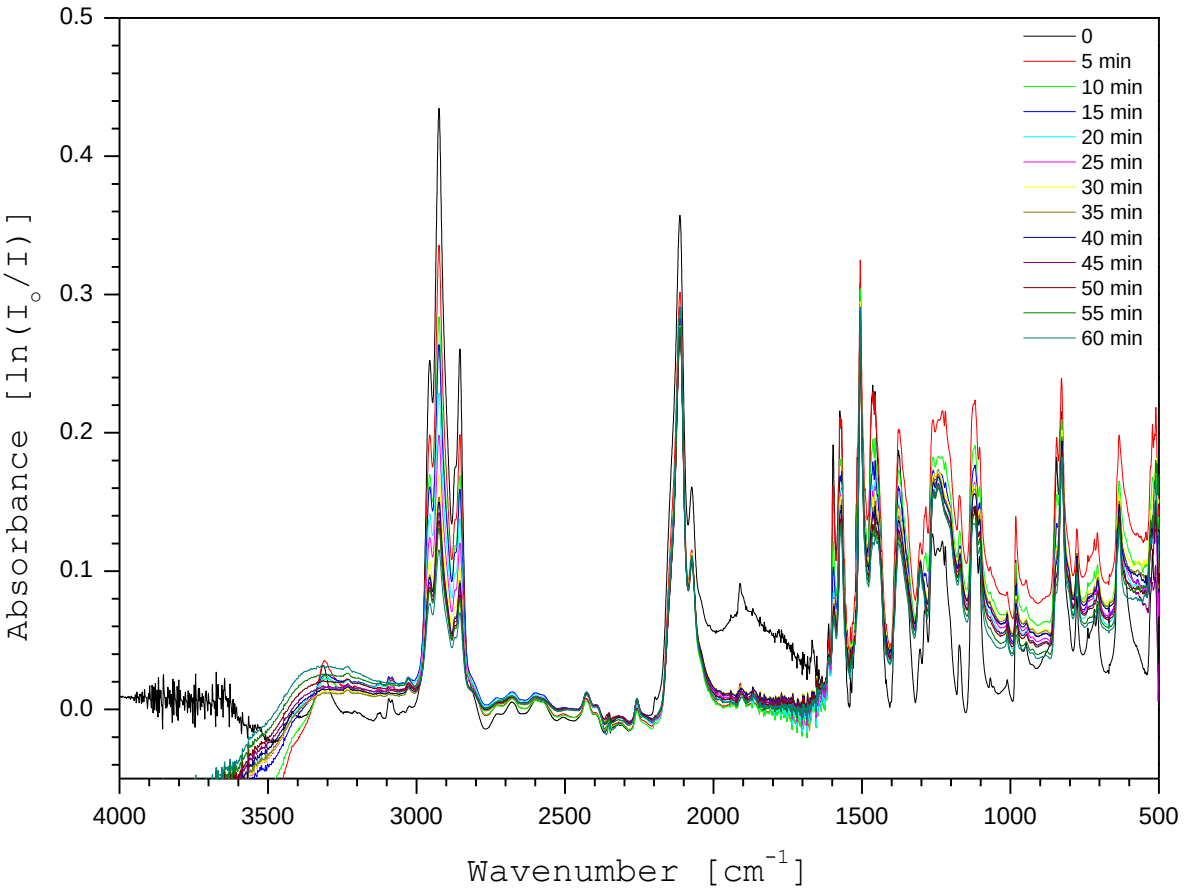

Figure 133 – IR spectral study observing the decomposition of *p*-hydroxyphenylpentazole over 1 h.

The high stability of *p*-hydroxyphenylpentazole requires a much longer study of the decomposition, with pentazole still remaining present after an hour. The crowded nature of the decomposition graph also makes interpretation difficult. The relationship between decomposition and the intensity of the *p*-hydroxyphenylpentazole and *p*-hydroxyphenylazide peaks can be simplified by simply plotting their respective peak intensities against time (figure 134). This clearly illustrates two points: a) the *p*-hydroxyphenylpentazole had indeed been synthesised and b) the decomposition can be effectively observed by monitoring the intensity of the azide and pentazole peaks using IR spectroscopy. It was expected that the decaying curve of the hydroxyphenylpentazole would be matched by the curve representing the produced hydroxyphenylazide. However this isn't the case; whilst the hydroxyphenylpentazole does appear to decay exponentially the hydroxyphenylazide curve is closer to a linear relationship.

Rather than indicating an issue with how the reaction has progressed this is most likely caused by the limitations of monitoring this decomposition using equipment that is not designed for low temperature chemistry.

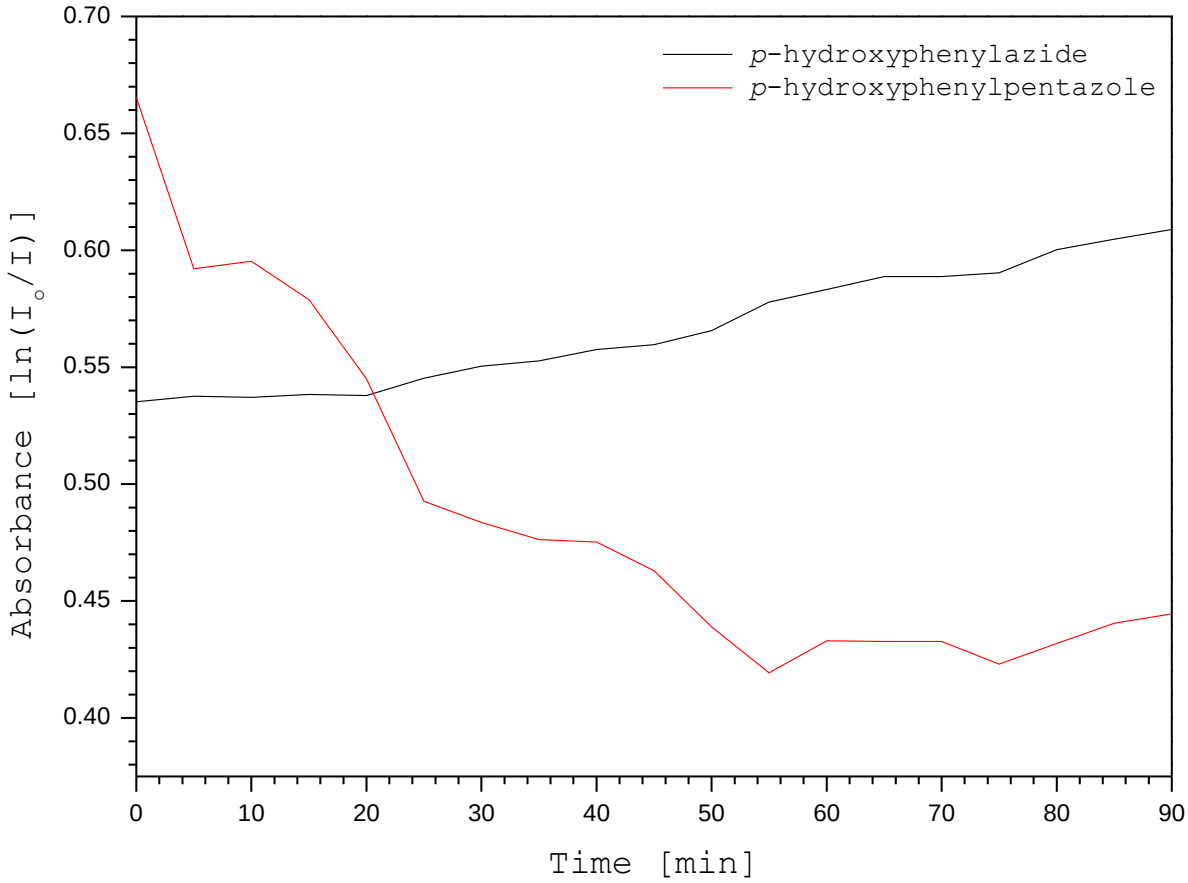

Figure 134 – Graph illustrating the change in peak intensity vs time with respect to both the *p*-hydroxyphenylazide peak and the *p*-hydroxyphenylpentazole peak. This information is adapted from figure 133, and illustrates the relationship between *p*-hydroxyphenylpentazole decomposition and *p*-hydroxyphenylazide generation.

Various crystallisations were attempted using DCM, Et_2O and toluene as crystallising solvents. It was important to choose a solvent which remains liquid at −78°C, as the low temperature nature of the preparation required cooling further to afford crystals, as shown by the crystallisation of both phenylpentazole and DMAP-pentazole. Both DCM and toluene did not produce crystalline material, even after a number of weeks at −78°C. The crystallisation using Et_2O was much more promising, producing a brown, crystalline mass. This was isolated and analysed using single crystal X-ray diffraction studies.

Upon submersion into the protective Nujol, the majority of the observed crystalline material melted into a brown liquid. The preparation of *p*-hydroxyphenylpentazole uses water as a solvent; therefore this can simply be explained by the crude product remaining wet. Nevertheless small, red-yellow crystals remained. These were quickly loaded into the cold nitrogen stream to protect the potentially temperature sensitive crystals. The data set was difficult to solve, possibly due to the contaminating nature of the aqueous melt, in addition to the likelihood of thermal sensitivity. Nonetheless, an attempt was made to solve the crystal structure, which indicates that the crystals could be those of the *p*-oxophenyldiazonium zwitterion. The formation of such a species would require the phenol proton of the *p*-hydroxyphenyldiazonium chloride salt to react with another reagent, possibly NaN_3 producing HN_3 and NaCl. The acidic nature of the reaction medium should minimise this side reaction. The observed crystals could also simply be the *p*-hydroxyphenyldiazonium cation, as the poor data set did not allow assignment of the protons. However the chlorine anion has a larger electron density and its absence suggests that the zwitterion could in fact be present. No acid was used during the separate crystallisation procedure; this could have facilitated the formation of the zwitterion. Disappointingly the poor quality of the crystals did not allow firm conclusions to be made.

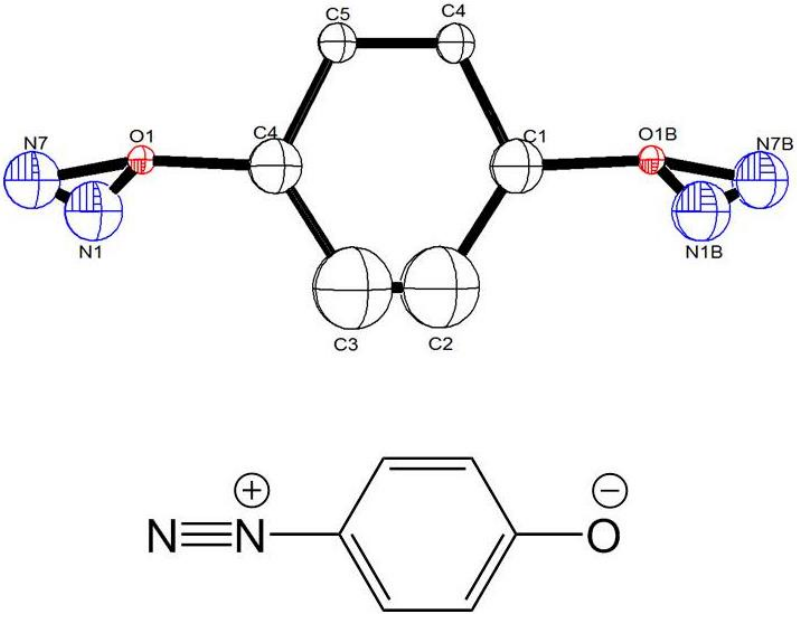

Figure 135 – Isotropic plot of the possible *p*-oxophenyldiazonium zwitterion (top) generated using ORTEP®. The molecule is disordered by rotation in the vertical axis, and a simplified chemdraw representation is included for clarity (bottom).

Preparation of the oxophenylpentazole (OPP) anion was attempted using tetrabutylammonium(TBA) hydroxide.

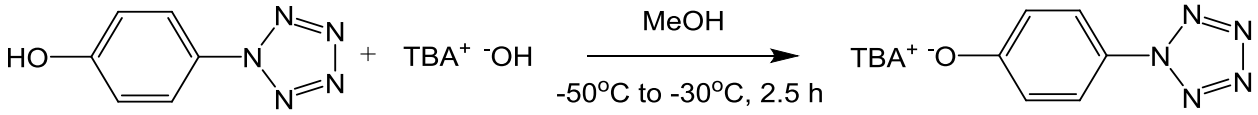

Scheme 37 – Attempted preparation of the tributylammonium salt of *p*-hydroxyphenylpentazole.

The resulting yellow solution was analysed using solution-cell IR spectroscopy. The decomposition of the dissolved TBA[OPP] was studied over 45 minutes (figure 136). This illustrated the significant peaks within the IR series; the growth of the peak at 2114 cm^{-1} (*) corresponds to the azide decomposition product whilst the dropping peak at 1584 cm^{-1} (*) is attributed to TBA[OPP].

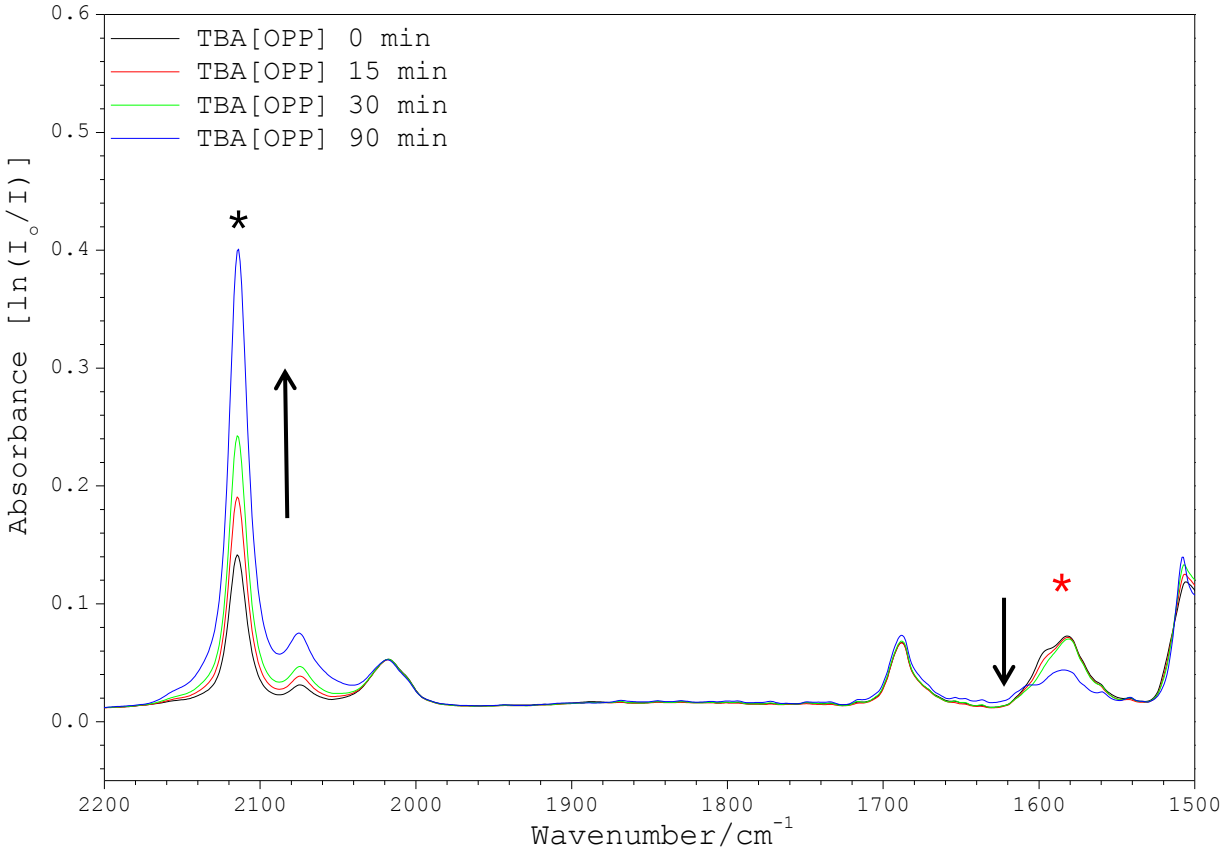

Figure 136 – 2200 cm^{-1} to 1500 cm^{-1} section of the IR spectral comparison detailing the decomposition of TBA[OPP]. The azide peak (*) and pentazole peak (*) are both highlighted.

The yellow solution was cooled to −78°C in an attempt to produce crystalline material. No crystals were observed after 72 hours and the DCM was deemed to be an unsuitable re-crystallisation solvent. It was removed under dynamic vacuum and replaced with toluene at −25°C. Although toluene dissolved $TBA^{+}Br^{-}$ well it did not dissolve the crude TBA[OPP] and instead resulted in a suspension. Subsequently Et_2O was also attempted and whilst this did result in a yellow solution it again did not yield crystalline material upon cooling to −78°C.

Although no re-crystallisation procedures were conceived the existing techniques for phenylpentazole and DMAP-pentazole suggest that it is simply a matter of finding a suitable solvent system. Time constraints restricted the number of solvents attempted, but a full investigation utilising a wide range of solvents would likely result in positive results.

5.3 Conclusions

The chemistry of this investigation was extremely challenging. This is highlighted by the incremental progress observed in the literature. Great strides have been made towards isolating the pentazole ring in a stable state;[32,102] however, at present it remains out of reach. The results from this study suggest that cleaving the C–N bond of an arylpentazole using a reducing agent is not a suitable method for the isolation of the N_5 ring. Attempts were made to cleave the C–N bond of DMAP-pentazole using the strong reducing agent sodium naphthalenide, and the milder reactant (^{mes}nacnac)Mg–Mg(nanac^{mes}) dimer. Whilst the sodium naphthalenide resulted in the production of DMAP-azide, the (^{mes}nacnac)Mg–Mg(nanac^{mes}) dimer did not react with DMAP-pentazole at the necessary low temperature. The combination of reduction potential and steric properties would be difficult to find, and based upon these results it seems as this is an unlikely path to success.

Prior stabilisation of the pentazole ring could result in the selective cleavage of the C–N bond. Although not attempted during this investigation, it would be of great interest to observe whether the pentazole ring could co-ordinate to a metal centre if the centre in question possessed a vacant site. An example of this is $W(CO)_5(MeCN)$, which contains a labile solvent molecule co-ordinated to the metal centre. Removal of the solvent molecule and subsequent reaction with an arylpentazole could allow the pentazole ring to replace it, "protecting" the ring in the process. If co-ordination is successful, a reducing agent could be forced to act upon the C–N bond, allowing the isolation and characterisation of free pentazolate.

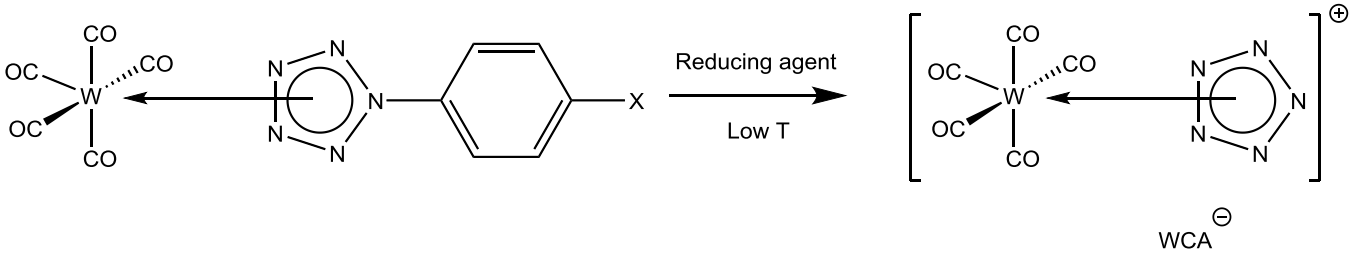

Scheme 38 – Reduction of W-stabilised arylpentazole (WCA = weakly co-ordinating anion).

In contrast, the attempted synthesis of a metal-bound arylpentazole was a highly encouraging study. Evidence was found within the ^{1}H NMR series that suggested the DMAP-pentazole had been synthesised, and upon warming the expected proton environments for the DMAP-azide were observed. This supports the conclusion that the DMAP-pentazole had indeed been synthesised as this observation can only be explained by the decomposition of DMAP-pentazole. However the metal-bound nature of the product is unclear, requiring further investigations to extend upon these results and fully characterise all products of the reaction. This could be achieved by performing a full-scale preparation and isolating the products in question. If re-crystallisation is possible, this would represent a unique result with great significance to this field.

The final part of this investigation concerned the crystallisation of existing arylpentazoles. Based upon the high stability of *p*-hydroxyphenylpentazole and its respective salts this was the focus of the first attempt. To perform further studies upon arylpentazoles it is vital that all material is crystalline. At present this is limited to just phenylpentazole and the familiar DMAP-pentazole. In order to further the pentazole knowledge base it is necessary to acquire crystallisation procedures for additional arylpentazoles, with substituents of different steric and electronic effects. The nature of the *para*- substituent allows flexibility upon the overall nature of the arylpentazole. Therefore, possessing a range of crystalline *para*- substituted arylpentazoles would allow an in-depth investigation into their respective stability, reactivity and mechanistic characteristics.

6. References

(1) Demko, Z. P.; Sharpless, K. B. *J. Org. Chem.* **2001**, *66* (24), 7945–7950.

(2) Klapötke, T. M.; Stein, M.; Stierstorfer, J. *Z. Anorg. Allg. Chem.* **2008**, *634* (10), 1711–1723.

(3) Clayden; Greeves; Warren; Worthers. *Organic Chemistry*; Oxford University Press: Oxford, 2001.

(4) Roh, J.; Vavrova, K.; Hrabalek, A. *Eur. J. Org. Chem.* **2012**, *31*, 6101–6118.

(5) Franke, P.; Groeneveld, W. *Transit. Met. Chem.* **1981**, *6*, 54–56.

(6) Franke, P. L.; Haasnoot, J. G.; Zuur, A. P. *Inorg. Chem. Acta* **1982**, *59*, 5–9.

(7) Ordejon, B.; de Graaf, C.; Sousa, C. *J. Am. Chem. Soc.* **2008**, *130*, 13961–13968.

(8) Kusz, J.; Spiering, H.; Gütlich, P. *J. Appl. Crystallogr.* **2004**, *37* (4), 589–595.

(9) Liu, F.-C.; Liang, J.-E.; Jin, J.-Y.; Lin, Y.-L.; Chu, Y.-J.; Yang, P.-S.; Lee, G.-H.; Peng, S.-M. *J. Organomet. Chem.* **2013**, *735*, 1–9.

(10) Shahroosvand, H.; Najafi, L.; Mohajerani, E.; Janghouri, M.; Nasrollahzadeh, M. *RSC Adv.* **2013**, *3* (18), 6323–6326.

(11) Li, S.; Wang, Y.; Qi, C.; Zhao, X.; Zhang, J.; Zhang, S.; Pang, S. *Angew. Chem. Int. Ed. Engl.* **2013**, *52*, 14031–14035.

(12) Aromí, G.; Barrios, L. a.; Roubeau, O.; Gamez, P. *Coord. Chem. Rev.* **2011**, *255*, 485–546.

(13) Wang, X.; Tang, Y.; Huang, X.; Qu, Z.; Che, C.; Wai, P.; Chan, H.; Xiong, R.; Road, P.; Kong, H. **2005**, *44* (15), 5278–5285.

(14) He, X.; Lu, C.; Yuan, D. *Inorg. Chem* **2006**, *45*, 5760–5766.

(15) He, X.; Wu, C.; Li, M.; Batten, S. R. *Inorg. Chem. Commun.* **2008**, *11*, 1378–1381.

(16) Gronde, I.; Mitzel, N. W. *Zeitschrift für Anorg. und Allg. Chemie* **2009**, *635*, 1313–1320.

(17) Wann, D. a; Gronde, I.; Foerster, T.; Hayes, S. a; Masters, S. L.; Robertson, H. E.; Mitzel, N. W.; Rankin, D. W. H. *Dalton Trans.* **2008**, No. 29, 3817–3823.

(18) Hill, M.; Mahon, M. F.; Mcginley, J.; Molloy, K. C. *Dalt. Trans.* **1996**, 835–845.

(19) Musher, J. *Angew. Chem. Int. Ed.* **1969**, *8* (1), 54–68.

(20) Shriver, D.; Atkins, P.; Langford, C. *Inorganic Chemistry*; Oxford, 1990.

(21) Eremets, M. I.; Gavriliuk, A. G.; Trojan, I. a; Dzivenko, D. a; Boehler, R. *Nat. Mater.* **2004**, *3* (8), 558–563.

(22) Orlandi, G.; Gagliardi, L. *J. Chem. Phys.* **2001**, *114* (24), 10733–10737.

(23) Christe, K. O.; Wilson, W. W. *J. Am. Chem. Soc.* **2004**, *126* (3), 834–843.

(24) Straka, M.; Pyykkö, P. *Inorg. Chem.* **2003**, *42* (25), 8241–8249.

(25) Christe, K. O.; Wilson, W. W.; Sheehy, J. A.; Boatz, J. A. *Angew. Chemie Int. Ed.* **1999**, *38*, 2004–2009.

(26) Atkins, P. *Physical Chemistry*; Oxford University Press: Oxford, 2006.

(27) Glukhovtsev, M. N.; Jiao, H.; Schleyer, P. V. R. *Inorg. Chem.* **1996**, *35* (24), 7124–7133.

(28) Vij, A.; Wilson, W. W.; Vij, V.; Tham, F. S.; Sheehy, J. a; Christe, K. O. *J. Am. Chem. Soc.* **2001**, *123* (26), 6308–6313.

(29) Christe, K. O.; Wilson, W. W.; Dixon, D. a.; Khan, S. I.; Bau, R.; Metzenthin, T.; Lu, R. *J. Am. Chem. Soc.* **1993**, *115* (5), 1836–1842.

(30) Klapötke, T. M. *Angew. Chem. Int. Ed.* **1999**, *38* (17), 2536–2538.

(31) Nguyen, M. T.; McGinn, M. A.; Hegarty, A. F.; Elguero, J. *Polyhedron* **1985**, *4* (10), 1721–1726.

(32) Butler, R. N.; Hanniffy, J. M.; Stephens, J. C.; Burke, L. a. *J. Org. Chem.* **2008**, *73* (4), 1354–1364.

(33) Vij, A.; Pavlovich, J. G.; Wilson, W. W.; Vij, V.; Christe, K. O. *Angew. Chem. Int. Ed.* **2002**, No. 16, 3051–3054.

(34) Huisgen, R.; Ugi, I. *Chem. Ber.* **1957**, *90* (12), 2914–2927.

(35) Carlqvist, P.; Ostmark, H.; Brinck, T. *J. Org. Chem.* **2004**, *69* (9), 3222–3225.

(36) Ugi, I. *Comp. Heterocycl. Chem.* **1984**, *5*, 839–845.

(37) Ugi, I.; Perlinger, H.; Behringer, L. *Eur. J. Inorg. Chem.* **1958**, *91*, 2324–2329.

(38) Muller, B. R.; Wallis, J. D.; Philipsborn, W. Von. *Angew. Chem. Int. Ed.* **1985**, *24*, 513–515.

(39) Muller, J. *Z. Naturforsch B* **1979**, *34*, 437–441.

(40) Perera, S. A.; Gregusová, A.; Bartlett, R. J. *J. Phys. Chem. A* **2009**, *113* (13), 3197–3201.

(41) Steinhauser, G.; Klapötke, T. M. *Angew. Chem. Int. Ed.* **2008**, *47* (18), 3330–3347.

(42) Fischer, D.; Klapötke, T. M.; Piercey, D. G.; Stierstorfer, J. *Chem. Eur. J.* **2013**, *19*, 4602–4613.

(43) Ghule, V. D.; Radhakrishnan, S.; Jadhav, P. M. *Struct. Chem.* **2011**, *22* (4), 775–782.

(44) Haiges, R.; Christe, K. O. *Inorg. Chem.* **2013**, *52* (12), 7249–7260.

(45) Wei, T.; Wu, J.; Zhu, W.; Zhang, C.; Xiao, H. *J. Mol. Model.* **2012**, *18* (8), 3467–3479.

(46) Saikia, a; Sivabalan, R.; Polke, B. G.; Gore, G. M.; Singh, A.; Subhananda Rao, A.; Sikder, a K. *J. Hazard Mater.* **2009**, *170* (1), 306–313.

(47) Housecraft, C.; Sharpe, A. *Inorganic Chemistry*, 3rd edn.; Pearson Education: London, 2007.

(48) Thiele, J. *Justus Liebigs Ann. Chem.* **1898**, *303*, 57–75.

(49) Hammerl, A.; Holl, G.; Klapötke, T. M.; Mayer, P.; Nöth, H.; Piotrowski, H.; Warchhold, M. *Eur. J. Inorg. Chem.* **2002**, 834–845.

(50) Xue, H.; Gao, Y.; Twamley, B.; Shreeve, J. M. *Inorg. Chem.* **2005**, *44* (14), 5068–5072.

(51) Ye, C.; Xiao, J.-C.; Twamley, B.; Shreeve, J. M. *Chem. Commun.* **2005**, No. 21, 2750–2752.

(52) Guo, Y.; Tao, G.-H.; Zeng, Z.; Gao, H.; Parrish, D. a; Shreeve, J. M. *Chemistry* **2010**, *16* (12), 3753–3762.

(53) Hammerl, A.; Hiskey, M. A.; Holl, G.; Klapotke, T. M.; Polborn, K.; Stierstorfer, J.; Weigand, J. J. *Chem. Mater.* **2005**, *17*, 3784–3793.

(54) Fischer, N.; Klapötke, T. M.; Reymann, M.; Stierstorfer, J. *Eur. J. Inorg. Chem.* **2013**, No. 12, 2167–2180.

(55) Deng, H.; Doonan, C. J.; Furukawa, H.; Ferreira, R. B.; Towne, J.; Knobler, C. B.; Wang, B.; Yaghi, O. M. *Science (80-.).* **2010**, *327*, 846–850.

(56) Férey, G.; Mellot-Draznieks, C.; Serre, C.; Millange, F.; Dutour, J.; Surblé, S.; Margiolaki, I. *Science (80-.).* **2005**, *309*, 2040–2042.

(57) Chen, B. *Science (80-.).* **2001**, *291*, 1021–1023.

(58) Horcajada, P.; Serre, C.; Maurin, G.; Ramsahye, N. A.; Balas, F.; Sebban, M.; Taulelle, F.; Vallet-Regi, M.; Ferey, G. *J. Am. Chem. Soc.* **2008**, *130*, 6774–6780.

(59) Horcajada, P.; Chalati, T.; Serre, C.; Gillet, B.; Sebrie, C.; Baati, T.; Eubank, J. F.; Heurtaux, D.; Clayette, P.; Kreuz, C.; Chang, J.-S.; Hwang, Y. K.; Marsaud, V.; Bories, P.-N.; Cynober, L.; Gil, S.; Férey, G.; Couvreur, P.; Gref, R. *Nat. Mater.* **2010**, *9* (2), 172–178.

(60) Horcajada, P.; Serre, C.; Vallet-Regi, M.; Sebban, M.; Taulelle, F.; Ferey, G. *Angew. Chemie - Int. Ed.* **2006**, *45* (36), 5974–5978.

(61) Lee, J.; Farha, O. K.; Roberts, J.; Scheidt, K. A.; Nguyen, S. T.; Hupp, J. T. *Chem Soc Rev* **2009**, *38* (5), 1450–1459.

(62) Wang, Z.; Chen, G.; Ding, K. *Chem. Rev.* **2009**, *109* (2), 322–359.

(63) Wang, X.-J.; Li, P.-Z.; Chen, Y.; Zhang, Q.; Zhang, H.; Chan, X. X.; Ganguly, R.; Li, Y.; Jiang, J.; Zhao, Y. *Sci. Rep.* **2013**, *3*, 1149.

(64) Pachfule, P.; Banerjee, R. *Cryst. Growth Des.* **2011**, *11*, 5176–5181.

(65) Bushuyev, O. S.; Peterson, G. R.; Brown, P.; Maiti, A.; Gee, R. H.; Weeks, B. L.; Hope-Weeks, L. J. *Chem. - A Eur. J.* **2013**, *19*, 1706–1711.

(66) Wu, B.-D.; Yang, L.; Wang, S.-W.; Zhang, T.-L.; Zhang, J.-G.; Zhou, Z.-N.; Yu, K.-B. *Zeitschrift für Anorg. und Allg. Chemie* **2011**, *637* (3-4), 450–455.

(67) Zhang, Q.; Shreeve, J. M. *Angew. Chem. Int. Ed. Engl.* **2014**, *53* (10), 2540–2542.

(68) Ek, S.; Rehn, S.; Wahlström, L. Y.; Östmark, H. *J. Heterocycl. Chem.* **2013**, *50*, 261–267.

(69) Nudelman, A. *J. Org. Chem.* **1997**, *62*, 7512–7515.

(70) James, L. Synthesis and Reactivity of Main Group Coordination Complexes Bearing N-containing Ligands, 2013.

(71) Portius, P.; Campbell, R. *Chem. Eur. J.* **2016**, *21*, 18690–18698.

(72) Portius, P.; Campbell, R. In Preparation, 2016.

(73) Portius, P.; Davis, M. In Preparation, 2016.

(74) Sedgwick, N. . *Z Elktrochem. Angew. P.* **1928**, *34*, 445–450.

(75) Holleman, A. F.; Wiberg, N. *Inorganic Chemistry*; Academic Press: Cambridge, 2001.

(76) Drago, R. *J. Phys. Chem.* **1958**, *62* (3), 353–357.

(77) Schwerdtfeger, P.; Heath, G. a.; Dolg, M.; Bennett, M. a. *J. Am. Chem. Soc.* **1992**, *114*,

7518–7527.

(78) Sutton, T. C. *Nature* **1934**, *133*, 463–463.

(79) Choi, C.; Prince, E.; Garrett, W. *Acta Cryst.* **1977**, *33*, 3536–3537.

(80) Peerless, B.; Keane, T.; Meijer, A. J. H. M.; Portius, P. *Chem. Commun.* **2015**, *51* (35), 7435–7438.

(81) Hassel, O. *Science (80-.).* **1970**, *170* (3957), 497–502.

(82) Portius, P.; Filippou, A. C.; Schnakenburg, G.; Davis, M.; Wehrstedt, K.-D. *Angew. Chem. Int. Ed.* **2010**, *49* (43), 8013–8016.

(83) Pirnat, J. *J. Mol. Struct.* **1980**, *58*, 547–554.

(84) Seyferth, D. *Society* **2001**, *III* (2), 1488–1498.

(85) Downs, A. J.; Hunt, N. I.; McGrady, G. S.; Rankin, D. W. H.; Robertson, H. E. *J. Mol. Struct.* **1991**, *248* (3-4), 393–406.

(86) Paneth, F.; Loleit, H. *J. Chem. Soc.* **1935**, 366–371.

(87) Bystrom, A.; Westgren, A. *Ark. Kemi.* **1943**, *17* (1).

(88) Edwards, A. *J Chem. Soc. A* **1970**, *111*, 2571–2753.

(89) Greis, O.; Martinez-Ripoll, M. *Z. Anorg. Allg. Chem.* **1977**, *432*, 105–112.

(90) Angoletta, M.; Caglio, G. *J. Organomet. Chem.* **1982**, *234*, 99–105.

(91) Yamamoto, Y.; Kosaka, Y.; Tsutsumi, Y. *Eur. J. Inorg. Chem.* **2003**, *16* (1981), 2–7.

(92) Portius, P.; Davis, M.; Campbell, R.; Hartl, F.; Zeng, Q.; Meijer, A. J. H. M.; Towrie, M. *J. Phys. Chem. A* **2013**, *117*, 12759–12769.

(93) Butler, R. N.; Fox, A.; Burke, L. A. *J. Chem. Soc., Perk. Trans. 2* **1998**, *2*, 2243–2247.

(94) Butler, R. N.; Stephens, J. C.; Hanniffy, J. M. *Tetrahedron Lett.* **2004**, *45* (9), 1977–1979.

(95) Gómez-Zavaglia, a.; Ismael, A.; Cabral, L. I. L.; Kaczor, A.; Paixão, J. a.; Fausto, R.; Cristiano, M. L. S. *J. Mol. Struct.* **2011**, *1003*, 103–110.

(96) Stasch, A.; Jones, C.; Bonyhady, S. J.; Green, S. P.; Nembenna, S. *Angew. Chem. Int. Ed. Engl.* **2009**, *48*, 2973–2977.

(97) Stasch, A.; Bonyhady, S. J.; Jones, C.; Nembenna, S.; Edwards, A. J.; Mcintyre, G. J. *Chem. Eur. J.* **2010**, *16*, 938–955.

(98) Green, S. P.; Jones, C.; Stasch, A. *Science (80-.).* **2007**, *318* (December), 1754–1757.

(99) Ferris, K. F.; Bartlett, R. J. *J. Am. Chem. Soc.* **1992**, *114* (12), 8302–8303.

(100) Tabei, K.; Ito, C. *B. Chem. Soc. Jpn.* **1968**, *41* (2), 514–515.

(101) Benin, V.; Kaszynski, P.; Radziszewski, J. G. *J. Org. Chem.* **2002**, *67* (4), 1354–1358.

(102) Geiger, U.; Haas, Y.; Grinstein, D. *J. Photochem. Photobiol. A Chem.* **2014**, *277*, 53–61.